

An Experimental Study of Plasma Fluctuations in the TCV and TEXTOR Tokamaks

THÈSE N° 5610 (2013)

PRÉSENTÉE LE 11 JANVIER 2013
À LA FACULTÉ DES SCIENCES DE BASE
CRPP - PHYSIQUE DU TOKAMAK TCV
PROGRAMME DOCTORAL EN PHYSIQUE

ÉCOLE POLYTECHNIQUE FÉDÉRALE DE LAUSANNE

POUR L'OBTENTION DU GRADE DE DOCTEUR ÈS SCIENCES

PAR

Cornelis Adrianus DE MEIJERE

acceptée sur proposition du jury:

Prof. O. Schneider, président du jury
Dr S. Coda, directeur de thèse
Dr S. Brunner, rapporteur
Prof. E. Gusakov, rapporteur
Dr P. Hennequin, rapporteur



ÉCOLE POLYTECHNIQUE
FÉDÉRALE DE LAUSANNE

Suisse
2013

An electronic version is available for download from
<http://library.epfl.ch/theses/?nr=5610>

Please cite this publication as:

C.A. de Meijere, "An experimental study of plasma fluctuations in the TCV and TEXTOR tokamaks", *PhD thesis no. 5610, École Polytechnique Fédérale de Lausanne (EPFL), CH-1015 Lausanne, Switzerland, December 2012.*

e-mail: kees.demeijere@epfl.ch, demeijere@gmail.com

Lausanne, December 19, 2012



ÉCOLE POLYTECHNIQUE
FÉDÉRALE DE LAUSANNE



Abstract

The main body of this thesis reports on the commissioning and first measurements with a novel tangential phase-contrast imaging (TPCI) diagnostic, which had previously been installed in the TCV tokamak. The instrument measures fluctuations in line-integrated electron density along 9 parallel chords within a 6 cm diameter CO₂ laser beam.

TPCI measurements reveal the first evidence in TCV of the geodesic acoustic mode (GAM), which is an oscillating zonal flow. Frequency, radial wavelength, radial extent and propagation are all in qualitative agreement with a gyro-kinetic simulation and recent theoretical work. The mode is found to have a modest, but measurable magnetic component, whose spatial structure is characterised for the first time in a toroidal plasma. For some experiments, clear evidence is found of the theoretically expected $m/n = 2/0$ mode structure, although in others the structure appears to be more complex.

Electron energy confinement in X2 heated TCV L-mode plasmas had previously been observed to increase on changing the triangularity (δ) of the poloidal plasma cross-section from $\delta = +0.4$ to $\delta = -0.4$. Measurements with the TPCI diagnostic reveal that this change coincides with a clear decrease in both the absolute level and the decorrelation time of broadband electron density fluctuations. This is in agreement with the conjecture that the increased confinement time is caused by a change in the turbulent state.

The second part of the thesis reports on a fluctuation study in the TEXTOR tokamak. At sufficiently weak toroidal magnetic field, NBI heated, limited TEXTOR plasmas exhibit bursts of beam-ion driven ‘fishbone’ and Alfvén modes, which are characterised using the multi-antenna reflectometer and Mirnov coils. In H-mode the fishbone triggers ELMs and in L-mode it triggers previously unobserved bursts of particle recycling, resembling the ELMs. The reflectometer phase shows statistically significant bispectral coherence between the fishbone and the Alfvén modes, indicative of non-linear coupling between them.

Additionally, using conditional averaging techniques, two ELM precursor modes are found that are not related to the beam-ions. The first is a global mode with toroidal mode number $n = -2$, which is also seen with the Mirnov coils. Bispectral analysis of the reflectometer signals shows that this mode modulates the amplitude of broad-band turbulence in the pedestal. The second ELM precursor is a down-chirping mode with a poloidal wavelength of 6 cm.

keywords: tokamak, plasma, phase-contrast imaging, reflectometry, zonal flow, edge-localised modes

Version Abrégée

La partie principale de cette thèse se rapporte à la mise en service et les premières mesures avec un nouveau diagnostique de contraste de phase tangentiel (TPCI), qui a été développé auparavant pour le tokamak TCV. Le dispositif mesure l'intégrale de fluctuations de densité électronique le long de neuf lignes de visée parallèles au sein d'un faisceau laser à CO₂ d'un diamètre de 6 cm.

Les mesures TPCI mettent en évidence pour la première fois dans TCV l'existence du mode géodésique acoustique (GAM), qui est un flux zonal oscillant. Sa fréquence, longueur d'onde, propagation et localisation sont toutes en accord qualitatif avec une simulation gyrocinétique globale de turbulence et avec de récentes études théoriques. Le mode possède une faible mais mesurable composante magnétique, dont la structure a été mesurée pour la première fois dans un plasma toroïdal. Pour certaines expériences la structure $m/n = 2/0$, qui est attendue théoriquement, est clairement observée; d'autres expériences montrent une structure plus complexe.

Le confinement des électrons dans des plasmas en mode L chauffés par X2, s'améliore fortement quand la triangularité δ de la section poloidale du plasma dans TCV passe de $\delta = +0.4$ à $\delta = -0.4$. Des mesures TPCI montrent que ce changement correspond à une réduction de l'amplitude et du temps de décorrélation des fluctuations de densité électronique à large bande. Ceci est cohérent avec l'hypothèse selon laquelle la croissance du temps de confinement est liée à un changement de l'état turbulent du plasma.

La deuxième partie de cette thèse se rapporte à une étude de fluctuations dans le tokamak TEXTOR. Pour un champ magnétique suffisamment faible, des plasmas limités et chauffés par injection de neutres dans TEXTOR montrent des éclats de modes dits 'fishbone' et Alfvéniques, déstabilisés par une interaction avec les ions suprathermiques du faisceau. Ces modes sont étudiés par le truchement d'un réflectomètre à antennes multiples et des bobines de Mirnov. En mode H, le fishbone déclenche des ELMs, et en mode L il déclenche des éclats de recyclage qui ressemblent aux ELMs. La phase du réflectomètre montre un niveau significatif de cohérence bispectrale entre le fishbone et les modes Alfvéniques, ce qui indique un couplage non-linéaire entre ces modes.

Une analyse de moyennage conditionnel démontre l'existence dans TEXTOR de deux autres modes qui sont également liés au cycle des ELMs, mais qui sont indépendants des ions suprathermiques. Le premier est un mode global possédant un nombre d'onde toroïdal $n = -2$. Une analyse de cohérence bispectrale de la phase du réflectomètre met en évidence que ce mode module l'amplitude de la turbulence dans la région à gradient élevé au bord du plasma. Le deuxième, dont la longueur d'onde poloidale est de 6 cm, a une fréquence qui décroît avant le déclenchement de l'ELM.

Mots clés: tokamak, plasma, contraste de phase, réflectometrie, flux zonal,

edge-localised modes

Contents

Abstract	iii
Version Abrégée	v
Contents	vii
1 Introduction	1
1.1 Nuclear fusion and tokamaks	1
1.2 Motivation for fluctuation studies	2
1.3 Synopsis of experimental results	5
1.4 Thesis outline	6
2 The phase-contrast imaging technique	7
2.1 Electromagnetic waves in a homogeneous plasma	9
2.2 Phase shifts in the WKB approximation	12
2.3 Measuring the phase shift	15
2.4 Localisation of the measurement	19
2.5 Optical transfer function of the phase-contrast method	21
2.6 Data analysis techniques	23
3 The tangential phase-contrast imaging diagnostic in TCV	27
3.1 The TCV tokamak	27
3.2 Geometry of the measurement	30
3.3 Beam path and plasma facing mirrors	34
3.4 Imaging optical system	38
3.5 Image detection and acquisition	44
3.6 Tests and characterisation of the imaging system with acoustic waves	45
3.7 Feedback vibration-control system	50
4 Turbulence and zonal flows in the TCV tokamak	63
4.1 The effect of triangularity on broadband fluctuations	64
4.2 Review of the literature on geodesic acoustic modes	70
4.3 Density component of the geodesic acoustic mode	74
4.4 Magnetic component and frequency of the geodesic acoustic mode	77
4.5 Numerical simulation of the geodesic acoustic mode in TCV	81
4.6 Numerical modelling of the TPCI signals	86

CONTENTS

5	Turbulence and beam-ion driven modes in the TEXTOR tokamak	91
5.1	Experimental technique	92
5.2	Experimental setup	100
5.3	Fluctuation measurements in the TEXTOR tokamak	106
5.4	Discussion of experimental results	116
6	Summary and suggestions for future work	121
6.1	Summary	121
6.2	Suggestions for future work	122
	Acknowledgements	125
	Bibliography	136
	Curriculum Vitae	137

Chapter 1

Introduction

Thermonuclear plasmas exhibit both global and local instabilities, which will play an important role in the performance of a future fusion reactor. This motivates the study of these phenomena in experimental fusion machines and the development of sophisticated measurement instruments (diagnostics).

This thesis reports on two experimental studies of plasma fluctuations in the TCV and TEXTOR devices. We discuss the motivation for these studies in §1.2, after a brief introduction to nuclear fusion (§1.1). The results of the thesis are summarised in §1.3, which is followed by a detailed outline of the rest of the document in §1.4.

1.1 Nuclear fusion and tokamaks

Fusion reactions of light atomic nuclei can potentially be harnessed for power generation (Freidberg 2007). Since the reaction cross sections only become appreciable at high temperatures (~ 1 keV or higher), the reactants exist in the plasma state. Additionally, the fusion rate scales with density: reactor plasmas must therefore be hot and dense. To keep the reaction going in steady state, heat losses to the environment must be balanced by the reaction products, complemented if necessary by external heating. For a fusion reactor to be viable, such losses must clearly be kept to a fraction of the useful power output. Thermal isolation of the plasma from its environment is therefore paramount.

Various magnetic confinement schemes exist, all based on the idea that pressure gradients in a plasma can be balanced by the Lorentz force, through a suitable configuration of current and magnetic field. The principal example is the tokamak configuration (Wesson 2011). It is characterised by toroidal symmetry, a strong, externally applied toroidal magnetic field, and a toroidal plasma current, as sketched in figure 1.1. This current generates a ‘poloidal’ magnetic field component, resulting in helical magnetic field lines. It is typically driven mainly through induction, limiting operation to pulses of finite duration. An important challenge in the development of a steady-state tokamak reactor is therefore the perfection of techniques for driving current by non-inductive means.

Although significant fusion rates can be achieved transiently in the largest of today’s tokamaks (Keilhacker et al. 1999), the quality of plasma confinement in these devices is insufficient for net power production. Since confinement improves with the size of the plasma, bigger machines are needed to demonstrate the feasibility of a fusion power

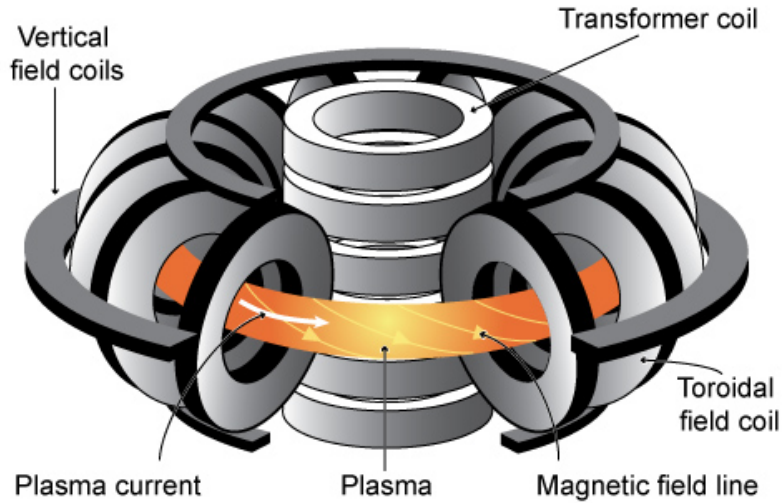


Figure 1.1: The tokamak configuration.

plant. Such a demonstration is the primary goal of the ITER tokamak, which is presently under construction. Crucial physics issues which will be addressed by experiments in ITER include the confinement of energetic fusion products, as well as the impact of edge instabilities (Ikeda 2007).

1.2 Motivation for fluctuation studies

Turbulence and zonal flows

The efficiency with which energy and particles are confined is determined by the rate of cross-field transport. Experimentally, this rate is typically seen to be significantly above the level expected on the basis of Coulomb collisions (the so-called ‘neo-classical’ transport). The difference is caused by small-scale convective flows associated with the broadband turbulence which is a universal feature of tokamak plasmas (Tynan et al. 2009). Turbulence arises from non-linear interaction of micro-instabilities, a broad class of modes whose theoretical description requires kinetic effects. These are effects coming from the dynamics of the distribution function in velocity space. Drift waves constitute an important example. Relevant sources of free energy include gradients of density, temperature (of electrons or ions) or current density, but also non-Maxwellian distribution functions.

A turbulent plasma is a complex physical system that exhibits self-organisation. An important example is the zonal flow phenomenon (Diamond et al. 2005). Zonal flows are a perturbation of the electric potential which is constant on magnetic surfaces, but oscillates radially. This results in sheared $\mathbf{E} \times \mathbf{B}$ flows. Zonal flows are driven exclusively by non-linear interaction with small-scale turbulence. Since sheared $\mathbf{E} \times \mathbf{B}$ flows tend to *reduce* turbulence amplitude, the interaction between zonal flows and turbulence is a self-regulating mechanism. The flows are linearly damped by ion collisions, and, being strictly parallel to the flux-surfaces, do not cause any radial transport. Consequently, they constitute a benign sink for turbulent energy.

Two types of zonal flows with different time scales exist in toroidal plasmas. The first has zero frequency and no density component. The second type, which is known as the geodesic acoustic mode (GAM), has a well defined frequency, which is of the order of the ratio of the sound speed and the major radius; the GAM also has a finite pressure component. These two features make the GAM much easier to detect and identify than the zero frequency zonal flow. Indeed, it has been observed in many tokamaks over the past decade (section 4.2), while direct experimental characterisation of the zero frequency zonal flow is scarce.

In a fluid description, the GAM is a radially localised mode, which can exist on any flux surface. Recent theoretical work has revealed that inclusion of finite gyro-radius and orbit effects leads to radial coupling between flux-surfaces, and the emergence of discrete eigenmodes. These modes have a radial wavelength that is longer than the turbulence scale length, but much shorter than the minor radius of the plasma (Itoh et al. 2006). Their frequency is constant over a certain radial range, and the modes typically propagate radially outward. This is qualitatively consistent with experimental observations (Ido et al. 2006), but awaits detailed confirmation. Such a study requires a multipoint measurement with a radial resolution of the order of a cm or better, and good radial coverage.

Characterisation of the toroidal and poloidal structure of the GAM has so far been limited to two- or three-point measurements (K. J. Zhao et al. 2006). In this respect, the recent theoretical finding that the GAM should have a measurable magnetic component outside of the plasma (Wahlberg 2009) is quite interesting, since multi-point measurement of magnetic field fluctuations by pickup coils is possible in many tokamaks.

Because it is not constant in time, the flow shear associated with the GAM is less effective in suppressing turbulent eddies than its instantaneous shearing rate would suggest. Even so, theory and numerical simulations show that it plays a significant role in the self-regulating behaviour of plasma turbulence, at least in situations where the dominant micro-instability is the ion-temperature gradient mode (ITG) (Hahm et al. 1999). Much less is known about situations where other micro-instabilities dominate. An important example is the trapped-electron mode (TEM), which is linked to the dynamics of electron which are magnetically trapped on the low-field side of the plasma. Turbulence related to this mode is believed to be responsible for a large fraction of electron transport in typical electron-heated TCV plasmas, which are characterised by a large difference in electron and ion temperatures. Interestingly, simulations suggest that zonal flows may not play an important role in the regulation of turbulence in such plasmas (Dannert et al. 2005). Experimental verification thus requires simultaneous measurements of small-scale turbulence and zonal flows.

Typically, for improved resilience against MHD instabilities (Hofmann, Sauter, et al. 1998), high-performance plasmas have a poloidal section resembling the letter D, where the flat side faces the central column of the tokamak. The shaping parameter ‘triangularity’ is positive in this case; negative triangularity corresponds to the flat side facing outwards. One of the unique assets of the TCV tokamak is its ability to create plasmas with cross-sections with a variety of shapes. Surprisingly, it has been found in TCV that under certain circumstances, progressively changing the triangularity from positive to negative results in a continuous increase of the confinement time (Camenen, Pochelon, et al. 2007). This may reflect a role of triangularity in the stability of TEM turbulence.

A novel tangential phase-contrast imaging diagnostic (TPCI) has recently been de-

signed and installed in TCV (Marinoni, Coda, et al. 2006; Marinoni 2009). The instrument measures line-integrated density fluctuations, but can achieve good radial resolution through a spatial filtering technique. The principal motivation in the construction of this diagnostic was the study of turbulence but it is also an excellent tool for the study of GAMs.

Edge-localised modes

Another example of self-organisation of a turbulent plasma is the H-mode transition, which occurs in toroidal plasmas when heating power exceeds a critical level (Wagner 2007). It is characterised by the spontaneous emergence of a stationary, sheared $\mathbf{E} \times \mathbf{B}$ flow in a zonal region in the edge of the plasma, which drastically reduces the turbulence amplitude. The resulting drop in turbulent diffusivity leads to a steep pressure gradient, and an increase in confinement time by a factor of two or more. The H-mode is a candidate operational scenario for a future fusion power plant. Interestingly, experimental observations have recently suggested that zonal flow dynamics may play a role in the transition to H-mode (Conway, Angioni, et al. 2011).

Edge-localised modes (ELMs) are quasi-periodic edge instabilities that transiently destroy the H-mode barrier, limiting density build-up and thereby allowing steady state H-mode operation. On the negative side, empirical scaling laws predict that the transient heat fluxes caused by ELMs in ITER will be so great that the lifetime of plasma facing components might be unacceptably short (Loarte et al. 2007). The development of ELM mitigation techniques, conceivably employing a real-time control response to an ELM precursor mode, is therefore a crucial challenge in fusion research.

ELMs have long been associated with the linear instability threshold of so-called peeling and ballooning modes in the steep pressure gradient in H-mode (Zohm 1996). Progress in fast camera techniques (Kirk et al. 2006) has elucidated the non-linear phase in the evolution of ELMs. It is characterised by the formation of *filaments* on the low field side of the plasma. These filaments may exist in a saturated state for some time; an ELM event is initiated when one or more filaments are expelled across the last closed flux surface. This mechanism was recently confirmed in unprecedented detail by electron-cyclotron emission (ECE) imaging, which offers a two-dimensional measurement of electron temperature (Yun et al. 2011).

Non-linear MHD simulations (Huysmans et al. 2009) can now reproduce the explosive expulsion of the filaments at least qualitatively, but simulating the entire ELM cycle is as yet impossible. Other questions remain as well. The filaments themselves carry only a small fraction of the total energy lost during ELMs (Kirk et al. 2006): the large transient fluxes are believed to be caused mainly by an observed increase in turbulent transport during ELMs (Coda et al. 2001). The physical mechanism by which the filaments affect the transport barrier remains as yet unclear. Also, measurements of the *density* component of the filaments, which may be quite distinct from the temperature (Huysmans et al. 2009), have thus far been limited to single snapshots by fast Thomson scattering (Kirk et al. 2006). Poloidal correlation reflectometry (Krämer-Flecken, Soldatov, Vowinkel, et al. 2010) has the potential to provide much more detailed measurements of density component of the filaments, and, simultaneously, of the small-scale turbulence. An imaging reflectometer configuration has especially high potential in this respect (Mazzucato, Mun-

sat, et al. 2002).

The questions concerning ELMs raised above, as well as the recent development of an ELMy H-mode scenario in the TEXTOR tokamak (Unterberg et al. 2009) provided the main motivation for the study presented in chapter 5 of this thesis. In the course of that work, however, it was found that the ELM cycle in TEXTOR is linked to bursts of fish-bones and Alfvén modes. These modes are of interest in their own right as well (Heidbrink 2008). In present day experiments such as TEXTOR, they are driven by energetic ions, which arise from externally applied neutral beam and ion cyclotron heating. However, in a fusion reactor such as ITER Alfvén modes in particular will be driven by energetic ^4He ions created in the fusion reaction. Predicting the magnitude of the associated radial transport of these ions is a crucial outstanding issue in fusion research: if too many ^4He ions will be lost before transferring their energy to the electrons, the fusion reaction will not sustain itself.

1.3 Synopsis of experimental results

It had previously been found in TCV (Camenen, Pochelon, et al. 2007) that electron heat diffusivity decreases substantially when the triangularity is changed from +0.4 to -0.4 in EC heated L-mode plasmas with effective collisionality $\nu_{\text{eff}} < 0.5$. Using the newly commissioned tangential phase-contrast imaging diagnostic in TCV, turbulent density fluctuations were measured in a series of repeat discharges with positive and negative triangularity. By moving the plasma position vertically, the measurement volume was scanned radially through the plasma. For $\delta = -0.4$ the line-integrated density fluctuations are weaker compared to $\delta = +0.4$, and the correlation time is shorter. This is in agreement with the conjecture that the turbulent state is affected by triangularity.

In the same $\delta = +0.4$ discharges, the geodesic acoustic mode (GAM) was identified in the TPCI signals. This constitutes the first observation of this mode in TCV. It is visible for $\rho_{\text{vol}} > 0.6$ and its amplitude grows steadily up to $\rho_{\text{vol}} = 0.85$, which is the outermost point for which we presently have measurements. The mode frequency is constant over this range (typically 26 kHz). A radial wavelength of ~ 3 cm was measured, along with radially outward propagation. Frequency, radial extent, wavelength and propagation direction are in rough agreement with a simulation with the gyro-kinetic particle-in-cell code ORB5 (Vernay et al. 2010), using the experimental equilibrium. These measurements complement similar observations in other tokamaks (K. J. Zhao et al. 2006).

The GAM in TCV has a modest, though clearly visible magnetic component, which shows strong coherence with the TPCI signal. Its structure was characterised with the poloidal and toroidal arrays of in-vessel magnetic probes (Moret, Buhlmann, et al. 1998). The magnetic field of the turbulence-driven GAMs had previously been observed in a single-point measurement in the T-10 tokamak (Melnikov et al. 2006), but our measurements constitute the first ones with spatial resolution. Poloidally, the mode has a standing wave structure, with strong antinodes for $\theta = \pm 140^\circ$. At the poloidal angle corresponding to these antinodes, the toroidal mode number is clearly $n = 0$, as expected. For some discharges, clear antinodes were also observed for $\theta = (0^\circ, 180^\circ, \pm 90^\circ)$. This is in agreement with the expected $m/n = 2/0$ MHD structure of the GAM (Wahlberg 2009). The GAM is in fact visible in the magnetic signals for many discharges in the TCV database. This allowed us to confirm the expected c_s/R frequency scaling (Conway, Tröster, et al. 2008).

At sufficiently weak toroidal magnetic field, NBI heated, limited plasmas in the TEXTOR tokamak exhibit bursts of beam-ion driven ‘fishbone’ and Alfvén modes, which are characterized for the first time using the multi-antenna reflectometer and Mirnov coils. In H-mode the fishbone triggers ELMs and in L-mode it triggers previously unobserved bursts of particle recycling, resembling the ELMs. The reflectometer phase shows statistically significant bispectral coherence between the fishbone and the Alfvén modes, indicative of non-linear coupling between them.

Additionally, using conditional averaging techniques, two ELM precursor modes are found that are not related to the beam-ions. The first is a coherent mode with toroidal mode number $n = -2$, which is also seen with the Mirnov coils. Bispectral analysis of the reflectometer signals shows that this mode modulates the amplitude of broad-band turbulence in the pedestal. The second ELM precursor is a semi-coherent, down-chirping mode with a poloidal wavelength of 6 cm.

1.4 Thesis outline

The remainder of this thesis is organised as follows. Chapter 2 is an introduction to the phase-contrast imaging technique. The principles of reduction of the effective integration length through spatial filtering are discussed. Chapter 3 is a technical description of the TPCI diagnostic, which has recently been designed and installed in TCV (Marinoni, Coda, et al. 2006; Marinoni 2009). The localisation possibilities are discussed through an explicit example, taking into account the shape of the flux surfaces in TCV. In discussing the hardware and optics, special attention is given to the problem of optical aberrations and mechanical vibrations, which were found to pose a serious problem.

In chapter 4 we present the first measurements with the TPCI diagnostic. Our results on turbulence and the GAM in TCV are compared with existing literature and a turbulence simulation. The TPCI measurements are also modelled using a synthetic diagnostic. Chapter 5 deals with our reflectometer work in TEXTOR; this chapter is an expanded version of Meijere et al. 2012. The experimental setup is described in some detail. Special attention is given to the correct interpretation of the reflectometer signals in the presence of strong density fluctuations. We also present a review of the phase-grating model for reflectometry.

Finally, a summary and some suggestions for future work are given in chapter 6.

Chapter 2

The phase-contrast imaging technique

The dispersion relation of electromagnetic waves in tokamak plasmas is mainly determined by the electron density and the magnetic field. Probing with externally launched beams can therefore provide information about these quantities. A variety of diagnostic techniques are based on this idea, employing vacuum wavelengths ranging from the μm to cm scale. In the μm range the plasma refractive-index deviates only slightly from one and anisotropy and other effects of the magnetic field are negligible. Within the interaction volume, refraction and diffraction can often be neglected as well: the only effect of the plasma on a collimated laser beam is then to introduce a small phase shift, proportional to the line integrated electron density along chords within the beam. Since the plasma density is inhomogeneous, different chords pick up a slightly different phase shift. In particular, density fluctuations with wavelengths shorter than the beam-width lead to a slight *rippling* of the wave fronts, as sketched in figure 2.1.

Because of diffraction, the ripples in the wave fronts only reflect the line-integrated density sufficiently close to the interaction volume, or an optical image of it: this is where the phase measurement should be performed. The phase-contrast method is an ‘internal reference’ or ‘common path’ interferometric technique for wave front sensing, employing a Zernike phase plate in a focal plane (Weisen 1988). As such, it is only sensitive to the ripples in the wave fronts, and not to the much larger phase shift that is common to all chords in the beam. Crucially, this also makes a phase-contrast setup insensitive to changes in the optical path length that are the result of mechanical vibrations. Such vibrations pose a serious problem in the practical implementation of a potentially more powerful double path interferometer setup, such as the Mach-Zehnder configuration (Nazikian et al. 1987).

As noted before, the phase shift is given by the line integral of density along a laser chord. Therefore, on a given part of the beam path, the strongest contribution comes from fluctuations which are perpendicular to it. Secondly, the perturbation wave vector is more or less perpendicular to the magnetic field in a magnetised plasma. Since the beam is straight and the field lines are not, these two criteria are satisfied by perturbation wave vectors that point in different directions for different positions along the beam, which allows a reduction of the effective integration length through spatial filtering in a focal plane. This technique has been applied in various phase-contrast systems with a vertically launched beam (Tanaka et al. 2008; Dorris et al. 2009). However, the achievable

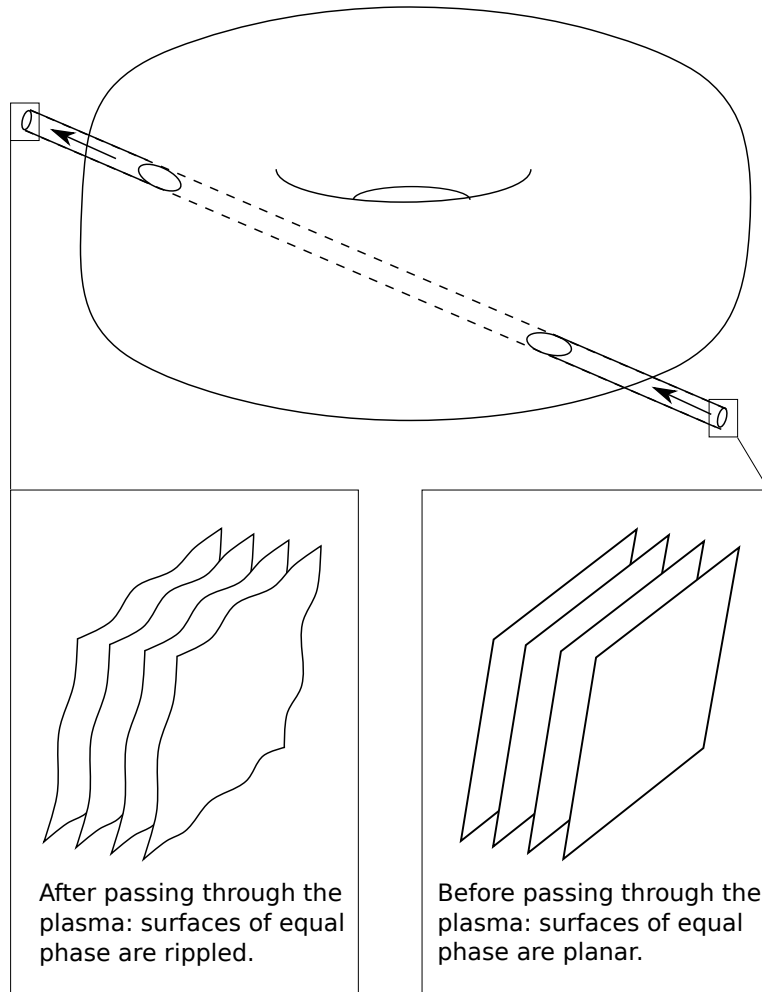


Figure 2.1: Principle of short-scale density fluctuation measurement in tokamak plasma with a μm wavelength laser beam.

localisation is much better in a *tangential* geometry, where the beam comes close to being parallel to the field lines (figure 2.1). Indeed, this is the novel feature of the TCV phase-contrast diagnostic (Marinoni, Coda, et al. 2006; Marinoni 2009).

The remainder of this chapter is organised as follows. In §2.1 we discuss the dispersion relation of electromagnetic waves in a homogeneous plasma. Although in the present chapter we only need the high-frequency limit of the dispersion relation, we also discuss plasma cutoffs and the role of the magnetic field, since these are essential effects in reflectometry (chapter 5). The WKB approximation for solving the wave equation in the presence of inhomogeneity is introduced in §2.2. In the limit of small wavelength of the probing beam the WKB solution leads to the interpretation of phase shifts in terms of line integrated density. The criteria for its validity are discussed for the particular case of the TCV tangential phase-contrast setup, which employs a collimated CO_2 laser beam (figure 2.1 and table 2.1). The basic principles of phase-contrast and other imaging interferometry techniques are presented in §2.3. §2.4 deals with the reduction of integration

2.1. Electromagnetic waves in a homogeneous plasma

length through spatial filtering in a focal plane and the corresponding differences between vertical and tangential viewing geometries. The optical transfer function of the phase contrast method is presented in §2.5. Finally, in §2.6 we list the definition of several statistical quantities that can be used to elucidate the spatial and temporal correlation structure of the TPCI signals. For a more rigorous and in-depth treatment of most of the topics covered in this chapter we refer to Coda 1997.

background density	n_e	$< 10^{20} \text{ m}^{-3}$
plasma frequency (electrons)	$\omega_p/(2\pi)$	$< 90 \text{ GHz}$
cyclotron frequency (electrons)	$\omega_c/(2\pi)$	$\sim 40 \text{ GHz}$
turbulence amplitude	$\delta n_e/n_e$	$\sim 1\%$
background gradient length	$n_e/\nabla n_e$	$> 2 \text{ cm}$
vacuum wavelength of laser light	λ	$10.6 \text{ }\mu\text{m}$
product of λ and electron radius	λr_e	$2.99 \times 10^{-20} \text{ m}^{-2}$
vacuum wave number of laser light	k_0	5928 cm^{-1}
frequency of laser light	$\omega/(2\pi)$	28.3 THz
length of beam path in plasma	L	$< 1 \text{ m}$
Gaussian beam half-width	w_0	$\sim 3 \text{ cm}$

Table 2.1: Some parameters of TCV and the tangential phase-contrast imaging system.

2.1 Electromagnetic waves in a homogeneous plasma

We wish to derive the dispersion relation for high frequency electromagnetic waves in a plasma. The starting point for our discussion is the following pair of Maxwell's equations:

$$\nabla \times \mathbf{E} = -\frac{\partial \mathbf{B}}{\partial t}; \quad (2.1)$$

$$\nabla \times \mathbf{B} = \mu_0 \mathbf{J} + \mu_0 \epsilon_0 \frac{\partial \mathbf{E}}{\partial t}. \quad (2.2)$$

Taking the curl of equation 2.1 and using equation 2.2 to eliminate \mathbf{B} gives

$$\nabla(\nabla \cdot \mathbf{E}) - \nabla^2 \mathbf{E} = -\mu_0 \frac{\partial \mathbf{J}}{\partial t} - \frac{1}{c^2} \frac{\partial^2 \mathbf{E}}{\partial t^2}. \quad (2.3)$$

Here, we have used the identity $\nabla \times (\nabla \times \mathbf{A}) = \nabla(\nabla \cdot \mathbf{A}) - \nabla^2 \mathbf{A}$. Without loss of generality, we can write

$$\mathbf{E}(\mathbf{x}, t) = \mathbf{E}_0 + \mathbf{E}_1(\mathbf{x}, t) \quad (2.4)$$

$$\mathbf{J}(\mathbf{x}, t) = \mathbf{J}_0 + \mathbf{J}_1(\mathbf{x}, t) \quad (2.5)$$

For the special case where \mathbf{E}_1 and \mathbf{J}_1 are plane waves varying as $\exp[i(\mathbf{k} \cdot \mathbf{x} - \omega t)]$ substitution in equation 2.3 gives

$$-\mathbf{k}(\mathbf{k} \cdot \mathbf{E}_1) + k^2 \mathbf{E}_1 = +i\mu_0 \omega \mathbf{J}_1 + \frac{\omega^2}{c^2} \mathbf{E}_1. \quad (2.6)$$

In a vacuum $\mathbf{J} = 0$ and $\mathbf{k} \cdot \mathbf{E}_1 = \nabla \cdot \mathbf{E} = \rho/\epsilon_0 = 0$, so that equation 2.6 simplifies to the dispersion relation $\omega^2 = k^2 c^2$. In a plasma $\mathbf{J} \neq 0$, since any electric field will cause movement of the charged particles. Suppose that in our plasma $\mathbf{E}_0 = 0$, $\mathbf{J}_0 = 0$ and the electron density $n_e(\mathbf{x}, t) = n_{e0} + n_{e1}(\mathbf{x}, t)$, where we assume a $\exp[i(\mathbf{k} \cdot \mathbf{x} - \omega t)]$ dependence for n_{e1} and $n_{e1} \ll n_{e0}$. Employing a linearised two-fluid model and neglecting the movement of the massive ions, we have

$$\mathbf{J}_1 = -n_{e0} e \mathbf{v}_{e1}. \quad (2.7)$$

The electron fluid velocity \mathbf{v}_{e1} is linked to the electric field through the (linearised) equation of motion:

$$-i\omega m_e \mathbf{v}_{e1} = -e\mathbf{E}_1 - e\mathbf{v}_{e1} \times \mathbf{B}_0. \quad (2.8)$$

Here, the force due to pressure gradients has been neglected in anticipation of the high phase speed of the waves compared to the thermal motion of the electrons ($v_\phi \gg v_{th,e}$); this is called the ‘cold plasma’ approximation.

For waves with frequencies $\omega \gg \omega_c$ (where $\omega_c = eB_0/m_e$ is the electron cyclotron frequency) the Lorentz force in equation 2.8 is negligible. We can then eliminate \mathbf{v}_{e1} in equation 2.7 by 2.8 and substitute the resulting expression for \mathbf{J}_1 in equation 2.6. Solutions to this equation have $\mathbf{k} \perp \mathbf{E}_1$ (purely transversal waves) and satisfy the dispersion relation

$$\frac{c^2 k^2}{\omega^2} = N^2 = 1 - \frac{\omega_p^2}{\omega^2}, \quad (2.9)$$

where N denotes the index of refraction, and the plasma frequency ω_p is defined by

$$\omega_p^2 = \frac{n_{e0} e^2}{\epsilon_0 m_e}. \quad (2.10)$$

For infrared and optical frequencies the condition $\omega \gg \omega_c$ is easily satisfied in tokamak plasmas, but for microwaves it must be relaxed. As a result, the system defined by equations 2.6, 2.7 and 2.8 becomes anisotropic: wave solutions now depend on the polarisation \mathbf{E}_1 and direction of propagation \mathbf{k} relative to \mathbf{B}_0 . For simplicity, we now restrict our analysis to propagation perpendicular to the unperturbed magnetic field, i.e. $\mathbf{k} \perp \mathbf{B}_0$ (figure 2.2).

A solution known as the ‘ordinary wave’ is found by assuming $\mathbf{E}_1 \parallel \mathbf{B}_0$ (‘O-mode’ polarisation). Using $\mathbf{k} \cdot \mathbf{E}_1 = 0$ in equation 2.6 it is clear that $\mathbf{J}_1 \parallel \mathbf{E}_1$ and thus $\mathbf{J}_1 \parallel \mathbf{B}_0$, showing that the Lorentz force term in equation 2.8 can be dropped once more: these waves satisfy the same dispersion relation we found before (equation 2.9). Physically, the current sheets that form in response to the O-mode electric field flow parallel to the background magnetic field, so that they are unaffected by it.

The solution known as the ‘extraordinary wave’ is found by assuming $\mathbf{E}_1 \perp \mathbf{B}_0$ (‘X-mode’ polarisation). The derivation of the dispersion relation of the extraordinary mode is somewhat involved (F. F. Chen 1984) and here we only reproduce the result:

$$\frac{c^2 k^2}{\omega^2} = N^2 = 1 - \frac{\omega_p^2 \omega^2 - \omega_p^2}{\omega^2 \omega^2 - \omega_h^2}. \quad (2.11)$$

The upper hybrid frequency is given by

$$\omega_h^2 = \omega_p^2 + \omega_c^2. \quad (2.12)$$

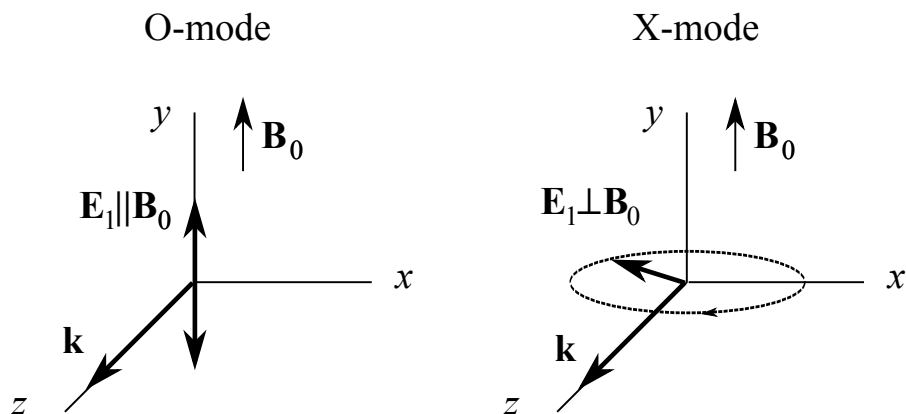


Figure 2.2: Geometry for electromagnetic waves propagating perpendicular to \mathbf{B}_0 (adapted from F. F. Chen 1984).

The complication comes from the fact that $\mathbf{E}_1 \perp \mathbf{B}_0$ forces the electron fluid to move *across* \mathbf{B}_0 , so that it is subject to the first order Lorentz force of equation 2.8. This results in the appearance of regions of compression and rarefaction in the electron fluid, and a corresponding longitudinal component of \mathbf{E}_1 , in addition to a transversal component. It turns out that these components oscillate 90° out of phase, so that for any given point in space \mathbf{E}_1 traces out an ellipse in the xy -plane for each wave cycle (figure 2.2).

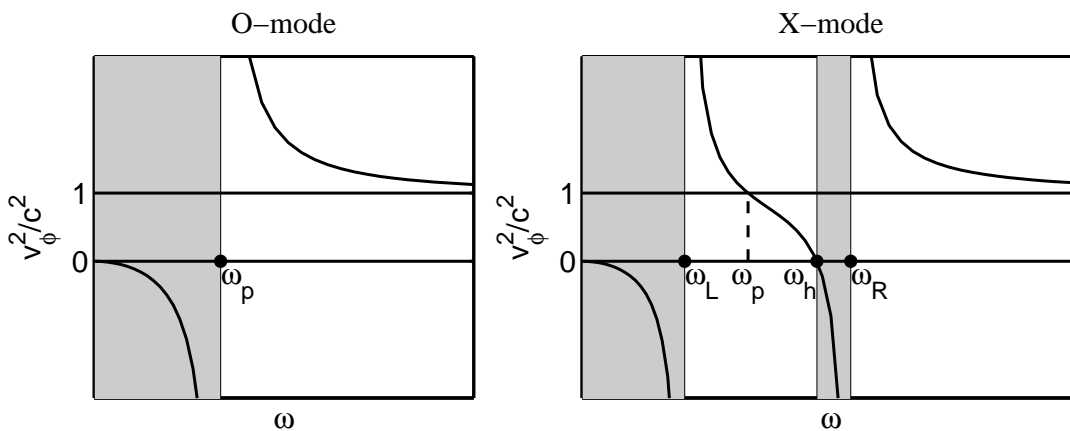


Figure 2.3: Phase speed in plasma of electromagnetic waves with $\mathbf{k} \perp \mathbf{B}_0$. The shaded regions indicate stopbands (adapted from F. F. Chen 1984).

If n_{e0} or \mathbf{B}_0 vary (slowly) in space, a propagating wave may encounter a cutoff or a resonance. A cutoff occurs in a plasma when the index of refraction $n = (c/v_\phi = ck/\omega)$ goes to zero (infinite wavelength for finite frequency). A resonance occurs when the index of refraction goes to infinity (zero wavelength for finite frequency). The effect of a cutoff is to reflect the wave, while a resonance leads to absorption. Stopbands occur when the index of refraction becomes imaginary, i.e. $\omega^2/(c^2k^2) = v_\phi^2/c^2 < 0$. These effects can be visualised by plotting v_ϕ^2/c^2 as a function of ω (figure 2.3). The ordinary wave has no resonance and a single cutoff frequency $\omega = \omega_p$; the region $\omega < \omega_p$ is a stopband. The

extraordinary wave has a resonance for $\omega = \omega_h$ and two cutoffs

$$\omega_R = \frac{1}{2} \left[\omega_c + (\omega_c^2 + 4\omega_p^2)^{1/2} \right]; \quad (2.13)$$

$$\omega_L = \frac{1}{2} \left[-\omega_c + (\omega_c^2 + 4\omega_p^2)^{1/2} \right], \quad (2.14)$$

which delimit two stop-bands. Here, the ‘L’ and ‘R’ subscripts refer to the left- and right-handed elliptical polarisation of the waves that exist in the first and second passbands, respectively. Finally, it may be seen from figure 2.3 that the phase velocity ($v_\phi = \omega/k$) in a plasma can be greater than the speed of light in vacuum. Of course, the group velocity $d\omega/dk \leq c$.

2.2 Phase shifts in the WKB approximation

Various complementary approximation schemes exist to simplify analysis of light propagation in inhomogeneous media. If the scale length of the inhomogeneity is long compared to the wavelength, the waves can be described in terms of rays, in what is called the geometrical optics or WKB approximation (Elmore et al. 1985). The problem is further simplified if the rays are parallel and refraction can be neglected. For propagation in the z -direction and omitting explicit mention of any (x, y) dependence, the wave field then takes the form

$$E(z, t) \approx A(z) \exp(i\varphi(z) - i\omega t), \quad (2.15)$$

where

$$\varphi(z) = k_0 \int_{z_0}^z N(z') dz'; \quad (2.16)$$

$$A(z) = A(z_0) \left(\frac{N(z_0)}{N(z)} \right)^{1/2}. \quad (2.17)$$

Here, $N(z)$ is the *local* index of refraction, and z_0 is a reference position where the phase φ and amplitude A of the wave are known.

If the medium is a plasma, and assuming that the frequency is sufficiently high that the magnetic field can be neglected ($\omega \gg \omega_c$), the index of refraction N is given by dispersion relation 2.9. Under the further assumption that $\omega \gg \omega_p$, N can be expanded to first order in ω_p^2/ω^2 , giving

$$N = \frac{ck}{\omega} \approx 1 - \frac{\omega_p^2}{2\omega^2}. \quad (2.18)$$

Substituting 2.18 in equation 2.16 and using the definition of the plasma frequency (equation 2.10) gives

$$\varphi(z) \approx k_0(z - z_0) - \lambda_0 r_e \int_{z_0}^z n_e(z') dz'. \quad (2.19)$$

Here, the classical electron radius r_e is defined by

$$r_e = \frac{1}{4\pi\epsilon_0} \frac{e^2}{m_e c^2} \quad (\simeq 2.818 \times 10^{-15} \text{ m}). \quad (2.20)$$

2.2. Phase shifts in the WKB approximation

The first term on the right-hand side of equation 2.19 is the phase shift in the absence of a plasma. The effect of having plasma in the wave path is a phase shift proportional to the line integral of electron density. This fact is exploited in various interferometry techniques for measuring plasma density in tokamak experiments, including the phase-contrast technique.

Using equation 2.19 and the parameters listed in table 2.1 we can now estimate upper limits for the phase shifts due to background plasma and fluctuations, experienced by the laser beam of the TCV phase-contrast diagnostic. Using an integration length of 1 m, we find 1 rad for the bulk shift and 0.01 rad for the fluctuating shift.

We must assess the validity of equation 2.19 for the case of the TCV phase-contrast system with its 10.6 μm wavelength. Table 2.1 shows that for TCV phase-contrast system, $\omega_p^2/\omega^2 < 10^{-5}$ and $\omega_c^2/\omega^2 \sim 10^{-6}$, so that the refractive index N (equation 2.18) is very close to one everywhere in the plasma. As a result, the amplitude (equation 2.17) is nearly constant along the rays. Another consequence is that partial reflections, which arise when $(d\lambda/dz)^2 \ll 32\pi^2 \approx 18^2$, can be neglected (Elmore et al. 1985). For a parabolic density profile with peak plasma frequency ω_p and N close to one, the maximum refraction angle can be estimated through $\theta_{\text{max}} \simeq \omega_p^2/\omega^2$ (Hutchinson 2005). We conclude that over an interaction volume of 1 m, rays deviate less than 10 μm from a straight line due to refraction, which partially justifies the approximation of straight rays.

Another implicit assumption in the straight ray approximation is that diffraction is negligible in the interaction volume. Since the refractive index is almost unity throughout the interaction volume, the wave field in the plasma is given to good approximation by the vacuum field, which, in turn, can be approximated by a Gaussian beam (Goldsmith 1992). Such a beam has an axially symmetrical electric field given by

$$E(\mathbf{x}_\perp, z) = \left(\frac{4P}{\epsilon_0 c \pi w^2} \right)^{1/2} \exp \left(-\frac{x_\perp^2}{w^2} + ik_0 z + \frac{i\pi x_\perp^2}{\lambda R} + i\phi \right), \quad (2.21)$$

where P is the total power of the beam, and

$$w = w_0 \left(1 + [z/z_c]^2 \right)^{1/2}; \quad (2.22)$$

$$R = z + z_c^2/z; \quad (2.23)$$

$$\phi = \arctan(z/z_c). \quad (2.24)$$

Here, the confocal or Rayleigh distance is defined by

$$z_c = \pi w_0^2/\lambda, \quad (2.25)$$

and we have dropped the subscript ‘0’ to denote the vacuum wavelength. Using the values from table 2.1 we obtain $z_c = 267$ m for the TCV phase-contrast setup. Since this is much greater than the length of the plasma column, we conclude that the neglect of diffraction solely due to finite beam diameter is justified. This is not necessarily true however for diffraction due to small-scale inhomogeneities in the \mathbf{x}_\perp direction, which can therefore render the WKB phase inaccurate. In the following we present an illustration of the breakdown of the WKB solution, which leads to the criterion for which scattering can be neglected.

Figure 2.4a depicts a slab with thickness L and density and index of refraction

$$N(x, z) = N_0 + \delta N \cos(k_{\perp} x). \quad (2.26)$$

Omitting the time dependence $\exp(-i\omega t)$, a light wave $E(x, z) = E_0 \exp(ik_0 z)$ is incident on the slab. Its frequency $\omega \gg \omega_p, \omega_c$, but no assumptions are made as yet about L , k_{\perp} and k_0 . The WKB solution for the wave field at $z = L$ is

$$E(x, L) = E_0 \exp(iN_0 k_0 L + i\delta\varphi \cos[k_{\perp} x]), \quad (2.27)$$

where $\delta\varphi = \delta N k_0 L$.

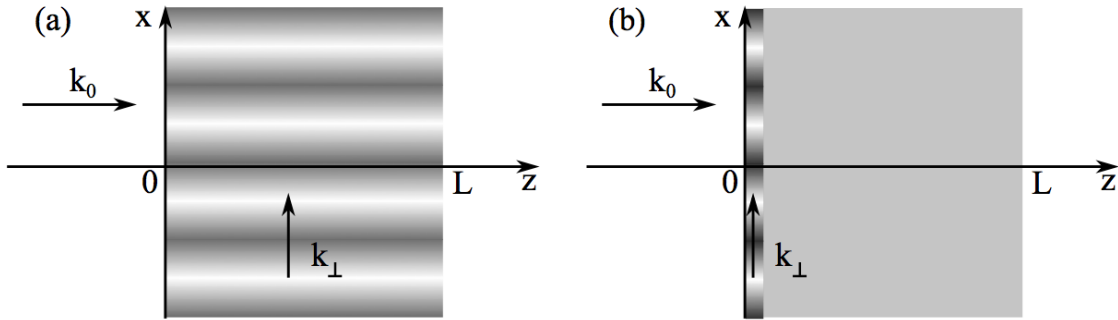


Figure 2.4: (a) Slab medium with perturbed index of refraction. (b) Stronger perturbation, but concentrated in a thin layer. In the Raman-Nath regime (condition 2.30) the wave field at $z = L$ is equal for (a) and (b).

In figure 2.4b the slab has homogeneous index of refraction N_0 , except for a thin phase grating at $z = 0$, which instantaneously introduces the phase shift $\delta\varphi \cos(k_{\perp} x)$ that was previously incurred over a distance L . The corresponding WKB solution at $z = L$ is of course still given by equation 2.27. For the case of the grating however, there is also a particularly simple solution that does not invoke the WKB approximation and includes scattering. The wave field just after the phase grating is $E_0 \exp(i\delta\varphi \cos[k_{\perp} x])$. For $\delta\varphi = \delta N k_0 L \ll 1$ this can be expanded to first order in $\delta\varphi$, giving

$$E(x, 0) \approx E_0 (1 + i\delta\varphi \cos[k_{\perp} x]). \quad (2.28)$$

Now, under the assumption that $k_{\perp} \ll N_0 k_0$, we can invoke the paraxial propagation operation (J. W. Goodman 2005) to obtain the field for $z = L$:

$$E(x, L) = E_0 \exp(iN_0 k_0 L) \left(1 + i\delta\varphi \exp \left[-\frac{iLk_{\perp}^2}{2N_0 k_0} \right] \cos[k_{\perp} x] \right). \quad (2.29)$$

Comparing solution 2.29 to the WKB solution 2.27, we see that the two do not differ much for

$$k_{\perp}^2 \ll \frac{\pi N_0 k_0}{L}. \quad (2.30)$$

We conclude that if condition 2.30 is satisfied the effect of scattering is unimportant and the WKB approximation is accurate. The total phase shift might as well be assumed to arise in a single, thin layer anywhere within the slab. This situation is called the Raman-Nath regime. In the other extreme, when $k_{\perp}^2 \gg \pi N_0 k_0 / L$, scattering plays an important

role in the field formation, and the WKB approximation is therefore inaccurate. This situation is called the Bragg regime. In the latter case equation 2.29 is of course inaccurate as well, since it does not account for the z extent of the perturbation. Incidentally, it may be seen from equation 2.29 that at a certain distance from the phase screen, the *amplitude* of a transmitted wave is also modulated. This effect is called ‘scintillation’.

Now we apply equation 2.30 to the case of the TCV phase-contrast system. For small phase shifts, and assuming that the integration length is the entire 1 m beam path in the plasma, the Raman-Nath condition (equation 2.30) is $k_{\perp} \ll 13 \text{ cm}^{-1}$; in reality the effective integration length is smaller.

2.3 Measuring the phase shift

We have seen in §2.2 that in the Raman-Nath regime (equation 2.30) the effect of a perturbed plasma column on the phase of a collimated beam is equivalent to that of a thin phase screen, which introduces an instantaneous phase shift given by the line-integrated density (equation 2.19). The latter quantity can therefore be obtained by a phase measurement close to the phase screen. If the measurement is performed a distance Δz from the object, the resolution in the \mathbf{x}_{\perp} direction deteriorates, so that only components of the phase shift with $k_{\perp} \ll (\pi k_0 / \Delta z)^{1/2}$ reflect the line-integrated density.

For measurements of the average plasma density only the $k_{\perp} = 0$ component is required, so that this effect is unimportant. However, our interest in this thesis is with short scale fluctuations, so the phase measurement must be carried out as close as possible to the object, in what is called the ‘near field’. It can be shown that (apart from a constant phase) the wave field in an optical image is a scaled copy of the field in the corresponding object plane (J. W. Goodman 2005). Therefore, in practice it is convenient to recreate the near field an arbitrary distance away from the object through imaging, and perform the phase measurement there.

Phase measurements are performed by interferometry: the perturbed wave is allowed to interfere with a reference wave and the resulting intensity is monitored. This is illustrated by the conceptually simple example of the imaging Mach-Zehnder setup (figure 2.5). A setup of this kind was implemented in the LT-4 tokamak by Nazikian et al. 1987, who referred to it as a ‘scintillation interferometer’. Suppose that in the image plane the electric field of the reference wave is $E_r \exp i\omega t$, and the field of the plasma arm $E_0 \exp i(\omega t + \varphi[\mathbf{x}_{\perp}])$. Omitting the time dependence, the total field in the image is then

$$E_{\text{im}}(\mathbf{x}_{\perp}) = E_r + E_0 \exp i\varphi(\mathbf{x}_{\perp}), \quad (2.31)$$

with corresponding intensity

$$\mathcal{E}(\mathbf{x}_{\perp}) = \frac{\epsilon_0 c}{2} (E_r^2 + E_0^2) \left(1 + \frac{2E_r E_0}{E_r^2 + E_0^2} \cos(\varphi[\mathbf{x}_{\perp}]) \right). \quad (2.32)$$

The phase shift can be split as follows:

$$\varphi(\mathbf{x}_{\perp}) = \varphi_0 + \tilde{\varphi}(\mathbf{x}_{\perp}), \quad (2.33)$$

where we assume $\tilde{\varphi}(\mathbf{x}_{\perp}) \ll 1$. The component φ_0 can be chosen arbitrarily by tuning the length of the reference arm: choosing $\varphi_0 = -90^\circ$ maximises the sensitivity to $\tilde{\varphi}(\mathbf{x}_{\perp})$.

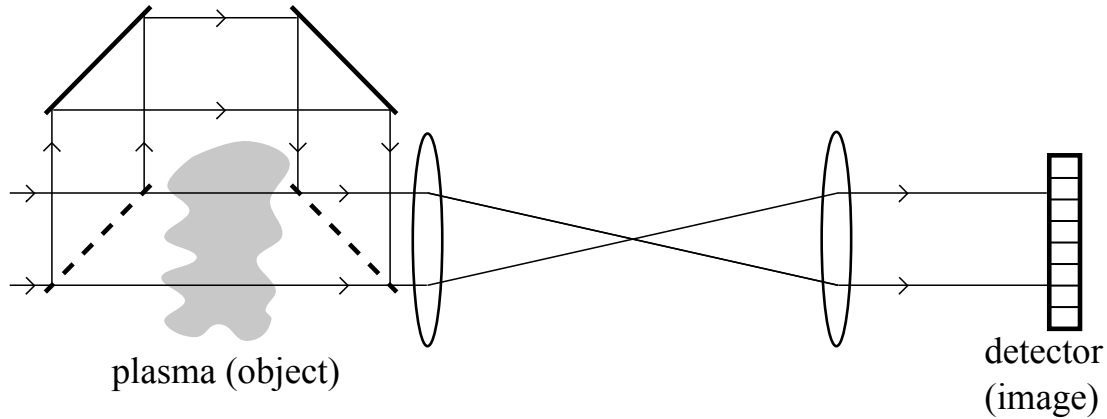


Figure 2.5: Imaging Mach-Zehnder interferometer (from Coda 1997).

Writing $\mathcal{E} = \mathcal{E}_{\text{dc}} + \tilde{\mathcal{E}}$ we then get

$$\tilde{\mathcal{E}}(\mathbf{x}_{\perp}) = \epsilon_0 c E_r E_0 \tilde{\varphi}(\mathbf{x}_{\perp}), \quad (2.34)$$

to first order in $\tilde{\varphi}$. Equation 2.34 shows that the measured intensity pattern in the image plane corresponds to the phase in the object plane.

It takes a change in optical path length of only $\lambda_0/4$ to change ϕ_0 from -90° to 0° , where the instrument has zero sensitivity to $\tilde{\varphi}$. This corresponds to $2.65 \mu\text{m}$ for the case of CO_2 laser light. Consequently, this setup is extremely sensitive to mechanical vibrations. Apart from various schemes to mechanically damp vibrations of the optics, the LT-4 interferometer therefore operated with a feedback-controlled piezoelectric mirror in the optical path to keep $\varphi_0 = -90^\circ$.

By using a phase-contrast imaging (PCI) setup, the problem of changes in optical path length is avoided altogether. We illustrate the principles of this method by considering the system of figure 2.6. For simplicity the incident wave is assumed to be planar (i.e. of infinite extent in the \mathbf{x}_{\perp} direction). The phase screen introduces a phase shift given by equation 2.33, where we assume again that $\tilde{\varphi}(\mathbf{x}_{\perp}) \ll 1$, while φ_0 can be large. Immediately after the object the wave field is given by $E_0 \exp i\tilde{\varphi}(\mathbf{x}_{\perp})$, where the constant phase φ_0 has been absorbed in E_0 . This may be expanded to first order in $\tilde{\varphi}$ to give

$$E_{\text{obj}}(\mathbf{x}_{\perp}) = E_0 (1 + i\tilde{\varphi}(\mathbf{x}_{\perp})). \quad (2.35)$$

Equation 2.35 states that the total wave field is a superposition of a strong component E_0 , and a weak component $iE_0\tilde{\varphi}(\mathbf{x}_{\perp})$, which we shall refer to as the ‘undiffracted’ and ‘diffracted’ fields, respectively. The phasor diagram of figure 2.7 illustrates the 90° phasing between the two field components.

Without a phase plate, the fields in the image and object planes are identical, apart from a constant phase: the corresponding intensity seen by the detector is then simply $\mathcal{E} = (\epsilon_0 c/2)|E_0|^2$, so that the phase screen is invisible. If one could somehow change the *relative* phasing of the undiffracted and diffracted fields by 90° , as shown in figure 2.7, the phasors would be aligned: the phase object would then cause a modulation of the *intensity* in the image, and thus be visible by a detector. The undiffracted wave now

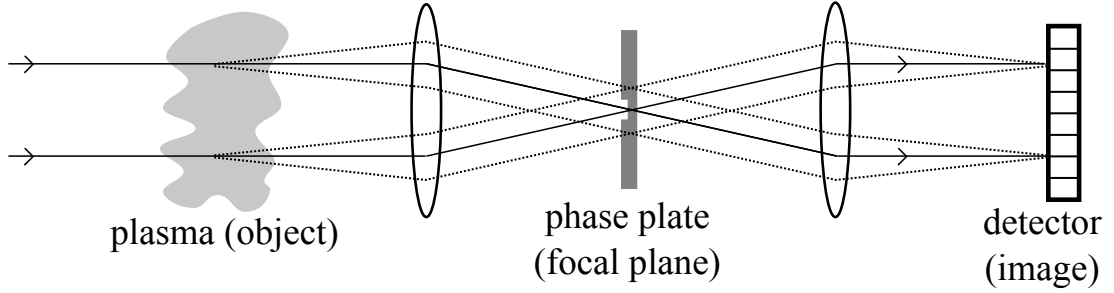


Figure 2.6: Principle of phase-contrast imaging. Full and dashed rays correspond to the undiffracted and diffracted field components, respectively. The depression in the centre of the phase plate introduces a 90° phase shift between these components.

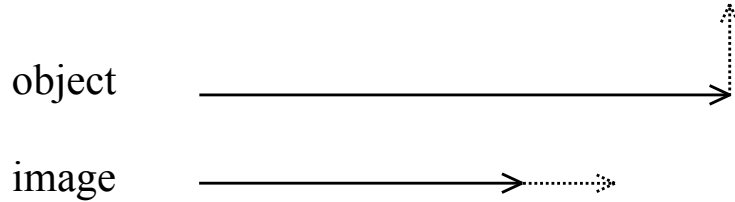


Figure 2.7: Phasor diagram of the undiffracted (continuous) and diffracted (dotted) wave fields in the object and image planes. The 90° relative phase shift, as well as the attenuation of the undiffracted phasor, is introduced by the phase plate.

effectively acts as a local oscillator. In contrast to the Mach-Zehnder setup discussed previously, any phase shift caused by a mechanical change in optical path length is identical for the local oscillator and the diffracted field. A phase-contrast imaging setup is therefore inherently insensitive to vibrations. The phasor diagram also shows that it may be beneficial to selectively decrease the *amplitude* of the undiffracted field (say by a factor $\rho^{1/2}$), since this increases the relative modulation depth of the intensity by the phase screen. Mathematically, the image field would be $E_0(\sqrt{\rho} + \tilde{\varphi}[\mathbf{x}_\perp])$, and the corresponding intensity $(\epsilon_0 c/2)|E_0|^2(\rho + 2\sqrt{\rho}\tilde{\varphi}[\mathbf{x}_\perp])$. The modulation depth, or phase-contrast, is therefore $\tilde{\mathcal{E}}(\mathbf{x}_\perp)/\mathcal{E}_{\text{dc}} \propto \rho^{-1/2}$.

We now address the issue of how the phase plate, which is localised in the focal plane of the first lens of figure 2.6, discriminates between ‘diffracted’ and ‘undiffracted’ components of the wave field. To this end it is instructive to view the field a distance z after the object as an angular spectrum of plane waves (J. W. Goodman 2005)

$$E(\mathbf{x}_\perp, z) = \int E_{\text{obj}}(\mathbf{k}_\perp) \exp\left(ik_0 z - \frac{ik_\perp^2}{2k_0} z + i\mathbf{k}_\perp \cdot \mathbf{x}_\perp\right) d^2 k_\perp, \quad (2.36)$$

where $E_{\text{obj}}(\mathbf{k}_\perp)$ is the spatial Fourier transform of $E_{\text{obj}}(\mathbf{x}_\perp)$ (equation 2.35). Each of the \mathbf{k}_\perp components propagates at a small angle $\theta = k_\perp/k_0$ with respect to the optical axis. After passing through the first lens in figure 2.6, each plane wave is therefore focussed onto a point

$$\mathbf{x}_{\perp,F}(\mathbf{k}_\perp) = \mathbf{k}_\perp F/k_0 \quad (2.37)$$

in the focal plane, where F denotes the focal length of the lens. This observation is of course a manifestation of the Fourier transforming property of lenses, which is the basis for all spatial filtering techniques in optics (J. W. Goodman 2005). Since the undiffracted wave has $\mathbf{k}_\perp = 0$, it is focussed exactly on the optical axis; the diffracted components with $\mathbf{k}_\perp \neq 0$ are focussed away from the axis. We conclude that the phase plate can affect the diffracted and undiffracted waves differently because these components are spatially separated in the focal plane. This is illustrated by the different rays in figure 2.6.

In tokamak PCI setups reflective phase plates are used, rather than the transmissive plate shown in figure 2.6. The required 90° phase shift between diffracted and undiffracted components is then achieved by a depression (‘phase groove’) of depth $\lambda/8$ in an otherwise flat mirror. Attenuation can be achieved by employing a fully reflective layer on a partially reflective substrate, as illustrated in figure 2.8.

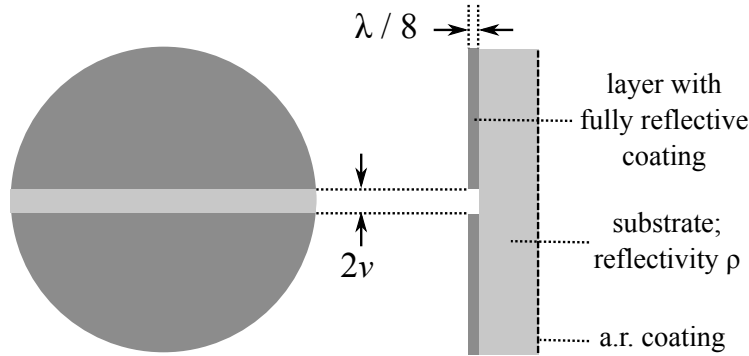


Figure 2.8: Typical design of a reflective phase plate.

Since the groove has a finite half-width v , equation 2.37 tells us that diffracted components with $k_\perp \leq k_0 v/F$ fall inside the groove. As a result, they are phase shifted along with the undiffracted $k_\perp = 0$ component and the relative dephasing by 90° is not achieved: these components are invisible in the image. The phase plate thus acts as a spatial high-pass filter with cutoff frequency

$$k_c = k_0 v/F. \quad (2.38)$$

One might be tempted to choose v as small as possible, in order to lose as little information as possible on $\tilde{\varphi}(\mathbf{x}_\perp)$. However, in reality the extent of the incident wave in the \mathbf{x}_\perp direction is limited, so that the focal points we discussed previously are actually spots with a finite width, due to diffraction. If the groove width is chosen smaller than the spot size, only a fraction of the power in the undiffracted wave is put to use as local oscillator, leading to a decrease in signal amplitude. A compromise must therefore be made between signal level and k_\perp coverage. If the incident beam is Gaussian (equation 2.21) with half-width w_0 , the focal spot will also be Gaussian with half-width $\lambda F/(\pi w_0)$. Using this as a typical compromise value for the groove half-width v gives $k_c = 2/w_0$.

Incidentally, it may be noted that if the imaging system consists of multiple lenses, the phase plate may also be located in an *image* of the focal plane of the first optic. In this case the effective focal length must be used for F in equation 2.38.

2.4 Localisation of the measurement

A phase-contrast imaging diagnostic measures line-integrated density fluctuations along parallel viewing chords within a laser beam, and therefore has no longitudinal resolution. However, we shall see in the following that it is still possible to obtain a measure of localisation along the chord, by exploiting the geometry of the magnetic field. The argument hinges on the existence of a wave-vector selection rule, which provides the *direction* of detectable perturbation wave vectors \mathbf{k} for a given sub-region centred around position z along the chord. The wave vector of the laser light is denoted by \mathbf{k}_0 . The first ingredient of the rule is the observation that density of wave vectors with $\mathbf{k} \cdot \mathbf{k}_0 \neq 0$ line-integrates to zero, as sketched in figure 2.9. This leads to the selection criterion $\mathbf{k} \perp \mathbf{k}_0$. Secondly, density perturbations in a magnetised plasma are elongated along the magnetic field lines, which leads to the criterion $\mathbf{k} \perp \mathbf{B}$. Combining the two criteria leads to the selection rule:

$$\mathbf{k} \parallel \mathbf{B} \times \mathbf{k}_0. \quad (2.39)$$

Figure 2.10 is a simple illustration of the utility of the selection rule. It shows two sub-regions (labeled ‘1’ and ‘2’) along a chord, for which the magnetic field \mathbf{B} has a different orientation with respect to the fixed coordinate system of the beam. In region 1 the measurement is sensitive to \mathbf{k} along the x-axis, resulting in the red intensity pattern in the image plane. In region 2 the selected \mathbf{k} also has a y-component; the resulting blue intensity pattern in the image plane is therefore inclined with respect to the x-axis. The total image intensity is a superposition of the contributions from positions 1 and 2, but these can easily be separated by a numerical two-dimensional Fourier decomposition. This requires a two-dimensional detector array, such as the one employed in the PCI diagnostic in the Large Helical Device (Tanaka et al. 2008). Alternatively, if a one-dimensional array or a single detector element is used, Fourier components may be selected optically by spatial filtering in a focal plane. This method is employed in the DIII-D phase-contrast diagnostic (Dorris et al. 2009). In either case, isolating spatial Fourier components of the image intensity in a given angular range amounts to reducing the effective integration length to a known, potentially short, sub-region of the total.

Referring to figure 2.10, we denote the angle of \mathbf{k} with respect to the x-axis by $\alpha(z)$. The reduction in integration length for a given angular width and orientation of the filter depends on how fast the direction given by the selection rule varies along the chord, i.e. $d\alpha/dz$. First we consider the case of a ‘vertically’ launched beam (i.e. parallel to the symmetry axis of the tokamak), which is the geometry employed in the previously mentioned DIII-D and LHD phase-contrast systems. Referring to the coordinate system of figure 2.10, we let y correspond to the toroidal (ϕ) direction, so that x is the radial (R) direction. Also, $\hat{k}_{R,\phi,z}$ and $\hat{B}_{R,\phi,z}$ denote the projections along the (R, ϕ, z) directions of the unit vectors in the direction of the selected \mathbf{k} and \mathbf{B} , respectively. It can thus be seen that for a vertically launched beam $\hat{k}_\phi = -\hat{B}_R$ and $\hat{k}_R = \hat{B}_\phi$. Denoting the point where the beam is tangent to the flux surface by $z = 0$, we see that $\alpha(z)$ is single-valued, which means that the method for longitudinal localisation is possible. However, the reduction in integration length is poor, since $\hat{B}_\phi \gg \hat{B}_R$: α does not change much over the chord. Also, $d\alpha/dz$ is approximately constant.

For a tangential beam geometry, such as the one employed in TCV (figure 2.1) the situation is quite different. For simplicity we assume that the beam is in fact horizontal

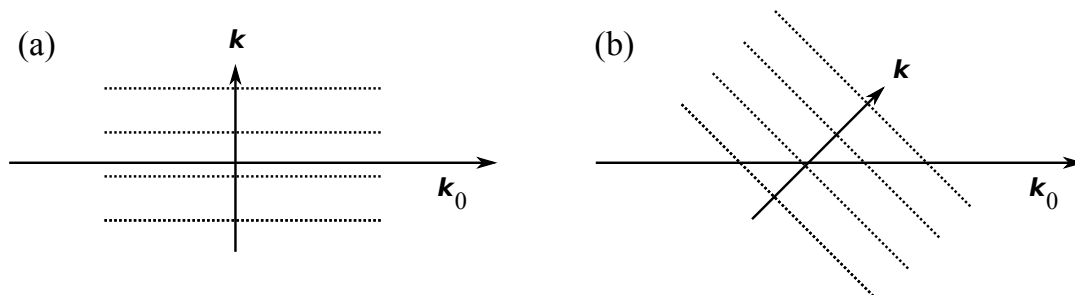


Figure 2.9: Dotted lines indicate wave fronts of the density perturbation. The perturbation in (a) gives a net contribution to the line-integration, but the one in (b) does not.

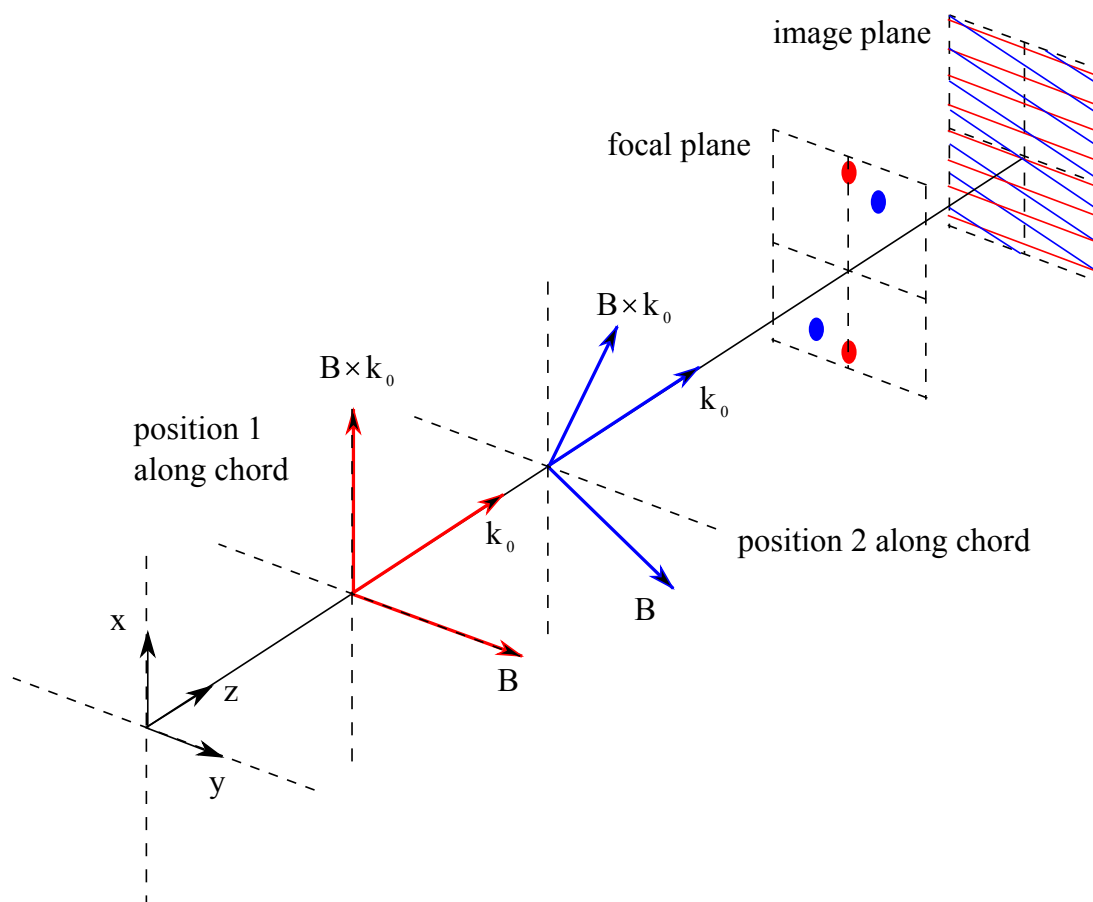


Figure 2.10: The principle of longitudinal localisation of a line-integrated measurement using the wave-vector selection rule $\mathbf{k} \parallel \mathbf{B} \times \mathbf{k}_0$. The optical axis is the z -axis. For each position, a single wave vector is assumed to satisfy the selection rule. Colour coding is used to discriminate between the contributions from position 1 and 2.

and in the mid-plane of the tokamak and zero safety factor everywhere. At the tangency point we now associate (x, y, z) with (z, R, ϕ) . The selected wave vector then lies in the z ('poloidal') direction everywhere along the chord, except at the tangency point, where all directions are allowed. If by filtering for example the y direction is selected, one obtains an extremely localised measurement of radial fluctuations around the tangency point. The inclusion of shear and a finite elevation angle of the beam above the horizontal makes the behaviour around the tangency point less extreme. In figure 3.4 we show that in TCV α typically executes a $\sim 100^\circ$ swing in the ~ 20 cm around the tangency point. As before, since the radial coordinate of the chord varies little around the tangency point, the measurement is radially very well localised. For example, a filter with a $\sim 30^\circ$ half-angle leads to a resolution of a few percent of the minor radius.

For a more in-depth treatment of the possibilities of localisation in the TCV phase-contrast system, and a detailed discussion of the design of the required spatial filters, we refer to Marinoni 2009.

2.5 Optical transfer function of the phase-contrast method

In §2.3 we have presented intuitive arguments that showed that the phase plate acts as a spatial high-pass filter with cutoff frequency $k_c = k_0 v/F$. Here we present the results from a more rigorous treatment of the optical transfer properties of the phase-contrast method, which will be needed in chapters 3 and 4. The section is a condensed version of §2.11 from Coda 1997, omitting most of the derivations.

Assuming that the Raman-Nath regime applies, the plasma acts as a thin phase screen, introducing an instantaneous phase shift $\varphi_0 + \tilde{\varphi}(\mathbf{x}_\perp, t)$ to the incident wave in the object plane. We assume again that $\tilde{\varphi} \ll 1$ rad, and we ignore the constant φ_0 . Our first goal is to find the corresponding intensity distribution $\mathcal{E}(\mathbf{x}_\perp, t)$ in the image plane. Let $E_{p0}(\mathbf{x}_\perp)$ denote the wave field in the object plane in the absence of density fluctuations. The total wave field in the object plane can be expressed as $E_{p0}(1 + i\tilde{\varphi})$. Neglecting time dependence and a constant phase factor, the corresponding wave field in the image plane is

$$E_{\text{im}}(M\mathbf{x}_\perp) = \frac{1}{M} \{T \circ [P_a E_{p0}(1 + i\tilde{\varphi})]\}(\mathbf{x}_\perp). \quad (2.40)$$

Here, M is the optical magnification of the system, T is the transfer function of the phase plate and the symbol 'o' denotes convolution. The pupil function is defined as

$$P_a(y) = \begin{cases} 1 & \text{if } |y| \leq a \\ 0 & \text{otherwise.} \end{cases} \quad (2.41)$$

The light intensity associated with the field of equation 2.40 is

$$\mathcal{E}(M\mathbf{x}_\perp) = \frac{\epsilon_0 c}{2M^2} |E_{\text{im}}(M\mathbf{x}_\perp)|^2. \quad (2.42)$$

This can be expressed as $\mathcal{E} = \mathcal{E}_{\text{dc}} + \tilde{\mathcal{E}}$, where

$$\mathcal{E}_{\text{dc}}(M\mathbf{x}_\perp) = \frac{\epsilon_0 c}{2M^2} |T \circ (P_a E_{p0})|^2(\mathbf{x}_\perp) \quad (2.43)$$

and, to first order in $\tilde{\varphi}$,

$$\tilde{\mathcal{E}}(M\mathbf{x}_\perp) = \frac{\epsilon_0 c}{M^2} \text{Im} \{ [T \circ (P_a E_{p0})] [T \circ (P_a E_{p0} \tilde{\varphi})]^* \} (\mathbf{x}_\perp), \quad (2.44)$$

where the asterisk denotes complex conjugation.

By virtue of equation 2.37 we can write the transfer function of the phase plate (figure 2.8) in \mathbf{k}_\perp space as

$$\hat{T}(\mathbf{k}_\perp) = 1 + P_{k_c}(k_x)(i\sqrt{\rho} - 1), \quad (2.45)$$

where P_{k_c} again denotes the pupil function (equation 2.41) and $k_c = k_0 v / F$. Taking the inverse Fourier transform of equation 2.45 gives the corresponding transfer function in object space:

$$T(\mathbf{x}_\perp) = \delta(\mathbf{x}_\perp) + (i\sqrt{\rho} - 1)\hat{P}_{k_c}(\mathbf{x}_\perp), \quad (2.46)$$

with

$$\hat{P}_{k_c} = \frac{1}{\pi x} \sin(k_c x) \delta(y). \quad (2.47)$$

Here, $\delta(x)$ is the delta function. Equations 2.43, 2.44 and 2.46 give the intensity distribution in the image plane for a given phase in the object plane, and can be easily solved numerically.

It can be shown that the PCI image formation process is described to good approximation by an optical transfer function $\mathcal{T}(\mathbf{K})$ in combination with a weighting function $W(\mathbf{x}_\perp)$. Consider the following sinusoidal input phase:

$$\tilde{\varphi}(\mathbf{x}_\perp) = \hat{\varphi}_{\mathbf{K}} \cos(\mathbf{K} \cdot \mathbf{x}_\perp + \zeta_0). \quad (2.48)$$

$\mathcal{T}(\mathbf{K})$ is defined through the response to this phase in the centre of the image:

$$\tilde{\mathcal{E}}(0) = \mathcal{T}(\mathbf{K}) \hat{\varphi}_{\mathbf{K}} \cos(\zeta_0). \quad (2.49)$$

Away from the centre we have

$$\tilde{\mathcal{E}}(\mathbf{x}_\perp) \simeq W(\mathbf{x}_\perp) \mathcal{T}(\mathbf{K}) P_a(|\mathbf{x}_\perp|) \hat{\varphi}_{\mathbf{K}} \cos(\mathbf{K} \cdot \mathbf{x}_\perp + \zeta_0), \quad (2.50)$$

where

$$W(\mathbf{x}_\perp) = \frac{E_{p0}(\mathbf{x}_\perp) \left[\hat{P}_{k_c} \circ (P_a E_{p0}) \right] (\mathbf{x}_\perp)}{E_{p0}(0) \left[\hat{P}_{k_c} \circ (P_a E_{p0}) \right] (0)} \quad (2.51)$$

accounts for the \mathbf{x}_\perp dependence of the signal level.

If the incident beam is Gaussian (equation 2.21) with a waist in the object plane and total power P , analytical expressions can be found for $\mathcal{T}(\mathbf{K})$. The field in the object plane is then

$$E_{p0}(\mathbf{x}_\perp) = \sqrt{\frac{4P}{\pi \epsilon_0 c w_0}} \frac{1}{w_0} e^{-|\mathbf{x}_\perp|^2 / w_0^2}. \quad (2.52)$$

In the limit of infinite aperture ($a \rightarrow \infty$) the transfer function can be formulated in terms of error functions ($\text{erf}(y) = (2/\sqrt{\pi}) \int_0^y e^{-\xi^2} d\xi$) by

$$\mathcal{T}(\mathbf{K}) = 2\sqrt{\rho} u_0(0) \left[\text{erf} Q - \frac{1}{2} \text{erf}(Q + K'_x) - \frac{1}{2} \text{erf}(Q - K'_x) \right], \quad (2.53)$$

where $Q = k_c w_0/2$, $\mathbf{K}' = w_0 \mathbf{K}/2$, and $u_0(0) = 2P/(\pi M^2 w_0^2)$ is the dc power flux in the centre of the image if the phase plate is replaced by a mirror. For finite aperture a one finds

$$\mathcal{T}(\mathbf{K}) = 2\sqrt{\rho}u_0(0) \int_{-a}^{+a} \frac{\sin(k_c x)}{\pi x} e^{-x^2/w_0^2} [1 - \cos(K_x x)] dx. \quad (2.54)$$

To find a good transfer function, one must balance two conflicting requirements. The first is that signal level should be acceptably high throughout the image. Secondly, the transfer function should be smooth for a wide range of \mathbf{K} . By studying equations 2.54 and 2.51 for fixed total power P of the beam, one finds that choosing $1.4 \lesssim Q \lesssim 1.8$ and $w_0/a \simeq 1$ gives a good compromise. Figure 2.11 shows an example.

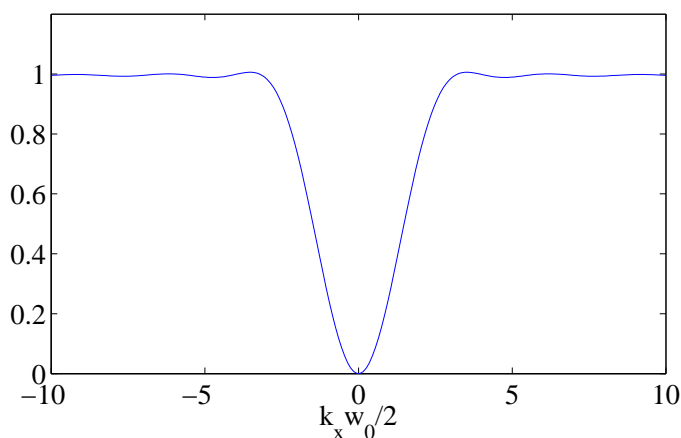


Figure 2.11: PCI optical transfer function. $Q = 1.5$; $w_0/a = 1$.

Finally, we note that the experimental sampling procedure of the image also has a contribution to the transfer function. The signal from each detector element is proportional to the light intensity integrated over the area of the element. Therefore, components of the image with sufficiently short wavelength are to some extent averaged out. For square elements with sides L , the transfer function of this averaging process is

$$\mathcal{T}_{\text{av}}(K) = \frac{\sqrt{2 - 2 \cos(KL/|M|)}}{KL/|M|}. \quad (2.55)$$

Here, k is a wave number in the object plane and M is the optical magnification.

2.6 Data analysis techniques

We now list the definition of several statistical quantities which will be used in chapter 4 to elucidate the spatial and temporal correlation structure of the TPCI signals $\tilde{n}(x, t)$, where x denotes the position in the object plane. A random, real-valued, and potentially non-stationary signal $\tilde{n}(x, t)$ has a two-point, time-delayed correlation function

$$R(x, t; \xi, \tau) = \langle \tilde{n}(x, t) \tilde{n}(x + \xi, t + \tau) \rangle, \quad (2.56)$$

where $\langle \dots \rangle$ denotes ensemble averaging. In practice, the ensemble consists of a set of sub-records of finite duration (Bendat et al. 2010). Taking the temporal Fourier transform of $R(\xi, \tau)$ yields the two-point cross-power spectral density:

$$S(x, t; \xi, \omega) = \int R(x, t; \xi, \tau) e^{i\omega\tau} d\tau. \quad (2.57)$$

This can be normalised to give the (complex) two-point coherence function

$$\gamma(x, t; \xi; \omega) = \frac{S(x, t; \xi, \omega)}{\sqrt{|S(x, t; 0, \omega)| |S(x, t; \xi, \omega)|}}. \quad (2.58)$$

Finally, the spatial Fourier transform of the coherence function yields the conditional spectrum

$$s(x, t; k|\omega) = \int \gamma(x, t; \xi, \omega) e^{-ik\xi} d\xi. \quad (2.59)$$

For stationary \tilde{n} the (x, t) dependence disappears in equations 2.56-2.59. It can be shown that in this case 2.59 is real and positive. The sign conventions chosen in equations 2.57 and 2.59 are such that the $\omega > 0$ component of a wave propagating in the positive x direction has $k > 0$.

The temporal Fourier transform in equation 2.57 is evaluated using fft procedures. In view of the small number (nine) and irregular spacing of spatial points (nine) we have available, the spatial Fourier transform in equation 2.59 cannot be evaluated by fft. Rather, we find a conditional spectrum $s(k|\omega)$ whose *inverse* Fourier transform matches γ (equation 2.58) to within the error bars. A solution to this ill-posed problem is found by minimising an entropy functional $F[s(k|\omega)]$ using Hildreth's method of interval constraints (Censor 1981). This is the same method used by (Coda 1997).

Finding the correlation function R_n of the density fluctuations on the basis of that of the phase R_φ signals is not possible in general. We now discuss the inverse problem, which can also be illuminating in certain cases. We will use simple analytical test functions for R_n , which are most conveniently expressed in flux coordinates $\{\rho_{\text{vol}}, \theta, \phi\}$. In the following we shall denote ρ_{vol} simply by ρ . The two-point correlation function of the phase in the object plane is given (through application of equation 2.19) by

$$R_\varphi(x_i, x_j) = \langle \varphi(x_i) \varphi(x_j) \rangle = (r_e \lambda_0)^2 \int_{u_{\text{in}}}^{u_{\text{out}}} \int_{v_{\text{in}}}^{v_{\text{out}}} R_n(\rho_i[u], \rho_j[v], \theta_i[u], \theta_j[v], \phi_i[u], \phi_j[v]) dudv. \quad (2.60)$$

The indices i and j designate the two integration chords corresponding to the points x_i and x_j in the object plane for which the correlation function is evaluated. The functions $(\rho_i[s], \theta_i[s], \phi_i[s])$ represent the flux coordinates of chord i , parametrized by the distance s along the chord; the subscripts 'in' and 'out' in the integration limits refer to the points where each chord intersects the last closed flux surface (we assume that the perturbation is zero outside of the closed magnetic surfaces).

The parametrized chord coordinates are readily obtained from the Psi-Toolbox, which is an in-house suite of Matlab routines for manipulating space- and time-dependent quantities in the variable geometries of TCV. The LIUQE equilibrium solver is used to calculate the flux function. We use numerical quadrature to evaluate the double integral in equation 2.60.

Even when R_n is spatially stationary, R_φ will in general not be stationary (Bendat et al. 2010). To get a measure of this non-stationarity we evaluate equation 2.60 on two sets of chord pairs. First we choose the innermost chord as reference, i.e. $\{i = 1; j = [1, 2, \dots, N]\}$, yielding $R_\varphi^{\text{in}}(\Delta x)$, with $\Delta x \geq 0$. N represents the number of chords used in the calculation. For the second set of chord pairs we choose the outermost chord as reference, i.e. $\{i = N; j = [1, 2, \dots, N]\}$, yielding $R_\varphi^{\text{out}}(-\Delta x)$ with $\Delta x \geq 0$. If R_φ were stationary, we would have $R_\varphi^{\text{in}}(\Delta x) = R_\varphi^{\text{out}*}(-\Delta x)$, where the asterisk denotes complex conjugation. We use the average of $R_\varphi^{\text{in}}(\Delta x)$ and $R_\varphi^{\text{out}*}(-\Delta x)$ as a stationary approximation of the non-stationary two-point correlation function of the phase; the maximum absolute difference between $R_\varphi^{\text{in}}(\Delta x)$ and $R_\varphi^{\text{out}*}(-\Delta x)$ reflects the departure from stationarity; this quantity is used as an error bar.

The quantity that is measured by the TPCI diagnostic is the intensity pattern $\tilde{\mathcal{E}}(Mx)$ in the image plane, which is related to the phase shift in the object plane through $\tilde{\mathcal{E}}(Mx) = (T \circ \tilde{\varphi})(x)$, where the circle denotes convolution and $T(x)$ is the phase-contrast optical transfer function in the spatial domain. If the phase shift to be imaged is a spatially stationary random process with spatial spectrum $\hat{R}_\varphi(k)$, the corresponding spectrum of the TPCI image is then

$$\hat{R}_{\mathcal{E}}(k) = |\hat{T}(k)|^2 \hat{R}_\varphi(k). \quad (2.61)$$

Chapter 3

The tangential phase-contrast imaging diagnostic in TCV

This chapter describes the tangential phase-contrast imaging (TPCI) diagnostic in TCV (Marinoni 2009). The instrument measures the line-integrated density along 30 parallel chords within a 6.5 cm wide CO₂ laser beam. The novel tangential beam geometry allows drastic reduction of the integration length through spatial filtering. The primary use of the diagnostic lies in the study of micro-turbulence.

We start with a brief presentation of the TCV tokamak and the physics research program in section 3.1. Section 3.2 discusses the magnetic geometry in the volume where the plasma interacts with the laser light, which is the crucial aspect of the TPCI concept. In section 3.3 we describe the hardware that constitutes the diagnostic, in the order of beam propagation, up to the objective optics. Special emphasis is placed on the port assemblies and on the in-vessel mirrors, which proved to limit the performance of the diagnostic through the introduction of optical aberrations. These aberrations, and their impact on the imaging optical system, are the subject of section 3.4. Next, we discuss the detection and acquisition of the image in section 3.5 and various tests of the optical system using acoustic waves in section 3.6. Finally, section 3.7.2 discusses the problem of vibrational focal shifts, as well as the principles and experimental performance of a feedback system used to compensate these shifts.

3.1 The TCV tokamak

The TCV tokamak (Hofmann, Lister, et al. 1994) is operated at the centre for plasma physics research (CRPP) of the Ecole Polytechnique Fédérale de Lausanne, Switzerland. Table 3.1 lists the most salient machine and plasma parameters. The tokamak was designed to study confinement and stability for a wide variety of plasma shapes. This is made possible by a set of sixteen independently controlled poloidal field coils, as well as a vacuum vessel (figure 3.1) that can accommodate highly elongated plasmas. Two additional poloidal field coils are located inside the vessel, for improved control of vertical instability.

A second unique feature of the TCV tokamak is its electron heating and current-drive system (T. Goodman et al. 2008). It features a total of nine gyrotron microwave sources,

Major radius	0.88 m
Minor radius	0.25 m
Inner height vacuum vessel	1.45 m
Toroidal magnetic field	< 1.54 T
Plasma current	< 1 MA
Elongation	$0.9 < \kappa < 2.8$
Triangularity	$-0.8 < \delta < 1$
Electron temperature	< 15 keV
Ion temperature	< 1 keV
Electron density	$< 2 \times 10^{20}$ m ⁻³
Energy confinement time	< 50 ms
Gyrotron power	4.5 MW

Table 3.1: Selected parameters of the TCV tokamak.

each with an output power of 500 kW. Six gyrotrons are operated at 82.7 GHz, which corresponds to the second harmonic of the electron gyro-frequency near $R = 0.9$ m. Each of the second-harmonic microwave beams is injected into the plasma through a lateral port and focussed to a small spot on the resonance layer. Crucially, the launching optics have two degrees of freedom, allowing power deposition at arbitrary radius as well as non-inductive current drive. The polarisation of the microwaves can be chosen arbitrarily; X-mode is usually preferred in light of its superior absorption. High density H-mode plasmas can be heated using three additional gyrotrons, which are operated at 118 GHz for resonance at the third harmonic of the electron cyclotron frequency. To optimise the absorption the beams are injected vertically, tangential to the resonant surface, by means of a (single) steerable launcher. X-mode heating in the second and third harmonics is usually referred to simply as ‘X2’ and ‘X3’.

Thanks to its gyrotron system, internal electron transport barriers can be created and studied in TCV (Coda, Asp, et al. 2007). These barriers have allowed steady state plasma operation where all current comes from the bootstrap effect (Coda 2008). The core of the real-time control system of TCV has recently been converted from analogue to digital and extended to include the gyrotron power and injection angles; these actuators can now be used to control MHD instabilities (Felici et al. 2012), as well as the current and pressure profiles. Studies of plasma shaping also continue to play a major role in the research program of TCV, the most prominent example being the recently developed ‘snowflake’ divertor configuration, which mitigates the heat flux to the wall and has also been found to significantly alter ELM dynamics (Piras et al. 2010). Other subjects being pursued include intrinsic rotation (Camenen, Bortolon, et al. 2010), H-mode studies (Rossel et al. 2012) and the physics of supra-thermal electrons (Klimanov et al. 2007).

More than two hundred magnetic pickup coils are installed inside the TCV vessel, between the wall and the graphite tiles (Moret, Buhlmann, et al. 1998). The signal of each probe is proportional to the time derivative of the magnetic field component along the probe axis, which lies in a poloidal plane and is aligned with the vessel wall. A subset of these probes is used in the control loop of the plasma shape. Since the probes have a broad frequency response (>100 kHz) and are absolutely calibrated, they are also a

powerful tool for studying MHD phenomena (Reimerdes et al. 1998).

The in-vessel coils are arranged in toroidal and poloidal arrays (figure 3.1). There are four complete poloidal arrays of 38 probes each, toroidally separated by 90 degrees. Three toroidal arrays are installed especially for MHD studies. One is located in the mid-plane, and the other two 35 cm above and below it, respectively. Each toroidal array consists of 8 equidistant probes on the high-field side and 16 on the low-field side. A total of 60 ADC channels are available for fast acquisition (up to 250 kHz) of probe signals for MHD studies. Thus, for any TCV discharge data from only one poloidal and one toroidal array can be digitised at a high sampling frequency. The choice of the toroidal array depends on the position of the plasma in the vessel.

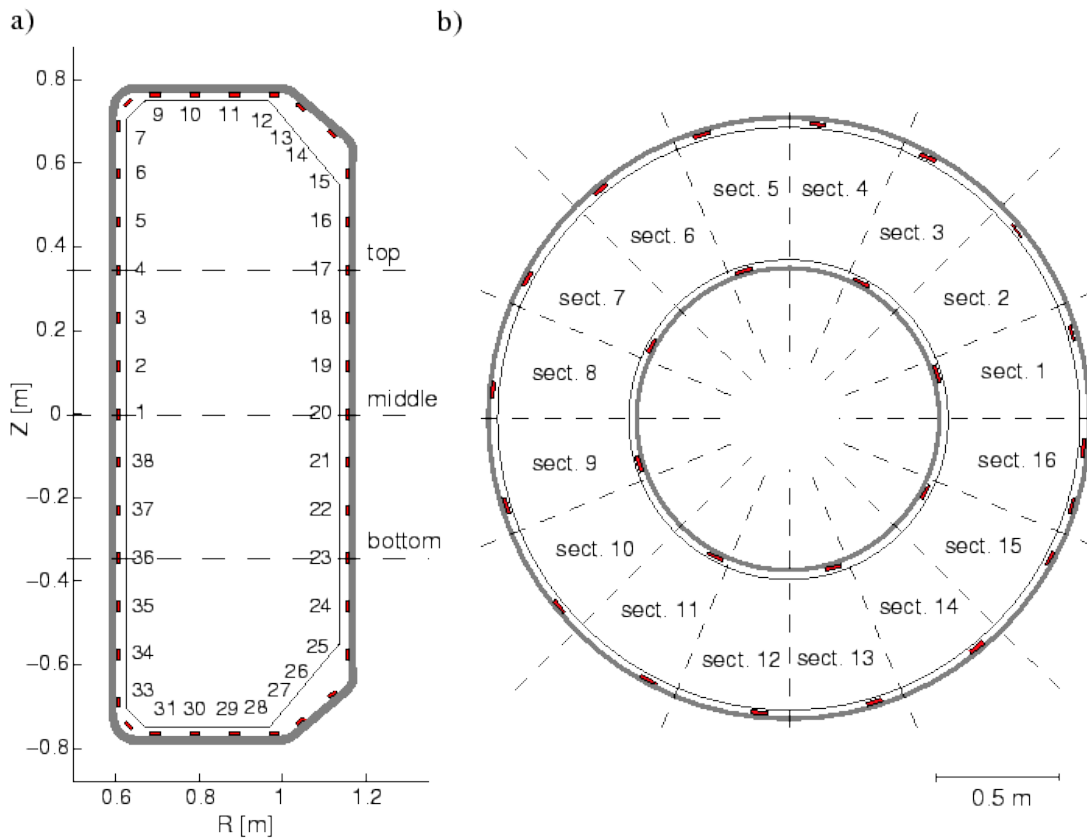


Figure 3.1: Poloidal (a) and toroidal (b) cross-sections of the TCV vessel, showing the layout of the fast magnetic probes.

Knowledge of the shape of the flux-surfaces is crucial in the analysis of TCV plasmas. Presently, a detailed equilibrium reconstruction is performed routinely after each discharge, using the in-house Grad-Shafranov solver LIUQE (Hofmann, Lister, et al. 1994). The solution is constrained using measurements from two opposing poloidal magnetic probe arrays inside the vessel and a number of external loops. Normally only magnetic measurements are used, but additional constraints, such as the measured pressure profile, can be added to improve the accuracy of the solution.

Electron temperature and density are measured using a 35-channel Thomson scatter-

ing diagnostic employing three collinear, vertical laser beams, each with a pulse rate of 20 Hz (Pitzschke 2011). The density measurement is corrected using the central chord of a 14-channel far-infrared Mach-Zehnder interferometer, which is also used in the density control loop. Soft X-rays in the 1-10 keV range are measured along 200 lines of sight in a poloidal plane (Anton et al. 1996). These data are used in tomographic reconstruction of the emission profile, which contains information on the density, temperature and impurity content of the plasma, and is used in MHD studies.

Turbulence has been extensively studied in the TCV scrape-off layer by means of electrostatic probes (Garcia et al. 2007; Graves et al. 2005). Apart from the new tangential phase-contrast imaging system, the only other core-turbulence diagnostic in TCV is a two-channel correlation ECE diagnostic, which has recently been commissioned (Porte 2012). The instrument has a fixed line of sight which is horizontal and lies in the equatorial plane. Its radiometer covers the 65-81 GHz range, which corresponds to the low-field side in TCV, approximately up to mid-radius. The antenna pattern provides an effective detection volume of 6 cm in the poloidal direction. Four additional channels are presently being added to the diagnostic.

3.2 Geometry of the measurement

Figures 3.2 and 3.3 show the in-vessel beam path. We recall that the beam is collimated. Its maximum full Gaussian diameter is 6.65 cm: using a wider beam results in clipping of the scattered components at the exit. In most commonly used configurations, however, the beam diameter has to be reduced even further. The entry and exit ports are toroidally separated by three sectors, i.e. 67.5° , and the angle of the beam over the horizontal is 19° . For comparison, the maximum pitch angle of the magnetic field in a TCV plasma is typically 10° . The minimum major radius R reached by the centre of the beam lies between 93.8 cm and 97.1 cm, depending on the position of the entry and exit assemblies, which can be moved radially. The magnetic axis in TCV plasmas is typically located at $R = 90$ cm. For the measurements described in chapter 4 the full beam diameter was 5 cm, and the minimum R for the central chord was 96 cm.

We have seen that the beam path is fixed to within ~ 3 cm in laboratory coordinates. However, in terms of *flux* coordinates $(\rho_{\text{vol}}, \theta)$ it can be changed very substantially by moving the plasma vertically inside the vessel. This unique capability of the TCV tokamak is illustrated in figure 3.3, which shows the flux contours for two times in discharge 45353. In figure 3.3a the magnetic axis is at $z = 0$ cm, and the tangency points for the different chords within the laser beam lie in the range $0.67 < \rho_{\text{vol}} < 0.83$. By shifting the plasma further down the tangency points can also be chosen in the scrape-off layer. In figure 3.3b the magnetic axis has been shifted to $z = 23$ cm, and the tangency points lie in the range $0.27 < \rho_{\text{vol}} < 0.48$.

As discussed in §2.4, for a given position s along the chord, the strongest contribution to the phase shift comes from fluctuations with wave vectors \mathbf{k} satisfying the selection rule $\mathbf{k}(s) \parallel \mathbf{k}_0 \times \mathbf{B}(s)$. Here \mathbf{k}_0 is the wave vector of the laser and \mathbf{B} is the magnetic field. It was also argued that in an approximately tangential beam geometry the direction of \mathbf{k} depends strongly on s , which allows shortening of the integration length by spatial filtering in a focal plane. This is illustrated in figure 3.4 for the two geometries of figure 3.3. For each s , $\mathbf{k}(s)$ is projected onto the image plane. The angle between this projection and

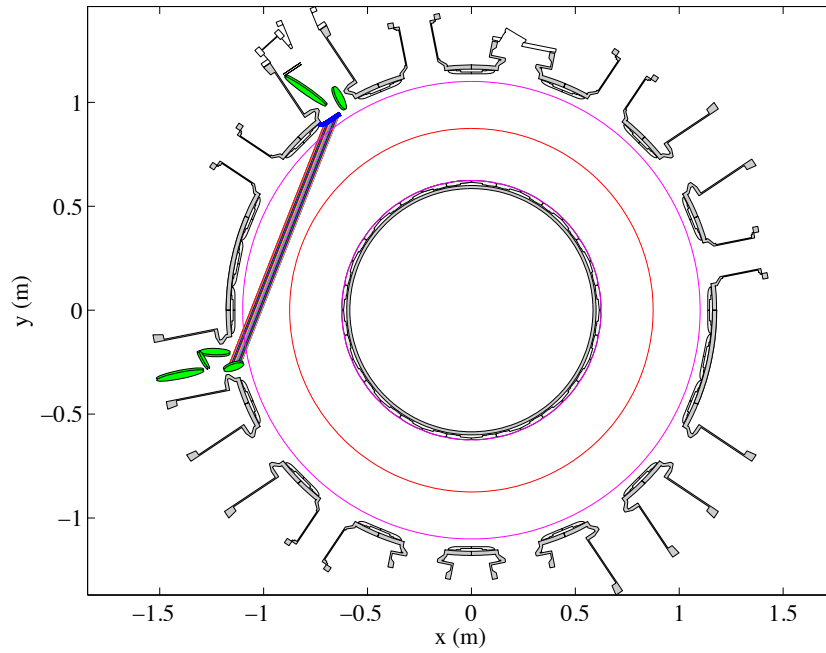


Figure 3.2: Toroidal cross section of the TCV tokamak showing the tangential beam geometry of the phase-contrast diagnostic. The magnetic axis is indicated in red, the outer and inner positions of the last closed flux surface in purple. The beam propagates in the positive y direction.

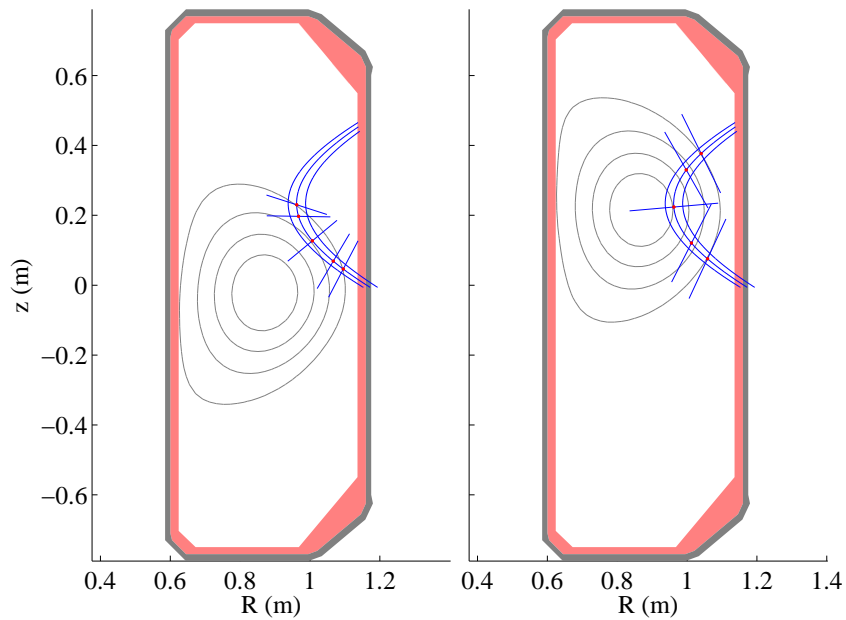


Figure 3.3: Poloidal projection of the beam path in the TCV vessel. The line segments indicate the poloidal projection of wave vectors satisfying the selection rule at different positions along the central chord. The beam propagates in the positive z direction.

that of the outward horizontal $\hat{\mathbf{z}} \times \mathbf{k}_0$ is denoted by $\alpha(s)$. Plots like these are used to determine the required orientation of the spatial filter.

For the physical interpretation of a wave vector it is of interest to project it along the flux-coordinate unit vectors $\hat{\boldsymbol{\rho}}$, $\hat{\boldsymbol{\theta}}$ and $\hat{\boldsymbol{\phi}}$. The corresponding ρ and θ direction cosines are shown in figure 3.4. The absolute value of the direction cosine along ϕ (not shown) is typically smaller than 0.15. It may be seen that \mathbf{k} is purely radial at the tangency point; away from it, it is a mix between radial and poloidal. In figure 3.3 the projection of \mathbf{k} in the poloidal plane is indicated by line segments on five points along the central chord.

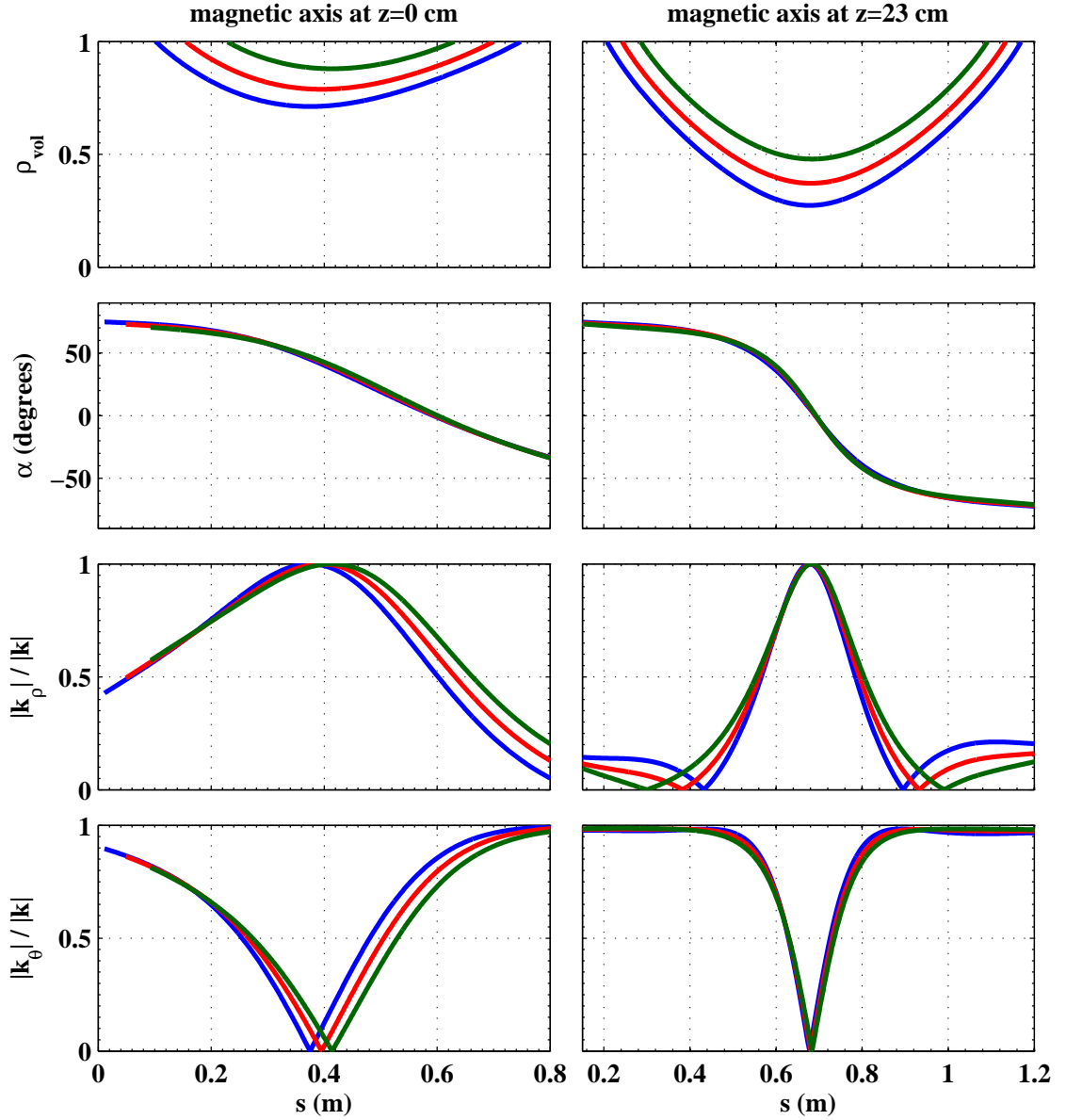


Figure 3.4: Various geometrical quantities (see text) as a function of distance s along the central and two extreme TPCI chords. The left column is associated with the geometry of figure 3.3a; the right column with figure 3.3b.

3.3 Beam path and plasma facing mirrors

Both the tokamak and the TPCI system are located in a secured area known as the ‘zone’, which is off-limits to personnel during plasma experiments. A cutaway drawing of the 0 and -1 levels of this area is shown in figure 3.5. The tokamak is situated on the 0 level. All of the focussing optics and all electronic and electrical equipment associated with the TPCI diagnostic is located on or around an optical table (Thorlabs 2x1 m breadboard) on the -1 level.

To generate the beam we use an RF excited waveguide CO₂ laser (Edinburgh Instruments model WL-8). This is the same laser that was used in the TCA phase-contrast diagnostic (Weisen 1988). It is located in the corner of the optical table; its power supplies are below the table. The beam has a 1.3 mm full Gaussian width and a nominal full divergence of 9 ± 1 mrad (measured value is 18 mrad). The polarisation of light is vertical $\pm 5^\circ$ and the laser has no grating. Its nominal output power is 8 W, but the measured value fluctuates between 6.5-7.3 W on a timescale of seconds. These fluctuations, which persist even after days of continuous operation, coincide with transitions between laser lines in the range 10.59-10.61 μm , as measured with a spectrum analyser. The laser is water cooled with a Neslab chiller (model Coolflow HX-75). The temperature of the cooling water drifts by up to $\pm 5^\circ\text{C}$ from the requested 15°C with this chiller, which may play a role in the observed power fluctuations of the laser. An interlock cuts the power supply of the laser when the flow of cooling water drops or when the temperature of the laser head gets too high.

A shutter (Lasermat model LS-10-12) is mounted directly after the laser aperture. It is integrated into the TCV security system and can only be opened when the TCV zone is evacuated. Various manipulations, such as alignment and calibration, require human intervention with the shutter open. To carry out these manipulations the security system can be put in a special state where access to the TCV zone is exclusive to TPCI personnel.

After the shutter the CO₂ beam passes through a beam combiner, where it is combined with a colinear visible laser beam for easy alignment. The alignment laser is a 635 nm, 100 mW diode (Scitec model SDL-635-LM-100T). ZnSe optics are transparent to this wavelength. To match the divergence of the CO₂ beam, the visible beam first passes through a tunable telescope. The mode purity of the diode is poor and as a result the intensity distribution of the expanded visible laser light is quite inhomogeneous. This is improved by placing a pinhole in the focal point of the telescope, sacrificing some intensity. The coalignment is performed with the aid of thermal plates, which reveal the CO₂ spot when illuminated with an ultraviolet lamp.

The combined beams are expanded to a collimated beam with full Gaussian width of 5.0 cm by two focussing optics in a refractive-reflective telescope configuration and several plane mirrors on kinematic mounts. All other mirrors in the optical path (with the exception of the in-vessel ones) are also mounted in optical gimbal or kinematic mounts, for dual-axis adjustment. The first telescope optic is a plano-convex ZnSe lens ($f = 25.4$ cm); the second is an off-axis parabolic mirror ($f = 1.905$ m; clear aperture 13 cm). To account for finite half-divergence θ of the beam coming from the laser aperture, the separation between the telescope optics to be $(1 + \theta f_2/w)f_1 + f_2$ and the distance from the input waist to the first optic $(1 + w/[\theta f_2])f_1$ in order to obtain a collimated beam with $1/e$ amplitude radius w . For the measurements of chapter 4 we employed a

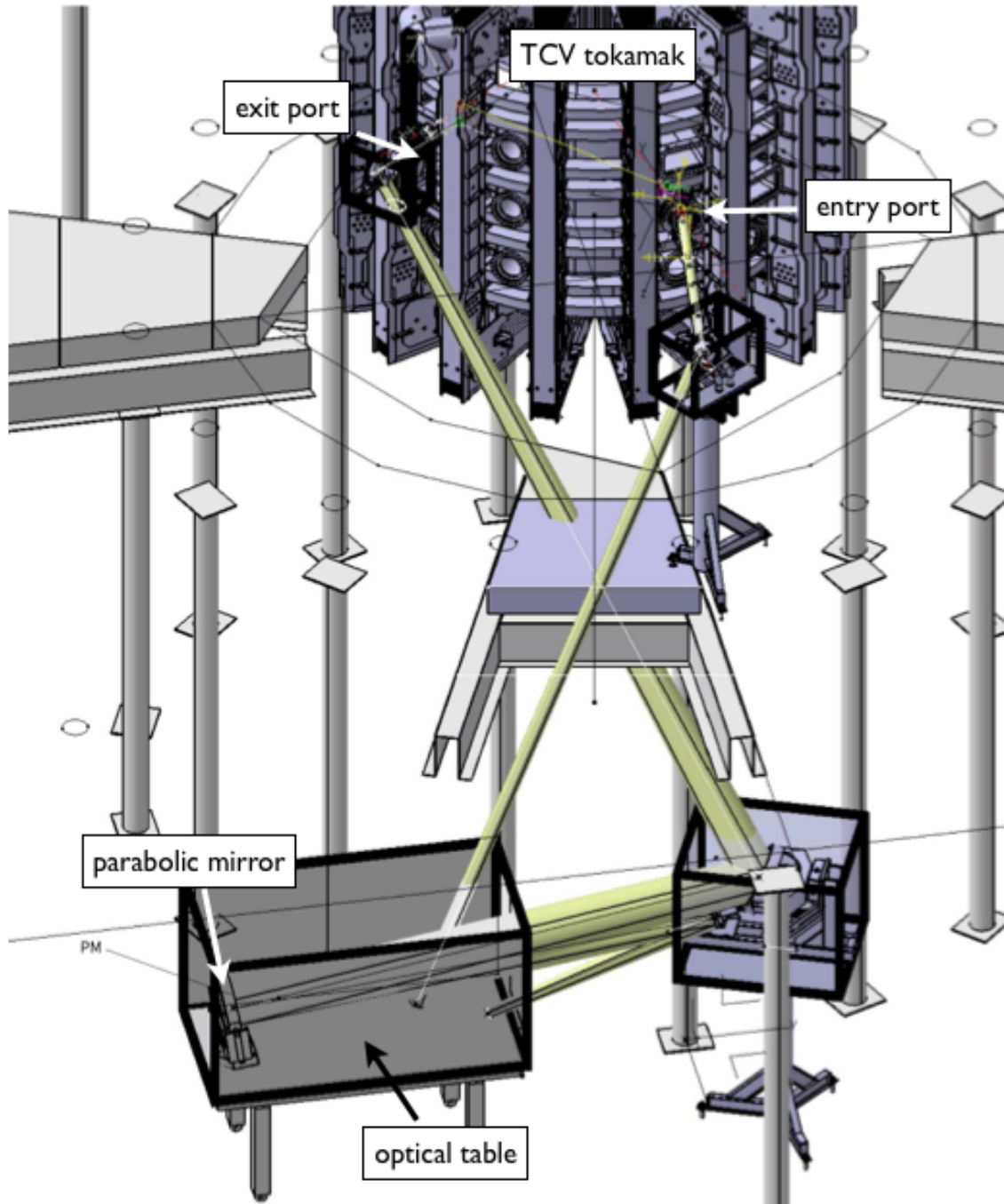


Figure 3.5: Cutaway drawing of the 0 and -1 levels of the TCV zone showing the tokamak and the TPCI diagnostic. The beam path is indicated in yellow. An aluminum and plexiglass tunnel connecting the two cages on the -1 level is not shown. For reference: the length of the optical table is 2 m. From Marinoni 2009.

pair of small plano-convex ZnSe cylinder lenses near the first focal point to correct for astigmatism introduced by the in-vessel mirrors (section 3.4).

The expanded beam is sent up to the TCV level by a 12 cm diameter mirror, which sits on a linear translation stage. The translation axis is oriented to keep the beam centred on the TCV entry assembly when the latter is moved radially. Polycarbonate tubes are planned to enclose the beam over its entire path outside of TCV and the optical table (figure 3.5), but have not yet been installed at the time of writing of this thesis. The beam crosses the floor between the -1 and 0 levels twice, through two separate holes. The regular floor elements around TCV are made of concrete, but the two elements in the TPCI beam path were remade in wood prior to drilling the holes, for easier manipulation. After the first crossing, a plane mirror (15 cm diameter) on the 0 level steers the beam to the equatorial port in sector 1 of TCV. The mirror is protected by a cage of aluminum and plexiglass, mounted on a free-standing steel pillar (figure 3.5).

We now briefly describe the entry (figure 3.6a) and exit mirror assemblies of the TPCI diagnostic; for the details of their design we refer to Marinoni 2009. The entry assembly consists of three plane elliptical mirrors (designated by M1-3), of which the last two are inside the vacuum, behind a ZnSe window. M3 sends the beam through TCV at an angle of 19° above the horizontal. The exit mirror assembly is located in the upper lateral port of sector 14, which is $\simeq 70^\circ$ toroidally removed from the entry port and $\simeq 46$ cm higher. It consists of two plane elliptical mirrors (designated by M4-5), both inside the vacuum, behind a ZnSe window. The supports of the two ZnSe windows are water-cooled to protect the O-rings in the vacuum seal during baking of the vessel. Bellows allow the entry and exit assemblies to be moved radially over 9.5 cm and 6.5 cm, respectively. In their outermost useful position the tips of the first mirrors are flush with the tiles that cover the low-field side wall of TCV; in their innermost position the entry and exit mirrors protrude 6 cm and 2 cm beyond the tiles, respectively. The required tilt of M3 and M4 depends on the radial position of the assemblies and can be changed over $\sim 2^\circ$ by a micrometer.

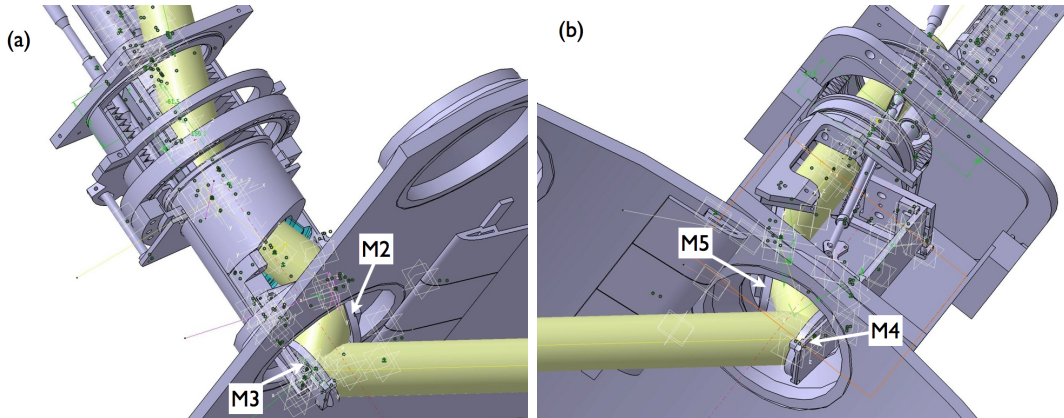


Figure 3.6: Cutaway drawing of the TPCI entry (a) and exit (b) port assemblies.

The surface of precision optical mirrors can quickly degrade in the tokamak environment, due to erosion and deposition. In-vessel mirrors of the TPCI diagnostic in TCV cannot be replaced routinely during an experimental campaign, since it requires removing

3.3. Beam path and plasma facing mirrors

the entire mirror assembly from the port and breaking the vacuum. Protective measures for these mirrors are therefore very important. Each of the four in-vessel mirrors of the entry and exit assemblies consists of a fused silica (SiO_2) substrate with a reflective coating, protected by a layer of SiO_2 . M2, M3 and M4 currently have a gold coating; M5 has an aluminium coating. Originally M2 also had an aluminium coating, but this degraded too rapidly. The surfaces of M2-4 are floating to protect them against ion bombardment; M5 is sufficiently far away from the plasma that this precaution is unnecessary.

Over the course of approximately 10,000 plasma discharges since 2007 the aluminium coating of M5 has degraded only marginally. The original gold coating of M4 has steadily degraded, but is presently still usable. The mirrors M2-3 in the equatorial entry port suffer most and have to be periodically replaced. For example, the reflectivity of M3 (originally possessing a Mo coating) decreased from 85% to 30% over ~ 9000 TCV shots; for ~ 8000 of these the mirror assembly was fully retracted. Analysis by scanning electron microscope shows that the mechanism which degrades the surfaces of our in-vessel mirrors is erosion rather than deposition. Moreover, the greater damage suffered by the midplane optics, which on average are closer to the plasma, indicates that plasma operation is more detrimental than glow discharge cleaning (which permeates the entire vessel). The transmission of the vacuum windows also decreases over time, but we have not yet measured this.

The mirrors M2-3 were replaced by new ones approximately 1300 discharges before the experiments of chapter 4. At the time of the experiments the combined transmission for the 5 cm diameter CO_2 laser beam through the two mirror assemblies was $\sim 40\%$, compared to $\sim 80\%$ with all the components in their initial state. This was in part due to an error in the radial positioning of the entry assembly, which left M3 protruding 1.2 cm beyond the tiles. Tens of plasmas with magnetic axis at the machine mid-plane were limited on the tip of M3, which was severely damaged. A set of graphite tiles has recently been installed to cover as much of the entry and exit ports as possible, without obstructing the beam. This minimises the angle over which the mirrors are exposed to bombardment by neutrals. Visible light is much more strongly attenuated than infrared on passage through TCV: the expanded beam of the alignment laser is difficult to see after passing through the tokamak.

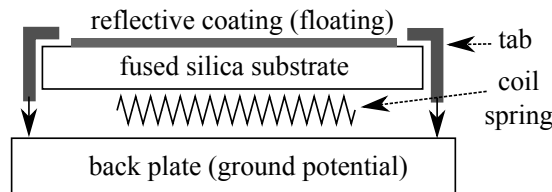


Figure 3.7: Illustration of the mounting strategy of the in-vessel mirrors. The use of four tabs and coil springs proved to deform the mirror surface by tens of μm , leading to strong optical aberrations.

During the experiments of chapter 4 each of the five mirrors of the entry- and exit assembly was held in place by four tabs pressing down on the edge of the mirror surface. To avoid deformation, the back of the mirror rested on coiled springs, kept in place by a groove in the back plate (figure 3.7). This proved to be a flawed design, because the force exerted by the spring, cantilevered by the fixed supports, introduced deformations of the mirror

surface of tens of μm , much greater than the $1\ \mu\text{m}$ tolerance. The resulting aberrations (section 3.4) were the limiting factor in the performance of the TPCI diagnostic so far. As a temporary solution the mirrors currently rest on three washers instead of the springs, and only the three corresponding tabs are tightened. Finally, we note that during plasma discharges the mirror assemblies vibrate much more strongly than expected for frequencies greater than 20 Hz. We discuss this problem and our attempts to solve it in section 3.7.

After passage through the tokamak the effective footprint of the beam diverges due to the scattered components and mechanical vibrations of the port optics. All optics and apertures in this part of the optical path are dimensioned to accommodate a 7.5 cm diameter beam with 2.3 mrad half-divergence. After leaving the exit port an oversized 23 cm diameter plane mirror sends the beam back down to the -1 level. The mirror is housed in a protective cage of aluminum bars and plexiglass, mounted on the TCV support structure. On the -1 level the beam is redirected to the optical table by a 40 cm diameter plane mirror. This mirror is also housed in an aluminium and plexiglass cage, mounted on a steel pillar (figure 3.5). The cage is connected to the enclosure of the optical table by a tunnel (not drawn in figure 3.5).

A large off-axis parabolic mirror serves as the objective of the imaging system. It is mounted in a gimbal mount in the back of the optical table (figure 3.9). It was found after the experiments that this parabola had been mounted upside down. The incident beam was therefore not parallel to the symmetry axis of the parent parabola, resulting in aberrations (mainly coma). Fortunately, the associated blur diameter is only $\simeq 1\%$ of the focal spot, which is negligible. The reflected beam comes out of the shadow of the incoming beam approximately 30 cm before the focal point; here, a 15 cm plane mirror finally sends the beam back to the optical table (figure 3.5). The rest of the beam path is confined to the optical table and is described in section 3.4.

3.4 Imaging optical system

As discussed in §2.4, the effective integration length of the TPCI measurement can be reduced through spatial filtering. For the TCV geometry the shortest achievable integration length can be shown to be approximately 5 cm, the limit being set by diffraction (Marinoni 2009). Therefore, the highest perpendicular wave number that can be interpreted in terms of geometrical optics is $k \simeq 60\ \text{cm}^{-1}$ (Raman-Nath regime, section 2.2). Meanwhile, the field of view of the TPCI system is limited by the effective clear aperture D of the port optics (nominally $D \simeq 7.5\ \text{cm}$). This means that a linear array of $kD/\pi \simeq 143$ elements is needed to simultaneously sample all the information in a one-dimensional section of a perfect TPCI image. Since our detector array only has 30 elements, we have to choose between field of view and resolution for a given measurement.

If full spatial coverage is required we employ a magnification $M = 0.12$ so that a 7.5 cm object is imaged exactly onto our 9 mm array. The corresponding Nyquist frequency is $13\ \text{cm}^{-1}$; image components with higher spatial frequency have to be filtered out by an anti-aliasing iris in a focal plane. The Raman-Nath length corresponding to $k = 13\ \text{cm}^{-1}$ is 1 m, comparable to the length of the interaction volume. Therefore, when the detector is placed in the image position corresponding to the middle of the interaction volume, it is in focus in its entirety: the detector does not have to be moved when different regions of the interaction volume are selected by spatial filtering.

3.4. Imaging optical system

If high spatial resolution is wanted we employ a magnification $M = 0.54$, so that the Nyquist frequency is exactly 60 cm^{-1} . This gives access to the smallest meaningful details of the object phase, but only over a 1.6 cm diameter. The Raman-Nath length corresponding to $k = 60 \text{ cm}^{-1}$ is 5 cm, so that only a portion of the interaction volume can be in focus for a given detector position. Therefore the focus shifts when different parts of the volume are selected by spatial filtering and the detector has to be moved over a few cm. No measurements have been performed yet in this configuration.

Figures 3.8a and 3.8b show the configurations for the low and high magnification setups, respectively. Both are based on a large off-axis parabolic mirror (designated by M10) and three small lenses (L2-4). When switching between the two, only lenses L3-4 and the spatial filter have to be moved. The parabola M10 has a diameter of 37 cm and had to be custom made (Marinoni 2009). The lenses L2-4 are off-the-shelf AR coated plano-convex ZnSe lenses, with a 5 cm diameter. The focal point created by M10 is imaged onto the phase plate by L2 (effective focal length: 1.17 m). L2 also creates an image plane before the phase plate, where the galvanometers are located (section 3.7.2). The spatial filter is located in the focal plane after L4; the effective focal length here is 4.96 m in the $M = 0.12$ setup and 0.80 m in the $M = 0.54$ setup. Figure 3.9 shows the arrangement of the optical table.

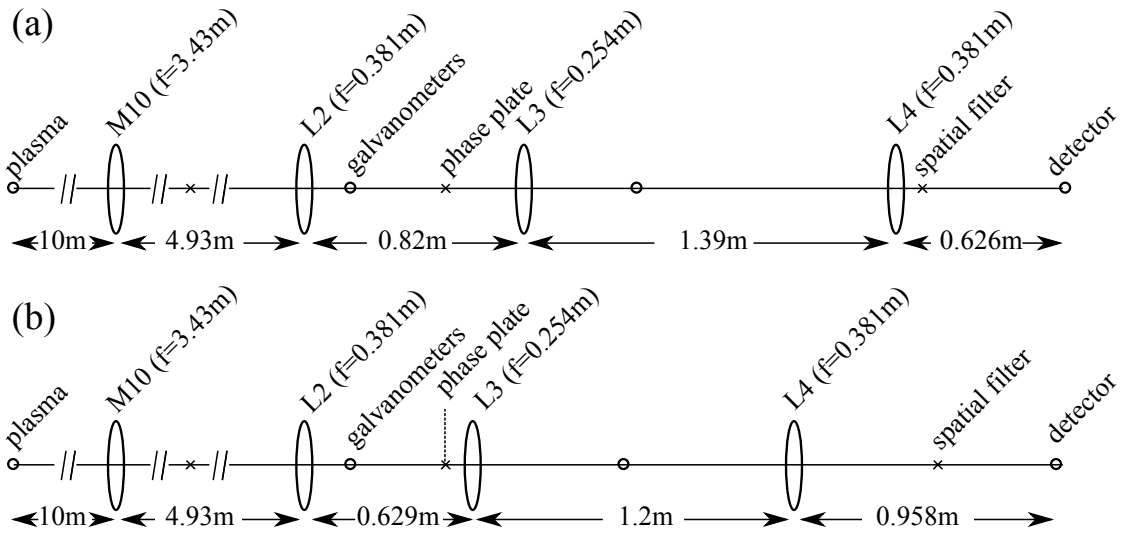


Figure 3.8: Schematics of the two imaging setups with $M = 0.12$ (a) and $M = 0.54$ (b). Circles denote object and image planes; crosses denote focal planes.

For the experiments of chapter 4 we chose the full field of view setup (figure 3.8a). However, for the setup with M3 and M4 flush with the tiles, the clear aperture of the port optics had been reduced from its nominal 5.9 to 5.0 cm by erosion. To work at $w_0 = a$ (cf. §2.5) the full Gaussian diameter of the CO_2 beam was reduced to 5.0 cm, and the magnification increased to $M = 0.18$ by decreasing the distance between L3 and L4 to 1.19 m. The corresponding nominal Gaussian half-width of the focal spot at the phase plate is $2F/(k_0 w_0) \simeq 158 \mu\text{m}$. In this configuration the effective focal length at the spatial filter changes to 3.34 m.

When the optical system was commissioned in the autumn of 2011 it was found that

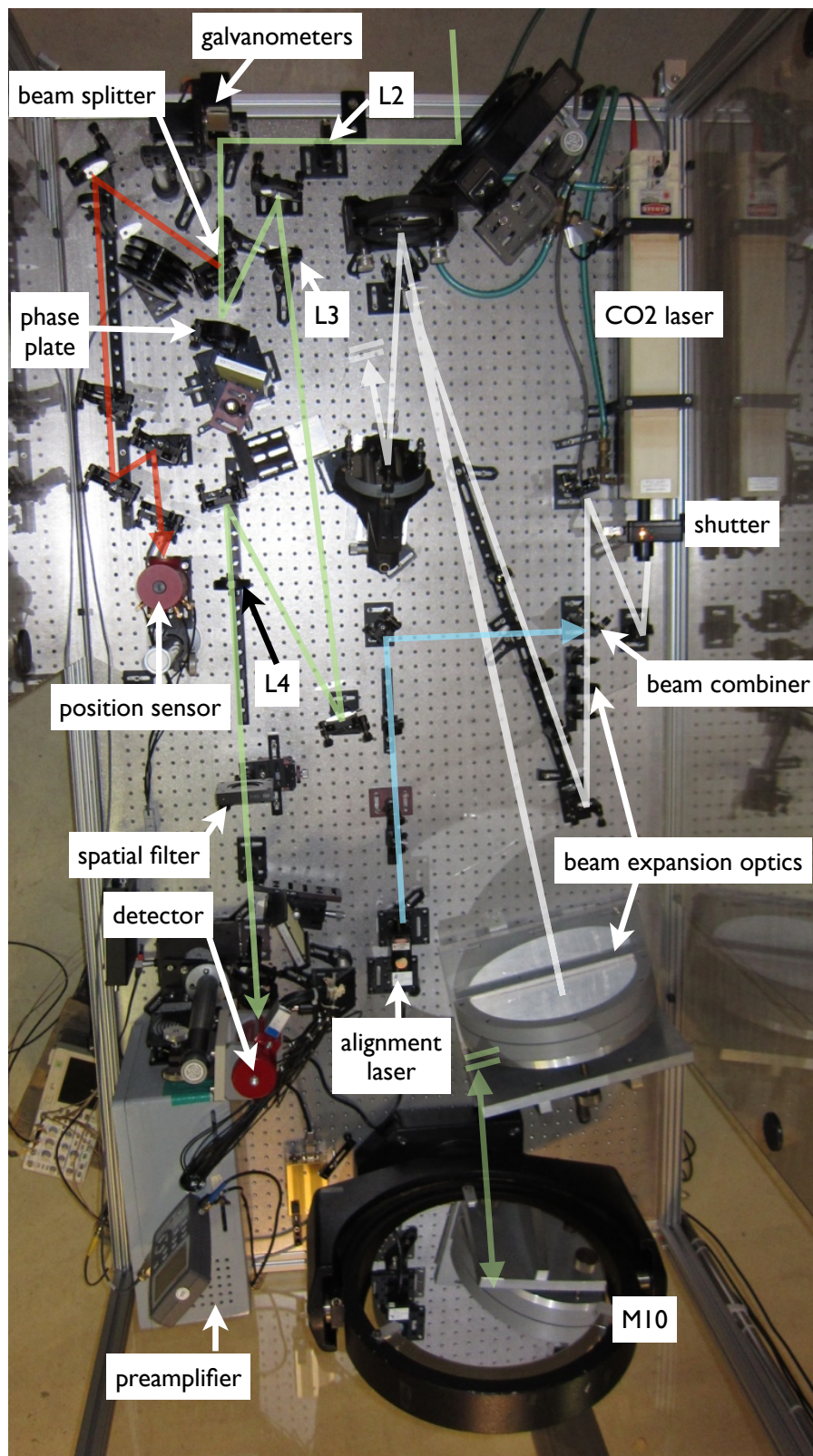


Figure 3.9: Top view of the optical table. M10 and L2-4 are the imaging optics.

both the CO₂ and the visible beam were astigmatic. The separation of the focal lines after the parabola M10 was $\delta f \simeq 30$ cm. Subsequent tests showed that the aberration came from the port optics, which could not be replaced in time for the experiments of chapter 4. Later, when the port assemblies were removed during an opening of TCV and tested in the lab, it was found that the mirrors were being deformed by the four-point mounting mechanism (section 3.3). The observed separation of the astigmatic focal lines is quantitatively consistent with perpendicular reflection off a mirror with positive and negative radii of curvature $|4f^2/\delta f| \simeq 160$ m in the two perpendicular directions, where f is the focal length of the parabola. Along the edge of a 10 cm diameter circular mirror these curvature radii correspond to a peak-to-peak deformation of 16 μm .

Aberrations in the object plane can be modelled by introducing a phase shift $\phi(x)$ in the unperturbed zero-order electric wave field in the object plane (equation 2.52):

$$E_0 \propto \exp(-x^2/w_0^2 + i\phi[x]). \quad (3.1)$$

Equation 2.44 can be evaluated numerically by FFT procedures. The effect of astigmatism can be studied by choosing $\phi = \phi_0(x/a)^2$, where a is the aperture radius. Figure 3.10a shows the effect of astigmatism of the observed magnitude on the rms response to a small amplitude, propagating sinusoidal phase perturbation. Note that the response in the central part of the image is suppressed. It may be noted that the dc light intensity in the image plane (figure 3.10b) shows a similar pattern; this offers a direct way of experimentally establishing the presence of aberrations.

The astigmatic part of the aberration introduced by the port optics was laboriously but effectively corrected with a pair of small ZnSe cylinder lenses, placed near the focal point of the first of the two telescope optics in the beam generation stage. We optimised the placement of these lenses by maximising the power transmitted through the phase groove (using the 400 μm ZnSe plate). However, for the optimum position of the corrective optics the transmitted power fraction was still only 75%, compared to the expected figure of 80%, which was indeed obtained when the port optics were bypassed. Clearly, the observed aberration was not purely astigmatism. This was also evident from the corrected focal intensity pattern, which showed structures apart from the main focal spot. The most striking effect of the residual aberrations was the dc intensity pattern in the image plane (figure 3.11a), which was still very different from the expectation (dashed blue curve in figure 3.10d). This inhomogeneity in the dc intensity can be qualitatively reproduced by posing $\phi(x) = \phi_0(x/a)^3$ in equation 3.1 (figure 3.10c,d). Here, we choose $\phi_0 = 1.8$ rad, which gives the observed 75% power transmission through the phase groove.

To become less sensitive to both aberrations and focal vibrations (section 3.7) we decided to use a wider phase groove, sacrificing sensitivity to long wavelengths. The only available option was a fully reflective plate with a groove width of 1.030 mm, corresponding to a cutoff wave number $k_c = 2.59 \text{ cm}^{-1}$ in our setup. Figures 3.10e,f show the calculated response and dc image intensity for zero aberration (dashed blue curves) and the same third order model aberration of figures 3.10c,d (red continuous curves). The closeness of the curves confirms that the transfer function is less sensitive to aberration with this wider phase plate. Indeed, we found experimentally that for proper alignment of the image on the detector all elements now gave a signal, with the expected centrally peaked amplitude. The measured dc image intensity is also approximately Gaussian (figure 3.11b).

As mentioned before, the optical transfer function description (equation 2.54) is not

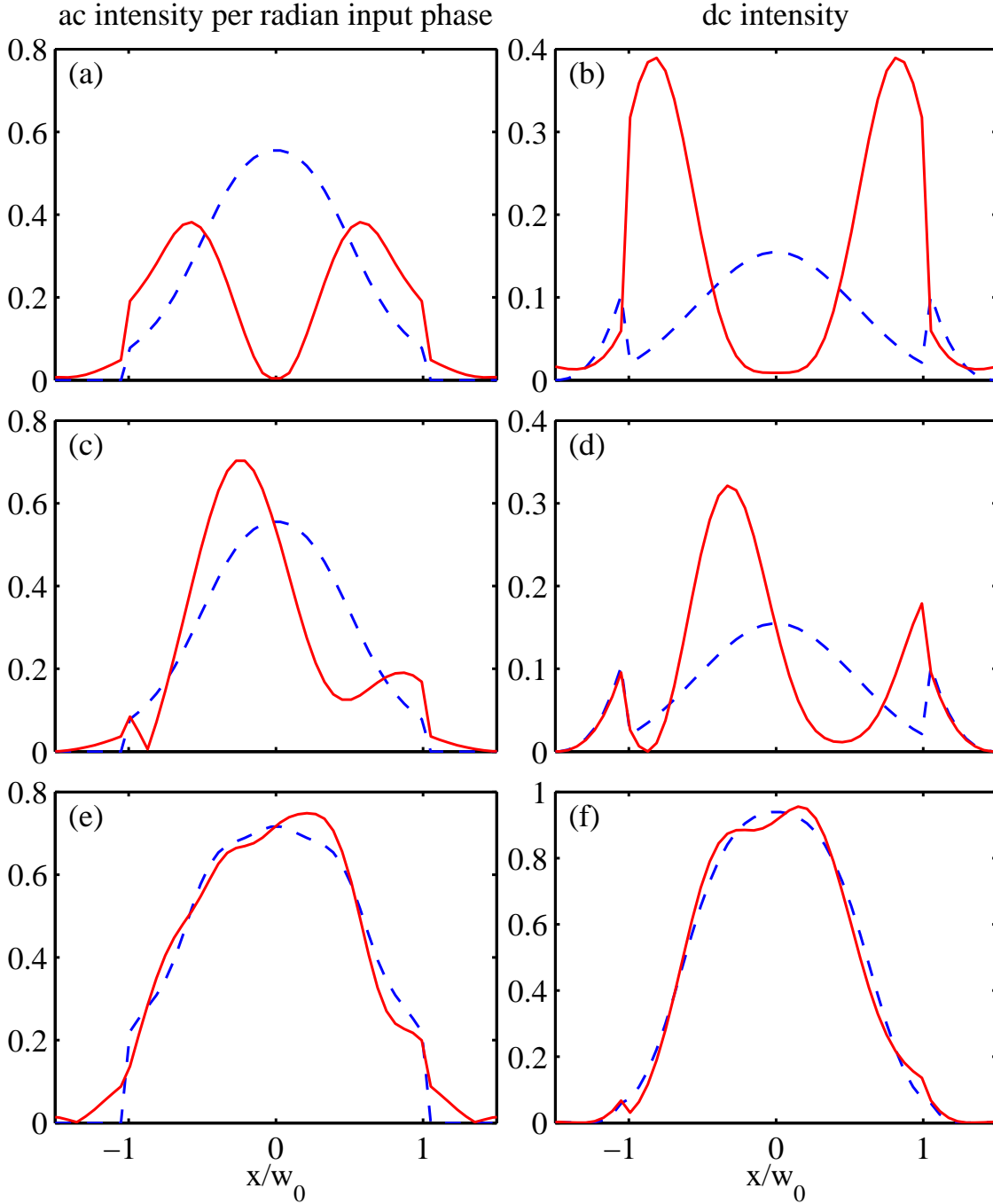


Figure 3.10: Calculated effect of various aberrations on the image of a sinusoidal phase perturbation for two different phase plates. Left and right columns show fluctuating and dc components of the image, respectively. Blue, dashed: no aberration. Red, continuous: aberrated beam. (a,b): $\phi(x) = \phi_0(x/w_0)^2$ with $\phi_0 = 2.4$ rad. (c,d,e,f): $\phi(x) = \phi_0(x/w_0)^3$ with $\phi_0 = 1.8$ rad. (a,b,c,d): ZnSe phase plate with $400 \mu\text{m}$ groove ($Q = 1.3$). (e,f): fully reflective phase plate with $1030 \mu\text{m}$ groove ($Q = 3.2$) Sinusoid has $k_{\perp} = 2.6 \text{ cm}^{-1}$. $a = w_0 = 2.5 \text{ cm}$ ($\alpha = 1$). The phase plate is shifted to maximise power on the groove.

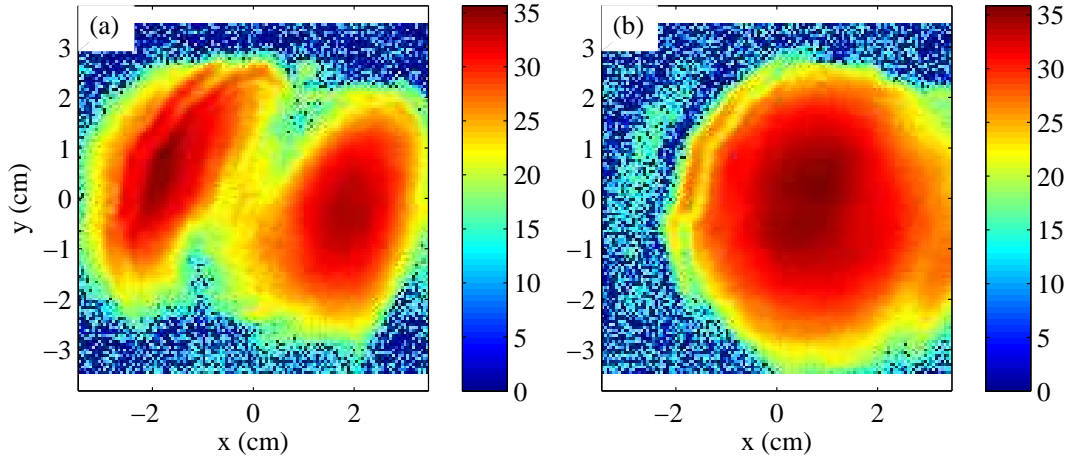


Figure 3.11: DC intensity patterns (dB scale) for different phase plates measured in the image plane with a beam profiler (Pyrocam III, Ophir-Spricon Inc.). The leading astigmatic aberration is corrected with two cylindrical lenses. Displayed coordinates are in the object plane, i.e. they are the measurement coordinates divided by the optical magnification $M = 0.18$. (a): ZnSe phase plate with $400 \mu\text{m}$ groove. (b): fully reflective phase plate with $1030 \mu\text{m}$ groove.

exact, because it does not account for spectral broadening. That is, in reality the spatial Fourier spectrum $\tilde{\mathcal{E}}(k_{\text{im}})$ of the image resulting from a purely sinusoidal input phase with wave number K also contains components other than K . The exact response to an arbitrary input phase can be obtained numerically from equation 2.44. Figure 3.12 shows the resulting k spectra for propagating sinusoids. It may be observed that for $K > k_c$ (i.e. right of the dash-dotted line) the spectral distribution peaks for $k_{\text{im}} = K$. This is not true for $K \lesssim k_c$, where it peaks for values $|k_{\text{im}}| > K$. A peak for negative k_{im} indicates that the image appears to propagate in the opposite direction. Moreover, the details of the response depend quite sensitively on shifts of the focal spot within the groove, as illustrated by the difference between the left and right-hand plots in figure 3.12. Clearly, spectral components of a phase-contrast image with $k_{\text{im}} \lesssim k_c$ cannot be taken at face value.

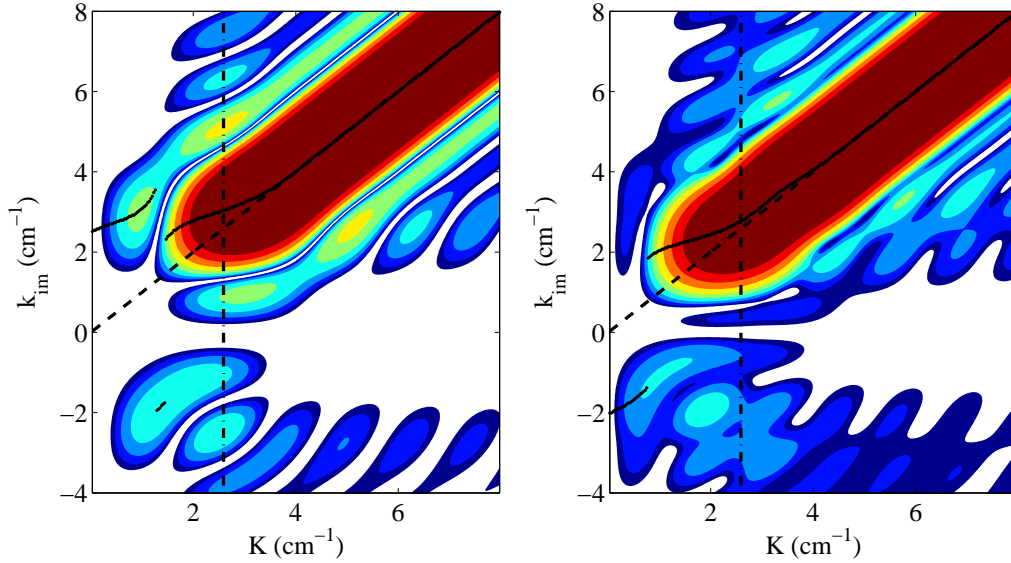


Figure 3.12: Contours of spectral density (see text) in dB scale; 2 dB step. Left: focal spot centred in phase groove. Right: focal spot shifted by $v/4$, with v the groove half-width. Dashed line indicates the ideal response. Dash-dot line indicates nominal cutoff wave number. Full line indicates the k_{im} of maximum spectral density in a vertical section. Calculation is performed for a clipped Gaussian beam ($w_0 = a = 2.5$ cm) and $k_c w_0/2 = 3.2$, which corresponds to the configuration employed for the experiments of chapter 4.

3.5 Image detection and acquisition

For the detection of the image we use a linear array of 30 photoconductive HgCdTe elements (Infrared Associates Inc., model HCT-60). This detector had previously been used in the TCA phase-contrast diagnostic (Weisen 1988). The array is housed in a down-facing dewar for operation at liquid nitrogen temperature (77 K). To properly align the array for any orientation of the spatial filter the dewar can be rotated axially over 180° . Each element of the array is a square with sides of length $250 \mu\text{m}$ (area $A = 0.0625 \text{ mm}^2$); the space between adjacent elements is $50 \mu\text{m}$. The bandwidth is rated at 1.6 MHz, but this has not yet been verified experimentally. The elements have responsivity $\mathcal{R} = 500 \text{ V/W}$ and a measured noise equivalent power (NEP) of $1.7 \text{ nW/MHz}^{1/2}$, which corresponds to an rms noise voltage of $1.1 \mu\text{V}$ over the 1.6 MHz detector bandwidth. The specific detectivity $D^* = \sqrt{A}/\text{NEP} = 1.5 \times 10^{10} \text{ Hz}^{1/2} \text{ cm/W}$. Saturation is reached for a light intensity $u_{\text{sat}} \simeq 1 \text{ mW/mm}^2$, i.e. $60 \mu\text{W}$ per element. Close to saturation the elements have an estimated shot noise of $1.3 \mu\text{V}$ rms over a 1.6 MHz bandwidth.

A multipin connector connects the 30 detector anodes and the common cathode to an electronics box which houses the preamplifiers and the biasing circuit. In the TCA setup the detector Dewar was mounted inside this box, but this does not allow it to rotate over a sufficient angle. The preamplifiers have 61 dB gain and a passband of 7 kHz–3 MHz (Marinoni 2009). With a cooled, unilluminated detector the measured noise at the preamplifier output is 40 mV rms over a 1.6 MHz bandwidth, which translates to an effective rms noise of $\tilde{v}_n \simeq 35 \mu\text{V}$ at the preamplifier input: the noise level in our measurements is clearly dominated by sources other than the intrinsic detector noise. In

3.6. Tests and characterisation of the imaging system with acoustic waves

particular, shot noise plays a negligible role in the signal-to-noise ratio, which is therefore simply

$$\text{SNR} \simeq \frac{\mathcal{R}^2 A^2 \tilde{\mathcal{E}}^2}{\tilde{v}_n^2}. \quad (3.2)$$

Here, $\tilde{\mathcal{E}}$ is the rms light intensity on the detector resulting from a phase shift $\tilde{\varphi}$ in the object plane. Now we assume that the wavenumber K of the phase shift is such that $\mathcal{T}(K)$ is more or less flat; we also assume that the phase groove is sufficiently wide to accommodate most of the focal spot ($Q \gtrsim 1$). Then, in the center of the image, we have $\tilde{\mathcal{E}} \simeq 2\sqrt{\rho}u_0\tilde{\varphi}$, where $u_0 = 2P_0/(\pi M^2 w_0^2)$ is the dc intensity in the absence of a phase plate and ρ is the reflectivity of the phase groove.

The SNR is maximised by operating with the highest possible value of u_0 without saturating the detector, i.e. $u_0 = u_{\text{sat}}/\rho$. Putting equation 3.2 equal to one and substituting for $\tilde{\mathcal{E}}$ yields the minimum detectable rms phase shift:

$$\tilde{\varphi}_{\text{min}} = \frac{\sqrt{\rho}\tilde{v}_n}{2\mathcal{R}Au_{\text{sat}}}. \quad (3.3)$$

Evaluating equation 3.3 for our system and using the reflectivities of BaF₂ ($\rho = 0.027$), ZnSe ($\rho = 0.17$) and a fully reflective groove ($\rho = 1$), we get $\tilde{\varphi}_{\text{min}} \simeq (0.1; 0.2; 0.6)$ mrad, respectively. The corresponding values of the total power of the beam, prior to attenuation by the phase groove, are $P_0 = (1.2; 0.19; 0.032)$ W, where we have used $w_0 = 0.025$ cm and $M = 0.18$.

Shortly before the experiments of chapter 4 14 detector elements failed simultaneously for an unknown reason. A further 7 elements had failed previously, leaving only 9 of the original 30 elements operational during the experiments (numbers 4-8-12-16-18-24-26-28-30). The closest available spacing is 600 μm instead of the original 300 μm , which halves the Nyquist spatial frequency k_N for a given magnification. For the $M = 0.18$ configuration used for the experiments in chapter 4 $k_N = 9.4 \text{ cm}^{-1}$. Disabled elements have infinite resistance and give no signal, but inspection under a microscope shows no visible damage. It seems unlikely that laser light can have destroyed the elements, since they were never exposed to sufficiently high intensity (J. Zhao et al. 1999); an electrical overload may be the cause of the damage.

Two 16-channel ADCs (D-Tacq model ACQ216), mounted under the optical table, are used to digitise the preamplifier outputs. A sampling rate of 12 MHz is employed; the ADCs have in-built 5 MHz anti-aliasing filters and enough memory for acquisition windows of up to 2.6 s for all channels, covering an entire TCV discharge. The resolution is 14 bits and the voltage range ± 3 V.

3.6 Tests and characterisation of the imaging system with acoustic waves

The index of refraction of air is a function of density, and therefore varies periodically in a sound wave. Conveniently, the range of wavelengths of interest in plasma turbulence (typically 1-10 cm) corresponds to sound waves with frequencies between 3.4 kHz and 34 kHz, which are easily generated in the laboratory. This makes acoustic waves a practical tool for testing and calibrating a PCI diagnostic (Weisen 1988; Coda 1997). The

fluctuating phase shift $\tilde{\varphi}$ incurred by a laser beam with wavelength $10.6 \mu\text{m}$ travelling through a pressure field \tilde{p} in air of 20°C is given by

$$\tilde{\varphi}(\mathbf{x}_\perp) = 1.1 \times 10^{-9} \int \tilde{p}(\mathbf{x}_\perp, z) dz \quad (3.4)$$

in the geometric optics approximation (Wolfe et al. 1985). Here, $\tilde{\varphi}$ is in radians, \tilde{p} in μPa and z in m. Absolute root-mean-square sound pressure levels are often expressed in decibels by normalising to a reference level $p_{\text{ref}} = 20 \mu\text{Pa}$. As an illustration, we note that a laser beam travelling through a sound wave-field with an SPL of 107 dB undergoes an rms phase shift of 1 mrad for an effective integration length of 20 cm.

If the interaction volume lies a distance d away from the object plane the phase-contrast signal decreases by a factor $\cos(dk_\perp^2/[2k_0])$ because of the scintillation effect (§2.2). Here, k_\perp and k_0 are the wave numbers of the sound wave and the laser light, respectively. In particular, for frequencies where $dk_\perp^2/(2k_0) = (n + 1/2)\pi$, where n is an integer, the signal disappears entirely. This effect can be exploited to accurately place the detector in the image plane. It also allows measurement of the optical transfer function $|\mathcal{T}(k_\perp)|$ even if the interaction volume is some distance away from the object plane. This is convenient, since the object plane typically lies inside the tokamak. We recall that in the centre of the image $|\mathcal{T}(k_\perp)|$ is defined by

$$|\mathcal{T}(k_\perp)| = \mathcal{E}_{\text{rms}}(k_\perp)/\varphi_{\text{rms}}(k_\perp). \quad (3.5)$$

We are not concerned here with the absolute value of $|\mathcal{T}|$, so we only need the *relative* values of φ_{rms} for different k_\perp (equation 3.4). Even so, the precise form of the sound wave-field is difficult to know with good accuracy. In practice the wave is often assumed to be spherical with radius R , in which case the effective integration length in equation 3.4 satisfies $L_{\text{eff}} \sim (R/k_\perp)^{1/2}$ (Weisen 1988). The relative sound pressure in the interaction volume for the different frequencies has to be measured with a microphone with a known frequency response. To avoid the complication of standing waves, and to ensure that the sound wave-field is only present in the desired interaction volume, tone bursts are used, of which only the first ~ 1 ms is used in the analysis.

At the time of the experiments of chapter 4 we did not have access to a microphone. Furthermore, the simple tweeter that we had acquired (Monacor, model MPT-001) proved to have a very irregular frequency response with multiple resonances (typical width 2 kHz) in the 10-35 kHz range, making it unusable for determination of the object position. Even so, when driven at the resonant frequencies in that range it produced sound waves that were easily visible in the PCI traces. For the experiments of chapter 4, this tweeter was mounted such that the interaction volume was approximately 2.8 m before the tangency point in TCV (in the direction of the laser beam), and 20 cm away from the tweeter. When projected onto the image plane the direction of sound propagation was parallel to the detector array. In a 100 ms time window before each plasma discharge a gated sine wave was applied to the tweeter. The estimated SPL in the interaction volume is 116 dB.

Figure 3.13 shows an example of the measured response of the PCI signals before discharge 45353. Using the known sound speed at room temperature (343.2 m/s) and the known centre-to-centre spacing of the detector elements (300 μm) the phasing of traces like the ones of figure 3.13 can be used to verify the optical magnification M . Measurements at various frequencies indicate that $M = 0.183 \pm 1\%$, in agreement with the nominal

3.6. Tests and characterisation of the imaging system with acoustic waves

value of $M = 0.18$ (section 3.4). Also, the signal amplitudes of the various channels in figure 3.13 show the expected central maximum (see figure 3.10e). These observations, together with the observed dc intensity pattern in the image plane (figure 3.11) gave us some confidence that the imaging system was in working order.

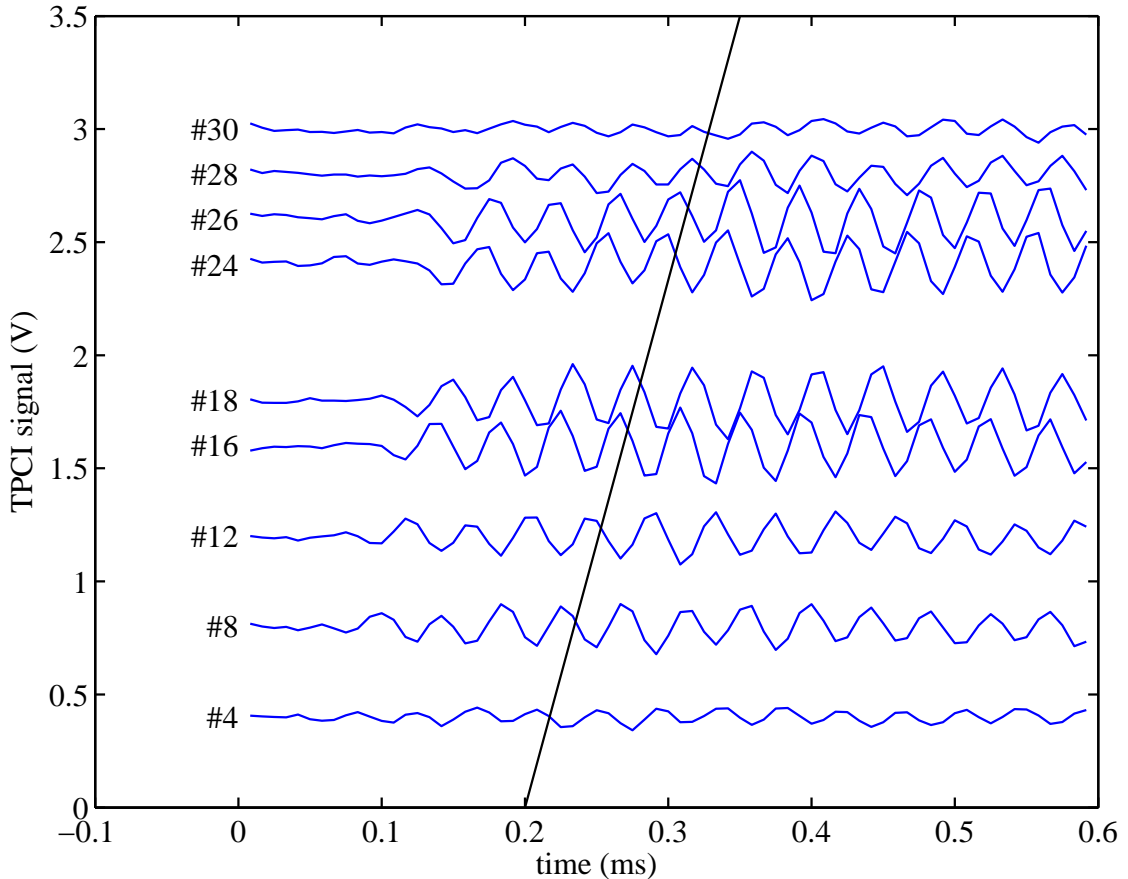


Figure 3.13: PCI signals in response to an acoustic wave burst (23.66 kHz). Signals are band-pass filtered (5-60 kHz) and have an offset proportional to the element position in the array. Estimated SPL in the interaction volume: 116 dB.

After the first TPCI measurements in December 2011, TCV was shut down for an extended maintenance period. Except for retracting the port assemblies, the TPCI optical setup (including the corrective cylinder lenses) was left untouched in order to carry out additional acoustic testing at a later time. The required ultrasonic tweeter and microphone became available roughly four months later. The tweeter is an electrostatic unit (Ultra Sound Advice, model S56), operating in the 15-200 kHz range. Its on-axis SPL at 65 cm decreases monotonically from 106 dB to 82 dB. For the measurement of the sound pressure level we used a calibrated microphone (Larson Davis, model 2520) and pre-amplifier (B&K, model 2618) on loan from the LEMA laboratory of the EPFL. The frequency response of this microphone is flat to within 1 dB from 20 Hz up to 100 kHz.

To find the object plane, the tweeter was mounted so that the interaction volume was 7.1 m before the tangency point in the plasma, which was the desired position of the object plane. Figure 3.14a shows the measured amplitude of a central detector element in the

array for a range of frequencies. The frequencies of the three nulls show that the actual object plane for the experiments in chapter 4 lies 1.4 ± 0.2 m after the tangency point in TCV, in the direction of the laser light. Equivalently, the image of the tangency point in TCV lies 4.6 ± 0.7 cm before the detector position. A discrepancy between detector plane and image plane of this magnitude typically arises in our setup if the spacing of the imaging optics and the detector itself is subject to random errors of 3%. In principle, the k_{\perp} spectra of chapter 4 can easily be corrected for this misalignment, through division by $\cos(dk_{\perp}^2/[2k_0])$. The change is less than 10% for $k_{\perp} < 6.2 \text{ cm}^{-1}$; it is a factor of two for $k_{\perp} = k_N = 9.4 \text{ cm}^{-1}$.

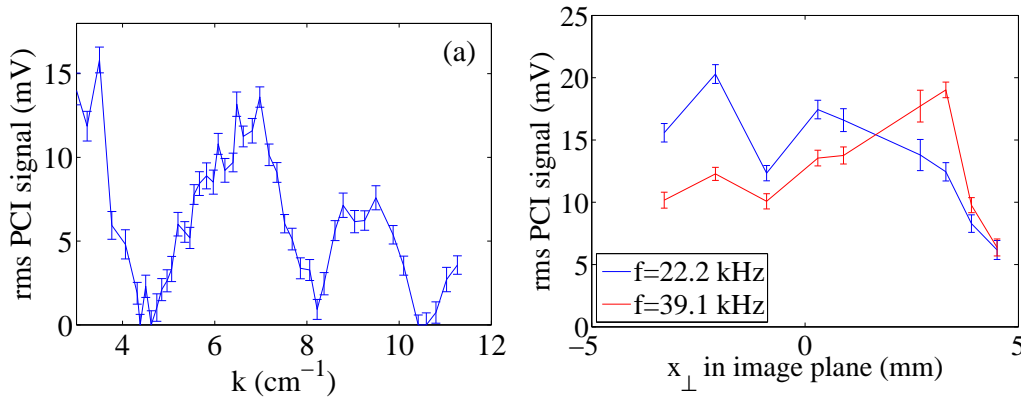


Figure 3.14: (a) PCI response to acoustic waves far from the object plane: the wave numbers for which nodes occur indicate that the distance between the interaction volume and the object plane was in fact 8.5 ± 0.2 m. The error bars reflect the statistical uncertainty in the calculation of the signal amplitude. (b) PCI response of all nine detector elements to acoustic waves in the object plane with two different frequencies. The difference in relative response between the elements is caused by optical aberrations.

We also attempted to measure the optical transfer function $|\mathcal{T}(k_{\perp})|$, but the results are inconclusive and unsatisfactory. For this measurement the interaction volume was located a distance $d = 0.9 \pm 0.2$ m after the (experimentally determined) object plane. This was the minimum possible distance to the object plane because of space constraints around the exit port assembly. The distance from the tweeter to the interaction volume was 30 cm; the microphone was placed 20 cm further. The phase-contrast signal is proportional to the laser power P , which fluctuates substantially on a timescale of seconds, and was therefore recorded for all points of the calibration. The measured PCI signal amplitudes for each acoustic frequency are normalised by

$$\cos(dk_{\perp}^2/[2k_0]) \times k_{\perp}^{-1/2} \times p_{\text{rms}} \times P.$$

Unfortunately, the details of the optical aberrations at the time of this calibration were not identical to those at the time of the plasma experiments four months earlier. Even though the focal spot and dc image intensity pattern looked qualitatively similar, the response to a sound wave was no longer peaked in the centre of the image, as shown in figure 3.14b. This figure also shows a significant dependence on frequency of the relative response between elements, which makes a description of the signals in terms of a single transfer function and weighting function inaccurate. This is also illustrated in figure 3.15, which shows the normalised PCI response in two positions in the image plane.

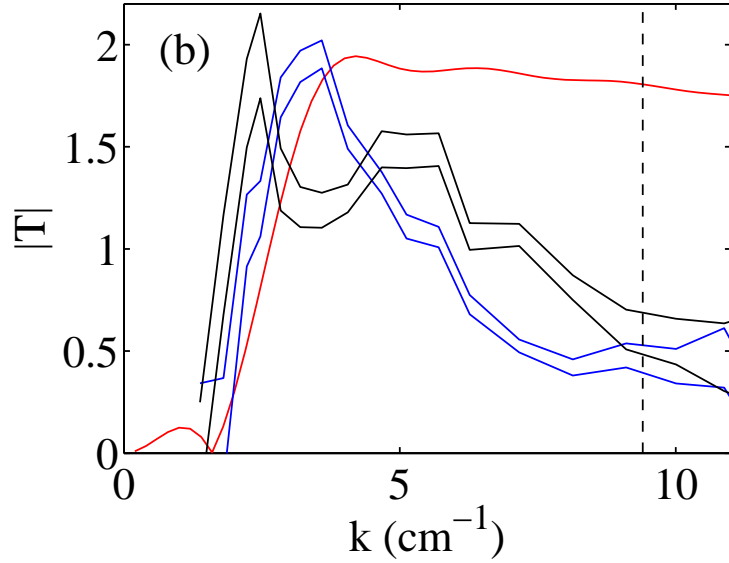


Figure 3.15: The blue and black curves are measured optical transfer functions $|\mathcal{T}(k_{\perp})|$ for two positions in the image plane, separated by 5.4 mm. The error range is determined by the statistical error plus the uncertainty in the distance d between the interaction volume and the object plane. The curves are rescaled to match the theoretical $|\mathcal{T}(k_{\perp})|$ in red. A dashed vertical line indicates the Nyquist spatial frequency. The phase plate has a fully reflective groove with width $1030 \mu\text{m}$.

Apart from the k_{\perp} dependent spatial inhomogeneity, the measured response also shows an unexpected drop throughout the image for $k_{\perp} > 3 \text{ cm}^{-1}$. This is not an expected effect from aberrations. We did not apply spatial filtering in a focal plane, and the beam path was unobstructed. An immediate repeat experiment gave the same result, excluding time variation of an unmonitored parameter.

Inaccuracy may arise in the normalisation procedure. The $k_{\perp}^{-1/2}$ term in particular has a strong impact. This factor is based on the assumption that the SPL is approximately constant over an integration length $\sim (R/k_{\perp})^{1/2}$. For highly directional sound beams this assumption is wrong, leading to an overestimate of the effective integration length. However, a more refined (numerical) calculation, which takes into account the nominal directionality of the tweeter as a function of frequency, suggests that the assumption is quite accurate for $R = 30 \text{ cm}$ and $k_{\perp} < 10 \text{ cm}^{-1}$.

Another possible source of inaccuracy in our measurement is the assumption that the ratio between the SPL measured by the microphone and the SPL in the interaction volume is independent of frequency. This assumption may be violated if the directionality of the tweeter depends strongly on frequency, and, at the same time, if the interaction volume and the microphone are not centred on the tweeter axis. Based again on the nominal directionality of the antenna pattern of the tweeter it seems unlikely that this is a problem for our setup. Still, it might be prudent to perform an experimental measurement of the directionality of the tweeter for different frequencies.

3.7 Feedback vibration-control system

The intersection of the phase groove and the slit of a spatial filter defines a rectangular area in the focal plane. Vibrational tilting of the various mirrors causes displacement of the focal spot. If the spot strays off this rectangle, the phase-contrast signal drops to zero: the two-dimensional vibrational motion must clearly be kept to within a fraction of the groove width for the diagnostic to work. We wish to quantify the impact of a given focal shift on the optical transfer function. We neglect the spatial filter, and take only the phase mirror into account. The focal shift δx on the phase mirror is expressed as $k_s = k_0 \delta x / F$, where F is the effective focal length. For the case of an infinite aperture and a Gaussian spot the optical transfer function can be expressed as (Coda 1997):

$$\begin{aligned} \mathcal{T}(K) \cos \theta(K) &= \sqrt{\rho} u_0(0) \left\{ \operatorname{erf}(Q + k'_s) + \operatorname{erf}(Q - k'_s) \right. \\ &\quad - \frac{1}{2} [\operatorname{erf}(Q + K'_x + k'_s) + \operatorname{erf}(Q + K'_x - k'_s) \\ &\quad \left. + \operatorname{erf}(Q - K'_x + k'_s) + \operatorname{erf}(Q - K'_x - k'_s)] \right\} \\ \mathcal{T}(K) \sin \theta(K) &= \frac{1}{2} \sqrt{\rho} u_0(0) [\operatorname{erf}(Q + K'_x + k'_s) - \operatorname{erf}(Q + K'_x - k'_s) \\ &\quad - \operatorname{erf}(Q - K'_x + k'_s) + \operatorname{erf}(Q - K'_x - k'_s)]. \end{aligned} \quad (3.6)$$

Here, $Q = k_c w_0 / 2$, $K'_x = K_x w_0 / 2$ and $k'_s = k_s w_0 / 2$. $\theta(K)$ is the phase shift between object and image. In figure 3.16 we plot $|\mathcal{T}(K)| = [\mathcal{T}^2(K) \cos^2 \theta(K) + \mathcal{T}^2(K) \sin^2 \theta(K)]^{1/2}$, to show the effects of various shifts for two widths of the phase groove.

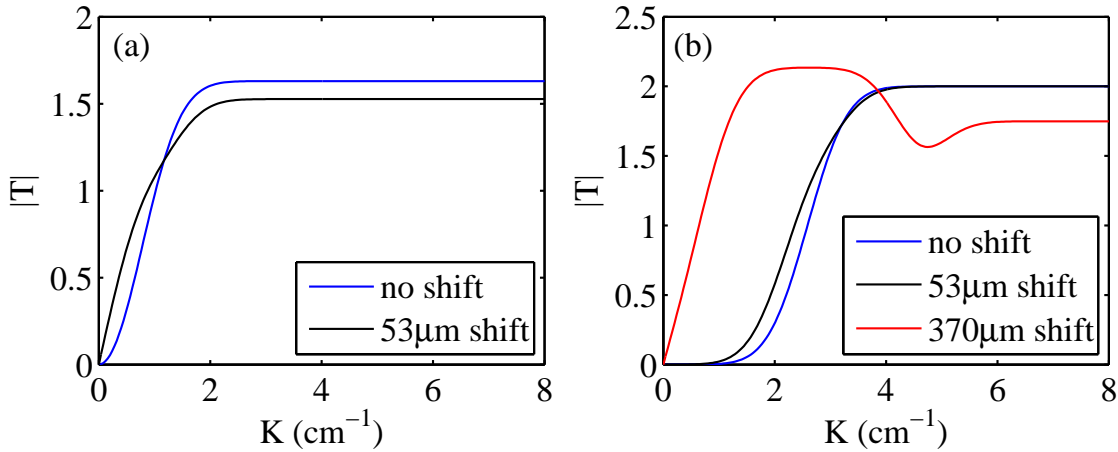


Figure 3.16: The effect of focal shifts on the TPCI optical transfer function for 300 μm (a) and 1 mm (b) phase-plate groove widths and $w_0 = 2.5$ cm.

The problem of excessive focal shifts was anticipated from an early stage in the development of the TCV phase-contrast diagnostic, because of the five vessel-mounted mirrors called for by the tangential beam geometry. Such mirrors are especially prone to vibration because of their proximity to the coils and plasma, and movements of the vessel itself. The four on-vessel mirrors of the DIII-D phase-contrast system, for example, caused rms focal shifts significantly greater than the groove width during tokamak operation. This severe

problem was solved with a feedback vibration-control system involving a pair of steerable mirrors (Coda 1997). By contrast, focal vibration was not an issue for the TCA (Weisen 1988) and Alcator C-MOD (Mazurenko 2001) phase-contrast systems, presumably because the beam geometry on those machines did not require any vessel-mounted mirrors.

Before the mirror assemblies were built, two tests had been performed to assess the amplitude and frequency range of expected vibrations during plasma operation (Marinoni 2009). Firstly, accelerometer measurements of the movement of the TCV vessel showed a dominant oscillation in the range 16-20 Hz, similar to what had been observed in DIII-D. Secondly, a mirror was provisionally mounted on the torus and its vibrational amplitude measured by visual inspection of the motion of a reflected laser spot: it was estimated at 0.1 mrad rms, comparable to the compound figure of 0.25 mrad measured for the four on-vessel mirrors of DIII-D phase-contrast system (Coda 1997). In the light of this anticipated similarity, and the excellent performance of the DIII-D feedback vibration-control system, an essentially identical system was built for the TCV phase-contrast diagnostic (§3.7.2).

After the mirror assemblies had been constructed and mounted on the torus, the vibrational focal shift was measured and studied in detail (§3.7.1). It was found that although the amplitude of the shift was as expected, the frequency spectrum was dominated by eigenmodes of the mirror mounts in the range 40-400 Hz rather than the 20 Hz eigenmode of the TCV vessel. Since the performance of the adopted feedback vibration-control system decreases with frequency, the residual rms amplitude of the focal shift in the TCV phase-contrast system ($k_s = k_0 \delta x / F \simeq 25 \text{ m}^{-1}$) is substantially greater than that obtained in the DIII-D system ($k_s \simeq 3 \text{ m}^{-1}$). The TCV figure corresponds to a physical shift 50 μm of the focal spot in the groove. Figure 3.16 shows the corresponding impact on the optical transfer function of the system.

3.7.1 Analysis of the undamped movements of the focal point

The movement of the focal point was measured for a variety of plasma discharges using the 100 mW, 635 nm alignment laser and a 20x20 mm² dual-axis lateral effect diode (model PSM2-20, On-Trak Photonics, Inc.). Various tests confirm that the observed signals really correspond to focal movements. First, measurements performed with different focal magnifications show that the signal level scales as expected. Second, powering the position amplifier by a battery instead of its usual AC/DC adapter does not change the signals, thus excluding pickup as the cause. Finally, measurements performed with the CO₂ laser and the HgCdTe quadrant detector show identical spectra to those obtained with the visible laser and the lateral effect diode.

Figure 3.17 shows a typical example of a measurement with the visible laser and the lateral effect diode. During the flat-top phase rms shifts of 0.3 mm (vertical) and 0.4 mm (horizontal) are observed. In addition, the horizontal position shows a slow drift of several mm. These displacements are greater than the half-widths of the available phase plates (0.15-0.5 mm), highlighting the importance of vibration-control. Assuming that the vibrations arise from mirrors located before the parabolic mirror, the corresponding compound angular mirror motion is $\theta_{\text{rms}} \simeq 0.2 - 0.3 \text{ mrad}$, comparable to the figure of 0.25 mrad measured in DIII-D.

Figure 3.18 shows the power spectral density during the flat top phase of figure 3.17. Unexpectedly, the 20 Hz eigenfrequency of the TCV vessel is not significant in the spec-

trum and the main contribution instead lies in the frequency range 40-60 Hz. By inspecting the vibrational spectra resulting from tapping on the different mirror assemblies in the TCV hall and the port assemblies, we established the frequency and spatial orientation of the eigenmodes of these optical components. Comparison with the vibration signals obtained during plasma discharges we were able to identify M1-5 (i.e. the vessel mounted mirrors) as the sources of the dominant vibrational modes observed during plasma operation. In particular, the 40 Hz and 60 Hz modes come from the exit assembly, while the modes with frequency higher than 200 Hz come mainly from the entry assembly. The mirror M6, which is mounted on the TCV torque frame, was found to contribute modestly to the 40 Hz range vibrations. The 1.3 kHz mode could not be excited manually; this mode was also observed in accelerometer measurements of the machine displacement and is related to the switched power supplies of the magnetic-field coils (alternator frequency times 12) (Marinoni 2009).

3.7.2 Feedback vibration-control system

The feedback vibration-control system implemented in the TCV TPCI diagnostic is essentially identical to the one used in DIII-D; we refer to Coda 1997 for a detailed discussion of the design considerations. Here, we discuss only its basic principles, the obtained performance, and some unresolved issues.

The negative feedback mechanism is illustrated in the block diagram of figure 3.19. A beamsplitter located approximately 17 cm before the phase plate extracts a fraction of the laser light from the main beam. This fraction passes through a lens, projecting an image of the focal plane onto a position sensor. The sensor produces two error signals, proportional to the deviation of the focal spot from the desired point in the two perpendicular directions. These error signals are treated by two electronic compensation circuits, each driving a rotatable mirror. The mirrors have perpendicular axes and are located approximately 30 cm before the phase plate. They steer the focal spot back to the desired point (figure 3.20), closing the feedback loop.

The closed loop transfer function $T(s)$ of the feedback loop of figure 3.19 is

$$T(s) = (1 + P(s)C(s)S(s))^{-1}, \quad (3.7)$$

where s is the Laplace variable, and $P(s)$, $C(s)$ and $S(s)$ are the analytic continuations of the frequency response $P(i\omega)$ of the position sensor, the compensation circuit $C(i\omega)$ and the scanner $S(i\omega)$, respectively. The position sensor (Infrared Associates, Inc.) consists of four photoresistive HgCdTe elements in a quadrant configuration. The detector array is housed in a side-looking dewar for operation at liquid nitrogen temperature (77 K). The signals from the quadrant detector are amplified and converted to an x and y-position signal by a model OT-301 ‘versatile position sensing amplifier’ (On-Trak Photonics, Inc.) set up for quadrant detector operation. The transfer function of the position sensing circuit $P(s)$ is essentially flat in the frequency range of interest.

Each scanner unit consists of a mirror (clear aperture 3 cm) mounted on a model G306 galvanometer motor, driven by a model AX-200 amplifier (General Scanning Inc.). The driver amplifiers have variable offset and gain. The measured transfer functions $S(s)$ of the x- and y-units are shown in figure 3.21. The part below ~ 1 kHz can be approximated to good precision by a underdamped oscillator with resonance frequency $\omega_n/(2\pi) \simeq 100$ Hz

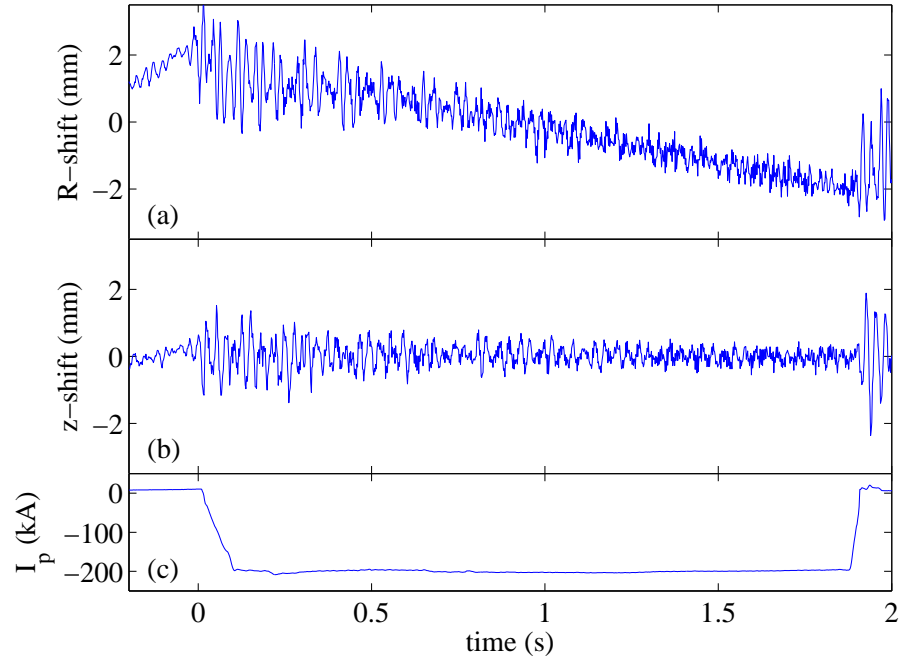


Figure 3.17: Movement of the focal spot on the phase plate, projected along the horizontal (a) and vertical (b) directions in TCV (discharge 44095).

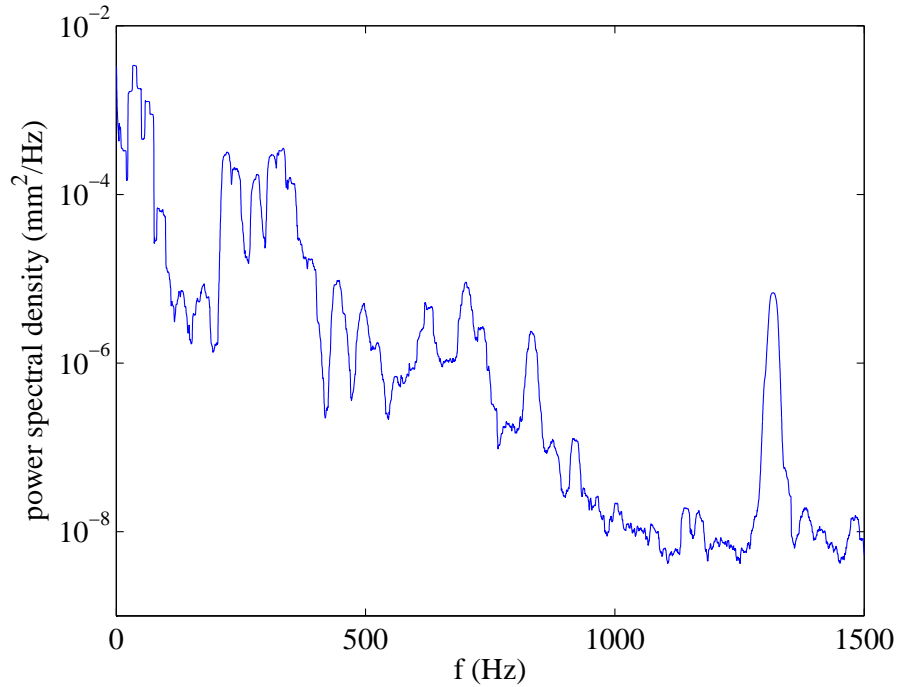


Figure 3.18: Power spectral density of the focal movement along the horizontal direction in TCV during the flat top phase of Fig. 3.17. Spectral smoothing interval: 18 Hz; relative statistical uncertainty: 18%.

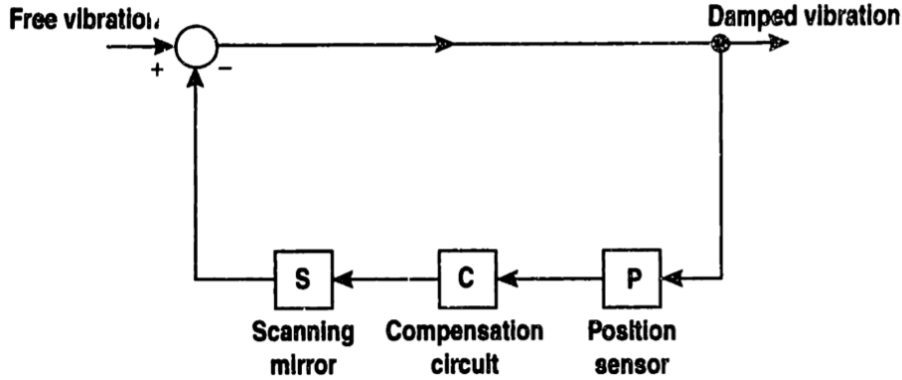


Figure 3.19: Feedback vibration-control system (from Coda 1997).

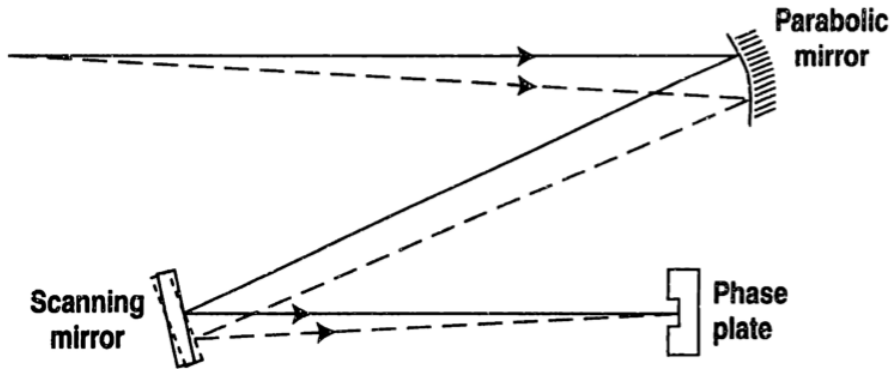


Figure 3.20: Illustration of the correction mechanism in the feedback system (from Coda 1997). For simplicity the lens between the parabola and the scanning mirror has been omitted.

and damping ratio $\zeta \simeq 0.1$, plus a time delay and increased roll-off:

$$S(s) = \frac{\omega_n^2}{s^2 + 2\zeta\omega_n s + \omega_n^2} \frac{e^{-s\tau}}{1 + s/\omega_d} S(0). \quad (3.8)$$

The parameters from the best fits of equation 3.8 to the measured response are listed in table 3.2. The difference in ω_n between the two axes is caused by a larger moment of inertia of the y-mirror. The loaded scanners have a secondary resonance around 3 kHz, which is not included in equation 3.8.

The purpose of the compensation circuits $C(s)$ is to allow feedback operation with high gain. The circuit is a combination of phase lead and lag networks, differentiators

	x-axis	y-axis
$\omega_n/(2\pi)$ (Hz)	107	90.6
ζ	0.0833	0.0718
$\omega_d/(2\pi)$ (Hz)	450	411
τ (μ s)	53.1	72.7

Table 3.2: Parameters of best fits of 3.8 to figure 3.21.

3.7. Feedback vibration-control system

	τ_a	τ_b	τ_c	τ_d	τ_e	τ_f	τ_g	τ_h	τ_{ro1}	τ_{ro2}	τ_{ro3}	τ_{ro4}
x	1.6	1.6	1.6	1.0	34	0.049	0.16	31	0.017	0.012	0.022	0.0014
y	1.8	1.6	1.7	1.4	30	0.049	0.17	29	0.012	0.012	0.022	0.0012

Table 3.3: Time constants (in ms) used for the x- and y-axis compensation circuits (equation 3.9).

and integrators with transfer function

$$C(s) = \frac{(1 + s\tau_a)(1 + s\tau_b)(1 + s\tau_c)}{(1 + s\tau_{ro1})(1 + s\tau_{ro2})(1 + s\tau_{ro3})(1 + s\tau_{ro4})} \frac{1 + s\tau_d}{1 + s\tau_e} \frac{1 + s\tau_f}{1 + s\tau_g} \frac{1}{1 + s\tau_h} C(0), \quad (3.9)$$

where the DC gain $C(0)$ is of the order of unity. It is implemented using two op-amps and several capacitances and potentiometers, for tuning the time constants of equation 3.9 (Coda 1997). The circuits are integrated in the electronics box under the optical table. Table 3.3 lists the time constants in equation 3.9 that were used for the x- and y-axis compensation circuits for the experiments of chapter 4. However, these were fixed before the actual vibration spectrum in TCV had been measured: it may well be possible that fine-tuning of the time constants could lead to better performance of the vibration suppression system.

The Bode plots of the open loop (PCS) and closed loop transfer functions (equation 3.7) are shown in figures 3.22 and 3.23 for the x- and y-axis, respectively. These plots are based on measurements of $S(s)$ (figure 3.21). This is important, since the secondary resonance around 3 kHz plays a role in the stability of the system. The response of the compensation circuit $C(s)$ was calculated using equation 3.9 and the time constants in table 3.3. The maximum gain of the open loop function PCS for which the feedback loop is stable is obtained from the Nyquist criterion: stability requires that $|PCS| < 1$ for frequencies f_{180° where $\arg(PCS) = 180^\circ$. Using a gain margin of 1.4 and a phase margin of 20° , we find that the maximum DC gains are 2400 and 1300, respectively, for the x- and y-axis. The actual DC gain of the feedback system can be measured by tilting a mirror in the beam path over a known angle and inspecting the resulting focal shift on the position detector. By carrying out this measurement just below the gain where instability occurs (located by steadily increasing the gain of the driver amplifiers), and dividing by the gain margin of 1.4, we obtain values of 1900 and 1200 for the x- and y-axis, in rough agreement with the expected values stated above.

3.7.3 Performance of the feedback vibration-control system

Figure 3.24 shows the vibrational focal shifts with and without feedback vibration-control. For the case with feedback, both the x- and y-systems were operated at their maximum stable gain. During the flat-top phase the residual rms shifts are $31 \mu\text{m}$ and $55 \mu\text{m}$ in the x- and y-directions, respectively. For spatial frequencies where the response $|\mathcal{T}(K)|$ is flat, the percentage change introduced by such shifts is $\simeq 7\%$ and $< 0.01\%$ for phase-plate groove widths of $300 \mu\text{m}$ and 1 mm , respectively. In the roll-over region the effect is much larger (figure 3.16): for $K_x = 2 \text{ cm}^{-1}$, corresponding to the spatial frequency of the mode discussed in chapter 4, we find that $|\mathcal{T}(K)|$ changes by a factor of two for the 1 mm groove.

Figure 3.25 shows the power spectral density of the damped and undamped focal shift. As expected from the closed loop transfer function (figures 3.22 and 3.23), components

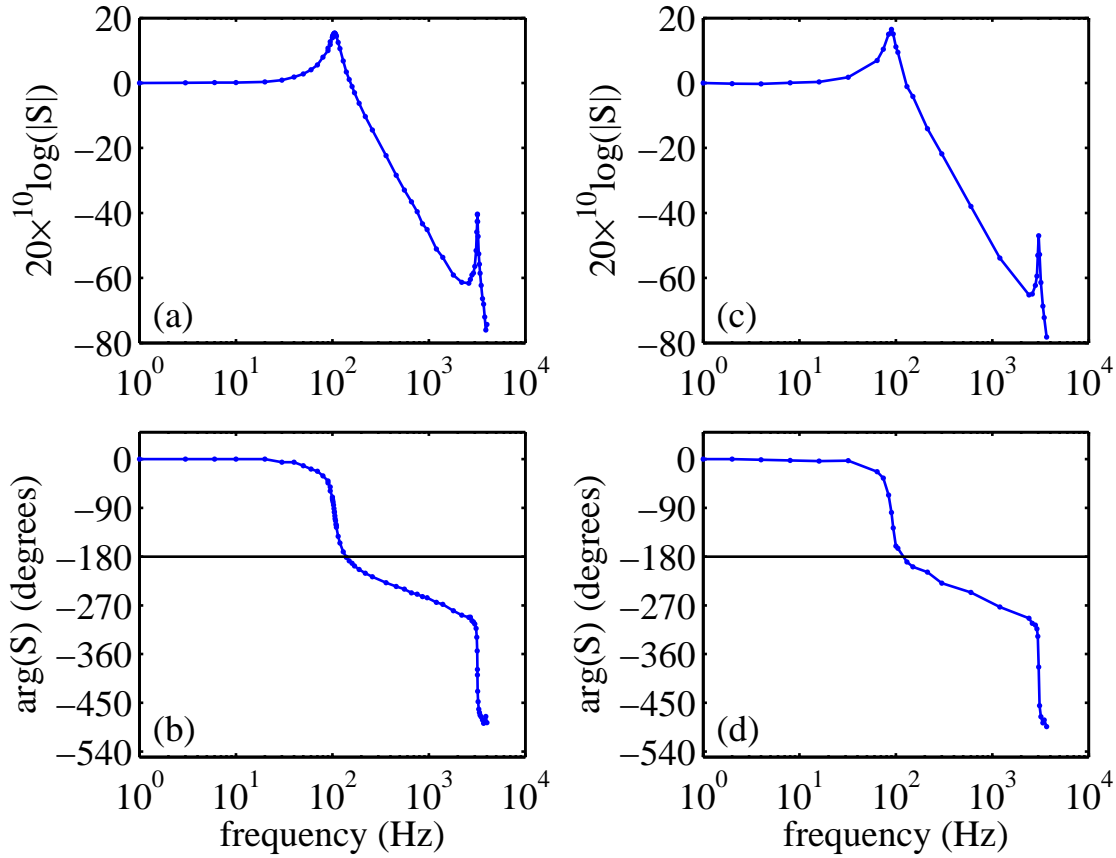


Figure 3.21: Frequency response of the rotatable mirrors used for the x-axis (*a,b*) and y-axis (*c,d*).

with $f < 800$ Hz are damped, while components with $f > 800$ Hz are amplified by the feedback vibration-control system. More than 60% of the power of the residual vibrations comes from modes in the frequency range $200 < f < 500$ Hz, while the range $f < 200$ Hz accounts for less than 3%. Future attempts to further reduce the focal shift should clearly focus on the higher frequency range.

Each of the vibrational eigenmodes that constitute the spectrum is a strongly under-damped harmonic oscillator with displacement x , inertia m , damping ratio ζ and eigenfrequency ω_0 . In fact, for several eigenmodes we were able to exactly identify the responsible motion by testing in the lab. Each of the identified motions corresponds to an elastic deformation (torsion and bending) of the metallic support on which the mirror back-plate is mounted; the plate and the support constitute the inertia. Play in the axis of M3 and M4 is thought to be unimportant. Estimates of the expected eigenfrequencies correspond very well to the observed values for cases that were easily analysed.

We assume that the excitation is a random force $\tilde{F}(t)$ with auto power spectrum $G_F(\omega)$. The auto power spectrum of the displacement $\tilde{x}(t)$ due to one mirror can then be expressed as

$$G_x(\omega) = \frac{|T(\omega)|^2 G_F(\omega)}{m^2 \omega^2 \left[(2\omega_0 \zeta)^2 + \frac{1}{\omega^2} (\omega_0^2 - \omega^2)^2 \right]}, \quad (3.10)$$

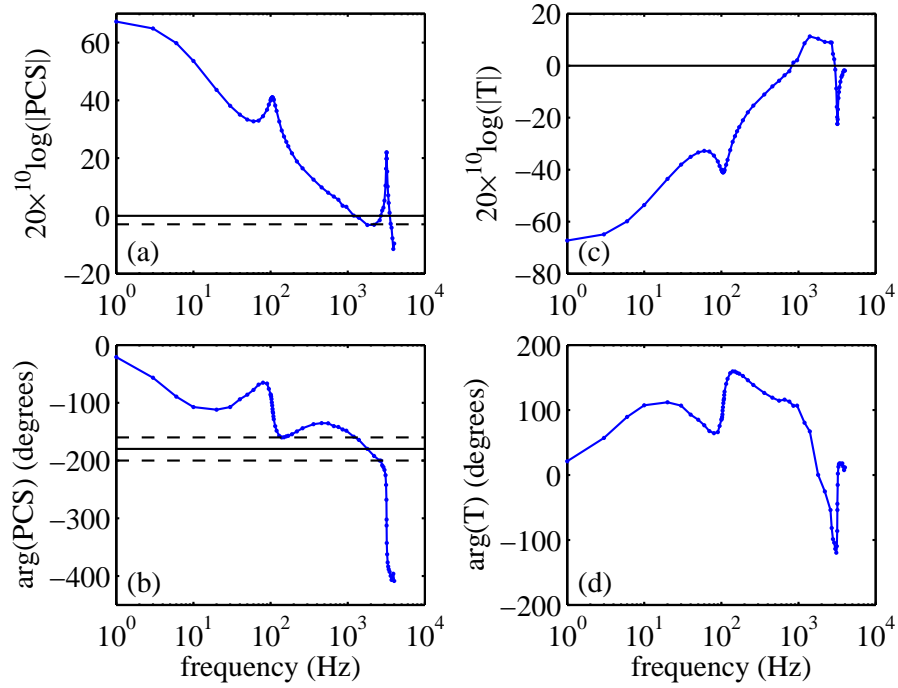


Figure 3.22: Bode plots of the open loop PCS (a,b) and closed loop $(1 + PCS)^{-1}$ (c,d) feedback transfer functions for the x-axis. The DC-gain of $|PCS|$ is 2400, which corresponds to the maximum stable value for a gain margin of 1.4 and a phase margin of 20° .

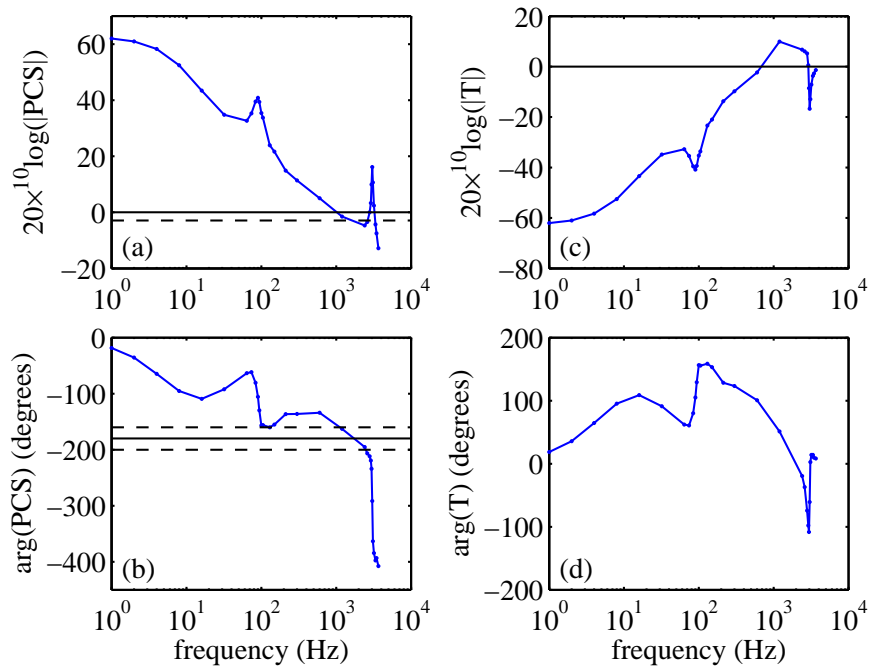


Figure 3.23: Bode plots of the open loop PCS (a,b) and closed loop $(1 + PCS)^{-1}$ (c,d) feedback transfer functions for the y-axis. The DC-gain of $|PCS|$ is 1300, which corresponds to the maximum stable value for a gain margin of 1.4 and a phase margin of 20° .

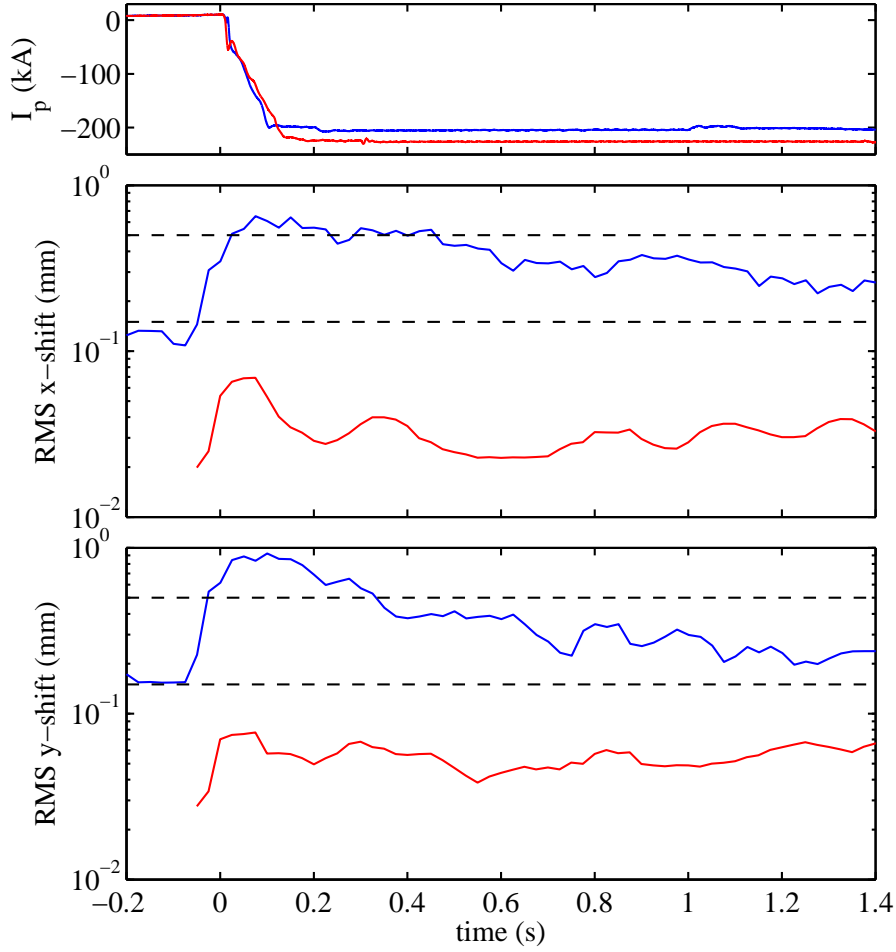


Figure 3.24: Focal shifts during a plasma discharge with (red) and without (blue) feedback vibration-control. The dashed lines indicate the groove half-widths (150 μm and 500 μm) of two of the considered phase mirrors.

where $T(\omega)$ is the closed loop transfer function of the feedback vibration-control system (equation 3.7). Taking the auto power spectra to be one-sided, the standard deviation σ_x of the displacement then satisfies

$$\sigma_x^2 = \frac{1}{\pi} \int_0^{\infty} G_x(\omega) d\omega. \quad (3.11)$$

The damping ratio of the observed eigenmodes is typically lower than 1%. Most of the spectral power is therefore concentrated in narrow frequency bands around the resonant frequency ω_0 , where we assume T and G_F to be constant. The integral in equation 3.11 can then be evaluated, giving

$$\sigma_x \approx |T(\omega_0)| \sqrt{\frac{G_F(\omega_0)}{4\zeta}} \frac{1}{m\omega_0^{3/2}}. \quad (3.12)$$

Equation 3.12 suggests several ways of decreasing the amplitude of focal vibrations.

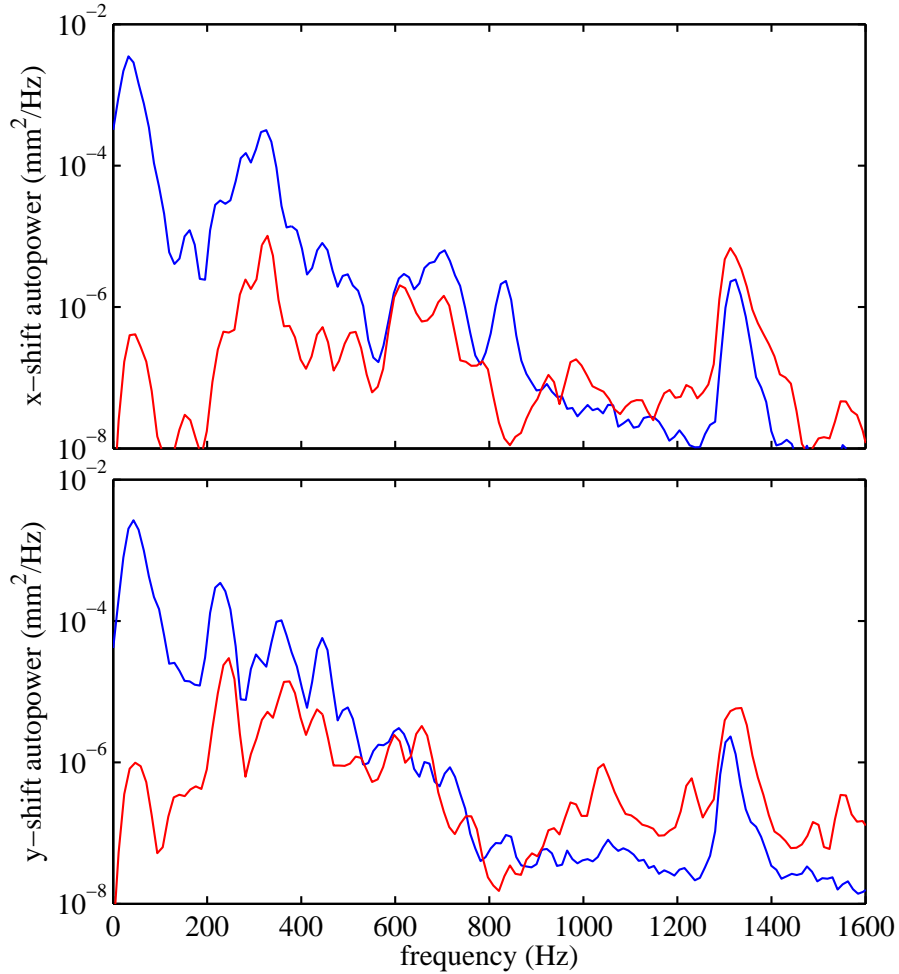


Figure 3.25: Autopower of the focal shift with (red) and without (blue) feedback vibration-control during the flat top phase of figure 3.24. Spectral smoothing interval: 20 Hz; relative statistical error: 20%.

The frequency response C of the compensation circuits (equation 3.9) can be fine-tuned to achieve stronger damping by the feedback loop, in particular for frequencies higher than ~ 200 Hz. No serious attempt to this end has been made so far, presumably leaving significant room for improvement of vibration suppression along the y-axis, in particular. Another possibility we could consider is to increase the damping ratio ζ , for example by bringing the back plates of the mirrors in contact with a dissipative material. This may in fact be easily achieved for the ex-vessel mirrors.

Another obvious possibility would be to decrease the driving force. The vibrations might be driven at least in part by Lorentz forces acting on induced eddy currents in the back plates of the mirrors. These have now been redesigned in order to reduce the possible paths for eddy currents (figure 3.26a). The modified port assemblies were recently installed, but no vibration measurements have been carried out yet. Vibrations propagating in the vessel during plasma operation may also play a role in exciting the eigenmodes, since many of them can be excited by simply tapping the ports from the

outside. The relative importance of these effects is unknown at present. We observe experimentally that the amplitude of modes with frequency lower than 100 Hz is correlated to the second derivative of the current in the Ohmic coils. No such correlation is seen for the higher frequency modes, possibly indicative of distinct drives.

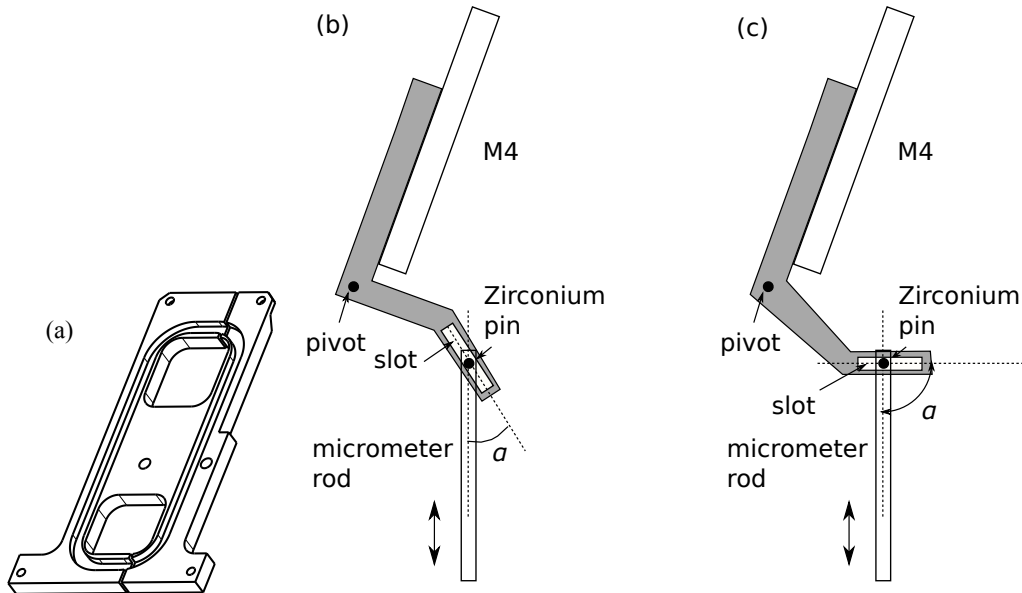


Figure 3.26: (a) Back plate for in-vessel mirror M2, redesigned to minimise eddy currents. (b) Present design of the tilting mechanism of in-vessel mirror M4 allows different angles for one micrometer position, through bending of the micrometer rod. (c) Reorienting the slot could solve this issue.

A final possibility suggested by equation 3.12 is to increase the eigenfrequency ω_0 of the vibrations by increasing the stiffness of the components on which the back plates are mounted. However, for frequencies between 100 Hz and 1 KHz, the overall increase of $|T(\omega)|^2$ is roughly 26 dB per decade, so $|T(\omega)| \propto \omega^{1.3}$ (figures 3.22 and 3.23), partially cancelling the $\omega^{-3/2}$ term in equation 3.12. This effect reduces the impact of stiffening the mounts, unless eigenfrequencies of a few kHz or more can be obtained. Moreover, the frequency dependence of the drive is unknown, and the damping coefficient is hard to predict in advance for a given mechanical design. In partial confirmation of these ideas, modifications in the summer of 2011 where two supports were made stiffer actually led to a slight *increase* in the damped vibration amplitude, even though the undamped amplitude was significantly reduced.

A major problem encountered during operation of the feedback system is the following: during plasma operation the focal spot not only suffers vibrational shifts, but also permanent DC shifts. Such DC shifts sufficiently large in some cases to move the focal spot off the quadrant detector (with feedback off): resetting the feedback system will then not bring the spot back to the centre of the phase plate, necessitating manual realignment. These shifts may be caused by pivoting of M4 around its axis; from lab tests it is known that bending of the micrometer rod and static friction of the zirconium pin in the slot can conspire to support a certain range of M4 angles for a given micrometer setting

3.7. Feedback vibration-control system

(3.26*b*). This problem may be solved by remaking the piece with the slot, so that the slot is perpendicular to the micrometer rod (3.26*c*).

Chapter 4

Turbulence and zonal flows in the TCV tokamak

Previously it had been found in TCV that electron heat diffusivity in X2 heated L-mode plasmas depends strongly on collisionality and triangularity (Camenen, Pochelon, et al. 2007). In particular, higher collisionality and lower triangularity led to longer electron energy confinement times. This effect could not be explained through purely geometrical effects on the gradients (Moret, Franke, et al. 1997), but is qualitatively consistent with the linear stability properties of the trapped-electron mode (TEM) (Marinoni, Brunner, et al. 2009). Turbulence associated with the TEM is believed to be the dominant mechanism for electron heat transport in such TCV discharges. To explore the turbulence in the various regimes with the newly operational tangential phase-contrast imaging (TPCI) diagnostic, a sequence of dedicated TCV discharges was performed. These experiments and the obtained results are described in §4.1. Although very clear differences are seen between the different regimes, the analysis is as yet incomplete.

In the analysis of the TPCI data after the triangularity experiments in TCV, a coherent mode was found, which could be identified as the geodesic acoustic mode (GAM). We present a survey of the literature on this mode in §4.2, focussing on its experimental characterisation. Our TPCI measurements of the density component of the GAM in TCV are described in §4.3. The results resemble those found in various other devices. A more surprising result is that the magnetic component of the GAM, although rather weak, is clearly measurable in TCV. This novel observation is described in section §4.4. Knowing the signature to look for, the GAM was subsequently identified in the magnetic signals from many discharges in the TCV database, so that the c_s/R frequency scaling could be confirmed. In §4.5 we compare the TPCI measurements with a global gyro-kinetic simulation of the TCV plasma, using the experimental equilibrium profiles.

All TPCI measurements discussed in this chapter were performed during a single week in December 2011, after which TCV was shut down for an extended maintenance period. In this period, the imaging system was affected by optical aberrations, which are discussed in §3.4. Spatial filtering was applied in some measurements, but these were later found to show significant inhomogeneity in the image, possibly related to a misalignment of the filter or the aberrations. Consequently, it was decided not to use these measurements. In the absence of spatial filtering, the TPCI measurements are line-integrated over the entire interaction volume, which complicates their interpretation.

In §4.6 the GAM measurements are analysed with a synthetic diagnostic employing the actual TCV magnetic geometry, to show that our interpretation is indeed consistent with the data.

During the experiments described in this chapter, the TPCI diagnostic was not absolutely calibrated. The direction of the plasma current and the toroidal magnetic field was the same for all experiments. The orientation of the TPCI detector array was also constant: the projections of the individual elements lie in a horizontal line in the object plane, with element numbers increasing for increasing major radius R . In spatial spectra of the TPCI signals we follow the convention that a wave with positive wave number K runs in the direction of increasing element numbers. When frequency spectra of TPCI signals are shown, frequencies below 10 kHz are hidden since these components are dominated by vibrations rather than plasma fluctuations. We used a fully reflective phase plate with full groove width 1.03 mm, which corresponds to a cutoff wave number $k_c = 2.59 \text{ cm}^{-1}$. The phase groove was perpendicular to the detector array, and the total optical magnification was $M = 0.18$.

Finally, we note that TPCI measurements were also performed in plasmas with electron internal transport barriers (eITBs), which constitute another unique turbulence regime that can be studied in TCV (Coda, Asp, et al. 2007). However, the data from these experiments have not yet been analysed.

4.1 The effect of triangularity on broadband fluctuations

The triangularity is defined as follows. The poloidal section of any flux surface can be parametrized in cylindrical coordinates by $(R[s], z[s])$. We denote the minimum and maximum values of $R(s)$ by $R_{\text{in,out}}$, respectively. Next, the values of $R(s)$ where $z(s)$ has its minimum and maximum values are denoted by $R_{\text{low,up}}$. The triangularity δ is then given by

$$\delta = \frac{R_{\text{out}} + R_{\text{in}} - R_{\text{up}} - R_{\text{low}}}{R_{\text{out}} - R_{\text{in}}}. \quad (4.1)$$

In the following we only refer to the triangularity of the last closed flux surface.

We now discuss the experimental scenario. All plasmas have either triangularity $\delta \simeq +0.4$ or $\delta \simeq -0.4$. Over the period $0.3 < t < 2.0$ s in each discharge, the magnetic axis of the plasma is scanned vertically from 0 cm to 23 cm above the mid plane in TCV. The elongation is kept fixed between $1.4 < \kappa < 1.5$. The target shape is reached for $t = 0.3$ s, which also marks the beginning of 0.9 MW of X2 electron heating (see §3.1), with the absorption spot fixed just inside the $q = 1$ flux surface ($\rho_{\text{vol}} < 0.5$). The heating remains constant throughout the steady state period of the discharge, which is typically terminated by a disruption around 2.1 s. The X2 heating is the dominant heat source in the plasma, since Ohmic heating does not exceed 0.25 MW. Hence, the heat flux at mid-radius is roughly equal for all discharges. However, due to the differences in electron heat diffusivity (which in turn are linked to changes in collisionality and triangularity) the electron energy confinement time (τ_e) is observed to vary between 4 ms and 8 ms in our measurements, in agreement with previous findings (Camenen, Pochelon, et al. 2007).

The plasma current reaches its steady state value of 220 kA for $t = 0.14$ s and the on-axis toroidal magnetic field is 1.5 T. The edge safety factor is $3.5 < q < 4.5$ for the negative triangularity shots and $4.8 < q < 5.2$ for the positive triangularity shots.

4.1. The effect of triangularity on broadband fluctuations

A scan of the vertical position of the magnetic axis corresponds to a radially inward scan of the tangency point of the TPCI chords. However, due to the difference in geometry of the flux surfaces, the range of this scan is different between the positive and negative triangularity discharges: for the central chord it is $0.32 < \rho_{\text{vol}} < 0.59$ for $\delta = -0.4$ shots, and $0.37 < \rho_{\text{vol}} < 0.79$ for $\delta = +0.4$. This is illustrated in figure 4.1*b*. Since at the tangency point the diagnostic is sensitive to purely radial wave vectors, radial modes localised to $\rho_{\text{vol}} > 0.59$ are not detectable in the negative triangularity shots. Since no spatial filtering was applied, fluctuations along the entire integration path may contribute to the signals. It should be clear from the above that interpretation of the signals in terms of density fluctuations, and comparison between the different geometries, is complicated. For now we take a pragmatic approach and simply characterise the measured signals. Finally, we note that for any given time during the scan the radial extent spanned by the tangency point of the extreme chords lies between $0.17 < \Delta\rho_{\text{vol}} < 0.2$, the larger value being reached towards the end of the scan.

As an illustration of the TPCI signals during the scan, figure 4.1 shows power in the high-pass filtered signals from the central chord for two discharges, one with $\delta = +0.4$ and the other with $\delta = -0.4$. Since there is an MHD mode at 30 kHz, the cutoff is chosen at 35 kHz. We first discuss the signal evolution of the $\delta = +0.4$ discharge. It may be seen that the broadband signal level increases sharply for $t = 0.2$ s, i.e. ~ 100 ms *before* the X2 power is applied ($t = 0.3$ s). This sharp increase coincides with a radially outward motion of the tangency point, from $\rho_{\text{vol}} = 0.6$ to 0.8 for the central chord (figure 4.1*b*). Surprisingly, no change in signal levels is visible when the gyrotrons are switched on. During the first few hundred ms of the scan the power steadily decreases by a factor of five. The same trends are seen for all three $\delta = +0.4$ discharges for which we have TPCI measurements, although the absolute signal levels vary by up to a factor of two (lower density gives lower signal level). By contrast, in the TPCI signals from the $\delta = -0.4$ discharges neither the coherent mode nor the strong evolution in broadband level is observed. The signal level is everywhere lower in absolute value than in the positive-triangularity case, and steadily decreases by 30% during the scan. As for $\delta = +0.4$, the switch-on of the gyrotrons has no perceptible effect on the signal level. The same trends are seen for all $\delta = -0.4$ discharges.

Figure 4.2*a* shows two power spectra of the TPCI signal from the central chord during a $\delta = +0.4$ discharge. The integration times are marked by the shaded regions in figure 4.1. The noise level was subtracted from these spectra. For $f < 100$ kHz the signal-to-noise ratio is 20-25 dB; it typically drops below one between 600 kHz and 900 kHz. A coherent mode is evident around 30 kHz in the first spectrum. The decay in spectral power is approximately exponential for $f \gtrsim 100$ kHz; below 100 kHz the spectrum flattens or peaks. The decay rate is ~ 40 dB/MHz at the start of the scans, and then evolves to ~ 30 dB/MHz. These values and their evolution during the scan are essentially identical for all discharges with $\delta = +0.4$ for which we have measurements.

The two power spectra shown in figure 4.2*b* correspond to the $\delta = -0.4$ discharge of figure 4.1, again evaluated on the shaded intervals. As in the case of the $\delta = +0.4$ discharge, the spectra decay exponentially for $f \gtrsim 100$ kHz. However, for $\delta = -0.4$ a clear knee is seen around 280 kHz, above which the decay is much slower. It is especially pronounced at the beginning of the vertical scan of the plasma, where the decay jumps from 47 dB/MHz to 20 dB/MHz. The modest drop in overall signal level during the

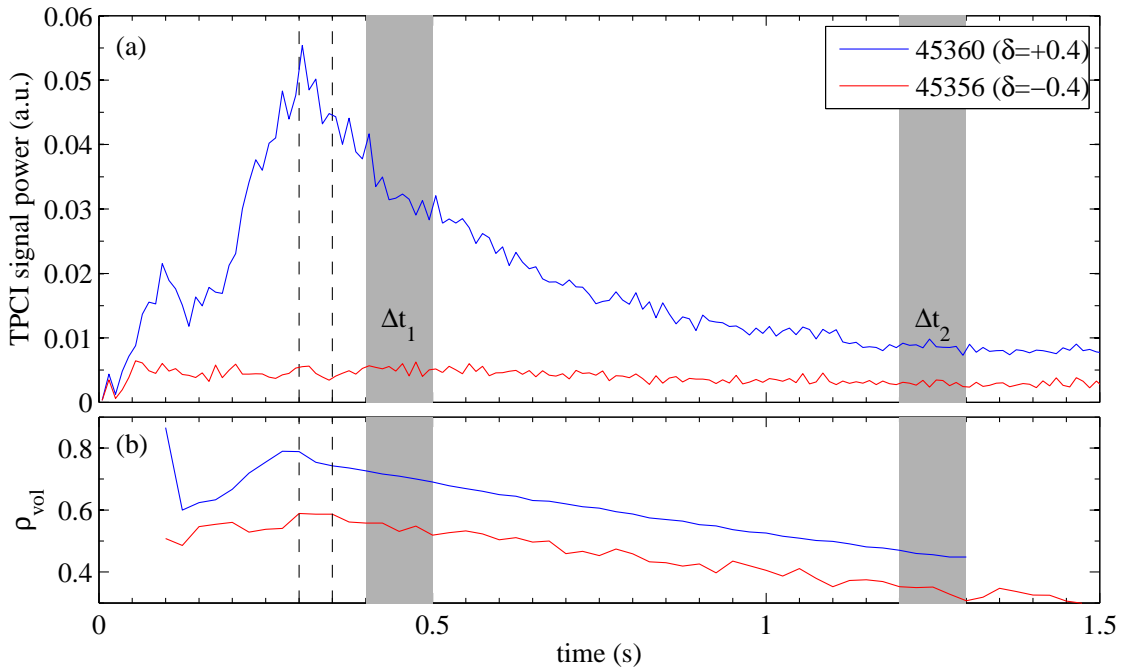


Figure 4.1: (a) Power in TPCI signals (central chord; integration time 10 ms) for two discharges with positive and negative triangularity, respectively. Signals are band-pass filtered on 35-800 kHz. Noise floor is 2×10^{-4} . (b) Radial position of tangency point of the central chord. Black dashed lines indicate the start of the X2 heating phase, which is 50 ms later for the $\delta = -0.4$ discharge. Shaded intervals are used for the spectra in figure 4.2.

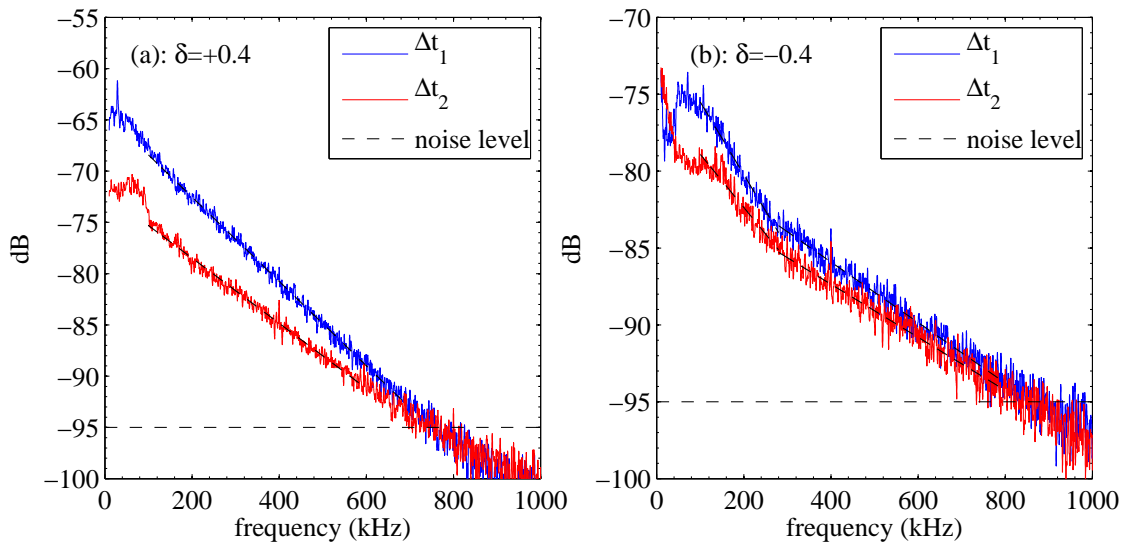


Figure 4.2: Power spectral density of the signal from the central TPCI chord during the shaded intervals in figure 4.2. Noise level has been subtracted. Note the difference in scale between (a) and (b).

4.1. The effect of triangularity on broadband fluctuations

vertical scan comes exclusively from the $f \lesssim 280$ kHz part of the spectrum; the spectral region $f \gtrsim 280$ kHz remains essentially constant throughout the discharge.

To elucidate the spatial correlation structure of the image we show several conditional spectra (equation 2.59) in figure 4.3. These spectra were calculated using all possible combinations of channels. In light of the uncertainty in the actual value of k_c (§4.6) we did not divide the measured conditional spectrum by the theoretical optical transfer function $\mathcal{T}(k)$ (equation 2.54). We do correct the spectra for the $d = 1.4$ m distance between the nominal and actual object planes, as discussed in §3.6; this is achieved by division by $\cos(dk^2/[2k_0])$, and renormalisation to ensure that $\int s(k|\omega)dk = 1$.

Horizontally elongated features with apparent wavenumber $k \simeq 1 \text{ cm}^{-1}$ are seen, especially in figures 4.3*b-c-d*. Inspection of the corresponding complex coherence functions in the spatial domain show that these features are not artefacts of the spectral reconstruction method (§2.6). Rather, since $|k| < k_c$, the considerations on spectral broadening of §3.4 strongly suggest that the wavenumber of the underlying density perturbation is in fact lower than 1 cm^{-1} . The TPCI measurements therefore cannot be used for spatial analysis of these features.

The only feature that falls comfortably outside of the cutoff region is the diagonal band for negative k in the early phase of the vertical scan of the plasma column (figures 4.3*a-c*). It is visible both for the positive and negative triangularity discharges, but for the positive triangularity spectrum it is much broader. In fact, the extent in frequency of the feature, both for positive and negative triangularity, corresponds exactly to a region of exponential decay in the respective auto-power spectra (figure 4.2).

We assume for the moment that the feature is caused by a poloidally propagating wave. Analysis of the geometry of the measurement shows that in both discharges the TPCI is sensitive to such a wave for $\rho_{\text{vol}} \gtrsim 0.8$, in the region where the beam exits the plasma. The observed k around 100 kHz in the TPCI spectra is consistent with propagation in the electron diamagnetic drift direction and a poloidal mode number $m = 75$. The effective integration lengths for $\delta = +0.4$ and -0.4 are 7 cm and 16 cm, respectively. In spite of the shorter integration length, the signal power is $\simeq 10$ dB higher for positive triangularity. If we could be sure that the feature is caused by a poloidal wave, this would show that the turbulence level in the plasma periphery is much higher for negative than positive triangularity, in line with the observed difference in confinement time.

On the other hand, if we assume that the feature is caused by a radial wave, the TPCI signal arises near the tangency point, which for the $\delta = +0.4$ discharge lies substantially further outward for the time window we are considering (figure 4.1*b*). The difference in signal level between the two discharges could then reflect a radial variation in turbulence level. Indeed, the signal level for $\delta = +0.4$ goes down as the tangency point moves inward (figure 4.1*a*).

The foregoing considerations illustrate that in spite of the clear differences in signal levels and spectra between the positive and negative triangularity discharges, it is difficult to draw even qualitative conclusions about differences in the turbulent state. This underlines the importance of spatial filtering, which could make this measurement unambiguous. In a future repeat of this experiment the range of the vertical shift of the plasma column should also be extended, so that the tangency volume scans the minor radius all the way up to the edge of the plasma for both positive and negative triangularity. Finally, turbulence simulations, especially in conjunction with a ‘synthetic diagnostic’ would also

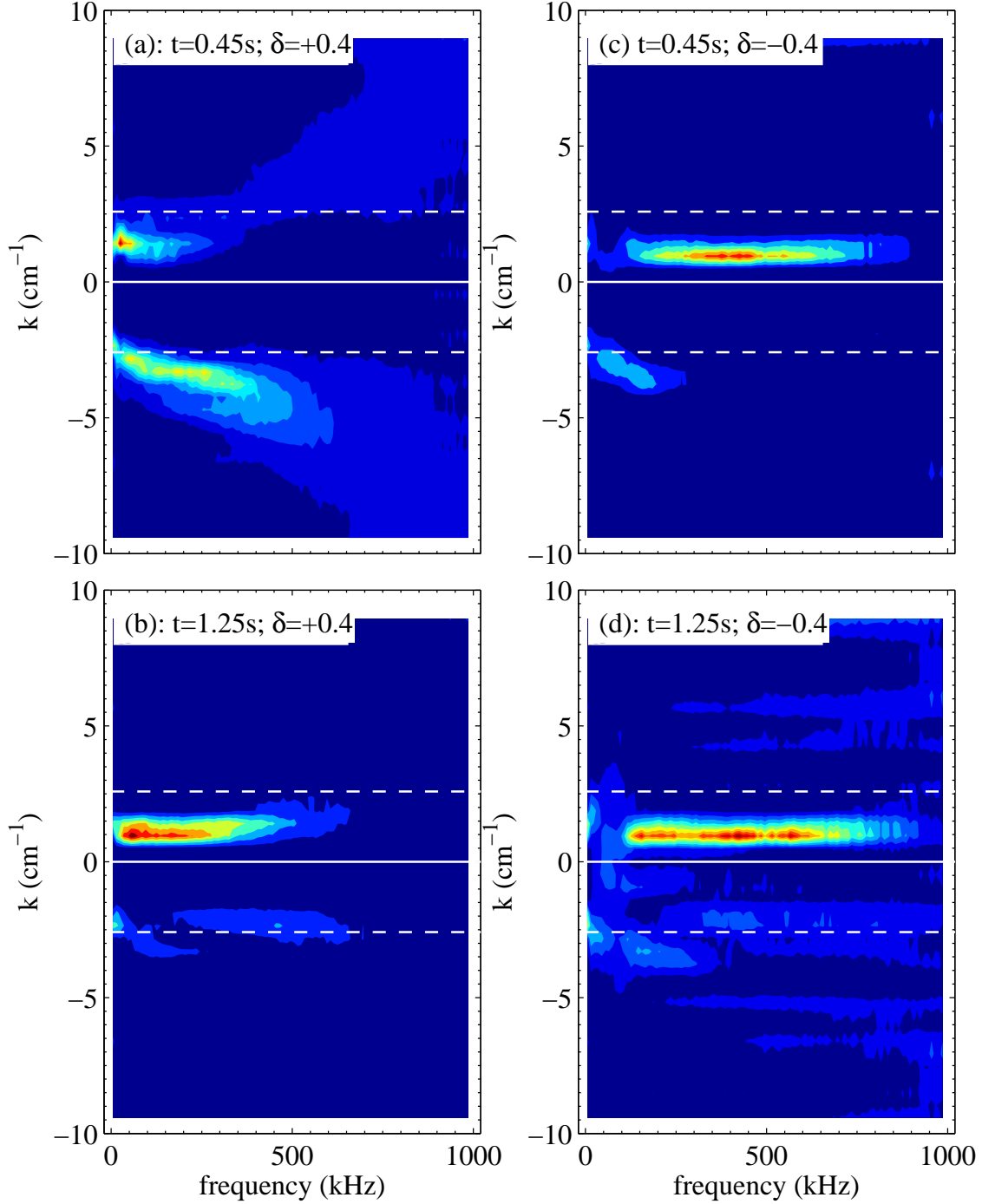


Figure 4.3: Conditional spectra, calculated on the shaded intervals in figure 4.1. The continuous line indicates $k = 0$; the dashed lines indicate the nominal cutoff wave vector $\pm k_c = 2.59 \text{ cm}^{-1}$. The Nyquist wave number is $k_{\text{Nyq}} = 9.4 \text{ cm}^{-1}$. Frequency smoothing over 10 kHz.

4.1. The effect of triangularity on broadband fluctuations

be extremely helpful to guide the interpretation of the TPCI measurements.

4.2 Review of the literature on geodesic acoustic modes

4.2.1 Results from theory and simulations

In the context of magnetically confined plasmas, zonal flows are a perturbation of the electric potential that is constant on magnetic surfaces, but oscillates in the radial direction (Diamond et al. 2005). In other words, they are electrostatic modes with $n = m = 0$, but finite radial wavenumber k_r . Crucially, since the flow is strictly poloidal, it does not cause radial transport and cannot tap into the free energy associated with the radial pressure gradient. As a result, zonal flows are linearly stable.

Two types of zonal flow with different time scales exist in toroidal plasmas. The first has a frequency much lower than the ion transit frequency, i.e. $\omega \ll v_{\text{th},i}/(qR)$. Here, $v_{\text{th},i}$ is the ion thermal velocity, q the safety factor and R the major radius. The plasma responds as an incompressible fluid and consequently the density perturbation is very small. The second type, which is known as the geodesic acoustic mode (GAM), has a finite frequency and a pressure component. In a fluid model of a single toroidal flux surface the angular frequency of the GAM satisfies the dispersion relation (Winsor et al. 1968)

$$\omega_{\text{GAM}} \simeq (2 + q^{-2})^{1/2} c_s / R. \quad (4.2)$$

Here, c_s represents the ion sound velocity

$$c_s = \sqrt{(T_e + \gamma_i T_i) / m_i}, \quad (4.3)$$

where γ_i is the adiabatic index of the ions. Equation 4.2 is valid if the flux surface has circular poloidal section and small inverse aspect ratio $\varepsilon = a/R$, where a is the minor radius. For non-circular cross-sections and finite ε equation 4.2 is modified by a factor of order unity (Bing-Ren et al. 2005).

In the presence of a temperature gradient and magnetic shear the GAM frequency (equation 4.2) is a smooth function of radius. At least two physical mechanisms exist by which discrete eigenmodes arise from the GAM continuum. The first mechanism requires a radial extremum in the GAM frequency, which may occur for reversed shear discharges. At the radial position of the extremum, typically deep in the core of the plasma, an $n = 0$ eigenmode can exist. The mode may be destabilised by supra thermal ions, which also play an important role in its dynamics (Berk et al. 2006; Nazikian, Fu, et al. 2008).

A second mechanism involves the finite gyro radius of ions, which allows modes on neighbouring flux surfaces to interfere with each other. It can be shown that in the presence of a temperature gradient this interference leads to discrete eigenmodes with constant frequency over a finite radial extent (Itoh et al. 2006; Gao et al. 2008). These eigenmodes have finite radial wavelength of order $\rho_i^{2/3} L_T^{1/3}$, where ρ_i is the ion Larmor radius and $L_T = T/\nabla T$ the temperature gradient scale length. The radial direction of propagation depends on q and T_e/T_i but is typically outward in the outer region of a tokamak plasma (Zonca et al. 2008). Eigenmodes of this type are commonly observed in the periphery of tokamak plasmas, both experimentally and in gyro kinetic simulations (Fujisawa 2009). They can be driven by three wave interaction with micro turbulence (Diamond et al. 2005; Zonca et al. 2008). Predicting the frequency and radial localisation of GAMs for a given equilibrium requires knowledge of the turbulent drive (Zonca et al. 2008).

4.2. Review of the literature on geodesic acoustic modes

Unlike the zero frequency zonal flow, the GAM has a finite density component \tilde{n} with mode numbers $n = 0$, $m = 1$. Its dependence on the poloidal angle θ is given by

$$\frac{\tilde{n}}{n_0} = - \left(\sqrt{2} k_r \rho_s \frac{e\tilde{\phi}}{T_e} \right) \sin \theta, \quad (4.4)$$

where k_r is the radial wave number, ρ_s is the gyro radius of an ion with the electron thermal velocity, T_e the electron temperature, and e the electron charge (Diamond et al. 2005). Equation 4.4 corresponds to a standing wave with nodes in the equatorial plane. Since $\tilde{E} = -\nabla\tilde{\phi}$, $\tilde{v}_{E \times B}$ is out of phase by 90° with respect to \tilde{n} and $\tilde{\phi}$.

The ideal MHD properties of the GAM have been studied in detail for circular poloidal section and small inverse aspect ratio $\varepsilon (= a/R)$, but keeping terms up to ε^2 (Wahlberg 2008; Wahlberg 2009). To first order in ε the perturbation is localised to a single flux surface. To higher order in ε radially extended $m = 2$ components are found, including a magnetic component whose θ component satisfies

$$B_\theta(t, \theta) = \exp(-i\Omega t) (\xi_2^s \cos[2\theta] + i\xi_2^a \sin[2\theta]), \quad (4.5)$$

where $\xi_2^{s,a}$ are real. The ratio ξ_2^s/ξ_2^a increases with $R\Omega_{\text{rot}}/v_A$ and depends on the details of the equilibrium. Here, Ω_{rot} is the toroidal rotation (angular) frequency of the plasma and v_A the Alfvén velocity. For a non-rotating plasma the ratio is zero: the magnetic field of the GAM is then a standing wave with nodes at $\theta = 0^\circ, 180^\circ$ and $\pm 90^\circ$. In the example discussed by Wahlberg 2008, $\xi_2^s/\xi_2^a \simeq 0.15$ for $R\Omega_{\text{rot}}/v_A = 0.04$. The amplitude of the $m = 2$ components scales with $q^2\beta$, where q is the local safety factor and β is the ratio of kinetic and magnetic pressure.

GAMs are linearly damped by ion-ion collisions at a rate $\simeq 4/7\nu_{ii} \propto n_e T_i^{-3/2}$. Unlike the zero-frequency zonal flow, which has $k_{\parallel} = 0$, the GAM is also subject to collisionless Landau damping at the rate $\simeq \omega_{\text{GAM}} \exp(-q^2/2)$ for small q ; for $q \gtrsim 2$ the dependence is more complicated and Landau damping remains substantial (X. Q. Xu et al. 2008).

4.2.2 Experimental observations of the GAM

Thanks to its finite frequency and density component the GAM is much easier to detect experimentally than the zero-frequency zonal flow. Indeed, their identification often relies on the observed $T^{1/2}$ frequency scaling. GAMs have been observed in many tokamaks with a variety of fluctuation measurements (Fujisawa 2009). The density perturbation has been studied with beam-emission spectroscopy (BES) (McKee, Fonck, Jakubowski, K H Burrell, et al. 2003b; Zoletnik et al. 2012), electrostatic probes (McKee, Fonck, Jakubowski, K H Burrell, et al. 2003b), heavy ion-beam probes (HIBP) (Ido et al. 2006; Melnikov et al. 2006), straight-incidence reflectometry (Krämer-Flecken, Soldatov, Reiser, et al. 2009) and far infrared interferometry (FIR) (Matsunaga, Kamiya, et al. 2012). The electric potential perturbation has been measured with electrostatic probes and HIBP. Observations of the magnetic component of the GAM are discussed later in this subsection.

The fluctuating flow velocity $\tilde{v}_{E \times B}$ can be measured indirectly through the associated advection of small scale density perturbations. Two methods exist for obtaining the latter quantity. The first requires two or more poloidally spaced point measurements of turbulent fluctuations and employs the (time varying) time delay for which the cross-correlation

function peaks (Zoletnik et al. 2012). This technique is often applied to BES and poloidal correlation reflectometry measurements (McKee, Fonck, Jakubowski, K H Burrell, et al. 2003b; Krämer-Flecken, Soldatov, Reiser, et al. 2009). The second technique exploits the time varying Doppler shift of backscattered microwaves on oblique illumination of a cutoff (Conway, Tröster, et al. 2008) or an upper hybrid resonance layer (Gurchenko et al. 2010).

GAMs have been observed in tokamaks of all sizes and in a wide variety of conditions, but not in H-mode (Conway, Angioni, et al. 2011). The mode amplitude increases for large safety factor q and low density, qualitatively consistent with the theoretically expected Landau and collisional damping (McKee, Gupta, et al. 2006; Conway et al. 2008). A positive correlation of the GAM amplitude and the temperature gradient has been reported, qualitatively consistent with its drive by turbulence (Conway et al. 2008). The mode is typically observed in the outer part of the plasma, but not outside of the last closed flux surface. The magnetic field of the GAM does extend outside of the plasma, since it has been measured with external pickup coils (Melnikov et al. 2006; Matsunaga, Kamiya, et al. 2012).

GAMs with different frequencies may exist simultaneously in a plasma, each localised around its own magnetic surface; the width of these radial zones is typically a few cm. The frequency of each mode is then determined by the temperature on that flux surface. Either through the finite radial extent of the mode (typically a few cm) or due to the finite radial resolution of the measurement two discrete peaks may be visible simultaneously in a single frequency spectrum (Conway, Tröster, et al. 2008). By contrast, observations in the FT-2 tokamak show a smooth dependence of mode frequency on radial position (Leerink et al. 2012).

In absolute terms, experimentally reported GAM frequencies are typically 10-50 kHz, depending of course on the size of the machine. For tokamaks with a non-circular poloidal cross-section, the observed mode frequency is significantly lower than that given by equation 4.2. For the ASDEX Upgrade tokamak the parametric frequency dependence was studied in detail (Conway, Tröster, et al. 2008). The frequency of modes whose amplitude peaks at $r/a > 0.95$ is approximated by the following heuristic relation:

$$\omega_{\text{GAM}} = 4\pi[(1 + \kappa_b)^{-1} - 0.3]c_s/R. \quad (4.6)$$

Here, κ_b is the elongation of the last closed flux surface and the sound speed c_s (equation 4.3) is calculated using an adiabatic index $\gamma_i = 1$ for the ion fluid.

The reported spectral width of the mode is typically a fraction of its frequency, with typical values in the range 0.5-5 kHz (FWHM). A quantitative study of the damping rate of the GAM through measurements of the spectral width with the UHR backscattering diagnostic was carried out in the FT-2 tokamak, but the results have not yet been published (Gusakov 2012). However, recent measurements by HIBP in the JIPPT-IIU tokamak revealed a remarkably broad GAM spectrum (FWHM $\simeq 20$ kHz) peaking around 40 kHz (Hamada, Watari, et al. 2011). These observation were made deep in the plasma core, near the $q = 1.5$ surface.

The poloidal correlation structure of the GAM has been studied in several experiments. BES measurements in DIII-D (McKee, Fonck, Jakubowski, K H Burrell, et al. 2003b; McKee, Fonck, Jakubowski, K. H. Burrell, et al. 2003a) at $\theta \simeq 0$ yield $\tilde{n}_{\text{GAM}}/n_0 \approx 0.25\%$, showing that the node predicted by equation 4.4 is imperfect. The vertical extent of the

BES measurement was 6 cm, covering only a small fraction of the poloidal cross-section of DIII-D. The measured $|m| < 3$ obtained for \tilde{v}_{GAM} (and thus $\tilde{\varphi}_{\text{GAM}}$) is consistent with the expected $m = 0$. By contrast, the measured $m \approx 10$ is not consistent with the expected $m = 1$ standing wave structure of equation 4.4. The density perturbation propagates in the electron diamagnetic drift direction in the laboratory frame, while the average $E \times B$ drift is in the opposite direction. Correlation measurements with HIBP in the JIPP-TIIU tokamak, using sampling volumes distributed over $0 \lesssim \theta \lesssim 30^\circ$ and approximately on the same flux surface, also show zero cross-phase of $\tilde{\phi}_{\text{GAM}}$, but non-zero cross-phase of \tilde{n}_{GAM} (Hamada, Nishizawa, et al. 2005). By contrast, reflectometry measurements in T-10 by Melnikov et al. 2006 showed zero cross phase between measurements of \tilde{n}_{GAM} at $\theta \simeq 60^\circ$ and 120° . The authors state that this demonstrates “that the mode has $m = 0$ ”.

The TEXTOR multi-antenna reflectometer allows the measurement of long range ($\Delta\theta \simeq 105^\circ$) and short range ($\Delta\theta \sim 5^\circ$) poloidal correlation of \tilde{n}_{GAM} and \tilde{v}_{GAM} . Short range correlation measurements of \tilde{n}_{GAM} around $\theta = 105^\circ$ yield zero cross-phase. Further, $\tilde{n}_{\text{GAM}}/n_0 \simeq 0.1\%$ for $\theta = 105^\circ$ compared to 0.01% for $\theta = 0$ (Krämer-Flecken, Soldatov, Koslowski, et al. 2006; Krämer-Flecken, Soldatov, Reiser, et al. 2009). These observations are consistent with the $m = 1$ standing wave structure of equation 4.4. Surprisingly, the following interesting cross-phase measurements are not mentioned in these publications: long range poloidal correlation of \tilde{n}_{GAM} ; short and long range correlation of \tilde{v}_{GAM} ; short and long range correlation between \tilde{n}_{GAM} and \tilde{v}_{GAM} .

In a more recent TEXTOR paper long range poloidal and toroidal cross-correlations between \tilde{v}_{GAM} and \tilde{n}_{GAM} are briefly mentioned (Zoletnik et al. 2012). BES is used to measure \tilde{v}_{GAM} at $(\theta, \phi) \simeq (0^\circ, 0^\circ)$. Short-range poloidal correlation reflectometry is used to measure \tilde{v}_{GAM} and \tilde{n}_{GAM} at $(\theta, \phi) \simeq (70^\circ, 105^\circ)$. Zero cross-phase is obtained for the long range correlation of \tilde{v}_{GAM} ; for long range correlation of \tilde{n}_{GAM} and \tilde{v}_{GAM} 90° cross-phase is measured. This is consistent with equation 4.4. It must be remarked though that these cross-phase measurements depend sensitively on the radial localisation of the spatially separated measurements, since the GAM appears to be (see below) a radially propagating wave (typically outward) with a wavelength of a few cm.

The axisymmetry of $\tilde{\varphi}$ associated with the GAM was first demonstrated in HL-2A by K. J. Zhao et al. 2006 using three arrays of electrostatic probes in the outboard mid-plane of the HL-2A tokamak, toroidally distributed over $\sim 60^\circ$. Similarly, on the outboard mid-plane of TEXTOR zero cross-phase was measured for two probes separated by $\Delta\phi = 180^\circ$ (Y. Xu et al. 2011).

The radial correlation structure of the GAM has also been discussed in several publications. Invariably, a radially oscillating structure is found with wavelength λ_r of a few cm. We denote the radial correlation length by l_r . The mode typically propagates radially outward. In DIII-D BES measurements showed $\lambda_r \simeq 6$ cm and $l_r \simeq 3$ cm (McKee, Fonck, Jakubowski, K H Burrell, et al. 2003b). A clear preferential propagation direction is seen, but its direction not mentioned explicitly. In JFT-2M HIBP and electrostatic probe measurements show $\lambda \simeq 7$ cm, with radially outward propagation at peak amplitude, but zero or inward propagation for locations further radially inward (Ido et al. 2006). In HL-2A electrostatic probes show purely radially outward propagation with $\lambda_r \simeq l_r \simeq 3$ cm (Lan et al. 2008). In TEXTOR, electrostatic probes show $\lambda_r \simeq 10$ cm, with radially outward propagation (Y. Xu et al. 2011). In T-10 correlation reflectometry shows $\lambda_r \simeq 4$ cm, but the propagation direction is not mentioned. Observations with microwave backscattering

diagnostics in TF-2 also show outward propagation and a radial correlation length shorter than one wavelength (Gusakov 2012).

Measurements of the magnetic component of GAMs driven by micro turbulence in the plasma periphery are rare. Several authors explicitly report that it is not detectable (Conway, Tröster, et al. 2008; Ido et al. 2006). Observations by HIBP and electrostatic probes of a mode in the TEXT tokamak, which in retrospect may be a GAM, are discussed by Tsui et al. 1993. The magnitude of its magnetic field was measured to be $|\tilde{B}|/B \simeq 10^{-5}$ using an insertable probe. A similar instrument was used to detect the magnetic field of the GAM in the T-10 tokamak (Melnikov et al. 2006). The authors report that the field was weak, but do not give its absolute value.

By contrast, the characterisation of the fast ion driven GAM eigenmode arising in the core of reversed shear plasmas relied in part on magnetic measurements with pickup coils outside of the plasma. In JET (Berk et al. 2006; Boswell et al. 2006) and DIII-D (Nazikian, Fu, et al. 2008) the magnetic field was reported to have the expected toroidal mode number $n = 0$, but its poloidal structure was not mentioned. The reported magnitude of the GAM magnetic field at the wall of DIII-D is $|\tilde{B}|/B \simeq 10^{-5}$, which the authors qualify as ‘particularly weak’. Recently, measurements with pickup coils in JT-60U also confirmed the expected poloidal $m = 2$ structure (Matsunaga, Kamiya, et al. 2012). In addition to the predicted $m = 2$ standing wave structure with nodes (of B_θ) for $\theta = \{0^\circ, \pm 90^\circ, 180^\circ\}$ (equation 4.5), poloidally propagating waves in both directions were also observed.

4.3 Density component of the geodesic acoustic mode

Figure 4.4 shows the spectra of a central TPCI channel and a Mirnov coil during a vertical scan of the plasma column in the TCV vessel. The coil and the TPCI sampling volume are separated toroidally by $\simeq 180^\circ$. In this discharge, a coherent feature is evident around 26 kHz in the signals from both diagnostics. Partial coherence exists between the TPCI and Mirnov signals for that frequency ($\gamma^2 = 0.3 \pm 0.06$), showing that the feature in both spectra is caused by a single, global mode. The mode is not visible in the signals from the soft X-ray tomography system. In the following we show that this mode is in fact the geodesic acoustic mode (GAM).

The mode is visible in all nine TPCI channels. Figure 4.5a shows their complex coherence $\gamma(\Delta x)$ at the mode frequency as a function of the separation Δx of the chords in the object plane; the sampling window was chosen around the time of peak amplitude ($t = 0.36$ s). All 36 unique channel pairs are included in the plot; points with $\Delta x < 0$ are mapped to $\Delta x > 0$ by $\gamma(-\Delta x) = \gamma^*(\Delta x)$, where the asterisk denotes complex conjugation. The error bars in the plot represent the statistical error due to ensemble averaging. These errors are typically much smaller than the difference between values for the complex coherence from different channel pairs with the same spatial separation $|\Delta x|$. This difference may be caused by uncertainty in the effective position of detector elements within the array and by spatial non-stationarity of the image. To arrive at a single-valued estimate of the complex coherence $\gamma(\Delta x)$ we use the average value for each Δx ; the maximum spread is taken as an effective error. The resulting complex coherence

4.3. Density component of the geodesic acoustic mode

function can be fitted reasonably well ($\chi_{\text{red}}^2 = 1.11$) with a curve of the form

$$\gamma_{\text{fit}} = \exp(iK\Delta x - |\Delta x|/l_c), \quad (4.7)$$

which is shown in figure 4.5a. We conclude that the signals conform quite well to a spatially coherent, outward propagating wave. The measured wavenumber ($K \simeq 2\text{cm}^{-1}$) is constant during the discharge. It must be noted that this value is lower than the nominal cutoff wavenumber ($k_c = 2.59\text{ cm}^{-1}$). As discussed in §3.4 and §4.1, the wavenumber of the underlying phase perturbation may therefore be lower. On the other hand, the apparent value is substantially higher than that of the elongated structures of figure 4.3, which have $k \simeq 1\text{ cm}^{-1}$.

As the plasma column moves up, the mode amplitude clearly peaks at different times for the TPCI and the Mirnov signals (figure 4.4), indicating that the observed evolution in amplitude reflects the spatial structure of the mode rather than a change in time of its overall amplitude. Under the assumption that the mode is radial, the main contribution to the phase shift measured by the TPCI arises around the tangency point for each integration chord. The upward motion of the plasma translates into a radially inward motion of the tangency points. Establishing the mode amplitude as a function of the tangency radii for the different chords then reveals the radial extent of the mode; this analysis is undertaken in the following.

To estimate the RMS amplitude σ of the mode on the basis of the (time varying) power spectral density $P(f)$ we use the power in a narrow frequency band Δf around the mode frequency f_0 and subtract the background level, estimated around a frequency f_{bg} :

$$\sigma^2 \approx \int_{f_0 - \Delta f/2}^{f_0 + \Delta f/2} P(f)df - \int_{f_{\text{bg}} - \Delta f/2}^{f_{\text{bg}} + \Delta f/2} P(f)df. \quad (4.8)$$

This is a reasonable approximation if the background power spectral density does not change much around the mode frequency. The signal of each channel is scaled by a constant factor to make the mode amplitudes of all channels fall onto a single curve, which is shown in figure 4.5b. The scaling factors are obtained through an automatic optimisation routine. It must be noted that the factors we obtain deviate substantially from the relative calibration factors that were derived from the acoustic relative calibration before the discharge 3.6. This reflects the inhomogeneity in the optical response due to residual aberrations 3.14b. We also note that the TPCI diagnostic was not absolutely calibrated at the time of this measurement.

The figure suggests that the mode is localised to $\rho_{\text{vol}} \gtrsim 0.65$ and that its amplitude increases roughly linearly at least up to $\rho_{\text{vol}} \simeq 0.86$, which is the outermost point covered in the scan. The RMS value of the broadband component (the black lines in figure 4.5b) also steadily increases with ρ_{vol} of the tangency point.

Finally, we remark that the TPCI signals do not show significant bicoherence.

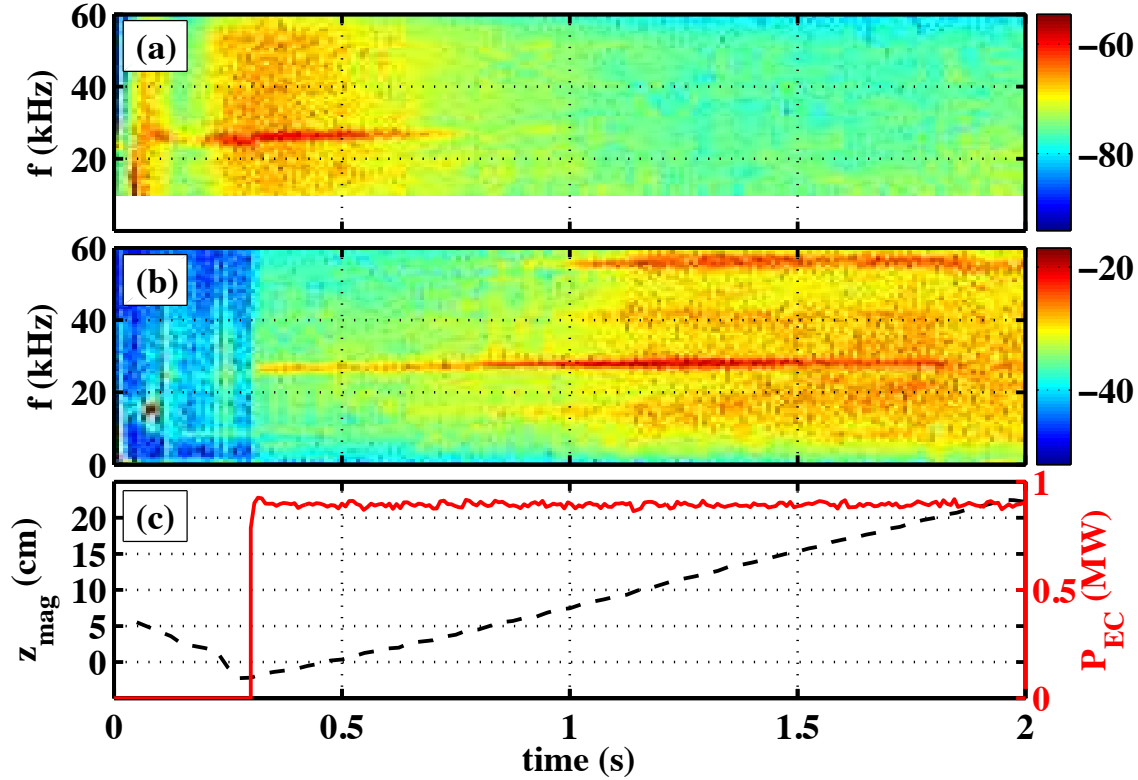


Figure 4.4: Power spectral density (dB scale) of TPCI detector 24 (a) and a magnetic probe in the high field side wall at $z=35$ cm (b) for TCV discharge 45353. Spectra calculated with integration time 10 ms; frequency smoothing over 1 kHz. c) Black, dashed, left scale: vertical position of magnetic axis (z_{mag}). Red, continuous, right scale: injected X2 electron cyclotron power.

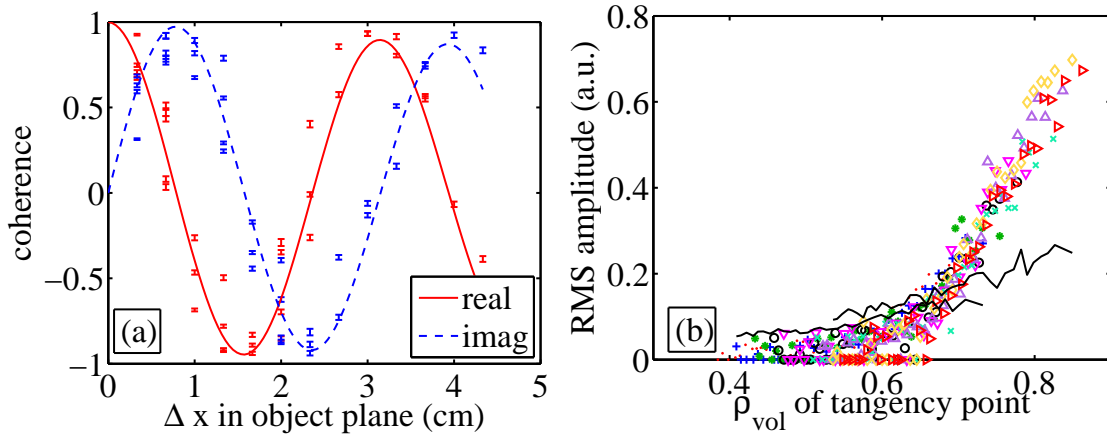


Figure 4.5: (a) Real and imaginary parts of the measured complex coherence of the TPCI signals at the frequency of the axisymmetric mode (26.4 kHz) for TCV discharge 45353, $0.32 < t < 0.4$ s. Frequency smoothing interval 500 Hz. The curves are a sinusoidal fit (equation 4.7) with parameters $K = 1.99 \text{ cm}^{-1}$, $l_c = 28.4 \text{ cm}$. (b) Coloured markers represent the RMS amplitude of the $n = 0$ mode in the TPCI signals (discharge 45353, $0.32 < t < 1.3$ s). Different marker symbols represent different detector elements. Continuous black lines are the RMS background level. These quantities are calculated with equation 4.8, using 25 ms integration time to get $P(f)$, $f_0 = 26.4 \text{ kHz}$, $\Delta f = 3 \text{ kHz}$ and $f_{\text{bg}} = 33.5 \text{ kHz}$.

4.4 Magnetic component and frequency of the geodesic acoustic mode

The GAM has a clear magnetic component, as is evident from figure 4.4*b*. Figure 4.6 shows the mode amplitude and phasing of all the magnetic probes of the high-field side upper toroidal array (cf. figure 3.1), for the same discharge discussed in §4.3. The Fourier series of the complex cross-power is dominated by $n = 0$, but also shows a minor $n = \pm 1$ component. The latter component is a standing wave in the laboratory frame, since it causes toroidal amplitude variation. Analysis of the poloidal mode structure is hampered by the fact that the signals of only 12 of the 38 probes of the poloidal array were available due to a malfunctioning ADC. Moreover, 8 of these 12 probes are below the mid-plane. This problem affects all discharges for which we have TPCI measurements so far.

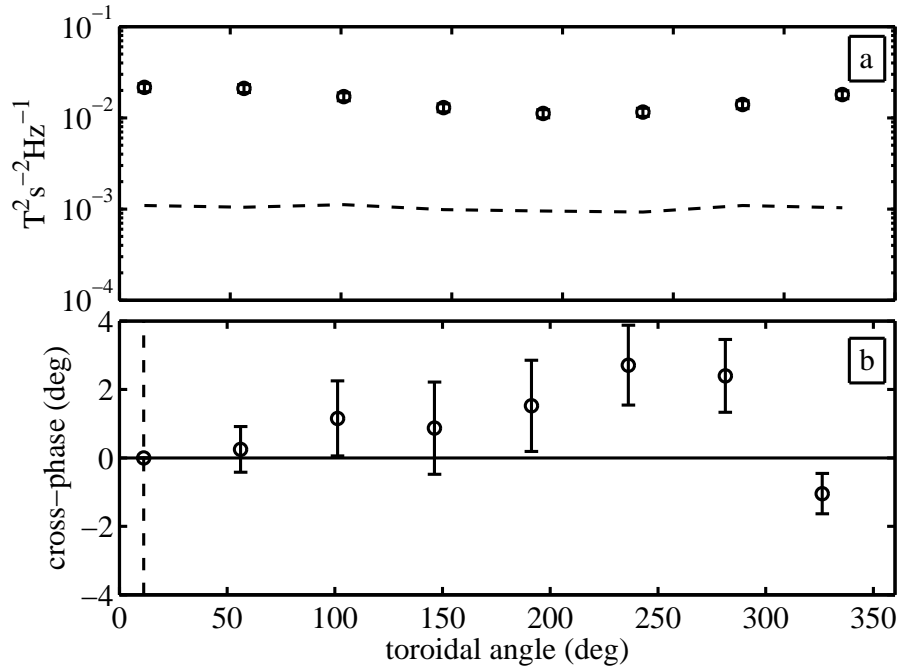


Figure 4.6: (a) Peak (circles) and background (dashed line) spectral power density around the frequency of the axisymmetric mode (27.8 kHz) in the high-field side upper toroidal magnetic probe array. (b) Cross phase between a reference probe (vertical dashed line) and all other probes in the array. Data from shot 45353; $1.0 < t < 1.2$ s; 2 ms integration time.

Nevertheless, the vertical scan of the plasma column during the discharge provides us with some poloidal resolution, since each probe effectively scans a range of poloidal angles θ in time. Figure 4.7 shows the mode power for all probes in the poloidal array (the background power has been subtracted). The poloidal angle is simply the geometrical angle between the magnetic axis and each probe in a poloidal section. Remarkably, the mode appears to have two antinodes for $\theta \simeq 140^\circ$ and $\theta \simeq -130^\circ$. The power level of the other probes of the poloidal array, including those on the low-field side wall, is too low ($< 1 \text{ T}^2 \text{s}^{-2}$) to be visible in figure 4.7. For the time window in which the $n = 0$ toroidal mode structure in figure 4.6 was measured, the $\theta \simeq 140^\circ$ antinode overlapped with the upper toroidal high-field side array in the TCV vessel.

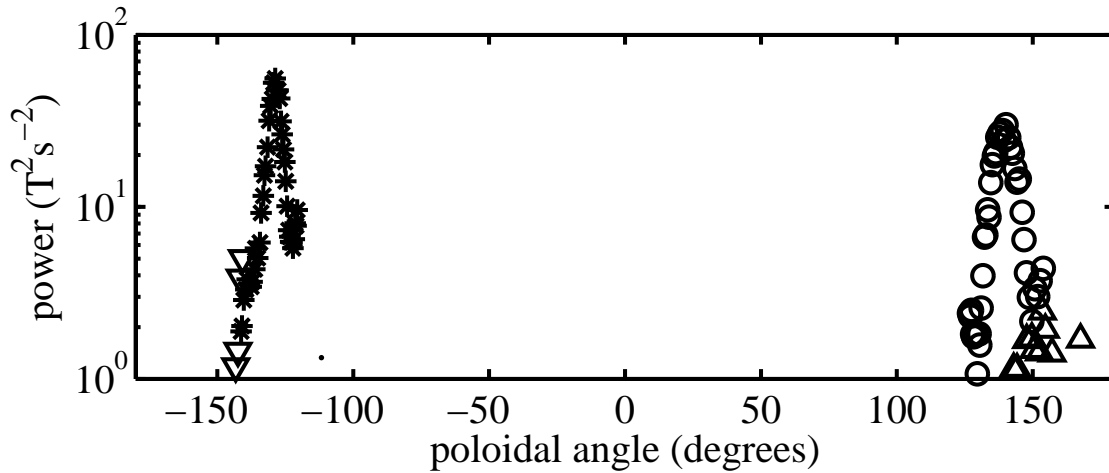


Figure 4.7: Mode power in band-pass filtered signals ($25 < f < 30$ kHz) from all magnetic probes in the TCV poloidal array. Background power is subtracted. Different marker symbols denote different magnetic probes. Data from discharge 45353 on $0.32 < t < 1.95$ s; 40 ms integration time.

The full width at half maximum of the spectral peak of the mode is typically 2 kHz, much larger than the spectral resolution of our sampling windows. The magnetic component of the mode is quite weak at the wall. Even when an antinode coincides with a magnetic probe, the peak-to-background ratio in the magnetic power spectrum is never much higher than 10 dB. Figure 4.7 shows that the strongest antinode (at $\simeq -130^\circ$) produces a vertical oscillating magnetic field with RMS amplitude 5×10^{-5} T at the inner wall of TCV, corresponding to $|\dot{B}|/B \simeq 3 \times 10^{-5}$.

We have inspected the magnetic spectra of all TCV discharges in the database with similar plasma shape as the one previously discussed, and for which the entire poloidal array had been acquired. For most of the investigated discharges a mode is seen (frequency between 20 kHz and 35 kHz) whose amplitude shows conspicuous peaks for $\theta \simeq \pm 130^\circ$; we take this as the signature trait of the GAM. Minima in amplitude (nodes) are observed for $\theta = 180^\circ$, $\pm 90^\circ$ and sometimes for 0° , but the standing wave ratio varies between discharges (compare figures 4.8a and 4.9a). Especially figures 4.8a,c are very suggestive of a poloidal standing wave with $m = 2$.

For nearly all investigated discharges the vertical position of the plasma is constant in time and the toroidal probe arrays lying in the equatorial plane of the plasma ($\theta = 0^\circ$ and 180°) are selected for acquisition. This is also the case for the spectra in figures 4.8 and 4.9. Since these poloidal angles correspond to (partial) nodes, the mode-to-background ratio is typically low in the toroidal arrays. Surprisingly, the Fourier series of the complex cross-power at the mode frequency is not dominated by $n = 0$ in the equatorial plane. Rather, the mode structure at this location is a standing wave with $n = \pm 1$. This may be seen from the nodes in figures 4.8b and 4.9b, and the phasing in figures 4.8d and 4.9d. This structure is seen on both the high-field side and low-field side toroidal arrays. We recall that for the discharge of figure 4.6, which shows zero toroidal phasing, one of the *antinodes* overlapped with the toroidal array.

One of the ways in which the GAM can be identified as such in an experiment, is by its signature frequency scaling. For a large aspect ratio plasma with circular poloidal

4.4. Magnetic component and frequency of the geodesic acoustic mode

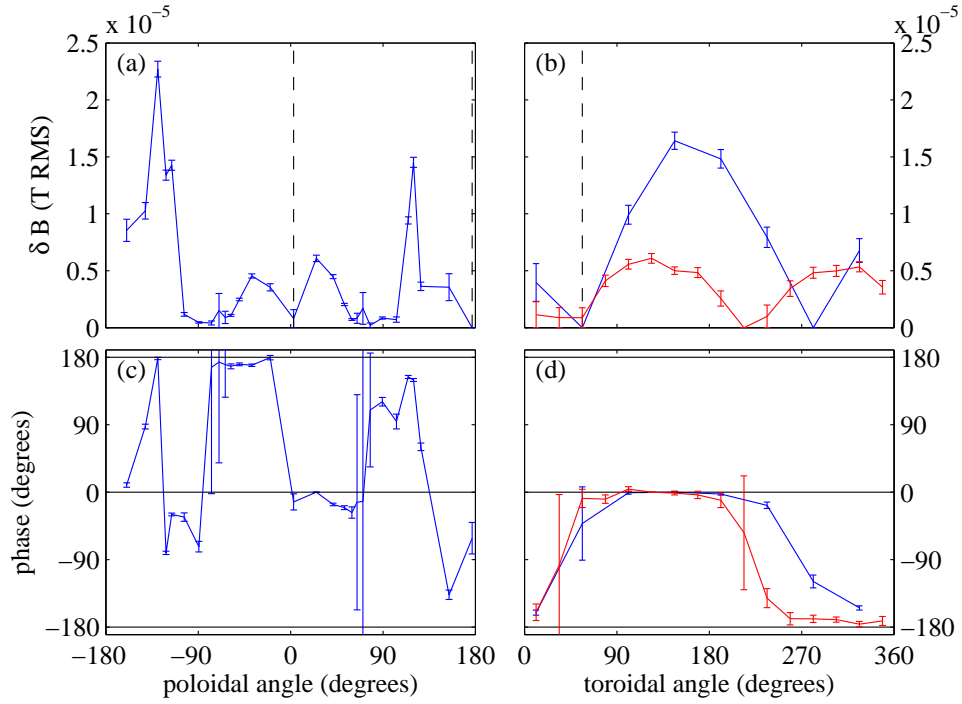


Figure 4.8: Magnetic structure of the GAM in discharge 41808 ($1.1 < t < 1.3$ s).

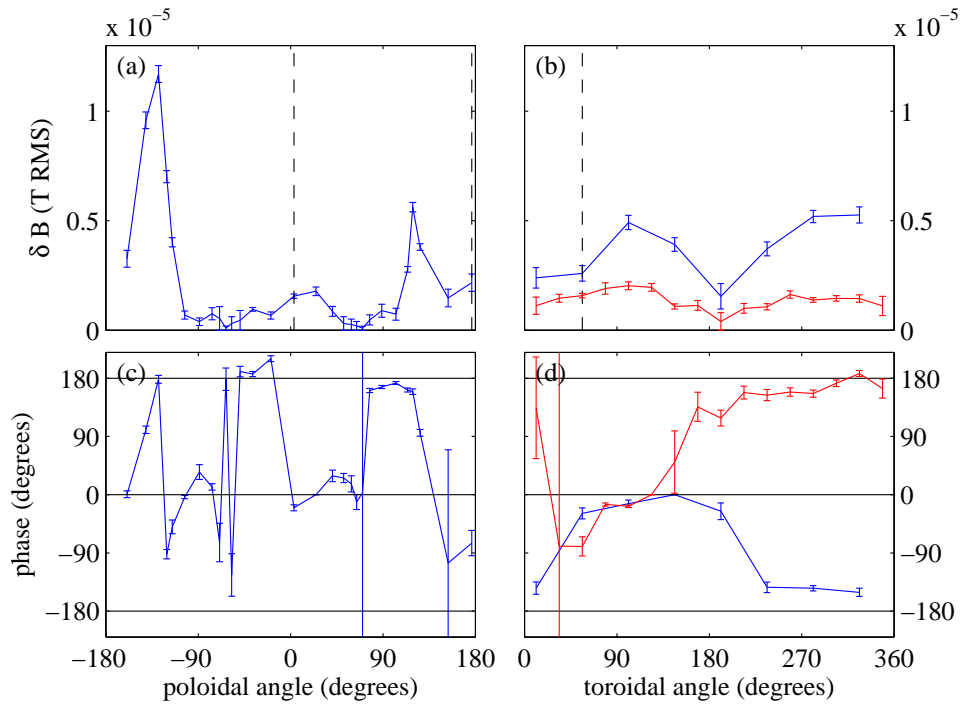


Figure 4.9: Magnetic structure of the GAM in discharge 41765 ($0.6 < t < 0.8$ s).

cross section, the mode frequency is

$$f_{\text{GAM}} = \sqrt{2}c_s/(2\pi R), \quad (4.9)$$

where $c_s = ([T_e + \gamma_i T_i]/m_D)^{1/2}$ is the ion sound speed. For shaped plasmas the frequency is modified by a factor of order unity (cf. section 4.2). To test the hypothesis that the axisymmetric mode is a GAM we have studied the correlation between its frequency and the plasma temperature, while keeping shape and safety factor constant. Because of the limited number of discharges (three) for which TPCI measurements of the mode are available, the magnetic rather than the density component of the mode is used to determine the frequency. A list was made of all limited TCV discharges with $0.4 < \delta < 0.5$, $1.4 < \kappa < 1.5$ and $3.9 < q_a < 5.7$ during the current flat-top phase. Here, κ denotes the plasma elongation and q_a the safety factor at the last closed flux surface. To avoid ambiguity due to aliasing, we imposed the additional criterion that the sampling rate of the magnetic probes should be ≥ 125 kHz. As of September 2012 these criteria are satisfied by around 140 discharges.

We inspected the magnetic spectra of each one of these discharges for the presence of antinodes at $\theta \simeq \pm 130^\circ$ and a node for 180° ; we further imposed that the peak-to-background ratio for the antinodes should be at least 3 dB, using a sampling window longer than 1 ms (the full width at half maximum of the spectral peak associated with this mode is invariably greater than 2 kHz). The majority (some 120 out of the 140) show a mode with the signature just given. Recurrent observations are that the mode frequency and amplitude increase when X2 power is applied and decrease when it is cut.

Electron temperature measurements (Thomson scattering) are available for every discharge of our set, but ion temperature measurements (CXRS) are not. Figure 4.10*b* shows the measured mode frequency as a function of $c_s/(2\pi R)$ only for discharges for which T_i from CXRS was available. Both T_e and T_i are taken at $\rho_\Psi = 0.9$ for all discharges, which corresponds to $\rho_{\text{vol}} \simeq 0.83$ in the investigated geometry. Figure 4.10*a* only shows points for which CXRS was not available; a fixed $T_i/T_e = 0.46$ ratio is assumed here, which is the average of the points in figure 4.10*b*. An adiabatic index $\gamma_i = 1$ is used for the ions. Note that the factor $\sqrt{2}$ of equation 4.9 had to be omitted to get better agreement with the absolute value of the observed frequency.

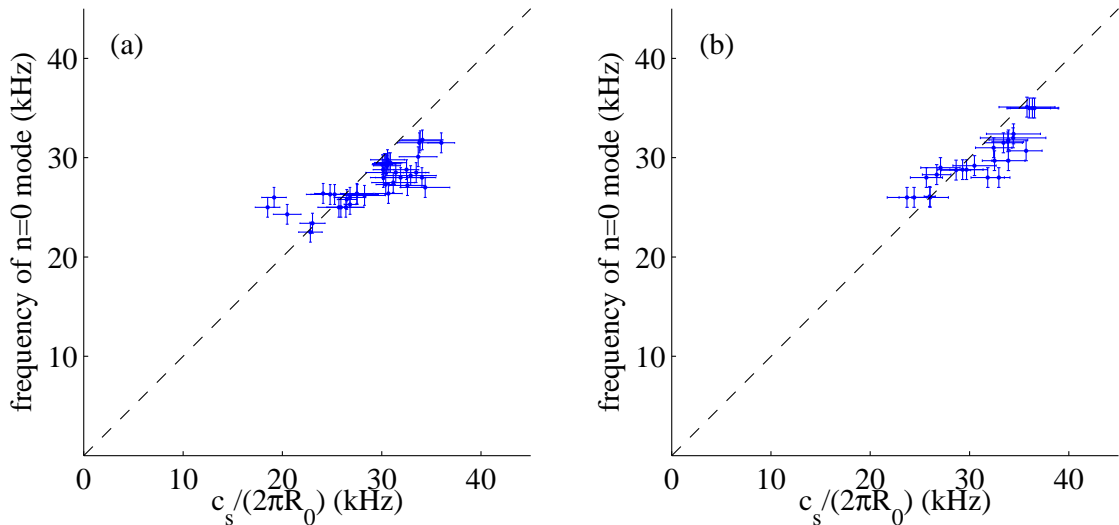


Figure 4.10: Frequency scaling of the GAM. The sound speed c_s in (a) is calculated using a fixed T_i/T_e ratio; in (b) measured values for both T_e and T_i are used (see text).

4.5 Numerical simulation of the geodesic acoustic mode in TCV

The geodesic acoustic mode is commonly observed in gyro-kinetic simulations of tokamak turbulence (Angelino et al. 2006). At the CRPP, global simulations are performed using the ORB5 code (Jolliet et al. 2007; Vernay et al. 2010). The code solves the non-linear, electrostatic gyrokinetic equations (including zonal flows) for an arbitrary axisymmetric MHD equilibrium, using a particle-in-cell δf scheme. Numerical noise, which is the principal drawback of the PIC scheme, is kept at an acceptable level through various techniques. An ORB5 simulation has been performed (Vernay 2012), using the MHD equilibrium of TCV discharge 45353 50 ms before the start of the X2 heating phase (§4.3). For the electron temperature and density profiles we used a spline fit of experimental profiles measured with Thomson scattering. In the absence of charge-exchange measurements, a fixed ratio $T_e/T_i = 3.75$ was assumed; this is a typical value for this type of discharge. The dynamic response of trapped electrons to electrostatic perturbations was calculated using a realistic kinetic model, since an initial simulation employing a simple Boltzmann response yielded only marginal instability.

The evolution of the plasma fluctuations was simulated for an interval of 1.29 ms. To keep the background equilibrium stationary, numerical heat and particle sources are employed. For each time-step, the $m = n = 0$ component of the radial electric field is stored, as well as the shearing rate, which is proportional to the radial derivative of E_r . Steady state is achieved roughly 0.4 ms after the start of the simulation. Figure 4.11 shows $\omega_{E \times B}$ as a function of time and radius (ρ_{vol}). The GAM is evident in the form of diagonal striations for $0.65 \lesssim \rho_{vol} \lesssim 0.85$, which indicate radially outward propagation. The mode is superimposed on non-oscillating zonal flows, with radial wavelength of roughly half the minor radius.

Figure 4.12a shows the simulated trace for $\rho_{vol} = 0.76$, indicating a peak-to-peak

amplitude of 8 km/s. This may be compared to a peak-to-peak amplitude of $\simeq 25$ km/s for the time-averaged $v_{E \times B}$, which executes a single cycle in the range $0.4 \lesssim \rho_{\text{vol}} \lesssim 1$. Figure 4.12*b* shows that the autocorrelation time of the GAM is 0.2 ms in the simulation, while the TPCI measurement gives a value 0.4 ms.

Figure 4.13*a* shows the auto-power spectrum of $v_{E \times B}$ as a function of radius, using only data for $t > 0.4$ ms. For $0.65 \lesssim \rho_{\text{vol}} \lesssim 0.85$ the spectra peak around 33 kHz. Both simulation and measurement show that the peak frequency is fixed for the entire range where the GAM is visible, even though T_e drops from 500 eV to 200 eV. On the basis of the frequency of the radially localised GAM, $f_{\text{GAM}} \simeq c_s/(2\pi R)$, one might have expected a 40% decrease in frequency, as would be predicted by a local simulation. The measurement therefore crucially reveals the role played by global effects, correctly predicted by the global simulation. There is, however, a 30% discrepancy in the absolute value of the global frequency, which is not yet resolved. A possible explanation of the discrepancy could be the omission of impurity ions in the simulation, which leads to an overestimate of the GAM frequency (Guo et al. 2010; Leerink et al. 2012).

Two weaker modes, with spectral power >9 dB below the dominant one, are also evident at 40 kHz and 45 kHz. These modes are centred at slightly more inward radii, but there is some radial overlap: for $\rho_{\text{vol}} \simeq 0.68$ the 32 kHz and 40 kHz peaks have similar amplitude, leading to the interference pattern in figure 4.11. We have thus far not observed multiple simultaneous peaks in the TPCI spectra, but the phenomenon has been observed in Asdex-upgrade (Conway et al. 2008). The dashed line indicates $f_{\text{GAM}} = \sqrt{2}c_s/(2\pi R)$, calculated using the equilibrium temperature profiles, showing that the three simulated modes have frequencies which correspond to within 10% to the theoretical GAM frequency for a circular poloidal section.

Figure 4.13*b* shows the rms of $v_{E \times B}$ as a function of radius, revealing a ten-fold increase in amplitude in the interval $0.62 < \rho_{\text{vol}} < 0.77$ followed by a drop to zero for $\rho_{\text{vol}} = 0.88$. The radial increase in amplitude agrees remarkably well with the TPCI measurements (figure 4.5*b*). However, in the experiment the increase in amplitude continues right up to $\rho_{\text{vol}} \simeq 0.86$, which is the outermost radius that was covered in our measurements. It must be noted though that the equilibrium density gradient that was used in the simulation was manually flattened somewhat for $\rho_{\text{vol}} > 0.9$ in order to avoid numerical instability. Since the details of the radial localisation of the GAM depend on the turbulence that drives it (Zonca et al. 2008), a more realistic profile may lead to a radially outward shift of the GAM. Since the temperature decreases with radius, this might also lead to a lower GAM frequency, more in line with the experimentally observed value. Finally, Landau damping is also weaker at the edge, so the autocorrelation time might also increase (X. Q. Xu et al. 2008).

Figure 4.14*a* shows a snapshot of the simulated flow speed versus radius. However, the radial structure of the GAM is best investigated statistically, using the complex coherence function around the peak frequency of 32 kHz (figure 4.14*b*). We conclude that the simulated GAM is fully coherent and propagates radially outwards over the entire radial interval where it has appreciable amplitude (figure 4.13*b*), in line with the experimental observation. A striking observation from figure 4.14*b* is the sharp decrease in radial wavelength for $\rho_{\text{vol}} > 0.77$, where the mode amplitude drops to zero. This effect is also evident from the curved shape of the striations in figure 4.11. The range of wavelengths that can be clearly determined from figure 4.14*b* is $0.057 \lesssim \Delta\rho_{\text{vol}} \lesssim 0.13$, which corresponds to

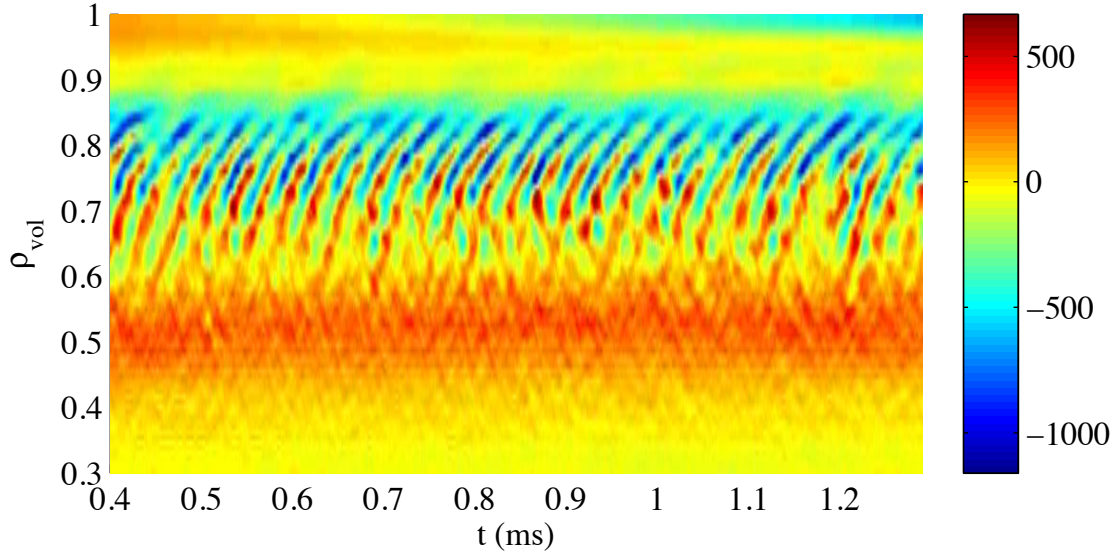


Figure 4.11: Simulated shearing rate (krad/s). The GAM is evident in the diagonal striations. The region $\rho_{\text{vol}} < 0.3$ is featureless.

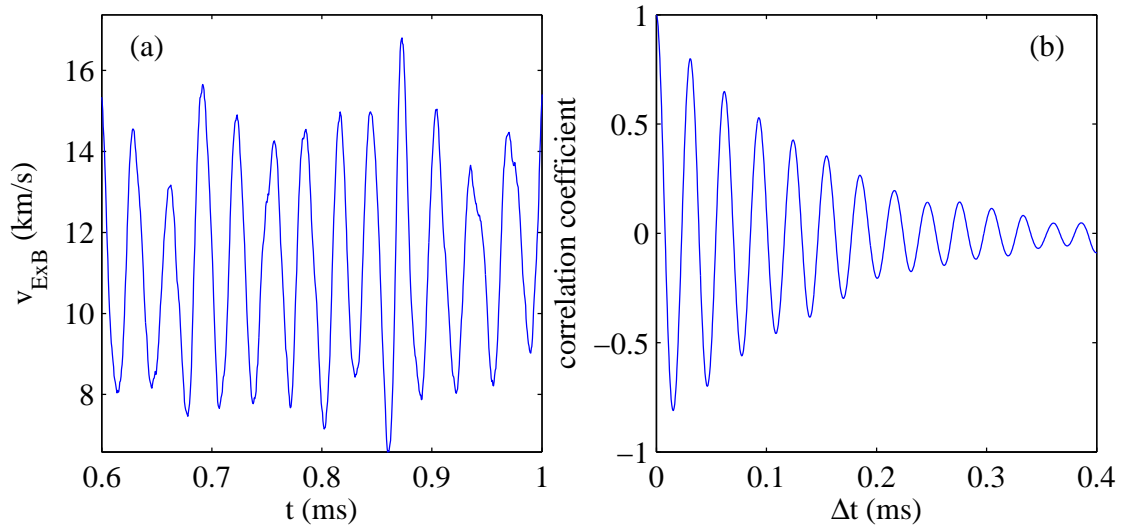


Figure 4.12: Simulated $E \times B$ poloidal flow velocity at $\rho_{\text{vol}} = 0.76$ (a) and its autocorrelation function (b). The $1/e$ correlation time is 0.2 ms.

$1.1 \lesssim \Delta R \lesssim 2.7$ cm in the TCV mid-plane. By contrast, the measured radial wavelength, projected on the mid-plane, is 2.2 cm, independently of radius. Possibly the decrease in wavelength occurs only beyond the radius of peak amplitude, which we have not yet located with the TPCI measurements. We have also inspected the complex coherence for the mode around 40 kHz in the simulation (figure 4.13*a*); its radial mode structure is found to comprise components propagating in both radial directions.

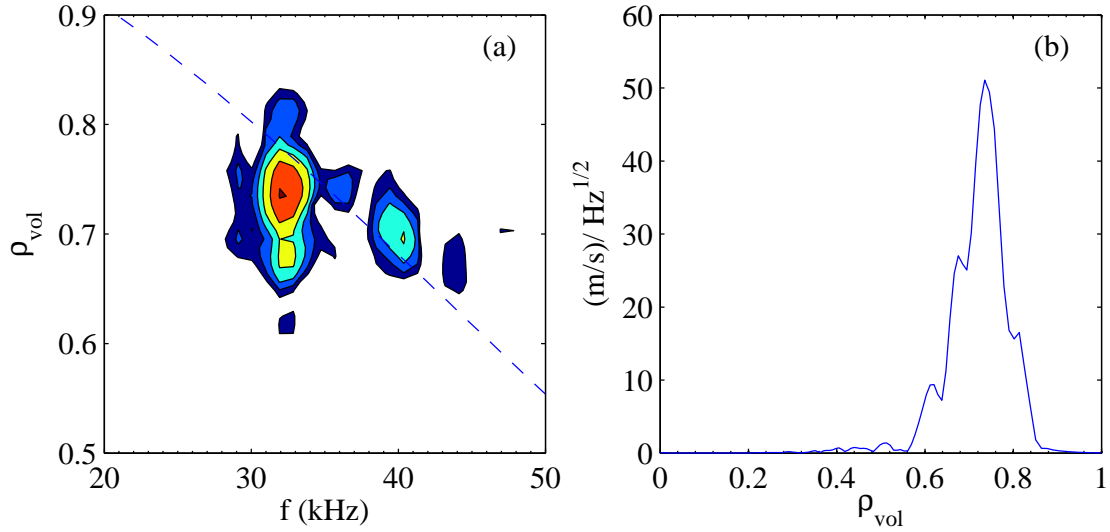


Figure 4.13: (a): Contours of spectral power density of simulated $v_{E \times B}$ (dB scale, step size 3 dB). Integration time: 0.89 ms; no spectral smoothing; Hamming window. The dashed line indicates $\sqrt{2}c_s/(2\pi R)$, calculated using the equilibrium temperature profiles. (b): Square root of a section of (a) for $f = 32$ kHz.

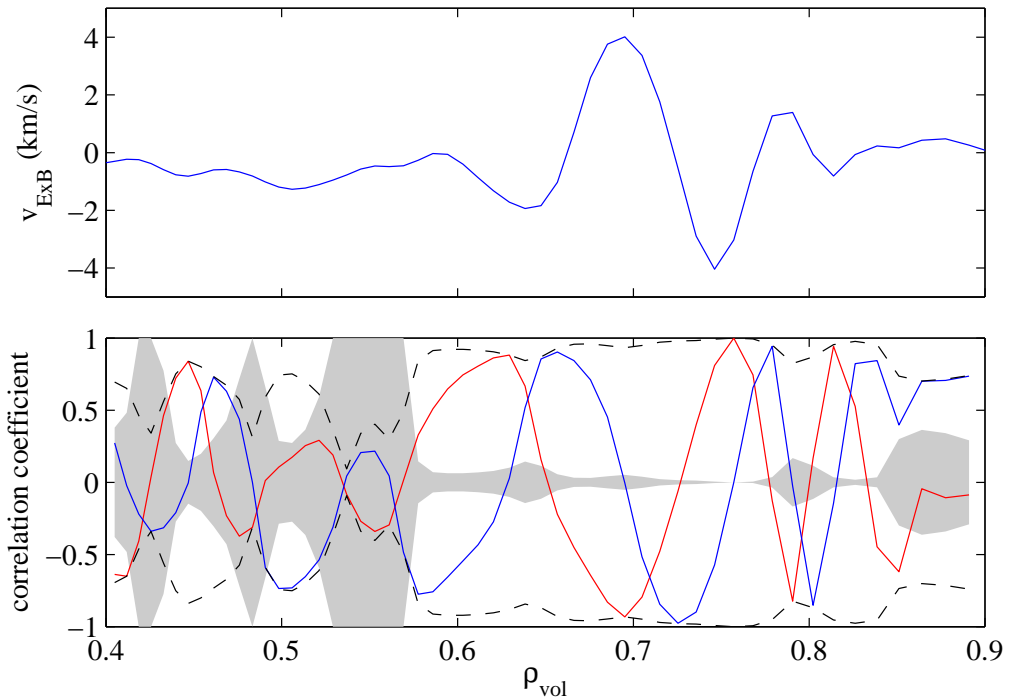


Figure 4.14: (a): Snapshot of simulated $v_{E \times B}$ for a fixed time; the zero frequency component is filtered out. (b): Complex coherence of the simulated $v_{E \times B}$ around the peak frequency of the GAM (32 kHz). Reference position is $\rho_{vol} = 0.76$. Integration time: 0.22 ms; averaging over 4 independent intervals. Red, blue and dashed curves are the real and imaginary parts and the envelope; the shaded region is the confidence interval. The mode propagates radially outward.

4.6 Numerical modelling of the TPCI signals

In section 4.3 we presented an analysis of the TPCI measurements of an axisymmetric mode, which we argue to be the GAM. The complex coherence $R_{\mathcal{E}}(x)$ at the mode frequency clearly shows a propagating wave with coherence length much longer than one wavelength (figure 4.5a). We wish to find a coherence function $R_n(\rho_{\text{vol}}, \theta, \phi)$ of the perturbed electron density in terms of plasma coordinates that is compatible with this $R_{\mathcal{E}}$. For a given R_n , the perturbed phase in the object plane R_{φ} can be obtained from equation 2.60. Unfortunately, since the apparent wavenumber of the mode ($k = 2.0 \text{ cm}^{-1}$ in $R_{\mathcal{E}}$) is smaller than the cutoff of the optical transfer function ($k_c = 2.59 \text{ cm}^{-1}$), the image is subject to significant spectral broadening (§3.4). Therefore, the apparent wavenumber may be larger than that of the projection of the underlying density fluctuation.

Here, we shall simply assume that this effect can be neglected. That is, we look for a correlation function of the perturbed electron density R_n that gives a phase perturbation $R_{\varphi}(x)$ with $k = 2.0 \text{ cm}^{-1}$. There is of course no unique solution even to this problem, since information is lost in the line-integration and the one-dimensional sampling of a two-dimensional image. Therefore, the problem involves subjective judgement on what constitutes a reasonable perturbation spectrum.

In the following we consider correlation functions of the form

$$R_n(\rho_1, \rho_2, \theta_1, \theta_2) = \sigma_n(\rho_1, \theta_1)\sigma_n(\rho_2, \theta_2) \exp(-|\Delta\rho|/l_r + ik_r\Delta\rho - |\Delta\theta|/l_{\theta} + im\Delta\theta), \quad (4.10)$$

where $\Delta\rho = \rho_2 - \rho_1$ and $\Delta\theta = \theta_2 - \theta_1$. Note that this function is axisymmetric and non-stationary (through σ_n). Our choice of test functions R_n is guided by the diagrams in figure 4.15, which show poloidal projections of the TPCI laser beam, the last closed flux surface and the tangency surface for discharge 45353. The dashed lines indicate the direction of wave vectors \mathbf{k} satisfying the selection rule, i.e. $\mathbf{k} \parallel \mathbf{k}_0 \times \mathbf{B}$. Figure 4.15a corresponds to the time when the amplitude of the GAM peaks in the TPCI signals; for figure 4.15b the amplitude has dropped to zero for all chords.

The simplest solution to the problem is an outward propagating, purely radial wave. It has a wavelength of a few cm and is radially localised in the outer part of the plasma. Such a wave contributes to the phase shift around the tangency surface. As the plasma moves up, the tangency surface for all chords moves radially in. The wave is weaker there, so the amplitude of the signals drops. Neglecting for the moment the radial amplitude dependence, the correlation function of such a wave can be expressed as

$$R_n(\Delta\rho) = \sigma_n^2 \exp(-|\Delta\rho|/l_n + ik_n\Delta\rho). \quad (4.11)$$

Using this R_n we have evaluated R_{φ} (equation 2.60) for various combinations of k_n and l_n , using the geometry of shot 45353 around $t=0.35\text{s}$, each time fitting R_{φ} with the function

$$R_{\varphi}^{\text{fit}}(x) = \sigma_{\varphi}^2(1 - c) \exp(-|x|/l_{\varphi} + ik_{\varphi}x) + c. \quad (4.12)$$

The real constant c accounts for the residual coherence between chords when l_{φ} becomes very small. Such coherence comes from the fact that in equation 4.11 the density perturbation is perfectly coherent on an entire flux surface. Therefore, chords that intersect the same flux surface are to some extent correlated, even if the the points of intersection are spatially far apart. Since the TPCI transfer function acts as a high-pass filter this offset

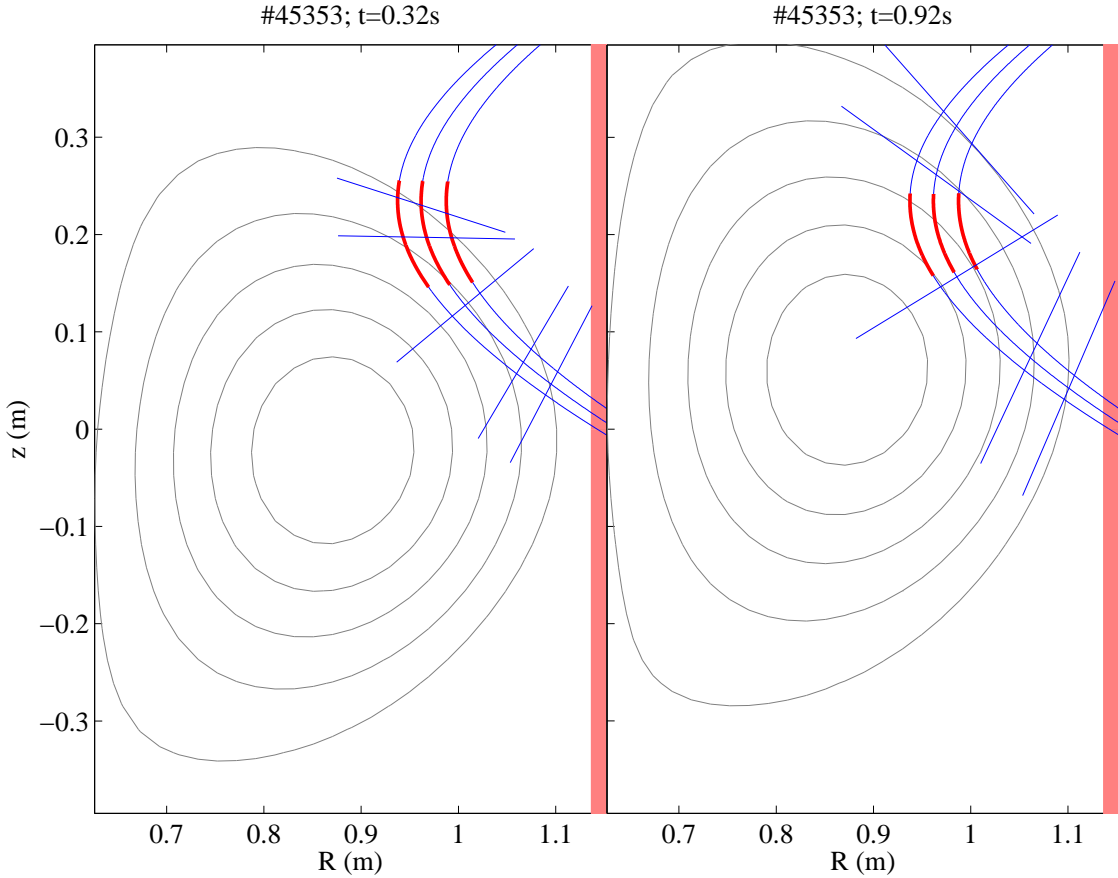


Figure 4.15: Detection geometry for discharge 45353. The three curves are the two extreme chords and the centre chord. The lines roughly perpendicular to the chords indicate the direction of wave vectors satisfying the selection rule along different positions along the centre chord. The part of the chords marked in red indicates the portion that would be selected by a horizontally oriented spatial filter with a 30° half-angle (note that for discharge 45353 no spatial filtering was applied). At $t = 0.32$ s the $n = 0$ mode is visible in all channels; for $t = 0.92$ s it has disappeared from all channels.

is invisible in the image. Figure 4.16 shows the fit parameters k_φ , l_φ and c (function 4.12) for a scan of k_n and l_n ; the values that we wish to reproduce are indicated by the dashed lines.

Under the various assumptions above (in particular the assumption that the axisymmetric mode is purely radial) we conclude the following from figure 4.16. First, $k_n = 58 \pm 5\%$, i.e. the mode has a radial wavelength of $0.108 \pm 5\%$ in terms of ρ_{vol} . Second, its radial correlation length, also in terms of ρ_{vol} , is $l_n > 0.7$, i.e. more than six wavelengths. As argued in the following, the radial extent of the mode is only a few wavelengths, much less than the obtained value for l_n . The main conclusion we draw from the analysis is that, at least for a radial mode, the effects of line integration in the TCV geometry do not lead to a long correlation length of the phase shift when the correlation length of the density perturbation is short.

In addition to reproducing the observed instantaneous complex coherence function of

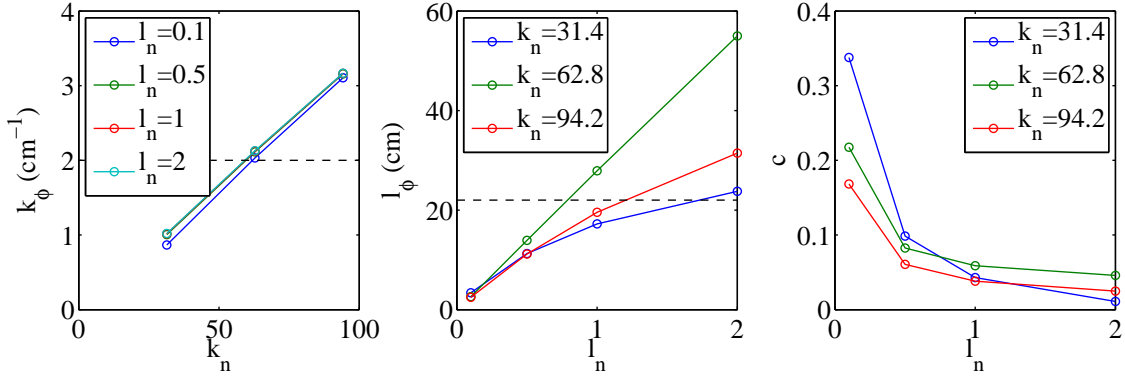


Figure 4.16: Calculated (horizontal) wave number k_ϕ , correlation length l_ϕ and ‘residual’ coherence c (equation 4.12) of the phase shift for various test correlation functions R_n of the density perturbation. The geometry of discharge 45353 around $t = 0.35$ s was used for the calculation. The experimentally observed values are indicated by dashed lines.

the TPCI image (figure 4.5a), R_n must also be consistent with the observed decay of the signal power when the plasma is moved up (figure 4.5b). For the present case of a purely radial mode, this decay can be easily accounted for by introducing a radial dependence in the mode amplitude:

$$R_n(\rho_1, \rho_2) = \sigma_n(\rho_1)\sigma_n(\rho_2) \exp(ik\Delta\rho), \quad (4.13)$$

where

$$\sigma_n(\rho) = \exp(-(\rho - \rho_0)^2/w^2). \quad (4.14)$$

The choice for a Gaussian radial dependence is for convenience and not motivated by physics considerations. We find that choosing $\rho_0 = 0.83$ and $w = 0.14$ in equation 4.14 leads to satisfactory agreement with the observation, as shown in figure 4.17. However, we note once more that the experimental RMS level of each of detector element was scaled to lie on a single curve.

We also did the calculation with an added $\sin(\theta)$ dependence in σ_n (equation 4.13) to model the $m = 1$ standing wave structure of the density component of a geodesic acoustic mode. Apart from reducing the RMS phase shift by a factor $\simeq \sin(60^\circ)$ this does not change the curve of figure 4.17 appreciably, since θ of the detection volume changes only by a few degrees during the vertical scan of the plasma column (figure 4.15). In fact, one can add a poloidal wave number component $\exp(im\theta)$ for $|m|$ up to 10 without strongly changing figure 4.17.

Now we consider the case of a purely poloidal wave propagating in the ion diamagnetic drift direction. This wave contributes to the phase shift close to the last closed flux surface, for $\theta \approx 70^\circ$ around $t = 0.32$ s (figure 4.15). Referring to equation 4.10 we choose $m = -45$; $k_r = 0$; $l_\theta = l_r = \infty$. These parameters reproduce the observed phasing of the TPCI image of the axisymmetric mode for discharge 45353 around $t=0.35$ s (figure 4.5). We have tried various radial and poloidal dependences of σ_n with the goal of reproducing the experimentally observed decay in RMS signal amplitude as the plasma is moved up. This proved impossible to achieve for all the chords simultaneously, suggesting that the axisymmetric mode cannot have a purely poloidal wave vector.

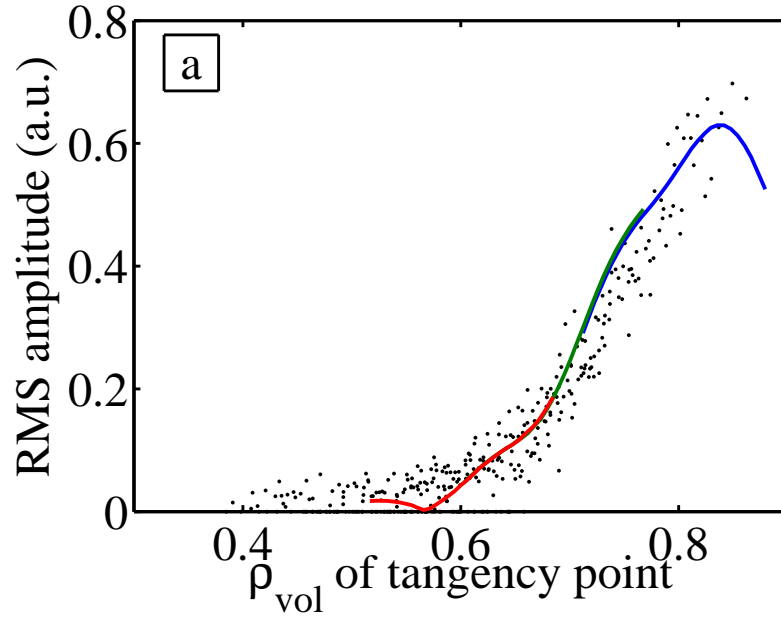


Figure 4.17: Comparison between experimental (black dots, cf. figure 4.5*b*) and synthetic signal amplitudes due to the $n = 0$ mode for a model correlation functions R_n given by equations 4.13 and 4.14. Coloured lines represent snapshots of RMS phase shift for entire chord set on three times during the vertical scan of the plasma: {red, blue, green} corresponds to $t = \{0.3; 0.525; 0.775\}$ s.

In conclusion, the most probable small-scale mode structure of the density component axisymmetric mode is an outward propagating radial wave with wavelength $0.108 \pm 5\%$ in terms of ρ_{vol} (correlation function 4.13). Around the tangency point of the TPCI detection chords, where such a mode contributes most to the phase shift, this wavelength corresponds to $\simeq 3.2$ cm. Within the (spatial) spectral resolution of the TPCI measurement the mode appears to be fully coherent. For $\rho_{\text{vol}} < 0.65$ the mode is undetectable in our measurements. For larger radii its amplitude increases steadily, at least up to $\rho_{\text{vol}} \simeq 0.86$.

Chapter 5

Turbulence and beam-ion driven modes in the TEXTOR tokamak

In this chapter we document observations on the evolution of coherent and turbulent fluctuations in density and magnetic field during the ELM cycle in the TEXTOR tokamak (Finken et al. 2007; Unterberg et al. 2009; Soldatov, Krämer-Flecken, Kantor, et al. 2010), mainly by exploiting the multi-channel correlation reflectometer (Krämer-Flecken, Soldatov, Vowinkel, et al. 2010). We expand on a previous study (Soldatov, Krämer-Flecken, Kantor, et al. 2010) by discussing two newly found ELM precursors on TEXTOR. We have also carried out a more accurate analysis of the prominent ELM precursor mode mentioned in Soldatov, Krämer-Flecken, Kantor, et al. 2010 and show that it is in fact a so-called ‘fishbone’ mode (Kass, Bosch, et al. 1998; Matsunaga, Aiba, et al. 2010). Previously unobserved bursts of beam-ion driven Alfvén modes accompany the fishbone, and are shown to interact with it non-linearly. The fishbone and the Alfvén modes are modes of the plasma core and are clearly not directly related to the edge transport barrier. Nevertheless, these modes are seen to trigger ELMs in TEXTOR H-mode. Remarkably, we find that in L-mode, too, the fishbone triggers spikes in recycling rate, sharing many characteristics with the ELMs. A condensed version of the material in this chapter has been published (Meijere et al. 2012).

The chapter is organised as follows. Section 5.1 starts with an introduction to fluctuation reflectometry, with special emphasis on the difficulties of quantitative interpretation of reflectometer correlation measurements. Because the coherent modes and turbulent fluctuations that are the subject of this chapter are highly non-stationary, we employ averaging over conditionally constructed ensembles for spectral analysis. Section 5.1 closes with a discussion of some statistical properties of the resulting estimates. The experimental setup is described in section 5.2: after a description of the limiter H-mode scenario on TEXTOR, we discuss the quality of the experimental reflectometer signals at considerable length. Our experimental observations are presented in section 5.3 and discussed in section 5.4.

5.1 Experimental technique

5.1.1 Fluctuation reflectometry

In the terminology of laboratory plasma physics a reflectometer is an instrument that launches a microwave beam into a plasma and detects the waves that are reflected off a cutoff. Reflectometers are used to measure density profiles and density fluctuations. The appealing aspects of the technique are the modest plasma access requirements, the simplicity and robustness of the hardware and its sensitivity to a wide range of fluctuations. On the other hand, quantitative interpretation of reflectometer signals is often prohibitively difficult. In this section we present the principles and limitations of reflectometry measurements, focussing in particular on the poloidal correlation setup used in TEXTOR. For a more complete review of the subject we refer to Mazzucato 1998a.

To start our discussion it is instructive to consider the case of a one-dimensional slab geometry, with vacuum for $x < 0$ and a plasma with steadily increasing density for $x > 0$. A plane wave with frequency ω and O-mode polarisation is launched from the vacuum in the positive x direction.. In the plasma the wave sees an index of refraction

$$N(x) = \left(1 - \frac{\omega_p^2(x)}{\omega^2}\right)^{1/2}, \quad (5.1)$$

where, as before, $\omega_p^2 = n_e e^2 / (\epsilon_0 m_e)$ is the plasma frequency (equation 2.10). We wish to know the phase delay ϕ of the reflected wave with respect to the incident wave. Since we are only interested in the contribution of the plasma, we perform our phase measurement at $x = 0$. Strictly speaking, the WKB approximation cannot be used to obtain ϕ , since k goes to zero at the cutoff at x_c . However, if the electron density profile is more or less linear in a layer with a width of the order of a few vacuum wavelengths around the cutoff, the solution near the cutoff can be expressed in terms of the Airy function (Ginzburg 1964). At a safe distance from the cutoff this function is then matched to incoming and reflected WKB waves, with the result that

$$\phi = \frac{2\omega}{c} \int_0^{x_c} N(x) dx - \frac{\pi}{2}. \quad (5.2)$$

Remarkably, the first term on the right-hand side of equation 5.2 is exactly the result one would obtain from applying the WKB solution right up to the cutoff.

Heterodyne detection schemes are preferable over homodyne schemes because of their superior sensitivity (Hartfuss et al. 1997). The accuracy of phase measurements is greatly improved by employing quadrature detection. Denoting the in-phase and quadrature signals by $I(t)$ and $Q(t)$, respectively, the ‘complex reflectometer signal’ is defined by $z(t) = I(t) + iQ(t)$; the phase and amplitude signals are then given by $\arg[z(t)]$ and $|z(t)|$, respectively. In the context of fluctuation measurements it is useful to represent the complex signal as the sum of a mean and a fluctuating phasor, i.e.

$$\tilde{z}(t) = \langle \tilde{z} \rangle + \delta \tilde{z}(t), \quad (5.3)$$

as depicted in figure 5.1.

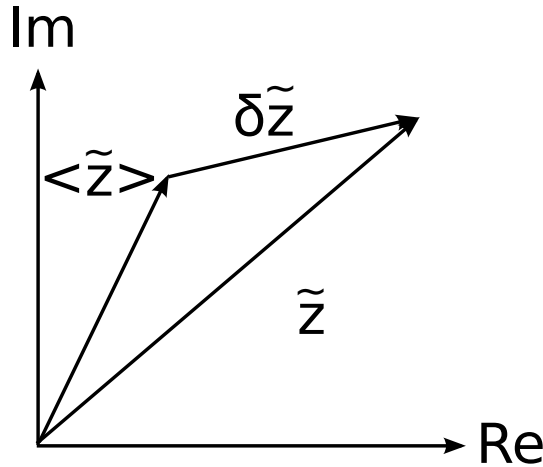


Figure 5.1: Phasor representation of a complex reflectometer signal.

Thanks to equation 5.2 reflectometers can be used to measure the electron density profile by sweeping the frequency of the probing wave and recording the phase. The quantity of interest is then the group delay $d\phi/d\omega$, from which the density profile can be obtained through an appropriate inversion (Mazzucato 1998a). Density profile measurements are certainly the most mature application of reflectometry (Sabot et al. 2006). However, the technique also has a long history in the study of density *fluctuations*. In fluctuation setups the plasma is usually probed with one or more microwave beams with fixed or stepped frequency. It is important that phase and amplitude fluctuations are detected separately, since they have different physical significance.

It was realised early in the history of fluctuation reflectometry that the complexity of the signal formation process makes it very hard or impossible to extract quantitative information on turbulent spectra from the signals (Mazzucato et al. 1993). In fact, even the inverse problem, i.e. to calculate the signals for a given turbulent spectrum, is not trivial. Part of the problem is that neither the first order Born approximation nor geometrical optics alone describes all the relevant wave physics in all situations of practical interest. The Born solution fails because the fluctuation amplitude is often too high, while geometrical optics fails because diffraction effects are often important. As a result, sophisticated analytical models (Gusakov et al. 2004) or full-wave simulations (Valeo et al. 2002) are needed to accurately model and interpret fluctuation reflectometry measurements.

In spite of these difficulties, fluctuation reflectometer setups of varying complexity are in use in several plasma experiments. For this thesis work measurements were performed with the TEXTOR fluctuation reflectometer (Krämer-Flecken, Soldatov, Vowinkel, et al. 2010), which features multiple antenna arrays viewing different parts of the torus (figures 5.2a-b). The operating principle of a single array are illustrated in figure 5.2c. Each array consists of a central emitter and several poloidally spaced receiver antennas. Geometrical optics suggests that the receiver antennas pick up rays that follow different trajectories in the plasma. From equation 5.2 we see that the phase signal detected by each receiver depends on a detection volume centred poloidally halfway between its symmetry axis and that of the emitter. Rigorous two-dimensional analysis in the linear

Born approximation shows that in general the effective radial extent of the detection volumes depends on the background density profile, the radial and poloidal wave number spectrum and amplitude distribution of the turbulence (Gusakov et al. 2006).

However, for the simple case of a radially extended poloidal mode of the form $\cos(m\theta - \Omega t)$, the poloidal mode number m can be determined through

$$m = 2\Delta\Psi(\Omega)/\Delta\theta. \quad (5.4)$$

Here, $\Delta\theta$ is the poloidal angle between the symmetry axes of the two receivers and $\Delta\Psi(\Omega)$ is the cross phase at the mode frequency between the corresponding complex reflectometer signals. Note that the cross-phase spectrum of complex signals $\tilde{z}_1(t)$ and $\tilde{z}_2(t)$ carries a spurious offset $\arg(\langle\tilde{z}_1\rangle\langle\tilde{z}_2^*\rangle)$ (e.g. figure 4 in Krämer-Flecken, Dreval, et al. 2004), which must be removed before application of equation 5.4. The considerations following equation 5.13 show that the cross-phase of the phase or amplitude signals can also be used for $\Delta\Psi$; being real quantities, these signals do not suffer from the problem of offsets in their cross-phase. In fact, we argue in subsection 5.2 that use of the complex signal should be avoided in some circumstances. Finally, we note that for shorter wavelength modes it is more appropriate to specify the poloidal wavenumber, k_x , related to m through $k_x = m/r_c$, with r_c the cutoff radius.

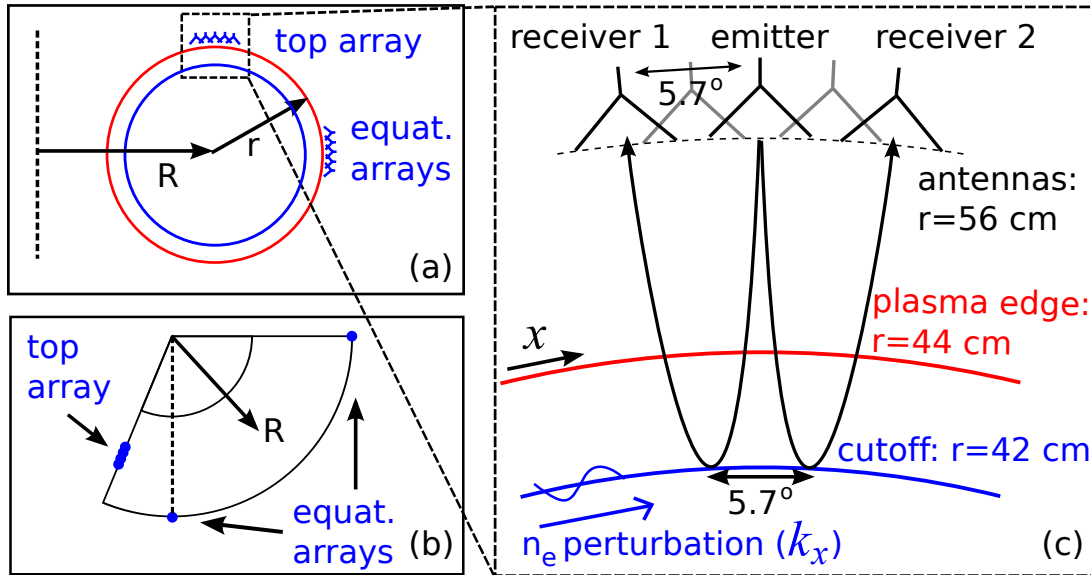


Figure 5.2: Schematic representation of the multi-antenna reflectometer, showing a poloidal (a) and a horizontal (b) projection of the TEXTOR tokamak. A magnified part of the poloidal projection is shown in (c), illustrating the principle of correlation measurements with a single array. The cutoff position corresponds to a typical H-mode density profile.

5.1.2 The random phase screen model

Non-linear effects in the signal formation process of the reflectometer lead to broadening of the spectra and suppression of coherence between antennas, which complicates the interpretation of the signals. Several experimentally observed non-linear effects can be

understood qualitatively in the framework of the random phase screen model (Nazikian et al. 1995), which we review in the following. We also discuss some explicit applications relevant for the analyses presented in this thesis. For a more recent and rigorous treatment of these effects we refer to Gusakov et al. 2002. The basis for the following analysis comes directly from Nazikian et al. 1995.

The key assumption in the phase grating model is that, for an observer outside the plasma, the effect on an incident wave of a perturbed plasma with a cutoff is the same as that of a corrugated mirror, placed certain distance beyond the cutoff. That is, the interaction in the plasma volume is replaced by a simple reflection followed by an instantaneous phase shift. The amplitude of the phase shift as a function of position is obtained from geometric optics considerations, but neglecting ray bending. In the simplest form of the model, curvature of the flux surfaces is neglected. Finally, the incident beam is taken to be a plane wave and the complex reflectometer signals are modelled as point measurements of the reflected wave field. In light of the qualitative nature of the present analysis we omit a discussion of the accuracy of these assumptions (Gusakov et al. 2002; Mazzucato 1998b).

Consider a mirror with normally distributed, random phase corrugations $\tilde{\psi}(x, t)$ with $\langle \tilde{\psi} \rangle = 0$; $\langle \tilde{\psi}^2 \rangle = \sigma_\psi^2$ and

$$\langle \tilde{\psi}(x, t) \tilde{\psi}(x + \xi, t + \tau) \rangle = \sigma_\psi^2 \gamma_\psi(\xi, \tau). \quad (5.5)$$

The mirror is perpendicularly illuminated by a plane wave with wave number k_0 . Apart from a constant phase, the reflected wave field at a distance y from the mirror is given, in the paraxial approximation, by

$$\tilde{z}(x, y, t) = \frac{z_0}{2\pi} \iint \exp\left(i\tilde{\psi}(x', t) + ik_x(x - x') + iyk_x^2/(2k_0)\right) dx' dk_x. \quad (5.6)$$

The symbol \tilde{z} denotes the reflected wave field, of which the complex reflectometer signal is assumed to be a point measurement. The amplitude of the incident wave is z_0 . To evaluate the first two moments $\langle \tilde{z} \rangle$ and $\langle \tilde{z} \tilde{z}^* \rangle$ of the reflected wave field we use

$$\langle \exp(i\tilde{X}) \rangle = \exp(-\sigma^2/2), \quad (5.7)$$

which holds for real-valued Gaussian random variables \tilde{X} with $\langle \tilde{X} \rangle = 0$ and $\langle \tilde{X}^2 \rangle = \sigma^2$ (J. W. Goodman 2000). The integrals in equation 5.6 now cancel out and we obtain

$$\langle \tilde{z} \rangle = z_0 \exp\left(-\sigma_\psi^2/2\right); \quad (5.8)$$

$$\langle \tilde{z} \tilde{z}^* \rangle(\xi, \tau) = |z_0|^2 \exp\left(-\sigma_\psi^2(1 - \gamma_\psi(\xi, \tau))\right). \quad (5.9)$$

Note that equations 5.8 and 5.9 have no y dependence: the first two moments of the complex reflectometer signal do not vary on propagation. For $\sigma_\psi^2 \ll 1$ we can linearize the exponentials in equations 5.8 and 5.9, giving

$$|\langle \tilde{z} \rangle|^{-2} \langle \tilde{z} \tilde{z}^* \rangle(\xi, \tau) = 1 + \sigma_\psi^2 \gamma_\psi(\xi, \tau) + \mathcal{O}(\sigma_\psi^4). \quad (5.10)$$

This shows that for sufficiently weak density perturbations, and apart from an offset, the poloidal correlation function of the phase grating is equal to that of the complex electric field, an important result for poloidal correlation reflectometry.

The correlation function of the *phase* of the complex electric field, denoted by $\tilde{\phi}(x, y, t) = \arg[\tilde{z}(x, y, t)]$ can be obtained by expanding the exponential in equation 5.6 in powers of $\tilde{\psi}(x, t)$, assuming $\tilde{\psi} = \mathcal{O}(\sigma_\psi) \ll 1$. The zeroth order term integrates to a constant. Using the relation

$$\arg[1 + \delta z] = \Im\{\ln[1 + \delta z]\} = \Im(\delta z) + \mathcal{O}(|\delta z|^2) \quad (5.11)$$

and omitting a constant offset due to $\arg[E_0]$, we find

$$\langle \tilde{\phi}\tilde{\phi} \rangle(\xi, y, \tau) = \frac{\sigma_\psi^2}{2\pi} \iint \gamma_\psi(x, \tau) \cos\left(k_\perp[x - \xi] + yk_\perp^2/(2k_0)\right) dx dk_\perp + \mathcal{O}(\sigma_\psi^3). \quad (5.12)$$

It is instructive to consider a phase grating with correlation function $\gamma_\psi(\xi, \tau) = \cos(K\xi)g(\tau)$, which represents a single, spatially coherent mode. Substituting in equation 5.12 and carrying out the integrals gives

$$\langle \tilde{\phi}\tilde{\phi} \rangle(\xi, y, \tau) = g(\tau)\sigma_\psi^2 \cos(yK^2/[2k_0]) \cos(K\xi). \quad (5.13)$$

A similar argument shows that the correlation function of the reflectometer *amplitude* signals $|\tilde{z}(x, y, t)|$ is obtained from equation 5.13 by replacing the term $\cos(yK^2/[2k_0])$ by $\sin(yK^2/[2k_0])$. This shows that plasma modes with long poloidal wavelength ($K \ll \sqrt{\pi k_0/y}$) modulate only the phase signal, while shorter wavelength modes lead to a mix of phase and amplitude modulation (Soldatov et al. 2009). It also justifies our statement in subsection 5.2.2 that, in addition to the cross-phase of the *complex* reflectometer signal, the cross-phases of the phase or amplitude signals can also be used to obtain the wavelength of the mode from equation 5.4.

For $\sigma_\psi^2 > 1$, the temporal and spatial spectra of the complex electric field $\tilde{z}(x, y, t)$ suffer non-linear broadening. We now find the spectrum corresponding to a phase screen with correlation function

$$\langle \tilde{\psi}\tilde{\psi} \rangle(\xi, \tau) = \sigma_1^2 \cos(K\xi - \Omega\tau) + \sigma_2^2(\xi)e^{-|\tau|/t_c}, \quad (5.14)$$

where $\sigma_2(\xi)$ decays with increasing ξ . The goal is to illustrate how the coherent mode can become completely invisible in the spectra of the complex signals when $\sigma_2 \gg 1$, regardless of its amplitude. The correlation function of the complex field is given by

$$\begin{aligned} \langle \tilde{z}\tilde{z}^* \rangle(\xi, \tau) &= |z_0|^2 \exp\left(-\sigma_1^2 - \sigma_2^2(0)\right) \exp\left(\sigma_1^2 \cos(K\xi - \Omega\tau)\right) \\ &\quad \times \exp\left(\sigma_2^2(\xi) \exp(-|\tau|/t_c)\right). \end{aligned} \quad (5.15)$$

To evaluate the time Fourier transform of equation 5.15, we first evaluate those of the last two exponentials individually, giving

$$S_1(\xi, \omega) = \sqrt{2\pi} \sum_{n=-\infty}^{\infty} I_n(\sigma_1^2) \exp(inK\xi) \delta(\omega + n\Omega); \quad (5.16)$$

$$S_2(\xi, \omega) = \sqrt{2\pi}\delta(\omega) + \frac{t_c}{\sqrt{2\pi}} \sum_{\pm} (-\sigma_2^2(\xi))^{\pm i\omega t_c} \left(\Gamma(\mp i\omega t_c, 0) - \Gamma(\mp i\omega t_c, -\sigma_2^2(\xi)) \right), \quad (5.17)$$

where δ and I_n are the Dirac delta function and the modified Bessel function, respectively, and $\Gamma(x, y)$ is the incomplete Gamma function. The Fourier transform of equation 5.15 is now obtained by convolution of equations 5.16 and 5.17:

$$\begin{aligned}
 S(\xi, \omega) = & |z_0|^2 \exp \left[-\sigma_1^2 - \sigma_2^2(0) \right] \sum_{n=-\infty}^{\infty} I_n(\sigma_1^2) \exp(inK\xi) \left[\sqrt{2\pi} \delta(\omega + n\Omega) + \right. \\
 & \left. \frac{t_c}{\sqrt{2\pi}} \sum_{\pm} \left[-\sigma_2^2(\xi) \right]^{\pm i(\omega+n\Omega)t_c} \times \right. \\
 & \left. \left(\Gamma \left[\mp i(\omega + n\Omega)t_c, 0 \right] - \Gamma \left[\mp i(\omega + n\Omega)t_c, -\sigma_2^2(\xi) \right] \right) \right].
 \end{aligned} \tag{5.18}$$

Suppose that we have an experimental measurement of $S(\xi_0, \omega)$, the cross power between two complex signals, with finite spectral resolution $\Delta\omega$ and sufficient poloidal separation between the antennas that $\sigma_2^2(\xi_0) \ll 1$. We proceed to estimate the corresponding coherence, $\gamma_E^2(\xi_0, \omega)$. Considering only the $n = -1$ term in equation 5.18, and using the fact that for $\omega = 0$ the second term in equation 5.17 simplifies to

$$\sqrt{2/\pi} t_c (\text{Ei}[\sigma_2^2(\xi)] - \ln[\sigma_2^2(\xi)] - a),$$

where Ei is the exponential integral and a is the Euler constant, the coherence becomes

$$\gamma_E^2(\xi_0, \Omega) = \left(1 + \frac{t_c \Delta\omega}{\pi} \left[\text{Ei}(\sigma_2^2) - \ln(\sigma_2^2) - a \right] \right)^{-2}. \tag{5.19}$$

The coherence is suppressed if the second term of equation 5.19 dominates over the first, independently of the amplitude of the coherent mode.

For $\xi = 0$, the delta function in the $n = 0$ term of equation 5.18 represents the contribution of the specularly reflected microwaves in the auto power spectrum of the complex reflectometer signal. Considering only the $n = 0$ term, it can be seen that the relative importance of the two terms of equation 5.19 is also what determines the visibility of specular reflection: when it is invisible (e.g. during ELMs and in L-mode) *any* coherent feature in the reflectometer spectra, independently of its amplitude or frequency, will be strongly suppressed. The spectral resolution attained in the analysis presented in this thesis is limited by the short duration (typically 0.5 ms) of the fishbone and Alfvén modes, giving $\Delta\omega \approx 12$ krad/s. Choosing $t_c = 10 \mu\text{s}$, we see that for broad-band density fluctuations with $\sigma_2^2 > 7$, our model predicts that the coherence is suppressed to $\gamma_E^2(\Omega) < 0.01$, independently of the amplitude of the mode.

We now give a heuristic discussion of the phase-runaway phenomenon on the basis of the phasor diagram of figure 5.1, representing the complex reflectometer signal $\tilde{z} = \langle \tilde{z} \rangle + \delta\tilde{z}$. In the analysis of any reflectometer phase signal, an unwrapping procedure has to be applied to remove 2π discontinuities. The interpretation of this procedure is clear when phase modulation arises from the specular component $\langle \tilde{z} \rangle$ of the wave field, i.e. by a shift in the cutoff position or strong, long wavelength mode activity. However, if scattering becomes sufficiently strong that $\text{std}[\delta\tilde{z}] \gtrsim |\langle \tilde{z} \rangle|$, and assuming that the real and imaginary parts of $\delta\tilde{z}$ are random and independent, the phasor \tilde{z} will loop around the complex origin at random times t and positions x , and in random directions. The unwrapping procedure now acts as an integrator of noise, causing the unwrapped phase signal to become a

random walk, or diffusive process. The power spectra of diffusive processes have a $1/f^2$ dependence (Brownian noise), with the absolute magnitude depending on the length of the sample window. Simulations show that the spatial spectra of the phase also have a $1/k_x^2$ dependence (Nazikian et al. 1995) and correlation length of the order of the vacuum wavelength of the probe beam, in agreement with the experimentally observed lack of coherence between antennas on TEXTOR.

Finally, we give a heuristic explanation of why high-frequency coherent modes may remain visible in the spectra of reflectometer phase signals in the presence of phase-runaway. Consider again a phase screen defined by

$$\langle \tilde{\psi} \tilde{\psi} \rangle(\xi, \tau) = \langle \tilde{\psi}_1 \tilde{\psi}_1 \rangle(\xi, \tau) + \langle \tilde{\psi}_2 \tilde{\psi}_2 \rangle(\xi, \tau), \quad (5.20)$$

with

$$\langle \tilde{\psi}_1 \tilde{\psi}_1 \rangle(\xi, \tau) = \sigma_1^2 \cos(K\xi - \Omega\tau) \quad (5.21)$$

and

$$\langle \tilde{\psi}_2 \tilde{\psi}_2 \rangle(\xi, \tau) = \sigma_2^2(\xi) \exp(-|\tau|/t_c). \quad (5.22)$$

We now employ equation 5.6 to find the complex wave field a distance y from the phase screen, assuming that the coherent mode is of sufficiently long wavelength ($yK^2/(2k_0) \ll 1$) that the effect of propagation is negligible, giving

$$\tilde{z}(x, y, t) \approx \frac{z_0}{2\pi} \exp(i\tilde{\psi}_1(x, t)) \times \iint \exp(i\tilde{\psi}_2(x', t) + ik_x(x - x') + iyk_x^2/(2k_0)) dx' dk_x. \quad (5.23)$$

The corresponding reflectometer phase signal is

$$\tilde{\phi}(x, y, t) = \arg[\tilde{z}(x, y, t)] = \tilde{\psi}_1(x, t) + \tilde{\phi}_2(x, y, t), \quad (5.24)$$

where

$$\tilde{\phi}_2(x, y, t) = \arg\left(\iint \exp(i\tilde{\psi}_2(x', t) + ik_x(x - x') + iyk_x^2/(2k_0)) dx' dk_\perp\right). \quad (5.25)$$

The correlation function of $\tilde{\phi}$ is

$$\langle \tilde{\phi} \tilde{\phi} \rangle(\xi, \tau) = \sigma_1^2 \cos(K\xi - \Omega\tau) + \langle \tilde{\phi}_2 \tilde{\phi}_2 \rangle(\xi, y, \tau), \quad (5.26)$$

where, for $\sigma_2^2 \gg 1$, $\langle \tilde{\phi}_2 \tilde{\phi}_2 \rangle$ is a $1/f^2$ Brownian noise spectrum associated with phase-runaway. However, equation 5.26 shows that this noise is simply added to the phase signal arising from the coherent mode, rather than being convolved with it, as for the complex reflectometer signal (equation 5.15). This may explain the observation (subsection 5.2.2) that coherent modes, in particular the high frequency Alfvén waves, are only visible in the phase signals in L-mode.

5.1.3 Analysis techniques

We wish to study plasma fluctuations associated with ELMs and other cyclic bursts of mode activity. Assuming that each burst is a realization of some statistical process, an average over a set of disjunct sub-records, chosen with respect to a fixed reference time for individual bursts, then corresponds to statistical ensemble averaging (Bendat et al. 2010). This technique, known as conditional or coherent averaging, is extensively used for the analysis presented here in order to improve the statistics of spectral estimates without sacrificing spectral resolution.

We define the reference times for ELMs by the times where the D_α signal crosses a critical level in the positive direction; the appropriateness of this choice is discussed in subsection 5.4.1. The low-frequency bursts that we shall identify as fishbone oscillations are invariably accompanied by Alfvén modes, which produce distinct, narrow spikes in digitally high-pass filtered (60 kHz cutoff) Mirnov coil signals. We use these spikes as reference times for the fishbone, setting an arbitrary threshold value at 50 times the median value. The results presented in section 5.3 do not depend strongly on the chosen threshold values.

For the investigation of nonlinear mode-mode coupling we have relied on bispectral techniques (Kim et al. 1979). For convenience we reproduce the estimators for the bispectral power density $B(k, l)$ and the bispectral coherence $\hat{b}^2(k, l)$ of the random process $\tilde{x}(t)$:

$$\hat{B}(k, l) = \frac{1}{M} \sum_{i=1}^M X_k^{(i)} X_l^{(i)} X_{k+l}^{*(i)}, \quad (5.27)$$

$$\hat{b}^2(k, l) = |\hat{B}(k, l)|^2 \left[\left(\frac{1}{M} \sum_{i=1}^M |X_k^{(i)} X_l^{(i)}|^2 \right) \left(\frac{1}{M} \sum_{i=1}^M |X_{k+l}^{(i)}|^2 \right) \right]^{-1}. \quad (5.28)$$

where $X_k^{(i)}$ denotes the k th component of the Fourier series of realization i in the ensemble. For our conditionally constructed ensembles we find significant correlation between $|X_k|^2$ and $|X_l|^2$, which makes the estimates for $\text{var}[\hat{B}]$ and $\text{var}[\hat{b}]$ derived by Kim et al. 1979 inaccurate, since they rely on the assumption

$$\langle |X_k|^2 |X_l|^2 |X_{k+l}|^2 \rangle \approx \langle |X_k|^2 \rangle \langle |X_l|^2 \rangle \langle |X_{k+l}|^2 \rangle. \quad (5.29)$$

Instead, we use a direct data-based estimator:

$$\text{var}[\hat{B}(k, l)] \approx \frac{1}{M^2} \sum_{i=1}^M |X_k^{(i)} X_l^{(i)} X_{k+l}^{*(i)} - \hat{B}(k, l)|^2. \quad (5.30)$$

In order to establish the statistical significance of the bispectral coherence estimate we use a criterion based on $\text{var}[\hat{B}]$:

$$|\hat{B}(k, l)|^2 > 3 \text{ var}[\hat{B}(k, l)]. \quad (5.31)$$

Using a factor lower than three results in the appearance of spots of apparent bispectral coherence throughout the bispectral plane. When we artificially randomize the phase of all Fourier components in our ensemble, the spots change position, but their overall

appearance and level of bispectral coherence does not change. Therefore, they cannot be the result of genuine phase relations between spectral components. In any case, the peaks in the bispectrum that we shall discuss in the following all have significantly higher bispectral coherence than these apparently spurious features.

The significance of the biphase $\arg[B]$ is somewhat subtle and is best illustrated by examining some simple model spectra for which it has a clear interpretation. In the case of a sinusoidal signal superimposed on a second harmonic component, i.e. $\tilde{x}(t) = a \sin(\Omega_0 t + \tilde{\phi}) + b \sin(2\Omega_0 t + 2\tilde{\phi} + \theta)$, the phase shift of the harmonic component can be extracted from $\arg[B(\Omega_0, \Omega_0)] = -\theta - \pi/2$. In the case of a sinusoidal signal being modulated by another sinusoidal signal at a different frequency, i.e. $\tilde{x}(t) = a \sin(\Omega_0 t + \tilde{\phi}) + b \sin(\Omega_1 t + \tilde{\psi})[1 + \epsilon \sin(\Omega_0 t + \tilde{\phi} + \theta)]$, the phase of the modulation can be obtained from $\arg[B(\Omega_0, \Omega_1 - \Omega_0)] = \arg[B(\Omega_0, \Omega_1)] = -\theta$. This can be generalized for $\tilde{x}(t) = a \sin(\Omega_0 t + \tilde{\phi}) + \tilde{f}(t)[1 + \epsilon \sin(\Omega_0 t + \tilde{\phi} + \theta)]$, where $\tilde{f}(t)$ is a broad-band random function with non-zero spectral power in the frequency interval $\Omega_1 < \Omega < \Omega_2$, giving $\arg[B(\Omega_0, \Omega)] = -\theta$ for $\Omega_1 - \Omega_0 < \Omega < \Omega_2$.

5.2 Experimental setup

5.2.1 Limiter H-modes in the TEXTOR tokamak

The goal of the study presented in this chapter was to characterise density fluctuations in the pedestal of TEXTOR limiter H-modes by reflectometry. ELMy H-modes have been obtained in limited plasmas on many tokamaks such as DIII-D (K. H. Burrell et al. 1989), TFTR (Bush et al. 1990) and TCV (Hofmann, Lister, et al. 1994), but the power threshold is typically significantly higher than for diverted plasmas (Kalupin et al. 2006). For the experiments described in this paper, we used the same operational scenario as the one reported by Soldatov, Krämer-Flecken, Kantor, et al. 2010: $B_t=1.3$ T, $I_p=235$ kA; 1.6 MW of co-current NBI (56 keV deuterium atoms; tangential at plasma center). The plasmas have circular poloidal cross-section, minor radius $a = 0.44$ m, major radius $R = 1.72$ m and were limited on the inner wall. The dynamic ergodic divertor coils (Finken et al. 2007; Unterberg et al. 2009) were not used.

Both in L and H-mode these discharges show strong bursts of MHD activity, which we argue to be beam-driven modes in section 5.3. These modes are not observed in other TEXTOR scenarios with similar or stronger neutral beam heating (e.g. the NBI heated discharges in Krämer-Flecken, Dreval, et al. 2004). The reason for this may be the relative weakness of B_t in the limiter H-mode scenario (1.3 T). The ratio of the parallel beam ion velocity to the Alfvén velocity is $v_{\parallel}/v_A \lesssim 0.7$ in the experiments of this paper. The Alfvén velocity is given by $v_A = B_t/\sqrt{\mu_0 \rho}$, where ρ is the mass density of the plasma. For the experiments in Krämer-Flecken, Dreval, et al. 2004 $B_t = 2.25$ T and $v_{\parallel}/v_A \lesssim 0.4$.

At the L-H transition the electron pressure gradient in the outer 2 cm of the plasma (measured using a Thomson scattering diagnostic in multi-pass laser configuration (Kantor et al. 2009)) increases from 20 Pa/cm to 150 Pa/cm in H-mode (Soldatov, Krämer-Flecken, Kantor, et al. 2010). Representative density profiles are shown in figure 5.3. At the same time, the base-line recycling rate decreases and phase-runaway (cf. section 5.2.2) in the reflectometer signals stops, consistent with the suppression of turbulent density fluctuations in the transport barrier. ELMs with a repetition frequency of typically 300 Hz

are identified by spikes in the recycling rate, accompanied by the transient reappearance of phase-runaway and a relaxation of the pressure profile (Soldatov, Krämer-Flecken, Kantor, et al. 2010). Since their frequency shows no clear dependence on the heating power, we have so far been unable to classify the observed ELMs as type-I or type-III (Finken et al. 2007).

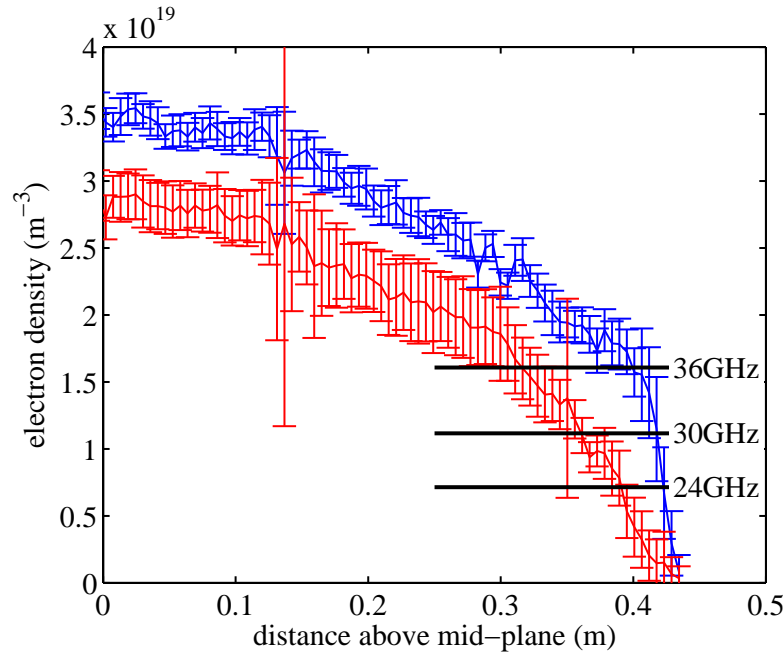


Figure 5.3: Electron density profiles from Thomson scattering. Blue: H-mode between ELMs. Red: L-mode.

The time derivative of the poloidal component of the magnetic field $\dot{B}_p(t)$ in TEXTOR is measured using two arrays of Mirnov coils inside the vessel. One array is spaced toroidally around the tokamak at the outboard mid-plane, the other is spaced poloidally from the outboard mid plane to the top of the vessel. The transfer functions of the coils have not been measured, but the cross-phases between different sets of coils at frequencies corresponding to narrow band structures in the power spectra always yield clear mode numbers. This gives confidence that the phase of the transfer functions is equal for the different coils that were used. The absence of calibration however precludes comparison of amplitude of modes between coils. Therefore, in particular, an assessment of the ballooning character of a magnetic mode is impossible for the present experiments. Furthermore, the coil signals were acquired at only 200 kHz for the present experiments, since detection of high-frequency Alfvén modes was not a stated goal of the study. The absence of anti-aliasing filters resulted in the Mirnov spectra being severely compromised by folded images of Alfvén waves with $f > 100$ kHz in the laboratory frame. Nevertheless, as will be shown, useful information can still be extracted from these spectra, particularly in conjunction with the reflectometer measurements.

5.2.2 The TEXTOR multi-antenna reflectometer

A heterodyne, multi-antenna reflectometer system (Krämer-Flecken, Soldatov, Vowinkel, et al. 2010) is operated on TEXTOR, featuring three antenna arrays located at different poloidal and toroidal angles on the torus (figure 5.2a,b). Each array consists of a central emitting antenna and two or four identical receiver antennas, spaced poloidally around the central one (figure 5.2c). The top array and the nearest equatorial array both have four receiver antennas, while the second equatorial array has two. The two equatorial arrays can operate in both X- and O-mode polarisation, while the top array is O-mode only. The measurements described in this thesis were all done in O-mode.

Two independent microwave generators are available for simultaneous probing of different cutoff layers. One generator employs YIG tuned oscillators and covers the frequency range 26-37 GHz; the other is based on voltage controlled oscillators and frequency multipliers and covers the range 24-40 GHz. The frequency of both generators can be stepped during a plasma discharge. Both generators consist of two phase-locked sources for heterodyne detection; the intermediate frequency is 20 MHz. For the measurements in this thesis work only the YIG generator was used, since we focussed on poloidal rather than radial correlation measurements. The available microwave frequency range corresponds to O-mode cutoff densities of $0.8\text{-}1.6 \times 10^{19} \text{ m}^{-3}$. For our experiments these densities correspond to cutoff layers 2-4 cm inside the last closed flux surface in H-mode (the pedestal region) and 5-12 cm inside the last closed flux surface in L-mode, as depicted in figure 5.3.

Six balanced microwave mixers are available for heterodyning and subsequent quadrature detection; manual waveguide switches allow different combinations of the ten receiver antennas to be selected. The in-phase and quadrature signals are usually digitised at a sampling rate of 1 MHz.

In section 5.1.2 we have discussed the non-linear response of reflectometer signals to strong density fluctuations in the context of the random phase-screen model. The incorrect assumption of linearity of the response can lead to incorrect conclusions. For situations where the complex reflectometer z signal depends linearly on the density fluctuations it satisfies the inequality

$$\text{std}(z) \ll |\langle z \rangle|, \quad (5.32)$$

which states that scattered components should be much smaller than the specularly reflected component (Mazzucato 1998b; Gusakov et al. 2002). Equation 5.32 is a sufficient condition for nonlinearity only for the case of perpendicular incidence reflectometry, but not for Doppler reflectometry, in which detection of the specular component is avoided on purpose. In the following we experimentally check the validity of inequality 5.32 for the signals acquired during the TEXTOR limiter H-mode experiments presented in section 5.3.

Phase runaway arises in perpendicular incidence reflectometry when the amplitude modulation of a reflectometer signal is comparable to its average amplitude, i.e. $\text{std}(|z|) \gtrsim \langle |z| \rangle$. This makes it an indicator of non-linear reflectometer response. Figure 5.4 shows an unwrapped phase signal around an L-H transition, which is marked by a drop in the base-line D_α light. In the 10 ms before the L-H transition, the phase changes by roughly 600 radians. If one would naively attribute this drift to the specular reflection, the resulting shift of the cutoff layer would be an impossible 4 m: it must instead be caused by the phase-runaway phenomenon. This proves that during L-mode the complex

reflectometer signals do not satisfy 5.32.

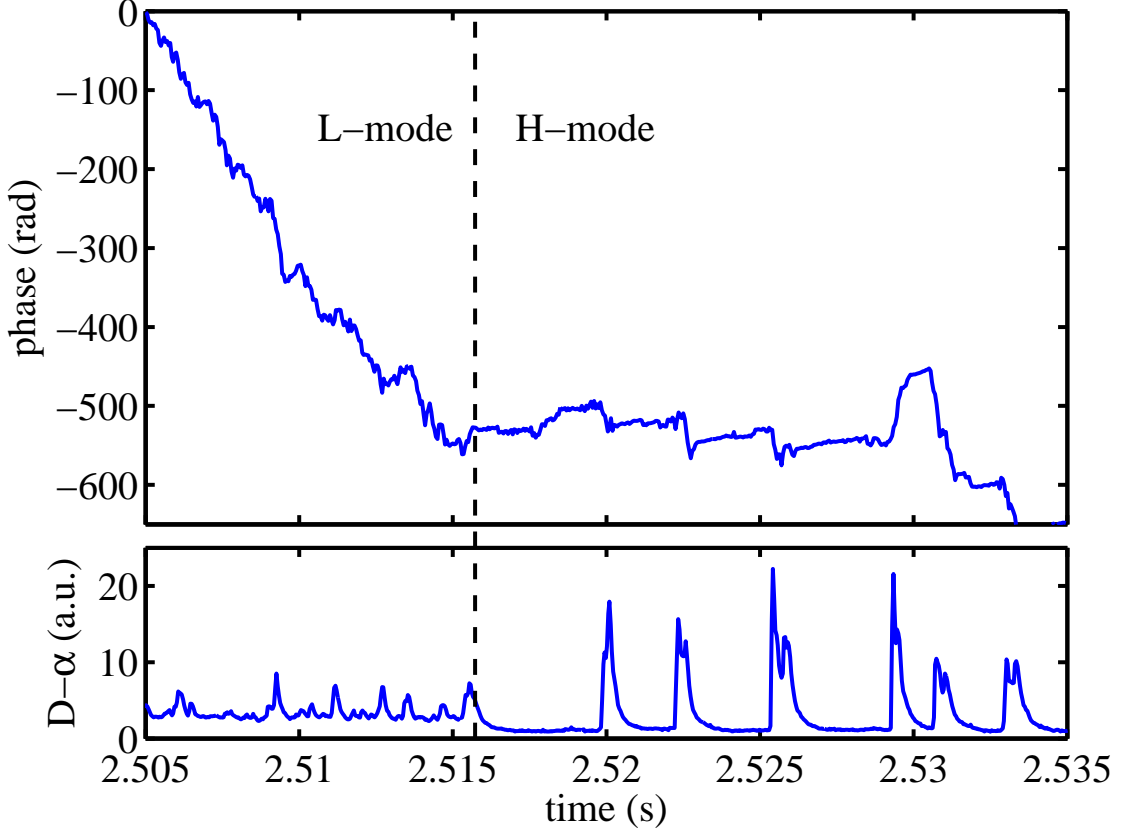


Figure 5.4: Unwrapped reflectometer phase for shot 110568.

In H-mode phase runaway mainly occurs during ELMs, although phase jumps are occasionally seen between ELMs as well. This proves that during ELMs inequality 5.32 is not satisfied either. The moving average and standard deviation of z and $|z|$ during the ELM cycle are shown in figures 5.5a and b, respectively. Typical values for the ratios $\text{std}(|z|)/\langle|z|\rangle$ and $\text{std}(z)/\langle z\rangle$ are listed in table 5.1 for data acquired between ELMs (interval 1), during ELMs (interval 2), as well as in L-mode. As expected from the discussion on phase runaway the ratio $\text{std}(|z|)/\langle|z|\rangle$ is significantly smaller between ELMs than during ELMs and during L-mode. However, even between ELMs, the ratio $\text{std}(z)/\langle z\rangle \gtrsim 1$ and inequality 5.32 is not satisfied. This means that even between ELMs the complex reflectometer signals z are not a linear function of the density fluctuations. Figure 5.6 shows the histograms of z between ELMs (1) and during ELMs (2). The crescent shape of the former illustrates the relatively weak amplitude modulation observed between ELMs.

The criterion for validity of the Born approximation is given by

$$\frac{\delta n_c^2}{n_c^2} \ll \left\{ \sqrt{\pi} l_{\text{cr}} L_n \frac{\omega_0^2}{c^2} \left[\ln \left(\frac{8L_n}{\pi l_{\text{cr}}} \right) + 0.71 \right] \right\}^{-1}, \quad (5.33)$$

where δn_c is the perturbation level, n_c the background density, l_{cr} the correlation length

	$\text{std}[z]/ \langle z \rangle $	$\text{std}[z]/\langle z \rangle$
between ELMs	1.3	0.3
during ELMs	6	0.5
L-mode	3	0.5

Table 5.1: Comparison of different scattering regimes. Integration time is 100 μs .

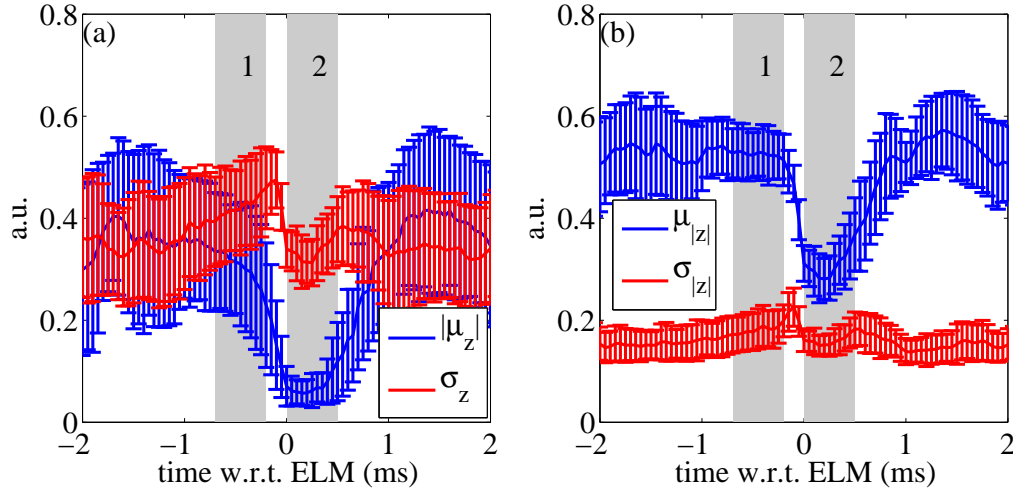


Figure 5.5: Moving average μ and standard deviation σ of the complex reflectometer signal z (a) and its absolute value $|z|$ (b). Integration time is 100 μs . Ensemble averaging over 50 ELMs in the interval $3.537 < t < 3.685$ s during shot 110568. The error bars represent the standard deviation within the ensemble.

of fluctuations and L_n the density gradient scale length (Gusakov et al. 2002). All these quantities should be taken at the cutoff layer. In H-mode, between ELMs, we have $L_n \simeq 2$ cm, while in L-mode $L_n \simeq 20$ cm. The radial correlation lengths are unknown, but tentatively taking $l_{cr} \simeq 2$ cm for both L- and H-mode yields, respectively, $\delta n_c/n_c \ll 0.9\%$ and $\delta n_c/n_c \ll 5\%$. Since we just established that for our experiments the reflectometer response is non-linear, we conclude that the density fluctuation amplitudes do not satisfy these inequalities. Nevertheless, the observed broadening varies significantly between the regimes of table 5.1. We now discuss what information can be extracted from the reflectometer measurements for the different regimes.

During ELMs and in L-mode the auto power spectra of the amplitude and complex reflectometer signals (z and $|z|$, respectively) are nearly completely featureless and show no significant coherence between antennas, even at the frequency of coherent modes (cf. equation 5.19). We attribute this to the non-linear response of the reflectometer. The correlation properties of these signals do not reflect those of density fluctuations during ELMs and in L-mode and we do not use them in section 5.3. The auto power spectra of unwrapped phase signals ($\arg(z)$) have a $1/f^2$ dependence and the spectral width increases with integration time. As discussed in section 5.1.2, this is a consequence of phase runaway. For the 0.5 ms integration intervals used in section 5.3 only coherent modes such as the fishbone and Alfvén waves stand out above this $1/f^2$ noise in the

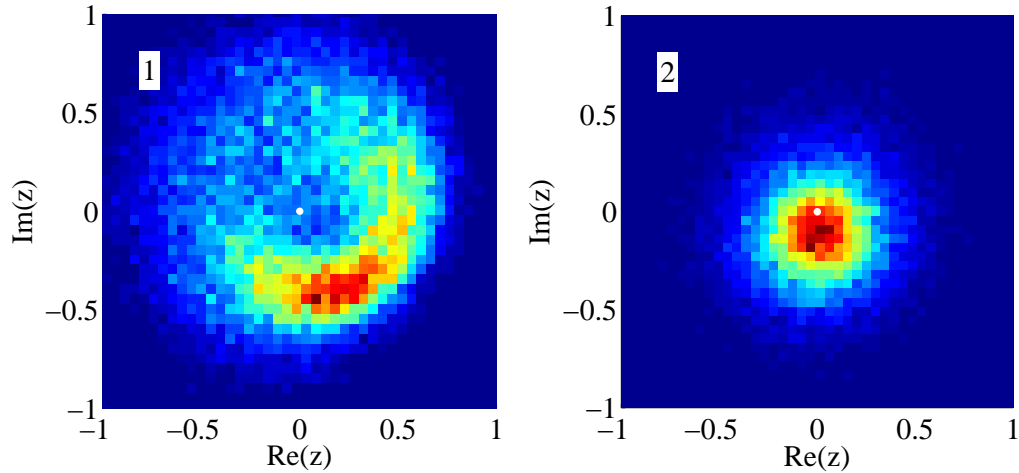


Figure 5.6: Histograms of the complex reflectometer signal z . The data come from the same ensemble used for figure 5.5. but selecting only the time interval (relative to the ELM) indicated by ‘1’ and ‘2’ in figure 5.5. The complex origin is marked by a white dot.

auto power spectra of the phase signals (cf. equation 5.26). The coherence between the antennas is not statistically significant, except at the frequency of these modes. Therefore, the phase signals can be used to detect the presence of coherent modes and to estimate their phasing (through the cross-phase between antennas).

Between ELMs, both coherent and broad-band features stand out in the spectra and significant coherence exists between antennas for a wide range of frequencies. Phase jumps caused by the suppression of the specular reflection are rare. Interestingly, the amplitude and phase signals are clearly sensitive to density fluctuations of different poloidal scales: modes with long poloidal wavelength ($k_x \ll 0.5 \text{ cm}^{-1}$) give pure phase modulation, while modes with $k_x > 0.5 \text{ cm}^{-1}$ give a mix of phase and amplitude modulation. All these observations indicate that the reflectometer signals between ELMs are less affected by broadening than during ELMs and in L-mode. This is in qualitative agreement with the relative values of the ratios $\text{std}(z)/|\langle z \rangle|$ from figure 5.5 and table 5.1.

It must be stressed again that even between ELMs, the complex signals depend non-linearly on the density fluctuations, since $\text{std}(z)/|\langle z \rangle| \simeq 1.3$ (table 5.1), leading to broadening of the broad-band features and ghost images of coherent features. The importance of the latter effect is illustrated in figure 5.7, which shows power spectra of the complex signal and the corresponding phase between ELMs. Magnetic measurements indicate strong MHD activity at 14 kHz, but no harmonics. Accordingly, the spectrum of the phase signal shows a single peak at 14 kHz, superimposed on $1/f^2$ noise caused by phase jumps. By contrast, the spectrum of the complex reflectometer signal shows multiple harmonics, with the second just 3 dB below the fundamental component. In the light of these considerations we do not use the complex signals in the analysis presented in section 5.3.

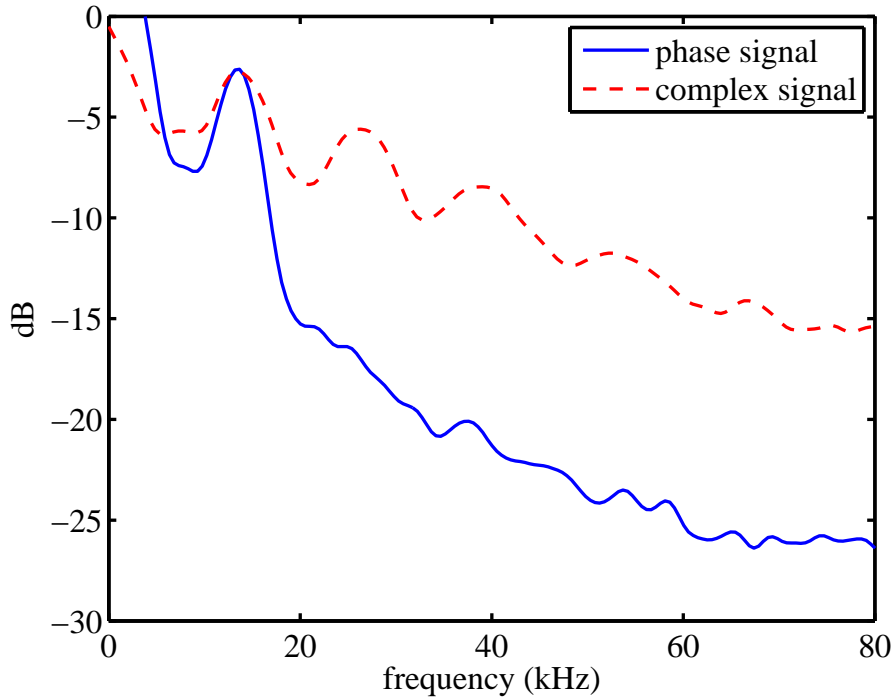


Figure 5.7: Auto power spectrum of a complex signal and the corresponding phase signal, scaled to equalise the power for the peak at 14 kHz. Spectral resolution is 2 kHz, statistical error 6%.

5.3 Fluctuation measurements in the TEXTOR tokamak

5.3.1 The fishbone mode

In NBI heated TEXTOR plasmas with weak toroidal magnetic field ($B_t = 1.3$ T), bursts of MHD activity are observed, dominated by a down-chirping (10-15 kHz in the laboratory frame) $n = 1$ mode propagating in the co-beam direction (figure 5.8). Magnetic measurements show that its poloidal structure outside the plasma is dominated by an $m = 3$ harmonic, propagating in the ion diamagnetic drift direction. The low signal to noise ratio of the TEXTOR soft X-ray camera array at the time of the experiment precluded measurements of the poloidal mode structure in the plasma core. In the following we refer to this mode as a ‘fishbone’ (McGuire et al. 1983), which is a $n = 1$ internal kink mode that is driven on the $q = 1$ flux surface by a resonance with trapped beam ions whose toroidal precession rate matches the mode frequency in the plasma frame.

Sawtooth crashes are often preceded by several ms of a saturated precursor mode at 9-10 kHz in the laboratory frame. This mode has the same apparent structure and propagation direction as the fishbone, but simultaneous observation of both modes in spectrograms of the Mirnov coil signals (not shown) clearly indicates that they are distinct. Inspection of the signals from a multi-chord soft X-ray camera system during sawtooth crashes shows that the sawtooth inversion radius, which corresponds to the $q = 1$ flux-surface, is at $r = 0.08$ m. Measurements with the charge exchange spectroscopy diagnostic (Delabie et al. 2008) show that the toroidal plasma rotation frequency at this radial position corresponds to within the measurement uncertainty to the observed saw-

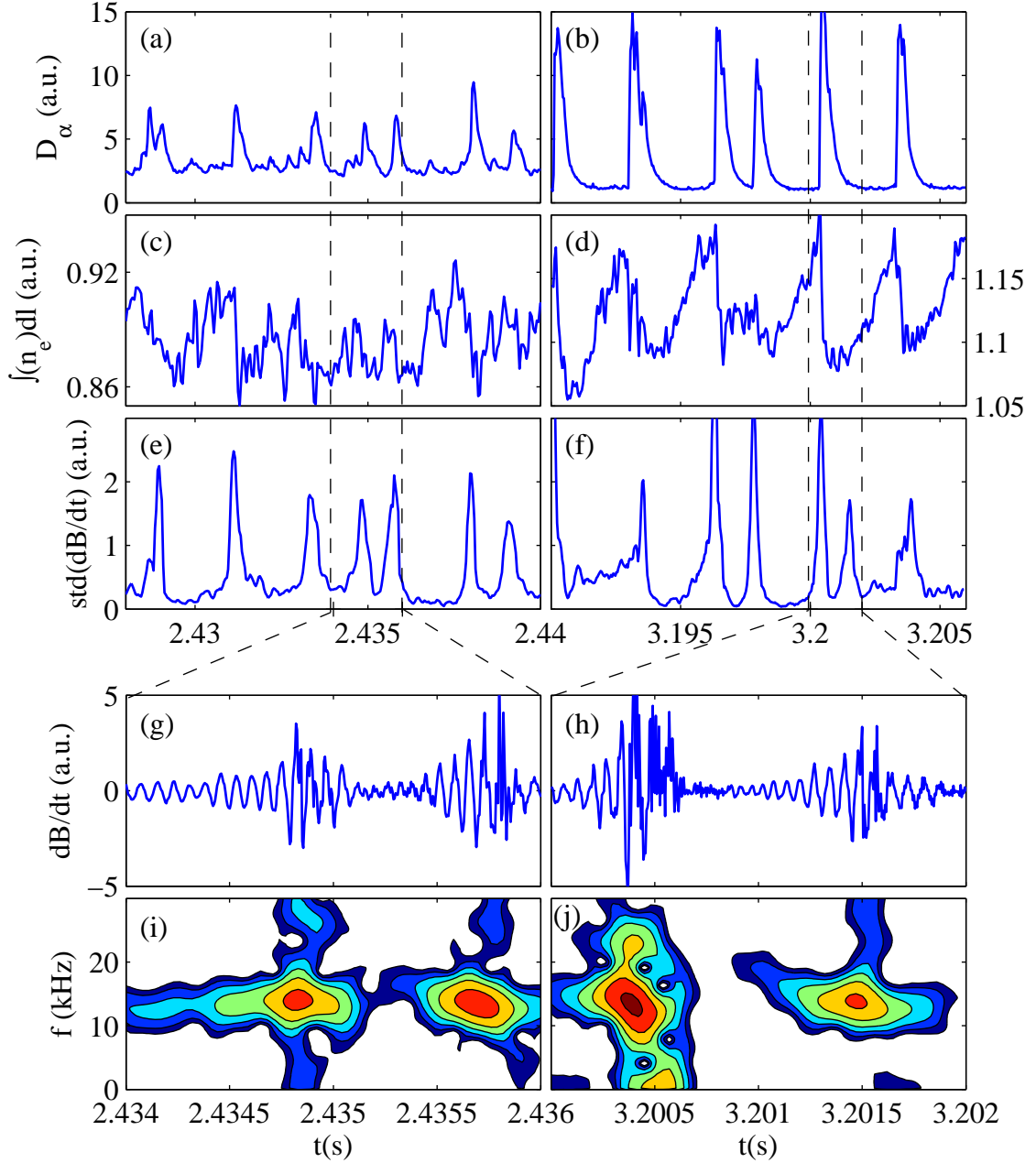


Figure 5.8: Time traces during TEXTOR shot 110568. The left column corresponds to L-mode, the right to H-mode. (a,b) Signal from filtered photodiode looking at limiter (sampling rate 25 kHz). (c,d) Line integrated electron density along a vertical chord at $R = 2.05\text{m}$. Note the different y-scale. (e,f) Moving standard deviation of dB_P/dt from Mirnov coil at outboard mid plane; window length 0.16 ms. (g,h) dB_P/dt . (i,j) Contours (spacing 4 dB) of spectral power density of dB_P/dt , calculated using a sliding Hamming window of length 0.32 ms.

tooth precursor frequency of 9-10 kHz (Chapman et al. 2008). By contrast, the fishbone frequency is always several kHz above the toroidal rotation frequency, indicating a finite frequency in the plasma frame.

The two modes referred to as 10 kHz and 13 kHz quasi-coherent modes in a previous publication on reflectometer measurements during TEXTOR limiter H-modes (Soldatov, Krämer-Flecken, Kantor, et al. 2010) are in fact, respectively, the sawtooth precursor and fishbone discussed in the present paper. However, in Soldatov, Krämer-Flecken, Kantor, et al. 2010 they had not been identified as such. Considerable confusion arose from limiting the analysis to the *complex* reflectometer signals. As argued in subsection 5.2.2 and in 5.1.2, the complex signals are misleading in the presence of strong scattering: coherent modes are best studied using the reflectometer *phase* signals. We now discuss where the analysis in Soldatov, Krämer-Flecken, Kantor, et al. 2010 must be revised.

Firstly, the statement that the mode only occurs in H-mode is incorrect, as can be seen by comparing the left and right columns of figure 5.8. The fact that the fishbone is only visible in the complex reflectometer signals during H-mode is purely an instrumental effect related to the complex signal (cf. subsection 5.2.2 and equation 5.19). Both in H- and in L-mode the fishbone is visible in the phase signals, which, contrary to the complex signals (Soldatov, Krämer-Flecken, Kantor, et al. 2010), are also partially coherent with the Mirnov coil signals (figure 5.9a). Secondly, the calculation of the poloidal mode number of the fishbone in Soldatov, Krämer-Flecken, Kantor, et al. 2010 was based on the erroneous assumption that the mode was edge localized and that its poloidal phase speed was given by the $E \times B$ flow in the electron diamagnetic drift direction. New analysis, based on the cross-phase between the phase signals from different reflectometer antennas, show that $m = 3$ and that the mode propagates poloidally in the ion diamagnetic direction, in agreement with magnetic measurements.

Inspection of the right column of figure 5.8 suggests that fishbone bursts are correlated to ELMs, which is confirmed by the histogram in figure 5.9b and was also noted in Soldatov, Krämer-Flecken, Kantor, et al. 2010. The fishbone typically starts to grow 0.5 ms before the D_α signal spikes, suggesting that the fishbone triggers the ELM. However, this correlation is not absolute: fishbones can occur between ELMs as well, e.g. at $t=3.2015$ s in figure 5.8; in these cases no concomitant variations in the D_α signals are observed. Conversely, since no fishbones are seen within ~ 5 ms after a sawtooth crash, ELMs occurring during that period are not accompanied by fishbones. The spikes in recycling rate associated with ELMs are accompanied by a transient drop in edge density and a non-oscillating $m/n = 0/0$ feature in the magnetic signals indicative of a transient drop in plasma current. Surprisingly, the fishbone appears to trigger such events in L-mode as well (left column of figure 5.8), although their amplitude is smaller.

Two regimes are distinguished in the drive mechanism of the fishbone (Porcelli 1991) - in the first, the thermal ions determine the mode frequency by their diamagnetic drift frequency: $\omega_{\text{di}} = (dp_{i,\perp}/dr)/(q_i n_i B_t r_0)$, where $dp_{i,\perp}/dr$ is the perpendicular ion pressure gradient, q_i and n_i the ion charge and density, respectively, B_t is the magnetic field strength and r_0 the radius where $q = 1$. For the TEXTOR experiments we estimate $|\omega_{\text{di}}/(2\pi)| \approx 4$ kHz, which corresponds approximately to the observed peak frequency of 5 kHz of the mode in the plasma rest frame.

For sufficiently high poloidal β the precessional fishbone is destabilized, whose frequency is determined by an average of the toroidal precession drift frequency of trapped

5.3. Fluctuation measurements in the TEXTOR tokamak

beam ions: $\omega_{\text{pr}} = E_{\text{tr}}/(q_i B_t r_0 R)$. Using the VENUS code (Fischer et al. 2002) we have simulated the dynamics of the beam-ion population for our H-mode TEXTOR experiments. No attempt was made to include transport of fast ions by the sawtooth or fishbone. We used measurements from the Thomson scattering and charge-exchange spectroscopy diagnostics for the plasma temperature and density profiles required as input for the code, assuming $n_e = n_i$. A parabolic q -profile was assumed, constrained by its known value of 3.7 near the plasma edge, the radial position ($r = 8$ cm) of the $q = 1$ surface and a guess for the value on the magnetic axis.

Figure 5.9c shows the simulated steady state distribution of suprathermal ions for intersection of the $q = 1$ surface and the equatorial plane. For all orbits crossing this point inside the trapping cone, the direction and rate of toroidal precession drift was determined. The black dots indicate the orbits with toroidal precession rate $4 \leq \omega_{\text{pr}}/(2\pi) \leq 6$ kHz, corresponding to the frequency of the fishbone in the plasma rest frame. This clearly shows that the ion phase space region that drives the fishbone mode is expected to be well populated.

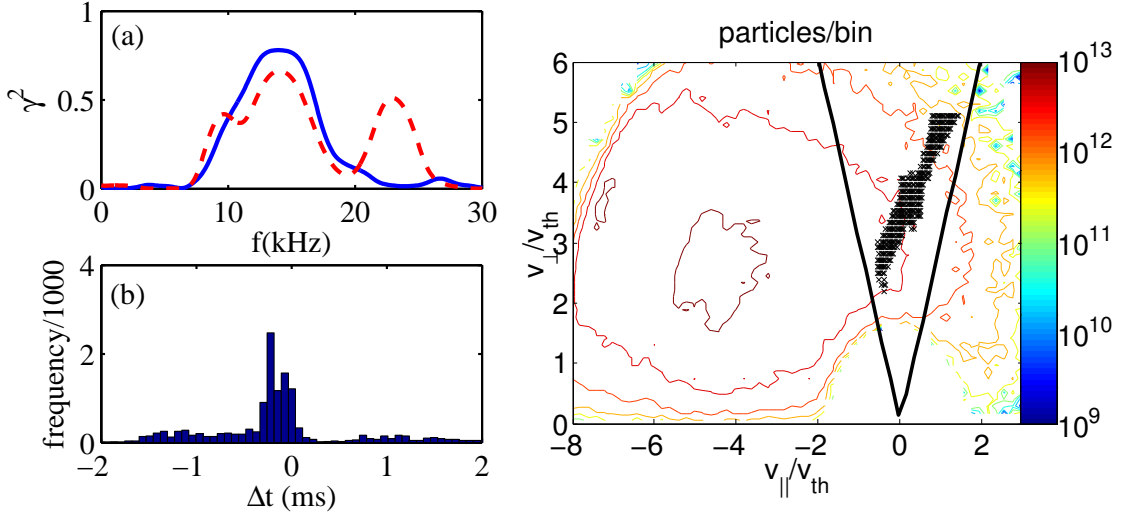


Figure 5.9: (a) Conditionally averaged coherence between reflectometer phase and Mirnov signal, both viewing top of plasma, toroidal separation 100° . Blue, continuous: 238 0.5 ms windows before Alfvén burst *not* associated with ELM ($\gamma_{\text{min}}^2 = 0.01$). Red, dashed: 890 0.5 ms windows before ELMs ($\gamma_{\text{min}}^2 = 0.003$; the 23 kHz mode is discussed in subsection 5.3.3). (b) Histogram of time intervals from peak power of fishbone to nearest ELM in discharge 110568. (c) Simulated distribution of suprathermal ions (VENUS code (Fischer et al. 2002)). Negative v_{\parallel} corresponds to the co-current direction. The black lines denote the trapping cone. The black dots indicate ions with toroidal precession rate $4 \leq \omega_{\text{pr}}/(2\pi) \leq 6$ kHz, corresponding to the frequency of the fishbone in the plasma rest frame.

Several parameters were scanned in L-mode to study the influence on the spikes in recycling rate and the fishbone. Increasing B_t to 1.6 T while keeping the edge safety factor constant by increasing the plasma current, the spikes in recycling rate disappear. The fishbone becomes weaker and its interval goes up to 5 ms. For $B_t > 2.0$ T the fishbone has not been observed on TEXTOR. A scan of the line averaged density from $2.0 - 3.3 \times 10^{19} \text{ m}^{-3}$ at $B_t = 1.3$ T increases the typical interval between fishbones from 2 to 4 ms. A scan of edge safety factor from 2.4 to 3.5 at constant toroidal magnetic field showed no effect

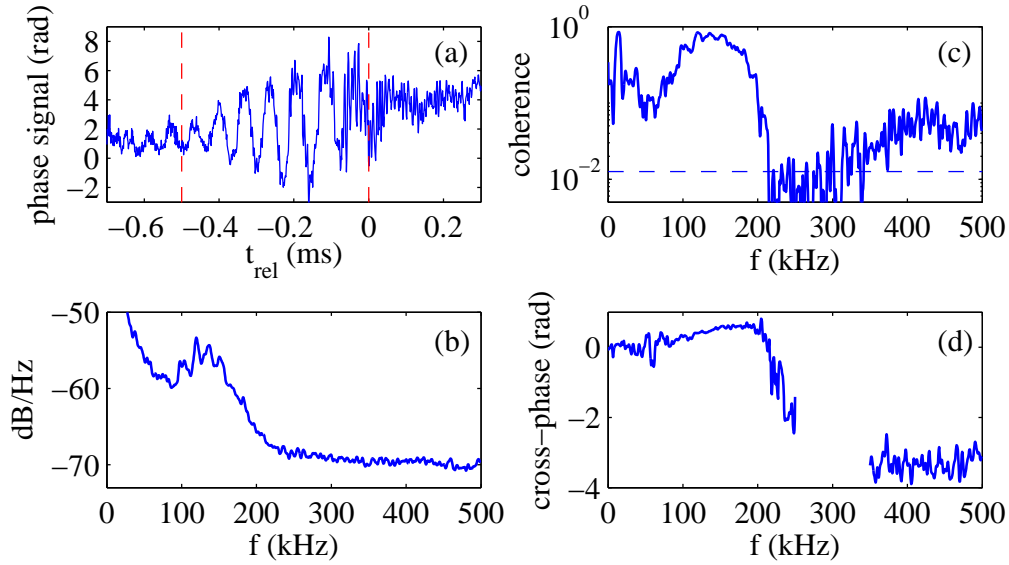


Figure 5.10: (a) Unwrapped reflectometer phase during a fishbone between ELMs (110568). $t_{\text{rel}} = 0$ corresponds to $t = 3.1594$ s. The part between the red dashed lines is one element of an ensemble of 238 such fishbones on which the spectra in (b), (c) and (d) are based. (b) Conditionally averaged spectral power of reflectometer phase signal. (c,d) Conditionally averaged coherence and cross-phase between phase signals from antennas with detection volumes poloidally separated by 2.9° . Dashed line indicates minimum significant coherence.

at all.

5.3.2 Beam ion driven Alfvén modes

For the experiments with $B_t = 1.3$ T, the fishbone mode is invariably joined by a short ($\sim 200 \mu\text{s}$) burst of high frequency MHD activity when it reaches its maximum amplitude. The bursts consist of a sequence of coherent modes, with frequencies between 80 and 200 kHz in the laboratory frame. Like the fishbone, these high frequency modes propagate in the ion diamagnetic drift direction (equation 5.4) and are suppressed during periods of roughly 5 ms after a sawtooth crash. They are not observed in TEXTOR for $B_t > 1.3$ T.

During H-mode, the high frequency modes can be clearly seen in the auto power spectra of reflectometer phase signals (figure 5.10b), while in L-mode they are only evident in cross spectra (figure 5.11). Since the Mirnov coils are digitized only at 200 kHz, the high frequency modes are not resolved in the magnetic spectra, complicating their analysis. After resampling the reflectometer phase at 200 kHz, deliberately aliasing the signal, significant coherence is found with the magnetic signals for the dominant 120 kHz peak in figure 5.10b (aliased at 80 kHz): the two diagnostics do clearly see the same mode. Spatial analysis of these aliased images in the magnetic spectra indicates $m \approx 8$ and $n = 3$, consistent with the sequence of poloidal harmonics with $6 < m < 10$ indicated by the phase signals from reflectometer antennas in the top array.

To establish whether the high frequency modes are toroidicity induced Alfvén eigenmodes (TAE), we wish to test if their frequency in the plasma frame is given by $f_{\text{TAE}} = v_A / (4\pi q R)$ (Heidbrink 2008). Here, v_A is the Alfvén velocity, q is the safety

factor and R the major radius. In general, correction of a mode frequency for the Doppler shift introduced by the plasma rotation requires knowledge the radial localization of the modes, which is unavailable for our experiments. However, the observation of a sequence of modes with toroidal mode numbers ($n, n+1, n+2$, etc.) at frequencies ($f, f+f_p, f+2f_p$, etc.) in the laboratory frame is an indication that these modes have a single frequency $f_0 = f - nf_p$ in the plasma frame, which itself rotates toroidally with a frequency f_p on the flux surface where the modes are excited (Strait et al. 1994).

Such a sequence of modes is seen in figure 5.11a. More careful inspection of the cross spectra of around 2.0 s actually reveals the presence of three modes, at 141, 154 and 167 kHz, although the last mode is not visible for the integration time used in the figure. These mode frequencies would correspond to a plasma rotation frequency $f_p = 13$ kHz, comparable to the measured value of 12 kHz on the magnetic axis for similar experiments. As mentioned earlier, direct magnetic measurements of mode numbers of the high frequency modes are not available. However, the phasing of the phase signals from reflectometer antennas separated toroidally by 90° (both viewing the equatorial plane on the low field side) is consistent with $(n_1, n_2, n_3) = (0, 1, 2)$ or $(4, 5, 6)$ or $(8, 9, 10)$, etc. An Alfvén mode with $n = 0$ is unlikely since it cannot be driven directly by fast ions (Heidbrink 2008). The ∇ symbols in figure 5.11c show the Doppler corrected mode frequency assuming $(n_1, n_2, n_3) = (4, 5, 6)$.

In the calculation of f_{TAE} , q and n_e should be taken at the radial position of maximum mode amplitude. Since we do not have a measurement of the radial mode structure, we employ a range of q and n_e in the calculation, resulting in the f_{TAE} range represented by the shaded area in figure 5.11c. We use $1 < q < 2$, since this is the range for which TAE are reported in the literature (Heidbrink 2008). For the upper and lower bounds on n_e we take the measured values at $r/a = 0$ and $r/a = 0.5$, respectively. The calculated f_{TAE} reproduces the experimentally observed trend, but in absolute value it is typically 1.5 times too high. The disagreement is not resolved by the large error bar of f_{TAE} . In subsection 5.4.1 we argue that the modes may still be TAE.

Reflectometer measurements on NSTX (Crocker et al. 2006) show non-linear interaction between the fishbone mode and high frequency Alfvén waves. To look for such mode coupling in TEXTOR, we have performed bispectral analysis of single reflectometer phase signals. We find significant bispectral coherence only between ELMs in H-mode, when scattering of the microwave beam is weak. In order to discriminate between effects related to the fishbone on the one hand and ELMs on the other, we average over conditionally constructed ensembles containing only the Alfvénic bursts occurring *between* ELMs (0.5 ms window length), resulting in the bispectral coherence spectrum of figure 5.12a. Using the conservative threshold expressed in equation 5.31, the only significant bispectral coherence occurs for the frequency of the fishbone (14 kHz in the laboratory frame), indicated by the white continuous line. The peaks at $f_1 = 14$ kHz and 28 kHz in Fig 5.12b are caused by the first and second harmonic of the fishbone, respectively. For the first harmonic $\arg[\hat{B}] \approx \pi$, so that $\theta \approx \pi/2$ (cf. model signals in section 2.6).

The peaks between 100 and 200 kHz in Fig 5.12b presumably point to interaction between the fishbone and the Alfvén modes, but their interpretation is not clear. The ones at 109 kHz and 140 kHz do not match the frequencies of the features observed in figure 5.10. The three peaks at $f_1 = 170$ -183-196 kHz are spaced by the fishbone frequency. The second order spectra of figure 5.10 show a discernible, though modest feature at

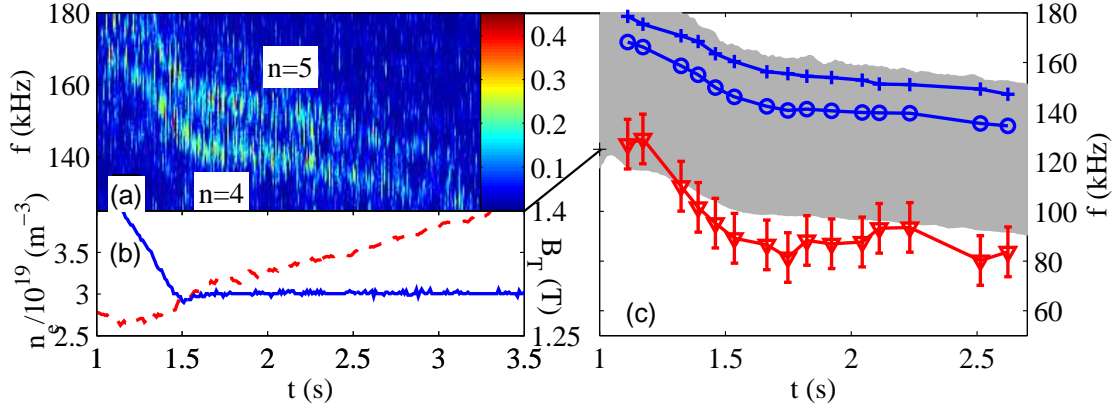


Figure 5.11: (a) Contours of coherence between phase signals from closely spaced reflectometer antennas for shot 112731 ($\gamma_{\min}^2 = 0.04$). (b) Peak electron density (red, dashed) and toroidal magnetic field (blue, continuous). (c) $n = (4, 5)$ frequencies, respectively, in the laboratory frame. ∇ is the Doppler corrected mode frequency in the plasma frame. The shaded area is the calculated frequency range for TAE in the plasma frame.

183 kHz. The biphasic at both $f_1 = 170$ and 183 kHz is 2.2 rad (Fig 5.12c), indicating that the 183 kHz mode could be amplitude modulated by the fishbone. Unfortunately, we have no measurement of the toroidal mode numbers (n_1, n_2) of the coupled Alfvén modes, so we cannot confirm the expected relation $n_2 - n_1 = 1$ (Crocker et al. 2006). In Section 5.4 we will discuss the interpretation of this bispectrum.

5.3.3 Broad-band density fluctuations between ELMs

Figure 5.13 shows the averaged evolution around ELMs of the coherence between phase (a) and amplitude (b) signals from neighbouring antennas. The phase signals (figure 5.13a) show the signatures of the fishbone (14 kHz) and Alfvén modes (between 100 and 200 kHz). All coherence between the phase signals is lost during ELMs (at $t_{\text{rel}} = 0$), but in the 1 ms period before the ELM an additional coherent feature at 23 kHz becomes visible. The timing of this mode with respect to ELMs is confirmed by analysis of the magnetic signals, which are strongly coherent with the reflectometer phase, as shown by the dashed red curve in figure 5.9a. Both magnetics and reflectometer measurements show that the mode propagates in the electron diamagnetic drift direction, i.e. in the opposite direction to the fishbone and Alfvén modes. It has toroidal mode number $n = -2$ and poloidal harmonics $m = -4$ and -5 . The apparent poloidal phase velocity is 33 krad/s in the laboratory frame.

The long wavelength modes (fishbone, Alfvén waves, and the $n = -2$ ELM precursor), which stand out in the coherence spectrum of the phase reflectometer phase signals (figure 5.13a), are invisible in that of the reflectometer amplitude signals (figure 5.13b). This is in agreement with the considerations in subsection 5.2.2. Instead, the coherence

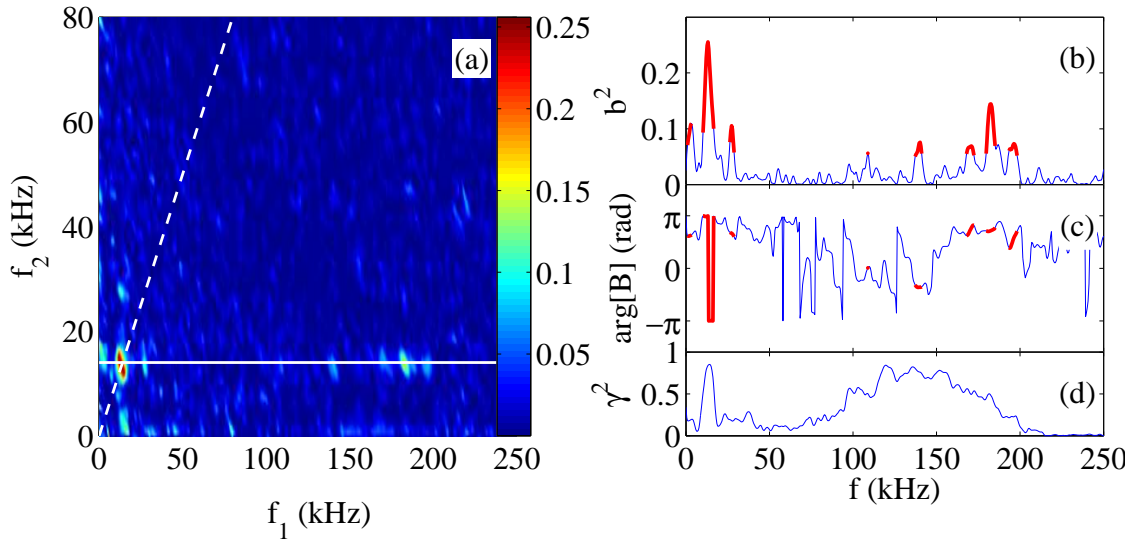


Figure 5.12: (a) Bispectral coherence (equation 5.28) of reflectometer phase signal, conditionally averaged over fishbones occurring *between* ELMs. The ensemble is the same as the one of figure 5.10(b,c,d). The dashed white line delimits the principal domain. (b,c) Bispectral coherence and biphase, respectively, on the continuous white line in (a), which indicates the fishbone frequency. The regions of significant coherence are indicated in red. (d) Second order coherence between phase signals from different antennas (same as figure 5.10c).

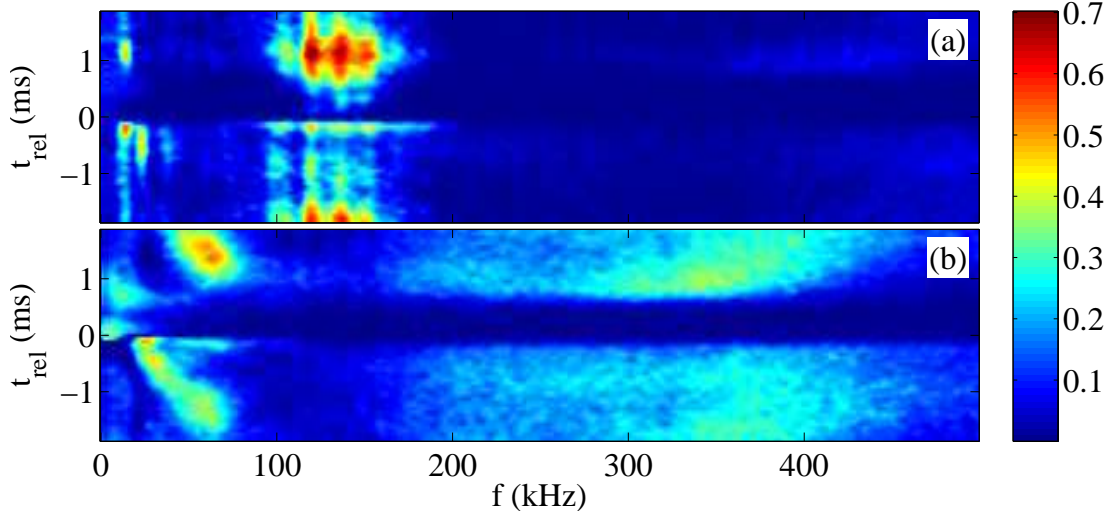


Figure 5.13: Ensemble averaged spectral coherence between phase (a) and amplitude (b) signals for different times relative to the 890 ELMs of discharge 110568 ($\gamma_{\min}^2 = 0.003$). $t_{\text{rel}} = 0$ corresponds to the ELM spike. The antennas are from the top array and have detection volumes that are poloidally separated by 2.1 cm. Each spectrum is calculated on a Hamming window of length 256 μs .

spectrum of the amplitude shows a quasi-coherent, down-chirping feature, whose coherence peaks at the onset of an ELM at $t_{\text{rel}} = 0$. Interestingly, its frequency at $t_{\text{rel}} = 0$ matches that of the previously mentioned coherent ELM precursor mode with $n = -2$. Figure 5.14a shows the auto power spectrum of an amplitude signal, calculated on a 0.5 ms window centered on $t_{\text{rel}} = 1.55$ ms (referring to figure 5.13): the quasi-coherent mode is evident as a peak. The reflectometer amplitude signal from one of the four antennas is not usable due to saturation of its microwave mixer. For the available three antenna combinations the spectral coherence at the peak frequency is shown in figure 5.14b as a function of the poloidal separation $\Delta\theta$ of the respective antennas. Figure 5.14c shows that the corresponding poloidal wave number $k_x \simeq 1 \text{ cm}^{-1}$ (equation 5.4), with propagation in the electron diamagnetic drift direction. Due to the presence of aliased images of the Alfvén modes in this part of the magnetic spectra, we were not able to isolate a possible magnetic component of this mode.

The other striking feature in figure 5.13b is the broad-band coherence of amplitude signals for $f > 200$ kHz in periods between ELMs; the coherence of the phase signals for this range is lower, though still statistically significant. Figure 5.14c suggest a poloidal mode number range $1.0 < k_x < 1.5 \text{ cm}^{-1}$ for this broad-band feature.

Figure 5.15 shows the bispectral coherence (a) and biphase (b) of the reflectometer phase, averaged over windows before ELMs, for shot 110568. In addition to the features related to the fishbone and Alfvén of figure 5.12, we now see features for $f_2 = 23$ kHz, which corresponds to the frequency of the $n = -2$ ELM precursor. The peak at $f_1 = 23$ kHz, which has biphase 2.0 rad, shows the presence and phasing ($\theta = 2.7$ rad, cf.

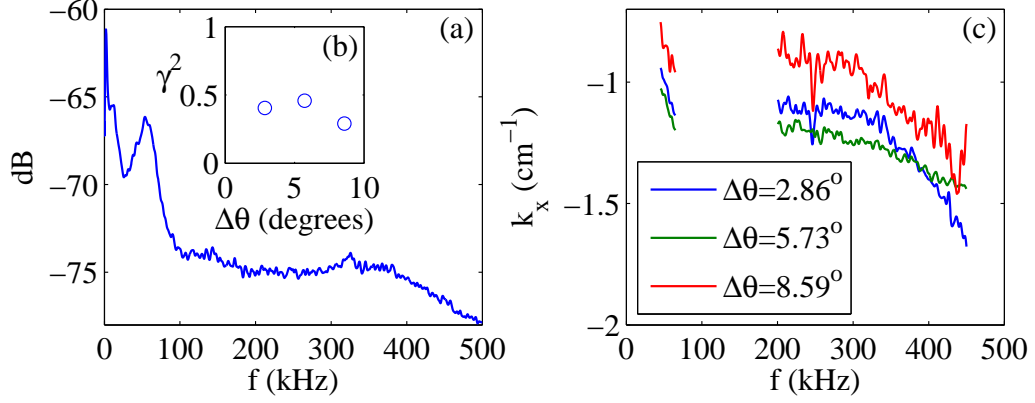


Figure 5.14: Spectra of reflectometer amplitude signals from the top array, averaged on a 0.5 ms window centered on $t_{\text{rel}} = 1.55$ ms of the ensemble of figure 5.13. (a) Auto power spectral density. (b) Coherence γ^2 at peak frequency (54 kHz); $\Delta\theta$ is the poloidal separation of the antenna axes; $\gamma_{\text{min}}^2 = 0.003$. (c) Estimated poloidal wavenumber k_x (equation 5.4) for the same antenna combinations as in (b).

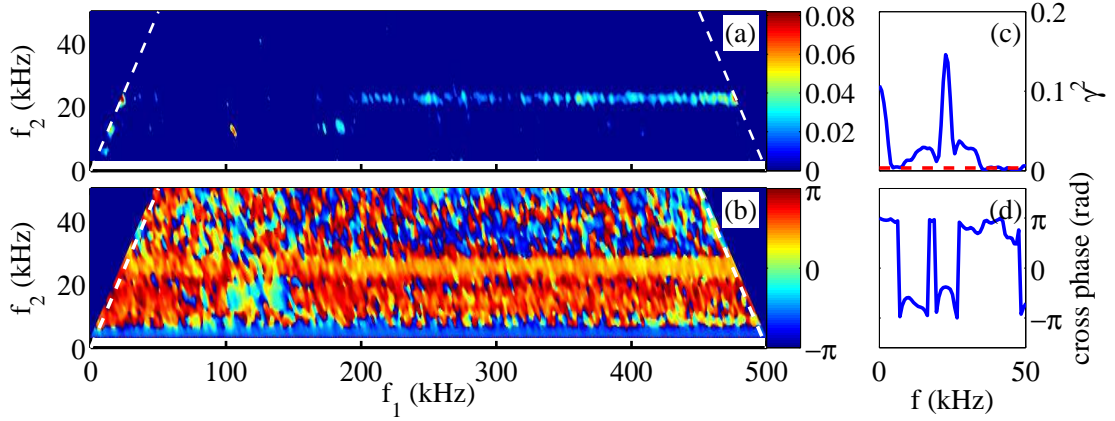


Figure 5.15: Ensemble averaged bispectral coherence b^2 (a) and biphas (b) of the reflectometer phase before ELMs. Only values within the principal domain (delimited by the white dashed line) are shown. In (a), b^2 is set to zero where condition 5.31 is not satisfied. (c) Ensemble averaged coherence between the reflectometer phase signal and the power in its spectral components with $f > 300$ kHz (see text). The dashed, red line indicates γ_{min}^2 . (d) The cross phase corresponding to (c). The ensemble for (a-d) is the same as the one used for figure 5.13a, but using only the data with $-0.5 < t_{\text{rel}} < 0$ ms.

model spectra in subsection 2.6) of its first harmonic. The band of significant bispectral coherence at $f_1 > 200$ kHz has constant biphas $\arg[B(f_1, f_2)] = 1.2$ rad. The same result is obtained from the phase signals from all four reflectometer antennas; by contrast, the reflectometer amplitude signals show no significant bicoherence.

Cross-bispectral analysis between phase and amplitude signals of the type $\hat{B}(k, l) = (1/M) \sum_{i=1}^M X_k^{(i)} Y_l^{(i)} Y_{k+l}^{*(i)}$ has also been performed. Here, X and Y refer to the phase and amplitude Fourier components, respectively (compare to equation 5.27). This shows a very similar strip of significant bicoherence to that of figure 5.15a: the magnitude is similar, as is the trend of a slight increase in coherence towards higher frequency.

The band of bispectral coherence and its biphas is suggestive of amplitude modulation of the broad-band phase signal with $f > 200$ kHz by the $n = -2$ ELM precursor with modulation phase $\theta = -1.2$ rad (cf. section 2.6). The same result is reached by directly looking at the time evolution of the power of spectral components of the reflectometer phase with $f > 200$ kHz, corresponding to the bicoherent spectral region. To easily resolve power fluctuations with 23 kHz we calculate auto power spectra on a moving 10 μ s Hamming window. The poor spectral resolution of this window forces us to integrate only the components with $f > 300$ kHz, in order to avoid spectral leakage from the strong Alfvén modes with $f < 200$ kHz. Figure 5.15c and d show the averaged coherence and cross phase, respectively, of the resulting signal with the reflectometer phase, based on the same ensemble as figure 5.15a and b. The coherence peaks at 23 kHz and the corresponding cross-phase is -1.2 ± 0.3 rad, in agreement with the interpretation of the previously discussed biphas.

5.4 Discussion of experimental results

5.4.1 Beam ion driven modes

We have characterized the quasi periodic bursts of MHD activity that are observed in TEXTOR plasmas with $B_t \leq 2$ T and co-current NBI heating. The bursts are found to be dominated by a ‘fishbone’ mode, which is a common phenomenon in neutral beam heated plasmas (Kass, Bosch, et al. 1998). We have also observed bursts of Alfvénic modes with $n = 3 - 6$, which occur when the fishbone reaches its peak amplitude. This phenomenon has previously been observed on several other tokamaks (Heidbrink, Bol, et al. 1986; Duong et al. 1993; Crocker et al. 2006). The Alfvénic modes are resonantly driven by passing energetic beam ions, whose drift motion satisfies a resonance condition which depends on the mode structure and frequency (Heidbrink 2008). For the plasmas with $B_t = 1.3$ T discussed in this paper, beam ions have $v_{\parallel} \simeq 0.7v_A$ in the plasma core before slowing down. This velocity is high enough for resonance with several types of Alfvénic modes (e.g. TAE, which require $v_{\parallel} = v_A/3$).

The Doppler corrected frequency of the Alfvénic modes is lower than that calculated for TAE (figure 5.11) using the simple relation $f_{\text{TAE}} = v_A/(4\pi qR)$, even when allowing for a large uncertainty in q and n_e . However, this relation does not take into account the effects of finite plasma pressure. The investigated TEXTOR plasmas typically have $\beta_N = \beta_t a B_t / I_p \simeq 3$; in DIII-D this value of β_N leads to observed TAE frequencies which are typically only 60% of $v_A/(4\pi qR)$ (Heidbrink, Strait, et al. 1993). Therefore, the modes described in this paper may still be TAE. Definitive classification of the observed Alfvénic

modes is impossible using the present data, in particular because the absence of magnetic measurements of sufficient temporal resolution means that toroidal mode numbers cannot be accurately measured. Secondly, insufficient sampling rate and low signal-to-noise ratio of the soft X-ray signals preclude determination of the poloidal and radial structure of the modes.

Bispectral analysis of TEXTOR reflectometer phase signals presented in this paper reveals coupling between the 13 kHz, $n = 1$ fishbone and several pairs of Alfvén modes, most prominently the pair with frequencies 183 kHz and 196 kHz in the laboratory frame. In the absence of mode number measurements the expected relation $n_1 + n_2 = n_3$ could not be checked. The peak value of the bicoherence is $b^2 \simeq 0.14$ for $(f_1, f_2) = (13, 183)$ kHz, significantly lower than the figure $b^2 \simeq 0.5$ obtained in the NSTX experiment (Crocker et al. 2006). However, the low bicoherence value may be due to low peak-to-background ratio and does not preclude strong mode coupling. Figure 5.10b shows that the peak-to-background ratio in the reflectometer phase spectrum of the coupled Alfvén modes is only a few dB, compared to $\simeq 20$ dB shown in (Crocker et al. 2006).

To explore how the low observed peak-to-background ratio may impact our bicoherence estimate, we consider three perfectly coupled sinusoids in the presence of a noise signal $\tilde{p}(t)$ with power spectral density $P(f)$:

$$\tilde{x}(t) = A \sin(\Omega_0 t + \tilde{\phi}) + B \sin(\Omega_1 t + \tilde{\psi}) + C \sin([\Omega_0 + \Omega_1]t + \tilde{\phi} + \tilde{\psi} + \theta) + \tilde{p}(t). \quad (5.34)$$

We evaluate the bicoherence of $\tilde{x}(t)$ using a spectral window with resolution Δf , giving

$$b^2(\Omega_0, \Omega_1) = \left(1 + \frac{P(\Omega_0)\Delta f}{(A/2)^2} + \frac{P(\Omega_1)\Delta f}{(B/2)^2} \left[1 + \frac{P(\Omega_0)\Delta f}{(A/2)^2} \right] \right)^{-1} \left(1 + \frac{P(\Omega_0 + \Omega_1)\Delta f}{(C/2)^2} \right)^{-1}. \quad (5.35)$$

Now we assume that the noise signal $\tilde{p}(t)$ is uncorrelated between antennas, while the sinusoids remain perfectly correlated. This allows us to estimate the inverse peak-to-background ratios through the coherence of figure 5.12d, which was evaluated using the same ensemble and spectral window as the bicoherence of figure 5.12a. Taking $\Omega_0/(2\pi) = 13$ kHz and $\Omega_1/(2\pi) = 183$ kHz, we find $P(\Omega_0)\Delta f(A/2)^{-2} \approx \gamma^{-1}(\Omega_0) - 1 \simeq 0.05$; similarly, $P(\Omega_1)\Delta f(B/2)^{-2} \simeq 0.41$ and $P(\Omega_0 + \Omega_1)\Delta f(C/2)^{-2} \simeq 1.0$. Substitution in equation 5.35 then shows that, even for perfectly coupled modes, we can not expect the bicoherence to exceed $b^2 \simeq 0.34$ in figures 5.12a and b. This shows that the coupling of the Alfvén waves to the fishbone may be stronger than suggested by the measured bicoherence.

We have found a strong correlation on TEXTOR between the fishbone and ELMs. The existence of this link on TEXTOR has been reported before (Soldatov, Krämer-Flecken, Kantor, et al. 2010), but in that publication the fishbone and Alfvénic modes were not identified. Synchronisation between fishbones and ELMs has previously been observed in NBI heated plasmas on Asdex-Upgrade (Kass, Bosch, et al. 1998) and JT-60U (Matsunaga, Shinohara, et al. 2010). Note that in the latter publication the mode triggering the ELMs is not referred to as ‘fishbone’, but rather as ‘energetic particle driven wall mode’ (EWM). Presumably the reason for this is that the investigated JT-60U plasmas do not have a $q = 1$ surface and the amplitude of the mode is radially peaked around $q = 2$ rather than $q = 1$. However, the EWM is a down-chirping, trapped beam-ion driven $n = 1$ mode and is phenomenologically very similar to the fishbones observed in TEXTOR and ASDEX-Upgrade.

On all three machines partial synchronisation occurs for plasmas with $\beta_N = \beta_t a B_t / I_p \geq 2.5$ and for the ASDEX-Upgrade experiments it is reported explicitly that no synchronisation occurs for $\beta_N < 2.5$. Another common observation is that the fishbone starts to grow significantly before the ELM appears on the D_α signal, suggesting that the fishbone triggers the ELM and not vice versa. This hypothesis is also supported by the observation that on JT-60U the ELM interval and energy content decrease significantly after the fishbone is destabilized (Matsunaga, Aiba, et al. 2010). Both groups speculate (Kass, Bosch, et al. 1998; Matsunaga, Aiba, et al. 2010) that a fishbone event can trigger an ELM by transiently increasing the edge pressure gradient.

Remarkably, on TEXTOR we observe that fishbones in L-mode also trigger spikes in recycling rate (figure 5.8a). Apart from their link to the fishbone, these L-mode spikes resemble the ELMs in H-mode in several respects: they have similar repetition frequency and they coincide with a similar transient dip in the plasma current and edge density. To our knowledge, the only published mention of ELM-like recycling spikes occurring in L-mode is from ASDEX-Upgrade (Kass, Günter, et al. 1998), where they were identified as type-III ELMs by their magnetic precursor modes. Our magnetic measurements on TEXTOR are compromised by folded images of the strong Alfvén activity, constituting a severe limitation of our analysis possibilities.

An important question is to what extent the L-mode spikes affect confinement. Contrary to the ELMs in H-mode (Soldatov, Krämer-Flecken, Kantor, et al. 2010), the L-mode spikes do not stand out in the density and temperature profile evolution measured with the TEXTOR high resolution Thomson scattering system. Conditional averaging of these data over more than four spikes is impossible, since the Thomson data are only available on 8 ms windows for each discharge. Unfortunately, diamagnetic loop measurements of the energy content of the plasma are unavailable for the experiments discussed in this paper: quantitative analysis of possible changes in confinement resulting from the L-mode spikes would require additional experiments.

It may be noted that fast ions expelled by instabilities such as fishbones or TAE can charge-exchange with neutrals at the plasma periphery and produce bursts of D_α light (Heidbrink, McKee, et al. 2011). This could potentially lead to confusion between fishbones and ELMs in our analysis, since we use the D_α signal for ELM-detection. Fortunately, the effect appears to be negligible for our experiments, since fishbones occurring between ELMs are invisible in the D_α signal (figure 5.8, $t=3.2015$ s).

5.4.2 Broad-band density fluctuations between ELMs

Bispectral analysis of the reflectometer phase (figure 5.15a-c) indicates that the $n = -2$ ELM precursor modulates the amplitude of broad-band density fluctuations in the pedestal. A global plasma mode well known to modulate turbulence by fluctuating $E \times B$ shear is the geodesic acoustic mode (GAM) (Diamond et al. 2005). GAMs have been extensively studied in Ohmic TEXTOR plasmas, using the multi-antenna reflectometer (Krämer-Flecken, Soldatov, Reiser, et al. 2009). Published bispectra of floating potential traces from Langmuir probes on the JFT-2M tokamak (Nagashima et al. 2006) during experiments where a GAM was shown to modulate small scale ($k_x \approx 1 \text{ cm}^{-1}$) turbulence, bear a striking resemblance to figure 5.15a. For a plasma with circular cross-section the GAM frequency is given by $f_{\text{GAM}} = (2\pi R_0)^{-1} \sqrt{2(T_e + T_i)/m_i}$ (Conway, Scott, et al.

2005). Temperatures around the cutoff layer in the H-mode experiments discussed in the present paper are 200-300 eV, which would give $20 < f_{\text{GAM}} < 24$ kHz for a hypothetical GAM, corresponding quite well to the observed frequency of our ELM precursor mode. But since the GAM has a standing wave structure in the laboratory frame with $n = 0$ and $m = 1$, we must clearly discard it as a candidate for the observed $n = -2$ ELM precursor, which remains as yet unidentified.

The fact that the down-chirping ELM precursor of figure 5.13b stands out clearly in the reflectometer amplitude signals is consistent with the estimated value (6 cm) of the poloidal wavelength, based on the cross phase of amplitude signals from different antennas (figure 5.14b). A mode with that wavelength is expected to produce phase and amplitude modulation in roughly equal measure for the TEXTOR geometry (Soldatov et al. 2009), but the phase component may well be drowned in the $1/f^2$ Brownian noise resulting from phase-runaway (cf. 5.1.2). Spectral broadening precludes interpretation of the decay of coherence in Fig 5.14b in terms of the coherence length of the mode (cf. equation 5.9).

Modulation of the global turbulence level would also lead to modulation of the reflectometer amplitude signals by rhythmic suppression of the specular reflection (cf. equation 5.8); however, this mechanism is inconsistent with the observed non-zero phasing in figure 5.14c.

Precursors to both type-I and type-III ELMs have been observed in various tokamaks (Reimerdes et al. 1998; Kass, Günter, et al. 1998; Coda et al. 2001; Antar et al. 2009). All of the modes mentioned in these publications have $5 < n < 15$, while the corresponding poloidal mode numbers are generally too high to be resolved by Mirnov coil arrays. Recent measurement with ECE imaging in the KSTAR tokamak show the appearance in the pedestal, before ELMs, of a mode with a poloidal wavelength of roughly 10 cm (Yun et al. 2011). This structure, which is thought to be a manifestation of so-called peeling-ballooning modes, can persist in a saturated state for several 100 μs , before several filaments grow explosively and initiate the ELM. A similar filamentary structure could be responsible for the ELM precursor on TEXTOR.

Chapter 6

Summary and suggestions for future work

Fluctuation measurements have been performed for the first time with the novel tangential phase-contrast imaging (TPCI) diagnostic in the TCV tokamak. As discussed in this thesis, the performance of the diagnostic during these experiments was sub-optimal due to various technical issues. Nevertheless, several clear physics results on plasma turbulence and zonal flows have been obtained and discussed. In a second project coherent mode activity linked to the TEXTOR ELM-cycle was explored by correlation reflectometry, revealing new and unexpected phenomenology.

6.1 Summary

A novel tangential phase-contrast imaging system had previously been installed in TCV. The instrument measures line-integrated density fluctuations along 9 chords within a 6 cm diameter CO₂ laser beam. The physical principles, hardware and commissioning process of the TPCI diagnostic have been described in this thesis. It was found that the in-vessel mirrors introduced significant optical aberrations. Unfortunately, these components could not be replaced in time for the first TPCI measurements performed for this thesis work. A part of the aberrations could however be compensated using corrective optics, and the impact of the remaining aberrations was reduced by the use of a wider phase plate groove. As a result, the spatial high-pass cutoff frequency of the instrument response was 2.59 cm⁻¹ instead of the originally planned 0.75 cm⁻¹.

The first study with the TPCI diagnostic in TCV consisted of turbulence measurements in a series of X2 heated L-mode discharges with positive and negative triangularity, which are known to have very different energy confinement time. By moving the plasma position vertically, the measurement volume was scanned radially through the plasma. Unfortunately, most of the signal arose from fluctuations with wave numbers below the instrument cutoff, so that the spatial structure of the turbulence could not be established. The autocorrelation spectra of the TPCI signals are much weaker and broader for $\delta = -0.4$ than for $\delta = +0.4$ discharges, qualitatively consistent with a reduced turbulence level.

In the same $\delta = +0.4$ discharges, the geodesic acoustic mode (GAM) was identified

in the TPCI signals. This constitutes the first observation of this mode in TCV. The magnetic component of the GAM is clearly measurable and shows strong coherence with the TPCI signal. A subsequent study of the magnetic signals in the TCV database revealed the mode in a large number of previous discharges, which allowed confirmation of the signature c_s/R frequency scaling of the mode. The magnetic field of the turbulence-driven GAMs had previously been observed in a single-point measurement in the T-10 tokamak, but our measurements constitute the first ones with spatial resolution. Poloidally, the mode has a standing wave structure, with strong antinodes for $\theta = \pm 140^\circ$. At the poloidal angle corresponding to these antinodes, the toroidal mode number is clearly $n = 0$, as expected. For some discharges, clear antinodes were also observed for $\theta = (0^\circ, 180^\circ, \pm 90^\circ)$. This is in agreement with the expected $m/n = 2/0$ MHD structure of the GAM. However, strong $n = \pm 1$ sidebands are also observed.

Using the TPCI measurements, the radial mode structure of the GAM could be established. The mode is visible for $\rho_{\text{vol}} > 0.6$ and its amplitude grows steadily up to $\rho_{\text{vol}} = 0.85$, which is the outermost point for which we presently have measurements. The mode frequency is constant over this range (typically 26 kHz). A radial wavelength of ~ 3 cm was measured, but this must be considered as an upper limit, since the measurements were affected by spectral broadening. The GAM propagates radially outward. The existence of the GAM as a discrete, strongly coherent, and outward propagating radial eigenmode of the TCV plasma is in excellent agreement with a simulation with the gyro-kinetic particle-in-cell code ORB5, using the experimental equilibrium. Some discrepancies exist on the absolute frequency and the radial extent of the mode, which must be investigated further.

The second project discussed in this thesis is a study of coherent modes during the ELM-cycle in limited, NBI heated TEXTOR plasmas. At sufficiently weak toroidal magnetic field, these plasmas were found to exhibit bursts of beam-ion driven ‘fishbone’ and Alfvén modes, which were characterized for the first time using the multi-antenna reflectometer and Mirnov coils. In H-mode the fishbone was found to trigger ELMs. Surprisingly, in L-mode it triggers previously unobserved bursts of particle recycling, resembling the ELMs. Bispectral analysis of the reflectometer phase signals was performed, showing non-linear coupling between the fishbone and Alfvén waves.

Additionally, using conditional averaging techniques, two ELM precursor modes were found that are not related to the beam-ions. The first is a coherent mode with toroidal mode number $n = -2$, which is also seen with the Mirnov coils. Bispectral analysis of the reflectometer signals showed that this mode modulates the amplitude of broad-band turbulence in the pedestal. The second ELM precursor is a semi-coherent, down-chirping mode with a poloidal wavelength of 6 cm.

6.2 Suggestions for future work

The performance of the TPCI diagnostic was far from optimal during the experiments described in this thesis. The optical aberrations introduced by the in-vessel mirrors have since been corrected and the mirror mounts have been remade to reduce the amplitude of focal vibrations. At the time of this writing it remains to be seen if these modifications will have the desired effect. If they do, it will allow aberration-free operation with the BaF₂ phase plate (300 μm full groove-width), as originally envisioned. This will improve

the sensitivity by a factor of six, and reduce the high-pass cutoff wavenumber of the instrument from 2.59 cm^{-1} to 0.75 cm^{-1} . The latter improvement in particular is critical, since most of the plasma fluctuation spectrum was not properly covered in the experiments of this thesis. We also plan to purchase a new 32- or 64-element detector array to replace the current one, in which only nine elements remain operational.

To exploit the tangential geometry of the TPCI diagnostic, spatial filtering in a focal plane is required. During the experiments described in this thesis a few measurements have already been performed with a filter in place, but its alignment with the focal spot was not sufficiently accurate, and the measurements could not be used. Further, the angular orientation of the projection of the detector array in the plasma has thus far only been accurate to within $\pm 10\%$. This figure will have to be improved for future experiments with spatial filtering, requiring in-vessel observations. It would also be extremely useful if the orientation of phase plate, filter and detector array could be changed between shots without losing alignment with the optical axis. This would require a carefully designed mounting scheme and/or a large dove prism.

A final important hardware issue is the stability of the optical path. The feedback vibration-control system compensates for small shifts in alignment, but we also frequently observed large, permanent shifts, which required manual realignment of the system between discharges. This issue must be resolved to make routine TPCI operation practical.

The relative simplicity of the GAM makes it an attractive subject for further study, which will likely yield novel results with limited effort. Future TPCI measurements should certainly be performed with a narrower phase-groove, to be able to confirm the radial wavelength. If properly aligned, a measurement with a spatial filter could also confirm unambiguously that the wave vector of the mode is indeed purely radial. The global gyrokinetic simulation discussed in this thesis shows a marked decrease in GAM amplitude and wavelength beyond a certain radius. Thus far, the TPCI measurements were not sensitive to radial modes in very edge of the plasma, but a slight modification of the vertical displacement of the plasma during the discharge will allow radial coverage up to the scrape-off layer. If the reduction in amplitude and wavelength is real, it will definitely be visible in such an experiment. This would constitute a valuable experimental confirmation of a gyro-kinetic simulation.

More refined simulations of the GAM in TCV are envisioned, which may improve the agreement with the experimentally observed absolute mode frequency and radial extent. Preferably, such simulations would employ a synthetic diagnostic of the TPCI signals. The required software already exists for the GENE code, and may be easily adapted for use in the global ORB5 code. It may also be mentioned that a Doppler reflectometer has been recently installed in TCV: this instrument allows measurement of the mean and fluctuating $\mathbf{E} \times \mathbf{B}$ velocity, which can be directly and quantitatively compared to the simulation results.

The shape of the poloidal section of the plasma is known to have an important effect on the GAM frequency and amplitude. A dedicated study in TCV could vastly extend the range of accessible shapes, adding to our knowledge about zonal flows.

Simulations with a synthetic diagnostic, as well as the practical implementation of the spatial filtering technique, will also play a vital role in the more ambitious effort of characterising broadband turbulence in TCV. The TPCI diagnostic allows the study of the gradient region in plasmas with an electron internal transport barrier (eITB). In fact,

Chapter 6. Summary and suggestions for future work

a series of dedicated eITB discharges has already been performed, but the data remain to be analysed.

Acknowledgements

First and foremost I wish to thank my supervisor Stefano Coda, without whom most of the work described in this thesis would have been impossible. Stefano is a patient and very reliable man, and he stood up for me on numerous occasions. His exceptional competence and engagement have been a source of inspiration throughout my time at the CRPP. Working with him has been a pleasure and a true privilege.

I am also grateful to Andreas Krämer-Flecken and Sergey Soldatov for allowing me to exploit their reflectometer diagnostic in TEXTOR and hosting me in Jülich. I gratefully acknowledge valuable discussions on various physics subjects with Laurent Villard, Evgeniy Gusakov, Pascale Hennequin, Ambrogio Fasoli, Holger Reimerdes and Duccio Testa. Federico Felici and Wouter Vijvers supported me with good advice on various subjects, and Mattia Albergante helped me by performing simulations of fast ions in TEXTOR. I further owe thanks to the entire technical and administrative staffs of the CRPP, but in particular to Yanis Andrebe. Various scientific equipment was kindly lent to me from outside the lab by Tobias Kippenberg, Stefan Weis, Miklos Porkolab, Hervé Lissek and Xavier Fallourd.

My predecessor on the TPCI project was Alessandro Marinoni, who designed and built the diagnostic together with Stefano Coda. Over the last year I have had the pleasure of working closely with my successor Zhouji Huang, who has greatly helped me both in the laboratory and with data analysis. I am grateful to Jon Graves for his interest in my work and for introducing me to Christer Wahlberg, who had previously developed the theory of the magnetic component of the GAM. Following a valuable suggestion by Stephan Brunner, Thibaut Vernay performed gyrokinetic simulations of the TCV plasma which I had investigated experimentally. Finding partial agreement between these simulations and my measurements was an exciting and very rewarding experience.

Thanks to the Swiss taxpayers I was able to live a princely life in their gorgeous country. My local social life I owe to Martijn Bosch and Dávid Wágner. Finally, I want to thank my friends and family in the Netherlands for their support, especially my parents.

Lausanne, 19 December 2012

Bibliography

- Angelino, P. et al. (2006). “Effects of plasma current on nonlinear interactions of ITG turbulence, zonal flows and geodesic acoustic modes.” In: *Plasma Phys. Controlled Fusion* 48.5, pp. 557–571. URL: <http://stacks.iop.org/0741-3335/48/557>.
- Antar, G. Y. et al. (2009). “On the onset of type I edge localized modes.” In: *Nuclear Fusion* 49.3, p. 032001. URL: <http://stacks.iop.org/0029-5515/49/i=3/a=032001>.
- Anton, M. et al. (1996). “X-ray tomography on the TCV tokamak.” In: *Plasma Physics and Controlled Fusion* 38.11, p. 1849. URL: <http://stacks.iop.org/0741-3335/38/i=11/a=001>.
- Bendat, J. S. and A. G. Piersol (2010). *Random Data: Analysis and Measurement Procedures*. Wiley Series in Probability and Statistics. Wiley. ISBN: 9780470248775. URL: http://books.google.ch/books?id=iu7pq6_vo3QC.
- Berk, H. L. et al. (2006). “Explanation of the JET $n = 0$ chirping mode.” In: *Nuclear Fusion* 46.10, S888. URL: <http://stacks.iop.org/0029-5515/46/i=10/a=S04>.
- Bing-Ren, S., L. Ji-Quan, and D. Jia-Qi (2005). “Geodesic Acoustic Mode in Toroidally Axisymmetric Plasmas with Non-Circular Cross Sections.” In: *Chinese Physics Letters* 22.5, p. 1179. URL: <http://stacks.iop.org/0256-307X/22/i=5/a=043>.
- Boswell, C. J. et al. (2006). “Observation and explanation of the JET chirping mode.” In: *Physics Letters A* 358.2, pp. 154–158. ISSN: 0375-9601. DOI: 10.1016/j.physleta.2006.05.030. URL: <http://www.sciencedirect.com/science/article/pii/S0375960106007031>.
- Burrell, K. H. et al. (1989). “Confinement physics of H-mode discharges in DIII-D.” In: *Plasma Physics and Controlled Fusion* 31.10, p. 1649. URL: <http://stacks.iop.org/0741-3335/31/i=10/a=012>.
- Bush, C. E. et al. (July 1990). “Peaked density profiles in circular-limiter H modes on the TFTR tokamak.” In: *Phys. Rev. Lett.* 65 (4), pp. 424–427. DOI: 10.1103/PhysRevLett.65.424. URL: <http://link.aps.org/doi/10.1103/PhysRevLett.65.424>.
- Camenen, Y., A. Bortolon, et al. (2010). “Experimental demonstration of an up-down asymmetry effect on intrinsic rotation in the TCV tokamak.” In: *Plasma Physics and Controlled Fusion* 52.12, p. 124037. URL: <http://stacks.iop.org/0741-3335/52/i=12/a=124037>.
- Camenen, Y., A. Pochelon, et al. (2007). “Impact of plasma triangularity and collisionality on electron heat transport in TCV L-mode plasmas.” In: *Nuclear Fusion* 47.7, p. 510. URL: <http://stacks.iop.org/0029-5515/47/i=7/a=002>.
- Censor, Y. (1981). “Row-Action Methods for Huge and Sparse Systems and Their Applications.” English. In: *SIAM Review* 23.4, pp. 444–466. ISSN: 00361445. URL: <http://www.jstor.org/stable/2029650>.

BIBLIOGRAPHY

- Chapman, I. T. et al. (2008). “Sawtooth stability in neutral beam heated plasmas in TEXTOR.” In: *Nuclear Fusion* 48.3, p. 035004. URL: <http://stacks.iop.org/0029-5515/48/i=3/a=035004>.
- Chen, F. F. (1984). *Introduction to Plasma Physics and Controlled Fusion*. Introduction to Plasma Physics and Controlled Fusion v. 1. Springer. ISBN: 9780306413322. URL: <http://books.google.ch/books?id=ToAtqznzr80C>.
- Coda, S. (1997). “An experimental study of turbulence by phase-contrast imaging in the DIII-D tokamak.” PhD thesis. Massachusetts Institute of Technology.
- (2008). “Fully Bootstrap Discharge Sustainment in Steady State in the TCV Tokamak.” In: *22nd IAEA Fusion Energy Conference, Geneva*. EX/2-3.
- Coda, S., E. Asp, et al. (2007). “The physics of electron internal transport barriers in the TCV tokamak.” In: *Nuclear Fusion* 47.7, p. 714. URL: <http://stacks.iop.org/0029-5515/47/i=7/a=023>.
- Coda, S., M. Porkolab, and K.H. Burrell (2001). “Characterization of density fluctuations during ELMs in the DIII-D tokamak.” In: *Nucl. Fusion* 41.12, p. 1885. URL: <http://stacks.iop.org/0029-5515/41/i=12/a=316>.
- Conway, G. D., C. Angioni, et al. (2011). “Mean and Oscillating Plasma Flows and Turbulence Interactions across the *L-H* Confinement Transition.” In: *Phys. Rev. Lett.* 106 (6), p. 065001. DOI: 10.1103/PhysRevLett.106.065001. URL: <http://link.aps.org/doi/10.1103/PhysRevLett.106.065001>.
- Conway, G. D. and the ASDEX Upgrade Team (2008). “Amplitude behaviour of geodesic acoustic modes in the ASDEX Upgrade tokamak.” In: *Plasma Phys. Controlled Fusion* 50.8, 085005 (11pp). URL: <http://stacks.iop.org/0741-3335/50/085005>.
- Conway, G. D., B. Scott, et al. (2005). “Direct measurement of zonal flows and geodesic acoustic mode oscillations in ASDEX Upgrade using Doppler reflectometry.” In: *Plasma Phys. Controlled Fusion* 47.8, pp. 1165–1185. URL: <http://stacks.iop.org/0741-3335/47/1165>.
- Conway, G. D., C. Tröster, et al. (2008). “Frequency scaling and localization of geodesic acoustic modes in ASDEX Upgrade.” In: *Plasma Phys. Controlled Fusion* 50.5, 055009 (18pp). URL: <http://stacks.iop.org/0741-3335/50/055009>.
- Crocker, N. A. et al. (July 2006). “Three-Wave Interactions between Fast-Ion Modes in the National Spherical Torus Experiment.” In: *Phys. Rev. Lett.* 97.4, p. 045002. DOI: 10.1103/PhysRevLett.97.045002.
- Dannert, T. and F. Jenko (2005). “Gyrokinetic simulation of collisionless trapped-electron mode turbulence.” In: *Physics of Plasmas* 12.7, 072309, p. 072309. DOI: 10.1063/1.1947447. URL: <http://link.aip.org/link/?PHP/12/072309/1>.
- Delabie, E. et al. (2008). “Charge exchange spectroscopy as a fast ion diagnostic on TEXTOR.” In: *Rev. Sci. Instrum.* 79.10, 10E522, 10E522. DOI: 10.1063/1.2955575. URL: <http://link.aip.org/link/?RSI/79/10E522/1>.
- Diamond, P. H. et al. (2005). “Zonal flows in plasmas; a review.” In: *Plasma Phys. Controlled Fusion* 47.5, R35–R161. URL: <http://stacks.iop.org/0741-3335/47/R35>.
- Dorris, J. R., J. C. Rost, and M. Porkolab (2009). “Localized measurement of short wavelength plasma fluctuations with the DIII-D phase contrast imaging diagnostic.” In: *Rev. Sci. Instrum.* 80.2, 023503, p. 023503. DOI: 10.1063/1.3065094. URL: <http://link.aip.org/link/?RSI/80/023503/1>.

- Duong, H.H. et al. (1993). “Loss of energetic beam ions during TAE instabilities.” In: *Nucl. Fusion* 33.5, p. 749. URL: <http://stacks.iop.org/0029-5515/33/i=5/a=I06>.
- Elmore, W.C. and M.A. Heald (1985). *Physics of Waves*. Dover Books on Physics Series. Dover Publications. ISBN: 9780486649269. URL: <http://books.google.ch/books?id=SLFCpTaEoDAC>.
- Felici, F. et al. (2012). “Integrated real-time control of MHD instabilities using multi-beam ECRH/ECCD systems on TCV.” In: *Nuclear Fusion* 52.7, p. 074001. URL: <http://stacks.iop.org/0029-5515/52/i=7/a=074001>.
- Finken, K.H. et al. (2007). “Influence of the dynamic ergodic divertor on transport properties in TEXTOR.” In: *Nucl. Fusion* 47.7, p. 522. URL: <http://stacks.iop.org/0029-5515/47/i=7/a=004>.
- Fischer, O. et al. (2002). “Neoclassical transport and alpha particle confinement in novel 3-D reactor systems.” In: *Nucl. Fusion* 42.7, p. 817. URL: <http://stacks.iop.org/0029-5515/42/i=7/a=304>.
- Freidberg, J. P. (2007). *Plasma Physics and Fusion Energy*. Cambridge University Press.
- Fujisawa, A. (2009). “A review of zonal flow experiments.” In: *Nuclear Fusion* 49.1, p. 013001. URL: <http://stacks.iop.org/0029-5515/49/i=1/a=013001>.
- Gao, Z. et al. (2008). “Eigenmode analysis of geodesic acoustic modes.” In: *Physics of Plasmas* 15.7, 072511, p. 072511. DOI: 10.1063/1.2956993. URL: <http://link.aip.org/link/?PHP/15/072511/1>.
- Garcia, O.E. et al. (2007). “Fluctuations and transport in the TCV scrape-off layer.” In: *Nucl. Fusion* 47.7, pp. 667–676. URL: <http://stacks.iop.org/0029-5515/47/667>.
- Ginzburg, V.L. (1964). *The propagation of electromagnetic waves in plasmas*. International series of monographs on electromagnetic waves. Pergamon Press. URL: <http://books.google.ch/books?id=xVx5AAAAIAAJ>.
- Goldsmith, P.F. (1992). “Quasi-optical techniques.” In: *Proc. IEEE* 80.11, pp. 1729–1747. ISSN: 0018-9219. DOI: 10.1109/5.175252.
- Goodman, J. W. (Aug. 14, 2000). *Statistical Optics (Wiley Classics Library)*. 1st ed. Wiley-Interscience. ISBN: 0471399167. URL: <http://www.worldcat.org/isbn/0471399167>.
- (2005). *Introduction To Fourier Optics*. McGraw-Hill physical and quantum electronics series. Roberts & Company. ISBN: 9780974707723. URL: http://books.google.ch/books?id=ow5xs_Rtt9AC.
- Goodman, T.P. and the TCV team (2008). “Experience in integrated control of the multi-megawatt electron cyclotron heating system on the TCV tokamak: the first decade.” In: *Nuclear Fusion* 48.5, p. 054011. URL: <http://stacks.iop.org/0029-5515/48/i=5/a=054011>.
- Graves, J. P. et al. (2005). “Self-similar density turbulence in the TCV tokamak scrape-off layer.” In: *Plasma Physics and Controlled Fusion* 47.3, p. L1. URL: <http://stacks.iop.org/0741-3335/47/i=3/a=L01>.
- Guo, W., S. Wang, and J. Li (2010). “Effect of impurity ions on the geodesic acoustic mode.” In: *Physics of Plasmas* 17.11, 112510, p. 112510. DOI: 10.1063/1.3493631. URL: <http://link.aip.org/link/?PHP/17/112510/1>.
- Gurchenko, A. D. et al. (2010). “Observation of turbulence exponential wave number spectra at ion sub-Larmor scales in FT-2 tokamak.” In: *Plasma Physics and Controlled Fusion* 52.3, p. 035010. URL: <http://stacks.iop.org/0741-3335/52/i=3/a=035010>.

BIBLIOGRAPHY

- Gusakov, E. Z. (2012). Private communication.
- Gusakov, E. Z. and A Yu Popov (2002). “Non-linear theory of fluctuation reflectometry.” In: *Plasma Phys. Controlled Fusion* 44.11, pp. 2327–2337. URL: <http://stacks.iop.org/0741-3335/44/2327>.
- (2004). “Two-dimensional non-linear theory of radial correlation reflectometry.” In: *Plasma Phys. Controlled Fusion* 46.9, pp. 1393–1408. URL: <http://stacks.iop.org/0741-3335/46/1393>.
- (2006). “Measurements localization in poloidal correlation reflectometry.” In: *Nucl. Fusion* 46.9, S829–S835. URL: <http://stacks.iop.org/0029-5515/46/S829>.
- Hahn, T. S. et al. (1999). “Shearing rate of time-dependent E x B flow.” In: *Physics of Plasmas* 6.3, pp. 922–926. DOI: 10.1063/1.873331. URL: <http://link.aip.org/link/?PHP/6/922/1>.
- Hamada, Y., A. Nishizawa, et al. (2005). “Zonal flows in the geodesic acoustic mode frequency range in the JIPP T-IIU tokamak plasmas.” In: *Nuclear Fusion* 45.2, p. 81. URL: <http://stacks.iop.org/0029-5515/45/i=2/a=002>.
- Hamada, Y., T. Watari, et al. (2011). “Detection of the kinetic geodesic acoustic mode (KGAM) near the centre region of JIPPT-IIU tokamak plasmas.” In: *Nuclear Fusion* 51.3, p. 033005. URL: <http://stacks.iop.org/0029-5515/51/i=3/a=033005>.
- Hartfuss, H. J., T. Geist, and M. Hirsch (1997). “Heterodyne methods in millimetre wave plasma diagnostics with applications to ECE, interferometry and reflectometry.” In: *Plasma Physics and Controlled Fusion* 39.11, p. 1693. URL: <http://stacks.iop.org/0741-3335/39/i=11/a=001>.
- Heidbrink, W. W. (May 2008). “Basic physics of Alfvén instabilities driven by energetic particles in toroidally confined plasmas.” English. In: *Physics of Plasmas* 15.5. 49th Annual Meeting of the Division of Plasma Physics of the American-Physical-Society, Orlando, FL, NOV 12-16, 2007, pp. 055501–1. ISSN: 1070-664X. DOI: 10.1063/1.2838239.
- Heidbrink, W. W., K. Bol, et al. (Aug. 1986). “Tangential Neutral-Beam-Driven Instabilities in the Princeton Beta Experiment.” In: *Phys. Rev. Lett.* 57.7, pp. 835–838. DOI: 10.1103/PhysRevLett.57.835.
- Heidbrink, W. W., G. R. McKee, et al. (2011). “‘Beam-emission spectroscopy’ diagnostics also measure edge fast-ion light.” In: *Plasma Physics and Controlled Fusion* 53.8, p. 085007. URL: <http://stacks.iop.org/0741-3335/53/i=8/a=085007>.
- Heidbrink, W. W., E. J. Strait, et al. (Aug. 1993). “Observation of beta-induced Alfvén eigenmodes in the DIII-D tokamak.” In: *Phys. Rev. Lett.* 71.6, pp. 855–858. DOI: 10.1103/PhysRevLett.71.855.
- Hofmann, F., J. B. Lister, et al. (1994). “Creation and control of variably shaped plasmas in TCV.” In: *Plasma Physics and Controlled Fusion* 36.12B, B277. URL: <http://stacks.iop.org/0741-3335/36/i=12B/a=023>.
- Hofmann, F., O. Sauter, et al. (Oct. 1998). “Experimental and Theoretical Stability Limits of Highly Elongated Tokamak Plasmas.” In: *Phys. Rev. Lett.* 81 (14), pp. 2918–2921. DOI: 10.1103/PhysRevLett.81.2918. URL: <http://link.aps.org/doi/10.1103/PhysRevLett.81.2918>.
- Hutchinson, I.H. (2005). *Principles of Plasma Diagnostics*. Cambridge University Press. ISBN: 9780521675741. URL: <http://books.google.ch/books?id=pUUZKLR00RIC>.

- Huysmans, G. T. A. et al. (2009). “Non-linear MHD simulations of edge localized modes (ELMs).” In: *Plasma Physics and Controlled Fusion* 51.12, p. 124012. URL: <http://stacks.iop.org/0741-3335/51/i=12/a=124012>.
- Ido, T. et al. (2006). “Geodesic–acoustic-mode in JFT-2M tokamak plasmas.” In: *Plasma Physics and Controlled Fusion* 48.4, S41. URL: <http://stacks.iop.org/0741-3335/48/i=4/a=S04>.
- Ikeda, K. (2007). “Progress in the ITER Physics Basis.” In: *Nuclear Fusion* 47.6. URL: <http://stacks.iop.org/0029-5515/47/i=6/a=E01>.
- Itoh, K. et al. (2006). “Geodesic Acoustic Eigenmodes.” In: *Plasma and Fusion Research* 1, pp. 037–037.
- Jolliet, S. et al. (2007). “A global collisionless PIC code in magnetic coordinates.” In: *Computer Physics Communications* 177.5, pp. 409–425. ISSN: 0010-4655. DOI: 10.1016/j.cpc.2007.04.006. URL: <http://www.sciencedirect.com/science/article/pii/S0010465507002251>.
- Kalupin, D. et al. (2006). “On the difference of H-mode power threshold in divertor and limiter tokamaks.” In: *Plasma Phys. Controlled Fusion* 48.5A, A309. URL: <http://stacks.iop.org/0741-3335/48/i=5A/a=S30>.
- Kantor, M. et al. (2009). “Thomson scattering system on the TEXTOR tokamak using a multi-pass laser beam configuration.” In: *Plasma Physics and Controlled Fusion* 51.5, p. 055002. URL: <http://stacks.iop.org/0741-3335/51/i=5/a=055002>.
- Kass, T., H.-S. Bosch, et al. (1998). “The fishbone instability in ASDEX Upgrade.” In: *Nucl. Fusion* 38.6, p. 807. URL: <http://stacks.iop.org/0029-5515/38/i=6/a=303>.
- Kass, T., S. Günter, et al. (1998). “Characteristics of type I and type III ELM precursors in ASDEX upgrade.” In: *Nuclear Fusion* 38.1, p. 111. URL: <http://stacks.iop.org/0029-5515/38/i=1/a=310>.
- Keilhacker, M. et al. (1999). “High fusion performance from deuterium-tritium plasmas in JET.” In: *Nuclear Fusion* 39.2, p. 209. URL: <http://stacks.iop.org/0029-5515/39/i=2/a=306>.
- Kim, Y. C. and E. J. Powers (June 1979). “Digital Bispectral Analysis and Its Applications to Nonlinear Wave Interactions.” In: *Plasma Science, IEEE Transactions on* 7.2, pp. 120–131. ISSN: 0093-3813. DOI: 10.1109/TPS.1979.4317207.
- Kirk, A. et al. (May 2006). “Evolution of Filament Structures during Edge-Localized Modes in the MAST Tokamak.” In: *Phys. Rev. Lett.* 96 (18), p. 185001. DOI: 10.1103/PhysRevLett.96.185001. URL: <http://link.aps.org/doi/10.1103/PhysRevLett.96.185001>.
- Klimanov, I. et al. (2007). “Generation of suprathermal electrons during sawtooth crashes in a tokamak plasma.” In: *Plasma Physics and Controlled Fusion* 49.3, p. L1. URL: <http://stacks.iop.org/0741-3335/49/i=3/a=L01>.
- Krämer-Flecken, A., V. Dreval, et al. (2004). “Turbulence studies with means of reflectometry at TEXTOR.” In: *Nucl. Fusion* 44.11, pp. 1143–1157. URL: <http://stacks.iop.org/0029-5515/44/1143>.
- Krämer-Flecken, A., S. V. Soldatov, H. R. Koslowski, et al. (2006). “Properties of Geodesic Acoustic Modes and the Relation to Density Fluctuations.” In: *Phys. Rev. Lett.* 97.4, 045006, p. 045006. DOI: 10.1103/PhysRevLett.97.045006. URL: <http://link.aps.org/abstract/PRL/v97/e045006>.

BIBLIOGRAPHY

- Krämer-Flecken, A., S. V. Soldatov, D. Reiser, et al. (2009). “Investigation of geodesic acoustic modes and related zonal flows at TEXTOR.” In: *Plasma Phys. Controlled Fusion* 51.1, 015001 (19pp). URL: <http://stacks.iop.org/0741-3335/51/015001>.
- Krämer-Flecken, A., S. V. Soldatov, B Vowinkel, et al. (2010). “Correlation reflectometry at TEXTOR.” In: *Rev. Sci. Instrum.* 81.11, 113502, p. 113502. DOI: 10.1063/1.3497305. URL: <http://link.aip.org/link/?RSI/81/113502/1>.
- Lan, T. et al. (2008). “Spectral characteristics of geodesic acoustic mode in the HL-2A tokamak.” In: *Plasma Physics and Controlled Fusion* 50.4, p. 045002. URL: <http://stacks.iop.org/0741-3335/50/i=4/a=045002>.
- Leerink, S. et al. (Oct. 2012). “Multiscale Investigations of Drift-Wave Turbulence and Plasma Flows: Measurements and Total-Distribution-Function Gyrokinetic Simulations.” In: *Phys. Rev. Lett.* 109 (16), p. 165001. DOI: 10.1103/PhysRevLett.109.165001. URL: <http://link.aps.org/doi/10.1103/PhysRevLett.109.165001>.
- Loarte, A. et al. (2007). “Transient heat loads in current fusion experiments, extrapolation to ITER and consequences for its operation.” In: *Physica Scripta* 2007.T128, p. 222. URL: <http://stacks.iop.org/1402-4896/2007/i=T128/a=043>.
- Marinoni, A. (2009). “Plasma Fluctuation Studies in the TCV Tokamak: Modeling of Shaping Effects and Advanced Diagnostic Development.” PhD thesis. Switzerland: Ecole Polytechnique Fédérale de Lausanne.
- Marinoni, A., S. Brunner, et al. (2009). “The effect of plasma triangularity on turbulent transport: modeling TCV experiments by linear and non-linear gyrokinetic simulations.” In: *Plasma Physics and Controlled Fusion* 51.5, p. 055016. URL: <http://stacks.iop.org/0741-3335/51/i=5/a=055016>.
- Marinoni, A., S. Coda, et al. (2006). “Design of a tangential phase contrast imaging diagnostic for the TCV tokamak.” In: *Rev. Sci. Instrum.* 77.10, 10E929, 10E929. DOI: 10.1063/1.2222333. URL: <http://link.aip.org/link/?RSI/77/10E929/1>.
- Matsunaga, G., N Aiba, et al. (2010). “Interactions between MHD instabilities in the wall-stabilized high-beta plasmas.” In: *Proceedings of the 23rd IAEA Fusion Energy Conference*, EXS/5-3.
- Matsunaga, G., K. Kamiya, et al. (2012). “Observation of energetic particle driven axisymmetric mode in the JT-60U tokamak.” In: *Proceedings of the 39th EPS Conference on Plasma Phys. Stockholm, 2 - 6 July 2012*, P2.062.
- Matsunaga, G., K Shinohara, et al. (2010). “Energetic particle driven instability in wall-stabilized high-beta plasmas.” In: *Nucl. Fusion* 50.8, p. 084003. URL: <http://stacks.iop.org/0029-5515/50/i=8/a=084003>.
- Mazurenko, A. (2001). PhD thesis. Massachusetts Institute of Technology.
- Mazzucato, E. (1998a). “Microwave reflectometry for magnetically confined plasmas.” In: *Rev. Sci. Instrum.* 69.6, pp. 2201–2217. DOI: 10.1063/1.1149121. URL: <http://link.aip.org/link/?RSI/69/2201/1>.
- (1998b). “Numerical study of microwave reflectometry in plasmas with two-dimensional turbulent fluctuations.” In: *Rev. Sci. Instrum.* 69.4, pp. 1691–1698. DOI: 10.1063/1.1148828. URL: <http://link.aip.org/link/?RSI/69/1691/1>.
- Mazzucato, E., T. Munsat, et al. (2002). “Fluctuation measurements in tokamaks with microwave imaging reflectometry.” In: *Review, Tutorial and Invited Papers from the 43rd Annual Meeting of the APS Division of Plasma Physics*. Vol. 9. 5. Long Beach,

- California (USA): AIP, pp. 1955–1961. DOI: 10.1063/1.1435564. URL: <http://link.aip.org/link/?PHP/9/1955/1>.
- Mazzucato, E. and R. Nazikian (Sept. 1993). “Radial scale length of turbulent fluctuations in the main core of TFTR plasmas.” In: *Phys. Rev. Lett.* 71.12, pp. 1840–1843. DOI: 10.1103/PhysRevLett.71.1840.
- McGuire, K. et al. (Mar. 1983). “Study of High-Beta Magnetohydrodynamic Modes and Fast-Ion Losses in PDX.” In: *Phys. Rev. Lett.* 50.12, pp. 891–895. DOI: 10.1103/PhysRevLett.50.891.
- McKee, G. R., R. J. Fonck, M. W. Jakubowski, K. H. Burrell, et al. (2003a). “Experimental characterization of coherent, radially-sheared zonal flows in the DIII-D tokamak.” In: *Physics of Plasmas* 10.5, pp. 1712–1719. DOI: 10.1063/1.1559974. URL: <http://link.aip.org/link/?PHP/10/1712/1>.
- McKee, G. R., R. J. Fonck, M. W. Jakubowski, K. H. Burrell, et al. (2003b). “Observation and characterization of radially sheared zonal flows in DIII-D.” In: *Plasma Physics and Controlled Fusion* 45.12A, A477. URL: <http://stacks.iop.org/0741-3335/45/i=12A/a=031>.
- McKee, G. R., D. K. Gupta, et al. (2006). “Structure and scaling properties of the geodesic acoustic mode.” In: *Plasma Physics and Controlled Fusion* 48.4, S123. URL: <http://stacks.iop.org/0741-3335/48/i=4/a=S09>.
- Meijere, C. A. de et al. (2012). “Observations on turbulence and beam-ion driven modes in TEXTOR.” In: *Plasma Physics and Controlled Fusion* 54.10, p. 105024. URL: <http://stacks.iop.org/0741-3335/54/i=10/a=105024>.
- Melnikov, A. V. et al. (2006). “Investigation of geodesic acoustic mode oscillations in the T-10 tokamak.” In: *Plasma Physics and Controlled Fusion* 48.4, S87. URL: <http://stacks.iop.org/0741-3335/48/i=4/a=S07>.
- Moret, J.-M., F. Buhlmann, et al. (1998). “Magnetic measurements on the TCV Tokamak.” In: *Review of Scientific Instruments* 69.6, pp. 2333–2348. DOI: 10.1063/1.1148940. URL: <http://link.aip.org/link/?RSI/69/2333/1>.
- Moret, J.-M., S. Franke, et al. (Sept. 1997). “Influence of Plasma Shape on Transport in the TCV Tokamak.” In: *Phys. Rev. Lett.* 79 (11), pp. 2057–2060. DOI: 10.1103/PhysRevLett.79.2057. URL: <http://link.aps.org/doi/10.1103/PhysRevLett.79.2057>.
- Nagashima, Y. et al. (2006). “Observation of coherent bicoherence and biphasic in potential fluctuations around geodesic acoustic mode frequency on JFT-2M.” In: *Plasma Physics and Controlled Fusion* 48.5A, A377. URL: <http://stacks.iop.org/0741-3335/48/i=5A/a=S38>.
- Nazikian, R., G. Y. Fu, et al. (Oct. 2008). “Intense Geodesic Acousticlike Modes Driven by Suprathermal Ions in a Tokamak Plasma.” In: *Phys. Rev. Lett.* 101 (18), p. 185001. DOI: 10.1103/PhysRevLett.101.185001. URL: <http://link.aps.org/doi/10.1103/PhysRevLett.101.185001>.
- Nazikian, R. and E. Mazzucato (1995). “Reflectometer measurements of density fluctuations in tokamak plasmas (invited).” In: *Rev. Sci. Instrum.* 66.1, pp. 392–398. DOI: 10.1063/1.1146357. URL: <http://link.aip.org/link/?RSI/66/392/1>.
- Nazikian, R. and L. E. Sharp (1987). “CO₂ laser scintillation interferometer for the measurement of density fluctuations in plasma confinement devices.” In: *Review of Scientific Instruments* 58.11, pp. 2086–2091. DOI: 10.1063/1.1139468. URL: <http://link.aip.org/link/?RSI/58/2086/1>.

BIBLIOGRAPHY

- Piras, F. et al. (2010). ““Snowflake” H Mode in a Tokamak Plasma.” In: *Phys. Rev. Lett.* 105 (15), p. 155003. DOI: 10.1103/PhysRevLett.105.155003. URL: <http://link.aps.org/doi/10.1103/PhysRevLett.105.155003>.
- Pitzschke, A. (2011). “Pedestal Characteristics and MHD Stability of H-Mode Plasmas in TCV.” PhD thesis. Lausanne. DOI: 10.5075/epfl-thesis-4917. URL: <http://library.epfl.ch/theses/?nr=4917>.
- Porcelli, F. (1991). “Fast particle stabilisation.” In: *Plasma Phys. Controlled Fusion* 33.13, p. 1601. URL: <http://stacks.iop.org/0741-3335/33/i=13/a=009>.
- Porte, L. (2012). In: *Proceedings of 17th Joint Workshop on Electron Cyclotron Emission and Electron Cyclotron Resonance Heating (EC-17), Deurne, The Netherlands, EPJ Web of Conferences 32, 03007*.
- Reimerdes, H., A. Pochelon, and W. Suttrop (1998). “Toroidally asymmetric ELM precursors in TCV.” In: *Nuclear Fusion* 38.3, p. 319. URL: <http://stacks.iop.org/0029-5515/38/i=3/a=101>.
- Rossel, J.X. et al. (2012). “Edge-localized mode control by electron cyclotron waves in a tokamak plasma.” In: *Nuclear Fusion* 52.3, p. 032004. URL: <http://stacks.iop.org/0029-5515/52/i=3/a=032004>.
- Sabot, R. et al. (2006). “A dual source D-band reflectometer for density profile and fluctuations measurements in Tore-Supra.” In: *Nuclear Fusion* 46.9, S685. URL: <http://stacks.iop.org/0029-5515/46/i=9/a=S04>.
- Soldatov, S. V., A. Krämer-Flecken, M. Kantor, et al. (2010). “Turbulence, flows and edge localized mode (ELM) dynamics in limiter H-mode plasmas in TEXTOR.” In: *Plasma Phys. Controlled Fusion* 52.8, p. 085001. URL: <http://stacks.iop.org/0741-3335/52/i=8/a=085001>.
- Soldatov, S. V., A. Krämer-Flecken, and C. N. Klimov (2009). “Investigation of the poloidal spectral resolution of O-mode reflectometry with two-dimensional full-wave modeling.” In: *Fusion Eng. Des.* 84.1, pp. 64–71. ISSN: 0920-3796. DOI: DOI:10.1016/j.fusengdes.2008.10.004. URL: <http://www.sciencedirect.com/science/article/B6V3C-4V5XP44-1/2/3b3a029bd862251ce54d918544ddaef8>.
- Strait, E. J., W. W. Heidbrink, and A. D. Turnbull (1994). “Doppler shift of the TAE mode frequency in DIII-D.” In: *Plasma Phys. Controlled Fusion* 36.7, p. 1211. URL: <http://stacks.iop.org/0741-3335/36/i=7/a=008>.
- Tanaka, K. et al. (2008). “Two-dimensional phase contrast imaging for local turbulence measurements in large helical device (invited).” In: *Review of Scientific Instruments* 79.10, 10E702, 10E702. DOI: 10.1063/1.2988821. URL: <http://link.aip.org/link/?RSI/79/10E702/1>.
- Tsui, H. Y. W., P. M. Schoch, and A. J. Wootton (1993). “Observation of a quasicohherent mode in the Texas Experimental Tokamak.” In: *Physics of Fluids B: Plasma Physics* 5.4, pp. 1274–1280. DOI: 10.1063/1.860918. URL: <http://link.aip.org/link/?PFB/5/1274/1>.
- Tynan, G. R., A. Fujisawa, and G. R. McKee (2009). “A review of experimental drift turbulence studies.” In: *Plasma Phys. Controlled Fusion* 51.11, 113001 (77pp). URL: <http://stacks.iop.org/0741-3335/51/113001>.
- Unterberg, B. et al. (2009). “The influence of resonant magnetic perturbations on edge transport in limiter H-mode plasmas in TEXTOR.” In: *J. Nucl. Mater.* 390-391, pp. 351–354. ISSN: 0022-3115. DOI: DOI:10.1016/j.jnucmat.2009.01.305. URL: <http://www.sciencedirect.com/science/article/B6V3C-4V5XP44-1/2/3b3a029bd862251ce54d918544ddaef8>.

- <http://www.sciencedirect.com/science/article/B6TXN-4VHSDP9-2/2/bba87f1d2c4f2b8fd258ed67127212cd>.
- Valeo, E. J., G. J. Kramer, and R. Nazikian (2002). “Two-dimensional simulations of correlation reflectometry in fusion plasmas.” In: *Plasma Phys. Controlled Fusion* 44.2, pp. L1–L10. URL: <http://stacks.iop.org/0741-3335/44/L1>.
- Vernay, T. (Oct. 2012). Private communication.
- Vernay, T. et al. (2010). “Neoclassical equilibria as starting point for global gyrokinetic microturbulence simulations.” In: *Physics of Plasmas* 17.12, 122301, p. 122301. DOI: 10.1063/1.3519513. URL: <http://link.aip.org/link/?PHP/17/122301/1>.
- Wagner, F. (2007). “A quarter-century of H-mode studies.” In: *Plasma Phys. Controlled Fusion* 49.12B, B1–B33. URL: <http://stacks.iop.org/0741-3335/49/B1>.
- Wahlberg, C. (Sept. 2008). “Geodesic Acoustic Mode Induced by Toroidal Rotation in Tokamaks.” In: *Phys. Rev. Lett.* 101 (11), p. 115003. DOI: 10.1103/PhysRevLett.101.115003. URL: <http://link.aps.org/doi/10.1103/PhysRevLett.101.115003>.
- (2009). “Low-frequency magnetohydrodynamics and geodesic acoustic modes in toroidally rotating tokamak plasmas.” In: *Plasma Physics and Controlled Fusion* 51.8, p. 085006. URL: <http://stacks.iop.org/0741-3335/51/i=8/a=085006>.
- Weisen, H. (1988). “The phase contrast method as an imaging diagnostic for plasma density fluctuations (invited).” In: *Rev. Sci. Instrum.* 59.8, pp. 1544–1549. DOI: 10.1063/1.1140193. URL: <http://link.aip.org/link/?RSI/59/1544/1>.
- Wesson, J. (2011). *Tokamaks*. 4th ed. Oxford University Press.
- Winsor, N., J. L. Johnson, and J. M. Dawson (1968). “Geodesic Acoustic Waves in Hydromagnetic Systems.” In: *Phys. Fluids* 11.11, pp. 2448–2450. DOI: 10.1063/1.1691835. URL: <http://link.aip.org/link/?PFL/11/2448/1>.
- Wolfe, W.L. et al. (1985). *The Infrared handbook*. Press Monographs. Environmental Research Institute of Michigan. URL: <http://books.google.ch/books?id=LDhSAAAAMAAJ>.
- Xu, X. Q. et al. (May 2008). “Tempest Simulations of Collisionless Damping of the Geodesic-Acoustic Mode in Edge-Plasma Pedestals.” In: *Phys. Rev. Lett.* 100 (21), p. 215001. DOI: 10.1103/PhysRevLett.100.215001. URL: <http://link.aps.org/doi/10.1103/PhysRevLett.100.215001>.
- Xu, Y. et al. (2011). “Observation of geodesic acoustic modes (GAMs) and their radial propagation at the edge of the TEXTOR tokamak.” In: *Plasma Physics and Controlled Fusion* 53.9, p. 095015. URL: <http://stacks.iop.org/0741-3335/53/i=9/a=095015>.
- Yun, G. S. et al. (July 2011). “Two-Dimensional Visualization of Growth and Burst of the Edge-Localized Filaments in KSTAR H-Mode Plasmas.” In: *Phys. Rev. Lett.* 107 (4), p. 045004. DOI: 10.1103/PhysRevLett.107.045004. URL: <http://link.aps.org/doi/10.1103/PhysRevLett.107.045004>.
- Zhao, J. et al. (1999). “Damage threshold of HgCdTe induced by continuous-wave CO₂ laser.” In: *Applied Physics Letters* 74.8, pp. 1081–1083. DOI: 10.1063/1.123488. URL: <http://link.aip.org/link/?APL/74/1081/1>.
- Zhao, K. J., T. Lan, et al. (June 2006). “Toroidal Symmetry of the Geodesic Acoustic Mode Zonal Flow in a Tokamak Plasma.” In: *Phys. Rev. Lett.* 96 (25), p. 255004. DOI: 10.1103/PhysRevLett.96.255004. URL: <http://link.aps.org/doi/10.1103/PhysRevLett.96.255004>.

BIBLIOGRAPHY

- Zohm, H. (1996). “Edge localized modes (ELMs).” In: *Plasma Phys. Controlled Fusion* 38.2, p. 105. URL: <http://stacks.iop.org/0741-3335/38/i=2/a=001>.
- Zoletnik, S. et al. (2012). “Methods for the detection of Zonal Flows using one-point and two-point turbulence measurements.” In: *Plasma Physics and Controlled Fusion* 54.6, p. 065007. URL: <http://stacks.iop.org/0741-3335/54/i=6/a=065007>.
- Zonca, F. and L. Chen (2008). “Radial structures and nonlinear excitation of geodesic acoustic modes.” In: *EPL (Europhysics Letters)* 83.3, p. 35001. URL: <http://stacks.iop.org/0295-5075/83/i=3/a=35001>.

Kees DE MEIJERE

Engineering Physicist

Rue Marterey 74
CH-1005 Lausanne
Switzerland
+41 76 24 20278
demeijere@gmail.com

EDUCATION

Ecole Polytechnique Fédérale de Lausanne, Switzerland

PhD in Physics (2007-2012 [expected]):

- Commissioning of a novel, laser-based phase-contrast imaging system in the TCV tokamak; characterization of the geodesic acoustic mode with this instrument
- Reflectometry measurements of turbulence and ELM precursor modes in the TEXTOR tokamak (Forschungszentrum Jülich, Germany)

Centre de Cadarache du Commissariat à l'Energie Atomique, France

Research internship (2007): development and implementation in the Cronos tokamak simulator of a simplified numerical model of particle fueling

Delft University of Technology, Netherlands

M.Sc. Applied Physics (2000-2007): a study of the relation between the current distribution and thermal diffusivity in the JET tokamak

PUBLICATIONS AND CONFERENCES

- <http://stacks.iop.org/0741-3335/54/i=10/a=105024>
- <http://ocs.ciemat.es/EPS2011PAP/pdf/P1.137.pdf>

LANGUAGES

- Dutch: native
- English: excellent
- French: good

PERSONAL INFORMATION

- Full name: Cornelis Adrianus DE MEIJERE
- Nationality: Dutch (Swiss B-permit)
- Civil status: unmarried
- Date of birth: July 10, 1982